Development of a High Energy Density Gas Diffusion Electrode for Li-O_2 Batteries

Max Jenkins

Corpus Christi College
University of Oxford

A thesis submitted for the degree of
Doctor of Philosophy

Trinity 2023

Abstract

The lithium-oxygen (Li-O_2) battery has the highest theoretical specific energy and energy density amongst modern energy storage technologies. If these can be realised in a practical device, the Li-O_2 battery could transform energy storage. There are, however, significant challenges which must be overcome before the move towards a practical device can be considered. These include the improvement of the reversibility of the positive electrode reactions, the development of a high-performance positive Gas Diffusion Electrode (GDE) and the stabilisation of the Li metal negative electrode. The following thesis deals with the second of these challenges, namely the development of a GDE which allows for sufficient O_2 mass transport to achieve high areal capacities at practical discharge rates.

In the first results chapter, a Gas Diffusion Polymer (GDP) is introduced into the GDE with the dual purpose of binding carbon together and transporting oxygen throughout the volume of the electrode. The GDP allows for areal capacities of 30 mAh cm^{-2} at discharge rates of 1 mA cm^{-2}. A new technique is introduced to quantify the distribution of lithium peroxide at the end of discharge, presenting evidence of the oxygen mass transport capabilities of the GDE.

The second results chapter introduces oxygen diffusion channels into the newly developed GDE. Li_2O_2 depth profiling experiments on a 500 μm thick electrode provides insight into the ideal channel architecture. The channels are then fabricated with the aid of sub-micron scale 3D-printing.

Acknowledging the instability of the cell during discharge and charge, the final results chapter explores the cyclability of high energy density GDEs. The accumulation of lithium carbonate causes cell death after only 12 cycles. By removing the lithium carbonate, the cell is able to sustain cycling for a further 10 cycles.

Development of a High Energy Density Gas Diffusion Electrode for Li-O_2 Batteries



Max Jenkins

Corpus Christi College

University of Oxford

A thesis submitted for the degree of

Doctor of Philosophy

Trinity 2023

Abstract

The lithium-oxygen (Li-O_2) battery has the highest theoretical specific energy and energy density amongst modern energy storage technologies. If these can be realised in a practical device, the Li-O_2 battery could transform energy storage. There are, however, significant challenges which must be overcome before the move towards a practical device can be considered. These include the improvement of the reversibility of the positive electrode reactions, the development of a high-performance positive Gas Diffusion Electrode (GDE) and the stabilisation of the Li metal negative electrode. The following thesis deals with the second of these challenges, namely the development of a GDE which allows for sufficient O_2 mass transport to achieve high areal capacities at practical discharge rates.

In the first results chapter, a Gas Diffusion Polymer (GDP) is introduced into the GDE with the dual purpose of binding carbon together and transporting oxygen throughout the volume of the electrode. The GDP allows for areal capacities of 30 mAh cm^{-2} at discharge rates of 1 mA cm^{-2}. A new technique is introduced to quantify the distribution of lithium peroxide at the end of discharge, presenting evidence of the oxygen mass transport capabilities of the GDE.

The second results chapter introduces oxygen diffusion channels into the newly developed GDE. Li_2O_2 depth profiling experiments on a 500 μm thick electrode provides insight into the ideal channel architecture. The channels are then fabricated with the aid of sub-micron scale 3D-printing.

Acknowledging the instability of the cell during discharge and charge, the final results chapter explores the cyclability of high energy density GDEs. The accumulation of lithium carbonate causes cell death after only 12 cycles. By removing the lithium carbonate, the cell is able to sustain cycling for a further 10 cycles.

Acknowledgements

First and foremost, I would like to express my sincere gratitude to my supervisor, Sir Peter Bruce. I have thoroughly enjoyed the opportunity to work under your supervision in what is a world-leading research group. I would also like to thank him, and EPSRC for funding me for the duration of my DPhil.

I would like to thank Dr Sunyhik Ahn for his help in starting my DPhil projects. His help and guidance have been invaluable. I would also like to thank Professor Xiangwen Gao for supporting my work in the latter stages of the DPhil. The Li-O_2 group members over the years have been brilliant. In particular Alex Pateman who showed me the ropes in Oxford and hosted many a great night in Oriel MCR. Ceren Zor, who has been a great friend. Daniel Dewar, who has been a great help in getting papers over the line and who has been extremely proactive with research. Marco Lagnoni, of the Univerity of Pisa, who has been a great friend and collaborator. Chloe Chau, who has also been a great friend and had the misfortune of sitting opposite me for two years. Thank you all.

Similarly, the wider Bruce group members have been great fun to spend time with over the years. The pub trips, dinners and nights out have been so enjoyable and the pessimistic chats about the state of batteries, our research, etc. have been very cathartic despite the fact we actually enjoy what we do.

I am probably most grateful to Oxford University Amateur Boxing Club where I truly found my people. At a University where people often try to be something they are not, that can feel exclusive and elitist, the boxers are down to earth, accepting and fun. I cannot possibly name all of those at OUABC that have had an impact on me during my time at Oxford. But shout out to Dave, Harley, Rob, Greg, Zoran and Suzanne (the coaching team) who may have never been properly acknowledged for what they do. All of the best people I have met at this University have been through the boxing club.

I would like to thank Freya, who has stayed by my side during the course of my DPhil and has been incredibly supportive, caring and understanding.

Finally, I would like to thank my Mum, Dad, and Sister who have been there for me for a little over 30 years now. They have supported me in every way possible. And Amari, my nephew (2 and a bit years old) who has provided insightful discussion, brilliant entertainment and thoughtful advice.

Declaration

I, Max Jenkins, hereby declare that this doctoral thesis, which is approximately 36000 words in length, has been written by me and is a record of work that I have carried out. The work presented here has not been submitted in any previous application for a higher degree.

Max Jenkins
Trinity 2023

Contents

List of Figures **xiii**

List of Tables **xvii**

List of Abbreviations **xix**

List of Publications **xxi**

1 Introduction **1**
1.1 Wider Context . . . 1
1.2 Introduction to the Li-O_2 Battery . . . 3
1.2.1 Inside the Battery . . . 3
1.2.2 How the Battery Operates . . . 4
1.3 Fundamental Electrochemistry of the Li-O_2 Battery . . . 6
1.3.1 Discharge Mechanism . . . 6
1.3.2 Charge Mechanism . . . 18
1.3.3 Parasitic Electrochemistry . . . 22
1.3.4 Redox Mediators . . . 30
1.4 Challenges at the Cathode . . . 35
1.4.1 Carbon Materials . . . 35
1.4.2 Pore Structure and Surface Area . . . 37
1.4.3 Polymer Binders . . . 41
1.4.4 Oxygen Mass Transport and Pore Clogging . . . 44
1.4.5 High-Capacity Cathodes . . . 50
1.5 Thesis Objectives . . . 55
1.6 References . . . 55

2 Experimental **67**
2.1 Materials Preparation . . . 68
2.1.1 Electrode Fabrication . . . 68
2.1.2 Water control measures . . . 69
2.1.3 3D-Printing . . . 71
2.2 Electrochemical Techniques . . . 74
2.2.1 Cell Assembly . . . 74
2.2.2 Galvanostatic Cycling with Potential Limitation (GCPL) . . . 74
2.2.3 Linear Sweep Voltammetry (LSV) and Cyclic Voltammetry (CV) 76
2.2.4 Chronoamperometry (CA) . . . 77

2.3 Characterisation . . . 78
2.3.1 Scanning Electron Microscopy (SEM) . . . 78
2.3.2 Energy Dispersive X-Ray Spectroscopy (EDX) . . . 80
2.3.3 Fourier Transform Infrared Spectroscopy (FTIR) . . . 81
2.3.4 Raman Spectroscopy . . . 84
2.3.5 Powder X-Ray Diffraction (PXRD) . . . 86
2.3.6 UV-vis Spectroscopy and Li_2O_2 Titration Technique . . . 87
2.3.7 BET Surface Area Analysis . . . 89
2.3.8 Mercury Intrusion Porosimetry (MIP) . . . 93
2.3.9 Thermogravimetric Analysis (TGA) . . . 94
2.3.10 Differential Electrochemical Mass Spectrometry (DEMS) . . . 95
2.3.11 Pressure Monitoring . . . 97
2.4 References . . . 98

3 Gas Diffusion Polymer as a Dual Purpose Binder 101
3.1 Introduction . . . 101
3.2 Experimental . . . 102
3.3 Results and Discussion . . . 105
3.3.1 Structural Characterisation of the Pristine GDE . . . 105
3.3.2 Optimisation of the GDE Composition and Thickness . . . 110
3.3.3 Rate Analysis and Li_2O_2 Distribution . . . 112
3.3.4 Visualisation of the Discharged GDE . . . 116
3.3.5 Chemical Characterisation of the Discharge Product . . . 118
3.4 Conclusion . . . 122
3.5 References . . . 123

4 A Gas Diffusion Electrode with O_2 Diffusion Channels 126
4.1 Introduction . . . 126
4.2 Experimental . . . 127
4.3 Results and Discussion . . . 130
4.3.1 Gas Diffusion Electrode Design . . . 130
4.3.2 O_2 Diffusion Channel Fabrication . . . 137
4.3.3 Discharge Behaviour and Li_2O_2 Distribution in Channel GDEs . . . 142
4.3.4 Characterisation of the Discharge Product . . . 144
4.4 Conclusion . . . 146
4.5 References . . . 147

5 The Accumulation of Li_2CO_3 in a Li-O_2 Battery During Cycling 149
5.1 Introduction . . . 149
5.2 Experimental . . . 150
5.3 Cycling Results and Discussion . . . 152
5.3.1 Cycling a Gas Diffusion Electrode with Dual Mediators . . . 152
5.3.2 Characterisation of the Cycling Products . . . 154
5.3.3 Li_2CO_3 Removal and Further Cycling . . . 159
5.3.4 Current Status of Li-O_2 Batteries . . . 163
5.4 Conclusion . . . 166
5.5 References . . . 166

6 Conclusions and Further Work 169

6.1 Conclusions 169
6.2 Further Work 171
6.2.1 Gas Diffusion Polymers 171
6.2.2 O_2 Diffusion Channels 171
6.2.3 Li_2CO_3 Accumulation 172

List of Figures

1.1 Schematic of a Li-O_2 Battery 4

1.2 A typical discharge-charge cycle of a Li-O_2 battery 5

1.3 Solution vs surface mechanism of oxygen reduction 7

1.4 Evidence for O_2^-/LiO_2 formation on discharge in Li-O_2 batteries 9

1.5 TEM image of discrete Li_2O_2 plates which make up a Li_2O_2 toroidal particle 11

1.6 Evidence for the solution mediated charge mechanism 21

1.7 Electrolyte degradation pathways with reactive oxygen species 24

1.8 DEMS data of isotopically labelled carbon collected by McCloskey *et al.* 29

1.9 Mechanism of DBBQ Redox Mediation 32

1.10 Schematic of the various forms of carbon commonly used in Li-O_2 batteries 36

1.11 Pore network model developed from nanocomputed tomography by Torayev *et al.* 40

1.12 Chemical structures of commonly used polymers in Li-O_2 batteries 42

1.13 PAN cross-linked CNT network by Cui *et al.* 44

1.14 Li_2O_2 distribution experiments from the literature 48

1.15 High-capacity cathodes with decoupled Li^+, e^- and O_2 pathways 51

1.16 Nature-inspired high-capacity cathodes for Li-O_2 batteries 53

2.1 Voltage profile on an $LiFePO_4$ electrode during discharge of a Li-O_2 cell . 70

2.2 Schematic of the two-photon polymerisation process 72
2.3 Swagelok cell design used for discharge experiments 75
2.4 Schematic of a scanning electron microscope 80
2.5 Schematic of the potential energy of a harmonic oscillator 82
2.6 Schematic of the induced dipole moment on a homonuclear diatomic by the electric field of radiation 84
2.7 Schematic of the photon released after relaxation from a virtual excited state 85
2.8 Schematic of X-rays diffracting off of planes of atoms in a crystal 87
2.9 Measurement of Li_2O_2 distribution in discharged gas diffusion electrodes 89
2.10 Illustration of the types of BET isotherm 90
2.11 Illustration of the commonly observed hysteresis types in nitrogen adsorption/desorption experiments 92
2.12 Schematic illustration of mercury intrusion into a capillary pore 95
2.13 Schematic illustration of a typical *ex situ* DEMS experiment setup 96
2.14 Cell setup for pressure monitoring experiments 97

3.1 Structure of Teflon AF2400 105
3.2 SEM and EDX mapping of the pristine gas diffusion electrode 106
3.3 N_2 adsorption/desorption analysis of gas diffusion electrodes 108
3.4 Mercury intrusion porosimetry analysis of gas diffusion electrodes 109
3.5 Optimisation of GDE formulation and thickness 111
3.6 Rate capability of the optimised gas diffusion electrode 113
3.7 Li_2O_2 distribution in the discharged gas diffusion electrodes 114
3.8 Discharge data for GDEs with varied PTFE content 115
3.9 Li_2O_2 distribution comparison between discharged gas diffusion electrodes utilising PTFE and GDP 116
3.10 SEM imaging of the discharged gas diffusion electrodes 117
3.11 *Operando* pressure monitoring during LSV 119
3.12 Chemical characterisation of discharged gas diffusion electrodes 121

4.1 N_2 adsorption/desorption analysis of gas diffusion electrodes 131
4.2 Mercury intrusion porosimetry analysis of gas diffusion electrodes 132
4.3 SEM image of a cross-section of pristine gas diffusion electrode 132
4.4 Discharge data and energy density plot with varied gas diffusion electrode thickness 133
4.5 Li_2O_2 distributions for varied gas diffusion electrode thickness 134
4.6 Discharge data and energy density plot at varied rates for 500 μm thick gas diffusion electrodes 135
4.7 Li_2O_2 distributions for 500 μm thick gas diffusion electrodes discharged at various rates 136
4.8 Cross-sectional optical image of the pillar template 138
4.9 SEM images of the 3D-printed pillar templates 140
4.10 TGA analysis of the 3D-printed template, GDP and PTFE 141
4.11 SEM images of the channeled gas diffusion electrodes 141
4.12 Discharge data and Li_2O_2 distribution comparison between channelled and non-channelled gas diffusion electrodes 143
4.13 Energy density comparison between channeled and non-channeled gas diffusion electrodes 144
4.14 Chemical characterisation of discharged channel gas diffusion electrodes . 145
4.15 SEM characterisation of discharged channel gas diffusion electrodes . . . 146

5.1 Cycling data for a gas diffusion electrode with dual mediators 153
5.2 gas diffusion electrode thickness after discharge and energy density plot . 154
5.3 FTIR spectra of the charged gas diffusion electrodes during cycling . . . 155
5.4 Distribution of Li_2O_2 after discharge over several cycles 156
5.5 Distribution of Li_2CO_3 and Li_2O_2 after cell failure 157
5.6 SEM images of the gas interface of the gas diffusion electrode over several cycles 158
5.7 *In situ* pressure monitoring during discharge and charge 159

5.8 *In situ* pressure monitoring during LSV and CA of a cycled electrode after charge 160
5.9 Acid treatment comparing a cycled gas diffusion electrode and a cycled gas diffusion electrode after $DBDMB^+$ treatment 161
5.10 SEM images of the gas diffusion electrode gas interface before and after Li_2CO_3 removal 162
5.11 Cycling data after Li_2CO_3 removal 162

List of Tables

3.1 Comparison of BET surface area and pore structure for gas diffusion electrodes formed using the GDP or PTFE 110

3.2 Peak positions and full-width half maximum values for Raman spectroscopy of the discharged cathode 121

4.1 Summary of MIP and BET results for gas diffusion electrodes 133

4.2 Summary of EDX results collected for gas diffusion electrodes during channel fabrication 142

5.1 Table for material-to-system analysis of discharge data in chapter 3 . . . 165

List of Abbreviations

2PP	Two-photon polymerisation
AN	Acceptor number
AQ	Anthraquinone
BET	Brunauer-Emmett-Teller
CA	Chronoamperometry
CAD	Computer-aided design
CC BY	Creative commons attribution license
CNT	Carbon nanotube
CV	Cyclic voltammetry
DABCO	1,4-diazabicyclo[2.2.2]octane
DBBQ	2,5-di-tert-butyl-1,4-benzoquinone
DBDMB	2,5-di-tert-butyl-1,4-dimethoxybenzene
DEMS	Differential electrochemical mass spectroscopy
DMA	N,N-dimethylacetamide
DME	1,2-dimethoxyethane
DMSO	Dimethyl sulfoxide
DN	Donor number
EDX	Energy dispersive X-ray
EIS	Electrochemical impedance spectroscopy
EPR	Electron paramagnetic resonance
FTIR	Fourier transform infrared
GCPL	Galvanostatic cycling potential limitation
GDE	Gas diffusion electrode
GDP	Gas diffusion polymer
GWL	General writing language
hG	Holey graphene
KB	Ketjen Black
LFP	Lithium Iron Phosphate
LiTFSI	Lithium bis(trifluoromethanesulfonyl)imide
LSV	Linear sweep voltammetry
MIP	Mercury intrusion porosimetry
NMR	Nuclear magnetic resonance
OER	Oxygen evolution reaction
OPA	One-photon absorption
ORR	Oxygen reduction reaction
PAN	Polyacrylonitrile
PE	Polyethylene
PFC	Perfluorinated carbon
PITT	Potential intermittent titration technique
PNM	Pore network model
PP	Polypropylene
PTFE	Polytetrafluoroethylene
PVdF	Poly(vinylidene fluoride)
RRDE	Rotating ring disk electrode
SAED	Selected area electron diffraction
SECM	Scanning electrochemical microscopy
SEM	Scanning electron microscopy
SERS	Surface enhanced Raman spectroscopy
STL	Standard tesselation language
TBA	Tetrabutylammonium
TEGDME	Tetraglyme
TEM	Transmission electron microscopy
TEMPO	2,2,6,6-Tetramethylpiperidine 1-oxyl
t-G	Thermally reduced graphene
TGA	Thermogravimetric analysis
TTF	Tetrathiofulvalene
UV	Ultraviolet
XANES	X-ray absorption near edge spectroscopy
XPS	X-ray photoelectron spectroscopy
XRD	X-ray diffraction

List of Publications

First Author

1. Jenkins, M. *et al.* The Accumulation of Li_2CO_3 in a Li-O_2 Cell with Dual Mediators *Faraday Discussions*, (2023)

Contributing Author

1. Pu, S. *et al.* Achieving Ultrahigh-Rate Planar and Dendrite-Free Zinc Electroplating for Aqueous Zinc Battery Anodes *Advanced Materials* **34**, 2202552 (2022)

2. Ahn, S. *et al.* Why charging Li-air batteries with current low-voltage mediators is slow and singlet oxygen does not explain degradation *Nature Chemistry* **15**, 1022-1029 (2023)

3. Jordan J. W. *et al.* A Lithium-Air Battery and Gas Handling System Demonstrator *Faraday Discussions*, (2023)

1

Introduction

Contents

1.1 Wider Context 1
1.2 Introduction to the Li-O_2 Battery 3
1.2.1 Inside the Battery 3
1.2.2 How the Battery Operates 4
1.3 Fundamental Electrochemistry of the Li-O_2 Battery 6
1.3.1 Discharge Mechanism 6
1.3.2 Charge Mechanism 18
1.3.3 Parasitic Electrochemistry 22
1.3.4 Redox Mediators 30
1.4 Challenges at the Cathode 35
1.4.1 Carbon Materials 35
1.4.2 Pore Structure and Surface Area 37
1.4.3 Polymer Binders 41
1.4.4 Oxygen Mass Transport and Pore Clogging 44
1.4.5 High-Capacity Cathodes 50
1.5 Thesis Objectives 55
1.6 References 55

1.1 Wider Context

Climate change is already affecting every inhabited region across the earth. Human activity contributes to many observed climate and weather extremes, and it is now more

evident than ever that our energy should be derived from renewable sources.[1] To meet the long-term targets of the Paris Agreement - to limit global warming to below 2 °C and *resolve* to pursue efforts to limit the temperature increase to 1.5 °C - rapid and sustained reductions in greenhouse gas emissions are required this decade.[2,3] Transport has the highest reliance on fossil fuels of any sector and made up approximately 25 % of global energy-related CO_2 emissions in 2019.[4] The electrification of the transport industry, particularly light-duty vehicles, can result in less reliance on oil-based fuels, and if running on low-carbon energy sources can reduce greenhouse gas emissions significantly.[5] Electric vehicle markets are expanding rapidly, with global electric vehicle sales rising by 140 % in the first quarter of 2021 compared to the same period in 2020.[5] This expansion is being driven by several factors, with the cost of the battery pack playing a central role.

Lithium-ion batteries currently dominate the energy storage market. This technology relies on the reversible shuttling of lithium ions and electrons between two host materials to deliver and store electrical energy. Early research identified $LiCoO_2$ and graphite as suitable cathode and anode materials, respectively.[6,7] In 1987, Yoshino combined these materials with a carbonate-based electrolyte and patented what is now called the lithium-ion battery, achieving a reversible capacity of 130 mAh g^{-1} (based on $LiCoO_2$).[8] Since commercialisation, incremental improvements have been made in terms of cost and energy density with new materials such as lithium manganese oxide, lithium iron phosphate, and Ni-Mn-Co oxide cathodes finding commercial application.[9–12]

Despite their success, lithium-ion batteries face increased scrutiny over their reliance on critical minerals such as lithium, cobalt and graphite and their corresponding social, environmental and geopolitical issues.[13] Fragile supply chains and diversification of energy storage applications are leading researchers to look *beyond lithium-ion*. This requires new chemistries that promise higher energy, longer lifetimes and cheaper, more sustainable materials. To this effect, the lithium-oxygen (Li-O_2) battery presents a promising alternative.[14,15]

The Li-O_2 battery, first conceptualised by Abraham in 1996, relies on the reaction

between lithium ions and oxygen forming lithium peroxide.[16] Based on the mass of lithium peroxide, a specific energy of ∼3500 Wh kg^{-1} can be calculated, an order of magnitude higher than our current state-of-the-art lithium-ion batteries. Similarly, the materials utilised in the battery are low-cost and abundant. If this specific energy and low cost can be realised in a practical device the Li-O_2 battery could provide a transformational energy storage device for electric vehicles.

1.2 Introduction to the Li-O_2 Battery

1.2.1 Inside the Battery

A battery is a chemical device that is used to generate electricity and is composed of one or more *electrochemical cells* connected in series or parallel. An electrochemical cell is a device that generates electricity from chemical reactions (discharge) or electrical energy can be applied to cause a chemical reaction to occur (charge). A cell consists of three main functional components: a positive electrode and a negative electrode that is separated by an electrolyte that is capable of conducting ions but is electronically insulating, schematically shown in Figure 1.1. The active materials of each electrode are chosen such that they will react spontaneously i.e. the Gibbs free energy change associated with the net cell reaction is negative, given by the equation:

$$\Delta G = -nF(E_e^C - E_e^A) \tag{1.1}$$

where ΔG is the Gibbs free energy change associated with the net cell reaction (kJ mol^{-1}), n is the number of electrons transferred per molecule and E_e^C and E_e^A are the equilibrium potentials of the cathode and anode respectively (V).

A basic Li-O_2 cell commonly utilises a porous carbon-based cathode* comprised of a conductive carbon bound together by a polymer. The carbon cathode is not the active

*Within the battery research field the positive and negative electrodes are referred to as the cathode and anode respectively. Strictly speaking, the cathode and anode are where the oxidative and reductive processes occur, in which case the convention only applies on discharge as the redox processes reverse on charge. The conventional use of 'cathode' and 'anode' will be used throughout this thesis.

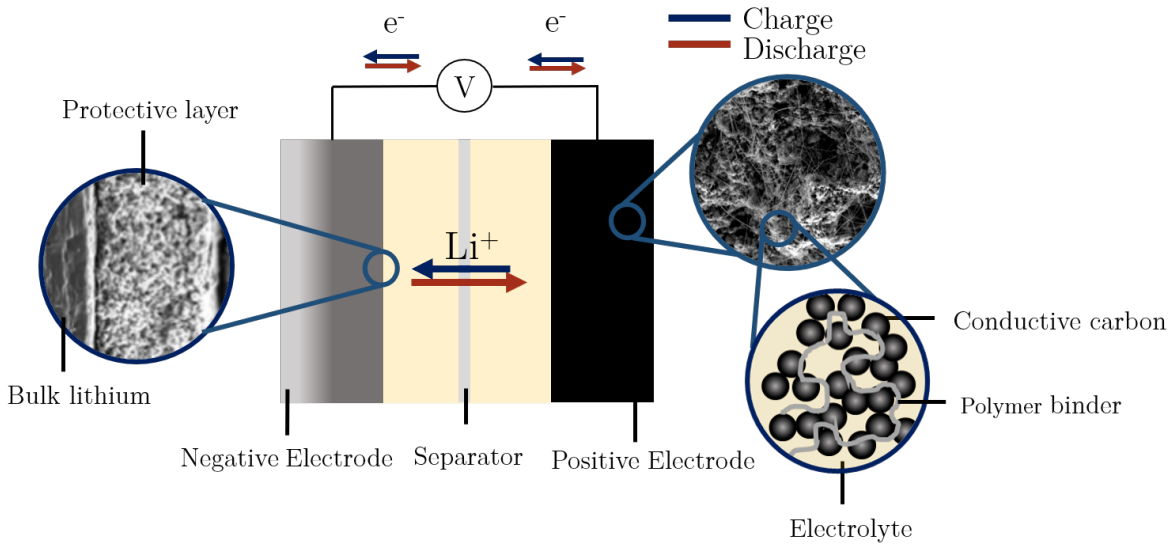


Figure 1.1: Schematic of a Li-O_2 battery. The cathode consists of a conductive carbon bound together with a polymer and the anode is lithium metal with a protective layer, such as a ceramic. The electrodes are separated with an electrolyte-filled separator. The electrolyte is Li^+ conductive but electronically insulating.

material but acts as a host to the active materials, namely oxygen and Li_2O_2. Carbon is usually chosen due to its lightweight, low-cost and chemical stability. The electrolyte is typically a non-aqueous solvent such as a glyme with a lithium-containing salt such as lithium bis(trifluoromethanesulfonyl)imide (LiTFSI). The electrolyte permeates the pores of the cathode and the separator allowing good conduction of Li^+ between the electrodes while making contact with the anode, which is typically lithium metal.

1.2.2 How the Battery Operates

A typical discharge-charge cycle is shown in Figure 1.2. Based on the standard Gibbs free energy of Reaction 1.2 an equilibrium voltage of 2.96 V vs Li^+/Li is calculated.

$$2Li_{(s)} + O_{2(g)} \leftrightarrow Li_2O_{2(s)} \tag{1.2}$$

The discharge profile exhibits a relatively flat plateau region where the discharge reaction proceeds at a near-constant voltage followed by an abrupt polarisation known as the "sudden death" region. The charge profile exhibits a sharp rise in potential followed by a plateau with another sharp rise in potential at the end of charge. The overpotential

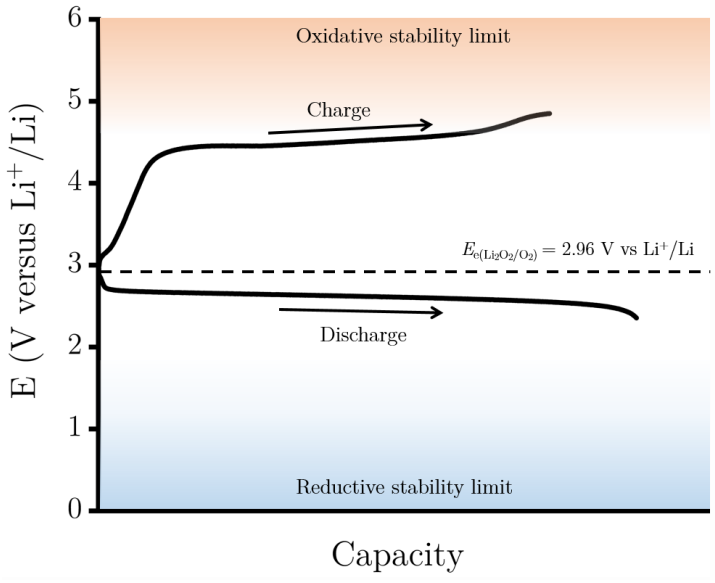


Figure 1.2: A typical discharge-charge cycle of a Li-O_2 battery. The discharge cycle exhibits a *sudden death* region at the end of discharge and a three-phase charge curve is observed with large overpotential. The red and blue shading indicates the oxidative and reductive potentials of an ether-based electrolyte.

on charge ($\sim$ 1 V) is greater than that on discharge ($\sim$ 0.2 V).

During discharge, dioxygen molecules enter the battery through the porous cathode, are dissolved into the electrolyte and are reduced forming superoxide. Simultaneously, the lithium metal anode is oxidised forming lithium cations in solution. Lithium peroxide is formed in a two-electron reaction at the cathode. The Li_2O_2 discharge product is insoluble in most non-aqueous solvents and immediately precipitates as it is formed. As Li_2O_2 builds up in the porous network of the cathode it prevents further diffusion of oxygen. As well as this, Li_2O_2 is electronically insulating and passivates the cathode as it formed. It is a combination of these effects that leads to polarisation and *sudden death* in the battery. Upon charge, Li_2O_2 is decomposed back into Li^+ and O_2.

1.3 Fundamental Electrochemistry of the Li-O_2 Battery

1.3.1 Discharge Mechanism

A comprehensive understanding of the discharge mechanism of Li-O_2 batteries is critical to exploiting their high capacities in a practical device. Oxygen reduction to Li_2O_2 in non-aqueous solvents has therefore received great research interest and is dependent on several factors, these include:

1. The Gutmann donor/acceptor number of the solvent
2. The Lewis acidity of the solvated lithium cation
3. Contaminants or additives in the electrolyte solution
4. The stability of the solvent to reactive oxygen species

Solution vs Electrode Surface Mechanism

The pathway of Li_2O_2 formation can occur via a *solution* or *electrode surface* route, which is dependent on the solvation and dissociation of the intermediate LiO_2.[17–22] The pathways are outlined below, where "ads" and "sol" refer to surface adsorbed or solution species respectively and are shown schematically in Figure 1.3.

In the *electrode surface* mechanism, the formation of LiO_2 via a one-electron reduction to superoxide and association with Li^+ occur at the electrode surface (Reaction 1.3). Li_2O_2 then forms via a second one-electron reduction at the surface (Reaction 1.4) or via disproportionation at the surface via Reaction 1.5

$$Li^+{}_{(\mathrm{sol})} + e^- + O_{2(\mathrm{sol})} \rightarrow LiO_{2(\mathrm{ads})} \tag{1.3}$$

$$Li^+{}_{(\mathrm{sol})} + e^- + LiO_{2(\mathrm{ads})} \rightarrow Li_2O_{2(\mathrm{ads})} \tag{1.4}$$

$$2LiO_{2(\mathrm{ads})} \rightarrow Li_2O_{2(\mathrm{ads})} + O_{2(\mathrm{sol})} \tag{1.5}$$

In the *solution* mechanism, oxygen is reduced to superoxide at the electrode surface and

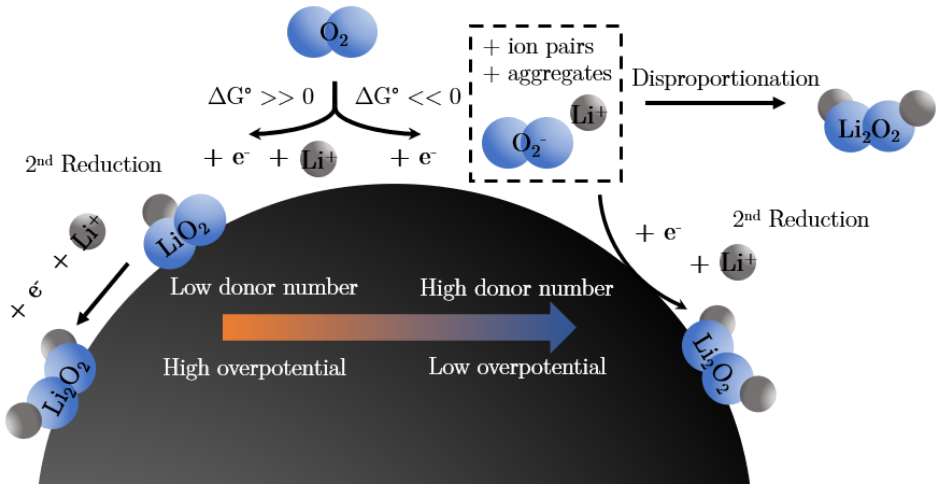


Figure 1.3: Schematic of the solution and surface mechanisms of lithium peroxide formation in aprotic solvents. The solution mechanism is followed when $\Delta G^0 \gg 0$ (high donor number (DN) solvents) and the surface mechanism is followed when $\Delta G^0 \ll 0$ (low DN solvents). Reproduced with permission from Johnson *et al.*.[20] Copyright 2014 Springer Nature.

diffuses into the electrolyte where it combines with a Li^+ cation (Reaction 1.6). The Li^+ and O_2^- are solvated by the solvent. The $LiO_{2(sol)}$ can then undergo disproportionation with another $LiO_{2(sol)}$ molecule to form Li_2O_2 and O_2 (Reaction 1.8). The Li_2O_2 is insoluble and immediately precipitates out of solution nucleating and forming Li_2O_2 crystallites.

$$Li^+{}_{(sol)} + e^- + O_{2(sol)} \rightarrow Li^+{}_{(sol)} + O_2{}^-{}_{(sol)} \tag{1.6}$$

$$2Li^+{}_{(sol)} + e^- + O_2{}^-{}_{(sol)} \rightarrow Li_2O_2 \tag{1.7}$$

$$2(Li^+{}_{(sol)} + O_2{}^-{}_{(sol)}) \rightarrow Li_2O_2 + O_{2(sol)} \tag{1.8}$$

Superoxide Intermediate

Strong evidence for the multi-step mechanisms proposed above have been provided by direct observation of the O_2^-/LiO_2 intermediates. Electrochemical techniques such as cyclic voltammetry (CV),[17,18,20,23–31] and galvanostatic control[20,23,32,33] have been used to generate and identify O_2^-/LiO_2 intermediates, including the use of Rotating Ring Disk Electrodes (RRDE).[20,25,28,31] These are often used in concert with chemical techniques, such as the addition of nitrotetrazolium blue chloride, which

gives a purple colour in the presence of O_2^-.[17] Or spectroscopic techniques such as Raman spectroscopy[20,23,26,29], electron paramagnetic resonance (EPR) spectroscopy[32], ultraviolet (UV)-vis spectroscopy[26,27], fluorescence spectroscopy[30] and selected-area electron diffraction (SAED), Figure 1.4.[33]

For example, Cao *et al.* showed strong evidence for superoxide generation during the ORR in 1 M lithium triflate in DMSO.[32] They used EPR spectroscopy, which probes materials containing unpaired electrons. Their study used a spin trap, 5,5-dimethyl-pyrroline-*N*-oxide, which can capture superoxide radical anions, forming stable free radicals, which can be observed in the EPR spectra. They took aliquots of the electrolyte during the ORR and observed increasing EPR signal due to superoxide generation, shown in Figure 1.4 (b). Interestingly, the researchers found no evidence of superoxide generation in the subsequent OER.

Peng *et al.* utilised Surface-Enhanced Raman Spectroscopy (SERS) to confirm the presence of O_2^- during CV in a tetrabutyl ammonium $(TBA)^+$-based acetonitrile electrolyte, the results are shown in Figure 1.4 (a).[23] They collected spectra on a roughened Au electrode and saw clear evidence of superoxide generation as the potential was reduced by the growth of peaks at 491 and 1109 cm^{-1} which are related to the Au-O and O-O stretch respectively. When switching to a Li^+-based electrolyte and holding the potential at 2.2 V vs Li^+/Li, the superoxide peak shifts to 1137 cm^{-1} due to the formation of LiO_2. At longer times, the disappearance of the LiO_2 peak at 1137 cm^{-1} coincides with the appearance of a Li_2O_2 peak at 808 cm^{-1}.

Yu *et al.* provided UV-vis spectroscopy evidence for superoxide generation during ORR. When sweeping the potential from the open circuit potential to 2 V vs Li^+/Li, they observed the growth of a peak at 252 nm in the UV-vis spectra, related to the $1\pi_u \rightarrow 1\pi_g$ transition of superoxide; the results are shown in Figure 1.4 (c) An interesting study by Luo *et al.* utilised SAED and detected the presence of LiO_2 in the initial stages of the ORR on CNTs in a solid-state nanoscale battery, shown in Figure 1.4 (e).[33] Interestingly, they found that LiO_2 is formed initially and undergoes disproportionation to form Li_2O_2 and O_2. They found that the O_2 gas that is produced inflates the LiO_2/Li_2O_2

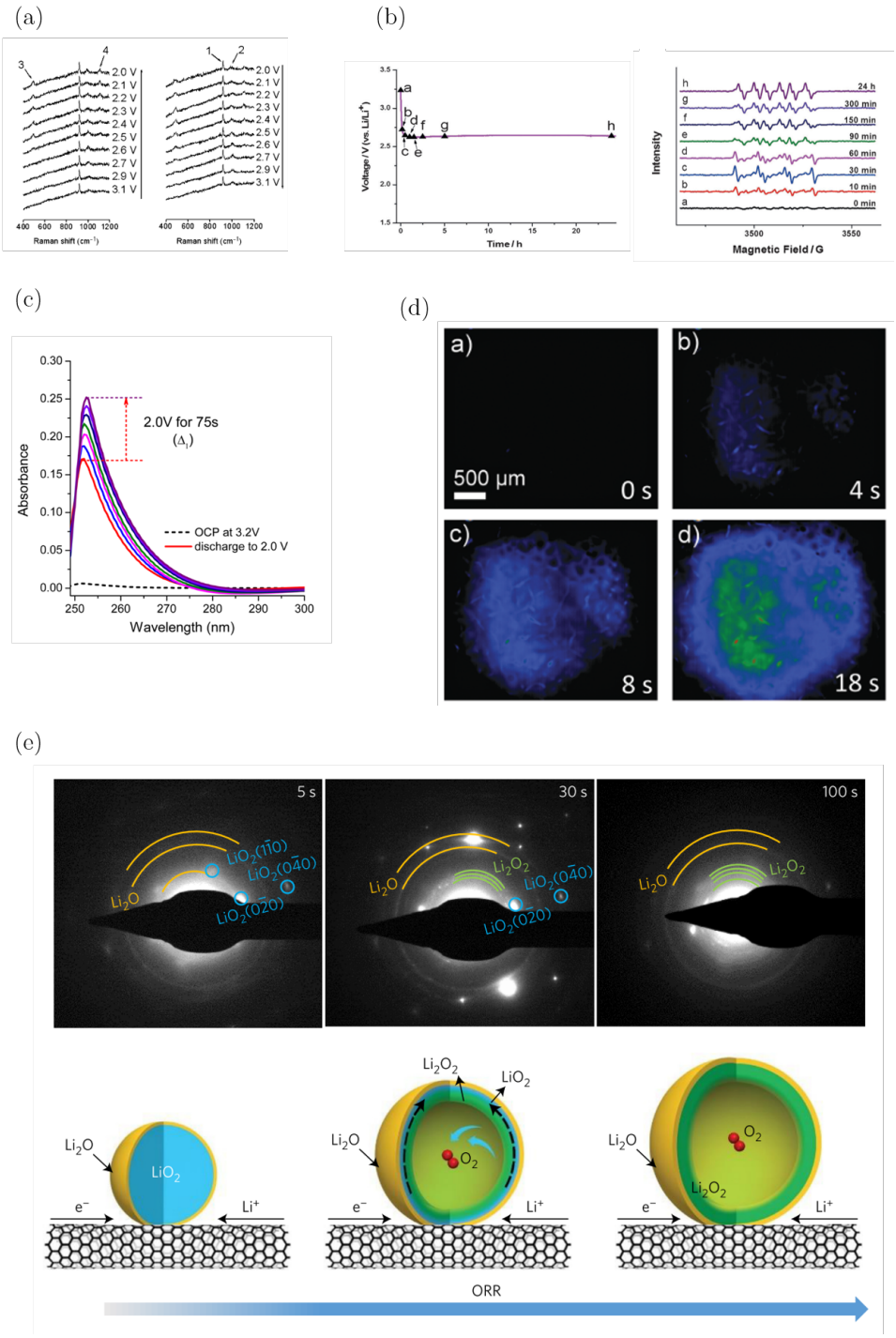


Figure 1.4: Evidence for O_2^-/LiO_2 formation on discharge in Li-O_2 batteries. (a) SERS spectra with peaks at 1109 cm^{-1} assigned to O-O stretch of adsorbed superoxide and the peak at 491 cm^{-1} assigned to the Au-O stretch of adsorbed superoxide. Reproduced under terms of the CC-BY license.[23]. Copyright 2011, Peng *et al.*, published by Angewandte Chemie International Edition. (b) Discharge profile, left, and EPR spectra, right, of oxygen saturated 1 M LiTf/dimethyl sulfoxide (DMSO) electrolyte with 10 mM 5,5-dimethyl-pyrroline-*N*-oxide, which becomes EPR active upon reaction with superoxide. Reproduced under terms of the CC-BY license.[32]. Copyright 2014, Cao *et al.*, published by ChemSusChem. (c) UV-vis spectra recorded in oxygen-saturated tetrabutyl ammonium (TBA)ClO_4-DMSO during a potential sweep to 2.0 V vs Li^+/Li. Adapted with permission from Yu *et al.*.[26] Copyright 2015 American Chemical Society. (d) Fluorescence microscopy of a dye which reacts selectively with O_2^-. Reproduced under terms of the CC-BY license.[30]. Copyright 2016, Schwager *et al.*, published by Faraday Discussions. (e) SAED evidence for LiO_2 during the formation of hollow sphere Li_2O_2. Reproduced with permission from Luo *et al.*.[33] Copyright 2017 Springer Nature.

particle resulting in a hollow sphere morphology. Using fluorescence spectroscopy, Schwager *et al.* provided evidence of the superoxide intermediate formed during the ORR, shown in Figure 1.4 (d).[30] They utilised a dye, 4-chloro-7-nitrobenzofurazan, which reacts selectively with O_2^-, forming a fluorescent molecule that excites at 470 nm and emits at 550 nm. They could observe superoxide through an optical microscope giving spatially resolved images of where it formed in a gas diffusion electrode.

Lithium Peroxide Precipitation and growth

Using scanning electron microscopy (SEM) and transmission electron microscopy (TEM), Mitchell *et al.* measured the nucleation and growth of Li_2O_2 particles during discharge at various discharge rates.[34] They discharged cells utilising a CNT cathode with 0.1 M $LiClO_4$ in 1,2-dimethoxyethane (DME) and disassembled cells at different points during discharge to observe the cathodes *ex-situ*. They observed that the cathode was largely bare at low discharge rates and that the Li_2O_2 particles were similar in size, suggesting that instantaneous nucleation occurs early in discharge at relatively few sites. At higher rates, a higher density of particles was observed with more irregular shapes, implying that further nucleation of Li_2O_2 particles precedes the growth of well-defined and larger disks or toroids. The small irregular particles that initially form then grow anisotropically as disc-shaped particles, shown schematically in Figure 1.5.

As discharge proceeds, the disc-like particles form toroidal-shaped particles via a kinetically controlled regime of Li_2O_2 layer-by-layer growth. TEM confirmed this, where the discrete plates could be observed from the side of a Li_2O_2 toroid, as shown in Figure 1.5. These results were corroborated by Xia *et al.* using SEM at various stages of discharge using a Ketjen Black/polytetrafluoroethylene (PTFE) cathode and 0.5 M LiTf in diglyme as the electrolyte.[35] They also observed the nucleation of many disc-like nanoparticles in the early discharge stages. The disc-like nanoparticles evolved into toroid-shaped particles which grew upright as discharge proceeded.

Liu *et al.* utilised Synchrotron X-ray diffraction (XRD) to measure the growth of Li_2O_2 *operando*. Similarly, they observed the two-stage growth mechanism consisting

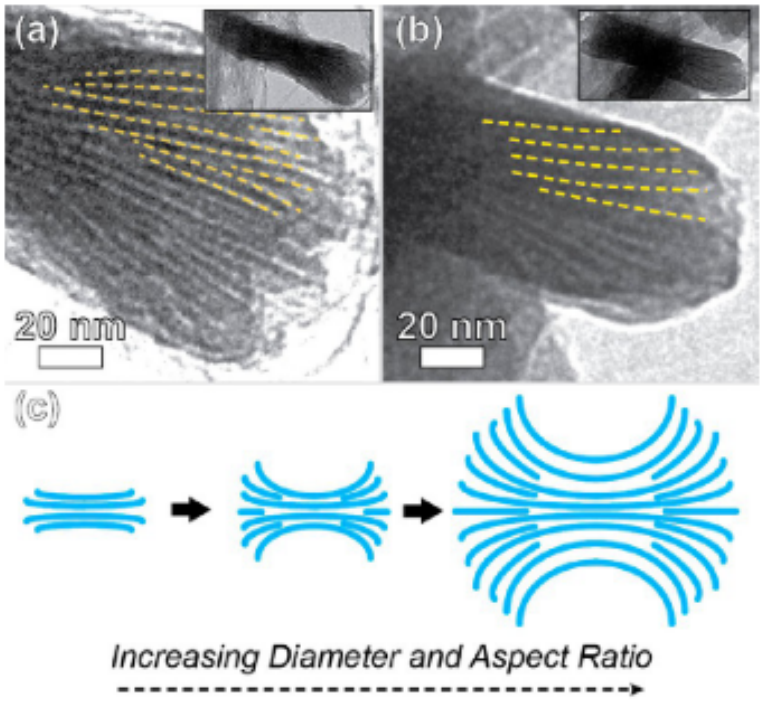


Figure 1.5: TEM image of discrete Li_2O_2 plates which make up a Li_2O_2 toroidal particle. The small irregular particles that initially form then grow anisotropically as disc-shaped particles. As discharge proceeds, the disc-like particles form toroidal-shaped particles via a kinetically controlled regime of Li_2O_2 layer-by-layer growth. Adapted with permission from Mitchel *et al.*.[34] Copyright 2013 American Chemical Society.

of the initial anisotropic growth of thin/flat plates followed by the evolution of toroidal particles.[36] The researchers concluded this from the measurement of the broadening of both the (100) and (101) reflections in the XRD pattern during the initial stages of discharge, followed by a decrease in the domain size of the (100) reflection and a constant (101) reflection in the second stage of discharge. The researchers similarly confirmed that the toroid particles comprised several Li_2O_2 crystallites with a large (001) face dominating the crystal shape.

Charge Transfer Through Li_2O_2

The rapid polarisation at the end of discharge, termed the "sudden death region", is primarily caused by charge transfer resistance due to the accumulation of electronically insulating Li_2O_2. Subsequently, the capacity delivered by porous carbon cathodes is well below the theoretical value predicted from the electrode porosity.[37] Obstruction of oxygen mass transport by pore blocking can be ruled out as the cause of polarisation, as

the same phenomenon is observed at a planar glassy carbon electrode.[37] There are two competing theories to describe charge transport though Li_2O_2, namely hole-tunnelling or the hopping of charged polarons and defects.[38]

The most convincing evidence for the hole-tunnelling mechanism is provided by measuring the charge transfer rate of an outer-sphere redox shuttle by electrochemical impedance spectroscopy (EIS) during discharge.[39,40] In their experiments, Viswanathan *et al.* found that the exchange current density of the Fc/Fc^+ redox couple dropped by an order of magnitude at the onset of discharge, followed by a gradual decrease until a Li_2O_2 layer 5-10 nm thick had formed on the electrode surface, at which point the reaction ceased.[39] They suggested that the output potential decays exponentially when the film thickness reaches a critical thickness, as the potential bias required to support the current increases exponentially.

The phenomenon can be described by a slight adaptation of the equation derived by Simmons to include the overpotential of Li-O_2 redox.[41] The equation describes electron tunnelling between similar electrodes through an insulating film:

$$J_{tun} = J_0 \left((\bar{\varphi} + e\eta) e^{-A\sqrt{\bar{\varphi}}} - (\bar{\varphi} + e\eta + eV)\, e^{-A\sqrt{\bar{\varphi}+eV}} \right) \tag{1.9}$$

where $A = (\sqrt{2m}4\pi\beta\Delta s)/h$ and $J_0 = e/(2\pi h(\beta\Delta s)^2)$, $\bar{\varphi}$ is the mean barrier height at equilibrium, η is the overpotential of Li-O_2 redox, V is the voltage across the film, Δs is the film thickness, β is the correction factor, m and e is the electron mass and electron charge respectively and h is Planck's constant.

From Equation (1.9), it can be seen that there are three key factors which limit J_{tun} (1) the gap between the valence band maximum of Li_2O_2 and the Fermi level of Li-O_2 redox represented by $\bar{\varphi}$ (2) the cell voltage, which is affected by redox overpotential, η, and the potential difference across the Li_2O_2 film, V (3) the thickness of the Li_2O_2 film, Δs, which appears in the exponential factor A and the pre-exponential factor J_0. Equation (1.9) describes an exponential decrease in J_{tun} with increasing thickness of Li_2O_2 film.

The competing theory to describe charge transfer through Li_2O_2 can be described by the hopping of hole polarons and charged defects. A *polaron* is the term used to describe an excess charge carrier localised in a potential well. It can be identified as a quasiparticle consisting of an electron or a hole surrounded by a cloud of virtual phonons.[42] Ong *et al.* provided computational evidence for the formation and migration of hole polarons in Li_2O_2.[43] They calculated migration barriers of 68 and 152 meV for intralayer and interlayer migration of free π^* hole polarons, suggesting anisotropic electronic conduction in Li_2O_2.[43] Siegel *et al.* carried out a comprehensive study into various low-energy defects and showed that negative Li^+ vacancies and hole polarons are the dominant charge carriers in Li_2O_2.[44] They later showed enhanced conductivity in amorphous Li_2O_2 compared to crystalline Li_2O_2 due to the increased concentration and mobility of negative Li^+ vacancies.[45]

The current density due to hopping of polarons and charged defects can be described by the following equation:[46]

$$J_{hop} = eD_h\frac{\delta n_h(x)}{\delta x} + \frac{e^2 D_h n_h(x)}{k_B T}\frac{\delta U_{bias}}{\delta x} \tag{1.10}$$

where D_h is the diffusion coefficient given by $D_h = 2va^2exp(-V_{\text{diff}}/k_BT)$, $n_h(x)$ is the concentration of hole polarons, U_{bias} is the potential difference across the film, v is the hopping attempt frequency and V_{diff} is the diffusion barrier for hole polarons. $n_h(x)$ is given by $n_h(x) = n_0 exp[-E_f(h_p^+)/k_BT]$ where $E_f(h_p^+)$ is the formation energy of the free hole and n_0 is the number of possible polaron sites per cm^3, 3 x 10^{22}. By combining equation (1.10) with the Poisson equation, Radin *et al.* accounted for space-charge effects whereby hole polarons accumulate within Li_2O_2 at its interfaces.[47]

A comparison of equations (1.9) and (1.10) shows some key differences. Luntz argued that each mechanism has a different dependency of current on film thickness with $J_{tun} \sim exp(-\Delta s)$ while $J_{hop} \sim \Delta s^{-1}$.[48] However, these relationships are tenuous as Δs also appears in the pre-exponential factor, J_0 in J_{tun} and the assumption that $n_h(x)$ and U_{bias} vary linearly in J_{hop} is incorrect. As well as this, Luntz *et al.* pointed out

that J_{hop} is temperature dependent whereas J_{tun} is temperature independent and that these differences could be exploited to distinguish between the two mechanisms.[46,48] By utilising galvanostatic discharge on a glassy carbon electrolysis cell, Luntz *et al.* showed a dramatic temperature dependence on discharge capacity at low currents which was absent at higher currents.[46] They argued that the temperature-dependent polaron hopping was only important at low currents, with the tunnelling mechanism dominating at all higher currents.[46], by considering the space-charge effects, Radin showed that J_{hop} decreases more rapidly than Δs^{-1}, which may explain sudden death.[47]

Interface of the Discharge Reaction

The reaction interface for the ORR/OER has important implications for Li-O_2 cell design. There are several interfaces where these reactions can take place, namely the interface between the electrode and electrolyte (in the initial stages of discharge where nucleation takes place), at the Li_2O_2/electrolyte interface and the Li_2O_2/electrode interface. Each of these reaction interfaces has implications about which charge transfer mechanism is taking place, as discussed above. This topic has little consensus in the literature; however, a few critical studies are discussed herein.

Several microscopy studies have identified the Li_2O_2/electrolyte interface as the reaction interface during discharge.[49–51] For example, Kushima *et al.* utilised *in situ* TEM with a liquid cell.[49] The cell consisted of a Au patterned working electrode with a $LiCoO_2$ counter electrode, 1 M LiTFSI in DMSO was used as the electrolyte. They observed the formation of Li_2O_2 whilst discharging at 2.2 V vs Li^+/Li. They saw that after the initial formation of Li_2O_2 on the electrode surface, further Li_2O_2 was accumulated on top of the previously formed reaction product. Interestingly, the Li_2O_2 film grew to a thickness of ∼100 nm, much greater than the 5-7 nm predicted for the hole-tunneling charge transfer mechanism. However, electronic conductivity on the Li_2O_2 surface has been calculated computationally, and the authors use this as a rationale for the thicker film.[52] As such, the authors suggested that Li^+ diffusion was limiting.[49] This result was corroborated by He *et al.*, who also utilised a liquid-cell setup,

instead using a tetraglyme (TEGDME)-based electrolyte.[50] They similarly observed a thick Li_2O_2 film made up of nanograins of Li_2O_2 which formed on top of each other, with Li^+ diffusion limiting the thickness of the films. Interestingly, the authors also observed the formation of Li_2O_2 in the electrolyte in isolation from the electrode and Li_2O_2 film. They took this as evidence of the disproportionation reaction between molecules of solvated LiO_2. A similar result was obtained by Liu and co-workers in a DMSO-based electrolyte.[51]

Huang *et al.* was able to probe the reaction interface during oxygen reduction using EIS.[53,54] They simulated EIS spectra that would be expected in the case of reaction at the Li_2O_2/electrode interface (interior interface) and reaction at the Li_2O_2/electrolyte interface (exterior interface).[53] They showed that the exterior case exhibits two semicircles in the EIS spectra, the high-frequency semicircle corresponds to the Li_2O_2 layer, and the low-frequency semicircle corresponds to the Li_2O_2/electrolyte interface. In the interior case, only one semicircle is exhibited corresponding to the Li_2O_2/electrode interface. They then carried out EIS after discharge to sudden death on a glassy carbon electrode in 0.1 M $LiClO_4$ in DMSO. They observed two semicircles in the spectra described by the exterior case, where charge transport across the Li_2O_2 layer occurs. They also ascribed the marked reduction in equilibrium potential from 2.96 V vs Li^+/Li to 2.85 V vs Li^+/Li to the formation of a new electrochemical interface (i.e. the Li_2O_2 surface) during discharge.

In contrast to the above results, Wang *et al.* provided evidence that the ORR occurs at the buried interface of the Li_2O_2/electrode interface.[55] They combined isotopic labelling of O_2 and SERS to probe the interface of a Au electrode during discharge in a DMSO-based electrolyte. Baring in mind that SERS is a surface-specific technique, by discharging initially with $^{18}O_2$ followed by discharge with $^{16}O_2$, they showed that the originally deposited $Li_2{}^{18}O_2$ was subsequently displaced by $Li_2{}^{16}O_2$ at the surface, showing instead that Li_2O_2 growth occurs at the Li_2O_2/electrode interface and that growth is limited by electron transport. However, this result relies on the assumption that the Li_2O_2 forms a non-porous uniform film. As seen previously, Li_2O_2 can form a

porous film up to 100 nm.[49–51] If the initially formed $Li_2{}^{18}O_2$ is instead covered by a layer of $Li_2{}^{16}O_2$ which can also occur in close proximity of the electrode surface, then the declining $Li_2{}^{18}O_2$ can still be explained by a reaction at the Li_2O_2/electrolyte surface. A recent study by Prehal *et al.* suggested that there is, in fact, no surface-based formation of a conformal Li_2O_2 film.[56] They used small- and wide-angle X-ray scattering along with RRDE and electron microscopy to show that, even in poorly solvating electrolytes, Li_2O_2 forms as stacks of thin Li_2O_2 platelets. Their study provides compelling evidence that mass transport of reactive species rather than electronic transport through a Li_2O_2 film limits the discharge capacity.

Factors Affecting the Solution Mechanism

The solution mechanism of Li_2O_2 formation, as detailed in equations 1.6 to 1.8, is desirable for the Li-O_2 battery. By forming Li_2O_2 in solution, the electrode surface is left exposed for electron transfer for longer into discharge, leading to much higher capacities. Similarly, by forming large particles of Li_2O_2 in solution, some parasitic chemistry involving the carbon surface can be avoided. As well as this, particulate Li_2O_2 has a lower surface-to-volume ratio, and parasitic chemistry between Li_2O_2 and the solvent can be minimised.

Several factors can affect whether a solution or electrode surface mechanism occurs on discharge. The rate of discharge can affect the morphology of Li_2O_2.[57–59] For example, Adams *et al.* showed that low current densities on discharge could lead to large toroidal particles of Li_2O_2.[57] As the current density increases, smaller aggregates of Li_2O_2 are formed until a quasi-amorphous film is observed at high current densities. They attribute this to the interplay between the rate at which LiO_2 is solvated, and the rate at which disproportionation occurs in solution and the direct electrochemical reduction of LiO_2 occurs at the surface.[57] At low rates, the solvation of LiO_2 occurs faster than the second electron reduction at the surface, leading to chemical disproportionation in solution. When Li_2O_2 reaches the solubility limit, it precipitates on the electrode surface. As the rate increases, the concentration of LiO_2 increases, and more disproportionation

and nucleation occurs, leading to more numerous Li_2O_2 aggregates. At the highest rates, Li_2O_2 can form by the second electron reduction at the surface (which incurs an overpotential penalty) or by disproportionation after surface migration, leading to a quasi-amorphous film. Giffith *et al.* obtained similar results, observing a needle-like geometry at high rates as opposed to a nanosheet or compact film.[58] The different morphologies observed may be due to the different electrolyte solvents used, TEGDME for Adams *et al.* and DME for Griffiths *et al.* (both with 1 M LiTFSI), on which the mechanism of formation of Li_2O_2 is critically dependent.

The solubility of the LiO_2 intermediate in the electrolyte can promote the solution route of Li_2O_2 formation and is influenced by the solvent,[18,20,60] salt,[22,61] and electrolyte additives.[21,62,63] For example, Johnson *et al.* showed that the solution or surface mechanism depends on the DN of the solvent.[20] In high-DN solvent, such as DMSO (DN = 30), the Gibbs free energy of the solvated LiO_2 is lower than that for the surface adsorbed $LiO_2{}^*$ and the equilibrium of equation 1.11 lies to the right:

$$LiO_2^* \rightleftharpoons Li^+_{(sol)} + O^-_{2(sol)} + ion\ pairs + higher\ aggregates\ (clusters) \tag{1.11}$$

The Gutmann DN is an empirical measurement of the ability of a solvent to solvate cations.[64] The trend of the solution to surface mechanism with high and low DN solvents agrees with cation solvation being a major determinant of LiO_2 solubility.[20]

Similarly, Aetukuri *et al.* showed that the Gutmann Acceptor Number (AN) of a solvent can promote the solution mechanism by solvating the $O_2{}^-$.[21] They showed that the addition of H_2O (AN = 55) to DME (AN $\sim$ 10) in increasing concentrations between a nominally dry electrolyte to 4000 ppm H_2O promotes a solution mechanism. They reasoned that Li_2O_2 forms initially by a surface mechanism, with the equilibrium surface being the oxygen-rich (0001) surface. In the presence of H_2O, the dissolution of $O_2{}^-$ is triggered. The solvated $O_2{}^-$ can then diffuse to a growing particle where it recombines with Li^+ forming $LiO_2{}^*$ and finally Li_2O_2 by disproportionation.[21]

Burke *et al.* showed that the electrolyte anion selection can affect whether a solution or surface mechanism occurs on discharge.[22] They compared NO_3^- and $TFSI^-$ and observed the trend of increasing discharge capacity with increasing concentration of NO_3^-. They used ^7Li NMR to show that NO_3^- has a high DN. Consequently, the interaction between Li^+ and NO_3^- lowers the Gibbs free energy of the solvated Li^+ over that of $TFSI^-$ and in turn, promotes the solvation of LiO_2.[22] These results were corroborated by Sharon *et al.* who explored a wider range of salts with various Li^+ dissociation levels.[61] In salt anions with high Li^+ dissociation, lower discharge capacities were achieved with a surface route of Li_2O_2 dominating. Salts with strong Li^+ association achieved higher discharge capacities with toroidal discharge products; they similarly observed the highest discharge capacities with NO_3^-. They attributed the solution mechanism to the strong interaction between Li^+ and NO_3^- producing a "less acidic" Li^+. This leads to a metastable LiO_2 intermediate, which can diffuse further from the cathode surface and form Li_2O_2 particles with growth in all directions.[61]

1.3.2 Charge Mechanism

The charging mechanism in Li-O_2 batteries is more complex and has less consensus in the literature. Whereas the discharge mechanism has been shown to proceed via a LiO_2 intermediate, with direct observation of LiO_2 and Li_2O_2 via several techniques (Section 1.3.1), the charging mechanism remains more elusive and several reaction schemes have been proposed. What is clear is that the oxidation of Li_2O_2 is not a simple reversal of the discharge mechanism, as evidenced by the larger overpotentials observed on charge (Figure 1.2)

Charge Mechanism

Early work by Peng *et al.* proposed that LiO_2 was not formed during charging of Li_2O_2, as evidenced by a lack of LiO_2 peaks in the SERS spectra obtained at oxidising potentials in an acetonitrile-based electrolyte (DN = 14.4), they suggested the direct two-electron oxidation of Li_2O_2:[23]

$$Li_2O_{2(s)} \rightarrow O_{2(g)} + 2Li^+_{(sol)} + 2e^- \tag{1.12}$$

Alternatively, the formation of LiO_2 as an intermediate during charge has been suggested, whereby the charge mechanism more closely resembles the reverse of discharge.[65]

$$Li_2O_{2(s)} \rightarrow Li_{2-x}O_{2(s)} + xLi^+_{(sol)} + xe^- \tag{1.13}$$

$$LiO_{2(sol)} \rightarrow O_{2(g)} + xLi^+_{(sol)} + xe^- \tag{1.14}$$

$$2LiO_{2(sol)} \rightarrow Li_2O_{2(s)} + O_{2(g)} \tag{1.15}$$

Later studies have suggested a solvent-dependent oxidation pathway that occurs via topotactic delithiation of Li_2O_2 to form an off-stoichiometric $Li_{(2-x)}O_2$ (Reactions 1.13-1.17), which is mediated by the solvation of LiO_2 in high DN solvents (Reactions 1.18-1.19) .[31,66,67] This can be summarised as so:

$$Li_2O_{2(s)} \rightarrow Li_{2-x}O_{2(s)} + xLi^+_{(sol)} + xe^- \tag{1.16}$$

$$Li_{2-x}O_{2(s)} \rightarrow O_{2(g)} + (2-x)Li^+_{(sol)} + (2-x)e^- \tag{1.17}$$

$$Li_{2-x}O_{2(s)} \rightarrow LiO_{2(sol)} + (1-x)Li^+_{(sol)} + (1-x)e^- \tag{1.18}$$

$$2LiO_{2(sol)} \rightarrow Li_2O_{2(s)} + O_{2(g)} \tag{1.19}$$

The topotactic delithiation of Li_2O_2 on charge was first proposed by Kang *et al.* who used DFT to show that off-stoichiometric $Li_{(2-x)}O_2$ phases are accessible at low overpotentials and that delithiation is kinetically favoured over the direct Li_2O_2 oxidation mechanism (Reaction 1.12).[67] Ganapathy *et al.* later utilised *operando* XRD to probe the charging mechanism in a TEGDME-based electrolyte (DN = 16.6).[66] They observed two distinct oxidation phases. In the initial sloping region between 2.8 and 3.4 V vs Li^+/Li, the oxidation of amorphous Li_2O_2 and small crystallites occurs. This is supported by the absence of any change in the intensity of diffracted peaks and no change in the parameters

obtained from Rietveld refinement other than a change in Li-occupancy.[66] Also, when higher discharge rates are employed to form more amorphous Li_2O_2, the initial sloping region on recharge is extended longer into charge. In the second stage, between 3.4 and 3.9 V vs Li^+/Li, a continuous drop in peak intensity was observed, accompanied by a continuous decline in Li-occupancy. They attribute this to a solid solution-driven mechanism as detailed in Reactions 1.13 and 1.17. Lu *et al.* corroborated these results by using Potentiostatic Intermittent Titration Technique (PITT) to probe the charging mechanism.[68] They observed three distinct charge phases at low charge rates. The PITT response of the initial sloping region was characteristic of a diffusion-dominated process akin to that of lithium intercalation/deintercalation.[68] The PITT current response of the second phase, which was a plateau between 3.4 and 4.1 V vs Li^+/Li, could be described qualitatively by a nucleation and growth process of reactive sites (e.g. lithium and/or oxygen vacancies) in a solid-solution reaction.[68] These results were corroborated by Gallant *et al.* who used PITT in a different electrolyte solvent to Lu, suggesting that the two-stage charging process is characteristic of electrochemically formed Li_2O_2.[69]

In a recent study, Wang *et al.* showed that soluble LiO_2 can be formed during charge in high DN solvents, which can mediate the solid-solution mechanism (Reactions 1.18-1.19).[31] They used RRDE and X-ray Absorption Near Edge Spectroscopy (XANES) to identify soluble LiO_2 in high DN solvents, DMSO and 1-methylimidazole (Figure 1.6).

They cited previous studies that didn't detect soluble LiO_2 using RRDE upon oxidising Li_2O_2 in high DN solvents and attributed this to the low surface area of the planar electrodes used. In these experiments, the disk electrode was swept through oxidising potentials while the ring electrode was held at the reduction potential of LiO_2. By increasing the surface area of their electrode by casting Vulcan Carbon (approx. 100 m^2 g^{-1}), Wang *et al.* were able to detect soluble LiO_2 at the disk while oxidising Li_2O_2 in DMSO (Figure 1.6, **d**). They detected no current at the ring electrode when oxidising Li_2O_2 in TEGDME (Figure 1.6, **a**). To unambiguously identify LiO_2 during charge, Wang *et al.* employed XANES spectroscopy. When charging an electrode with pre-filled Li_2O_2 in TEGDME, the peak at 530.3 eV decreases with no new peaks

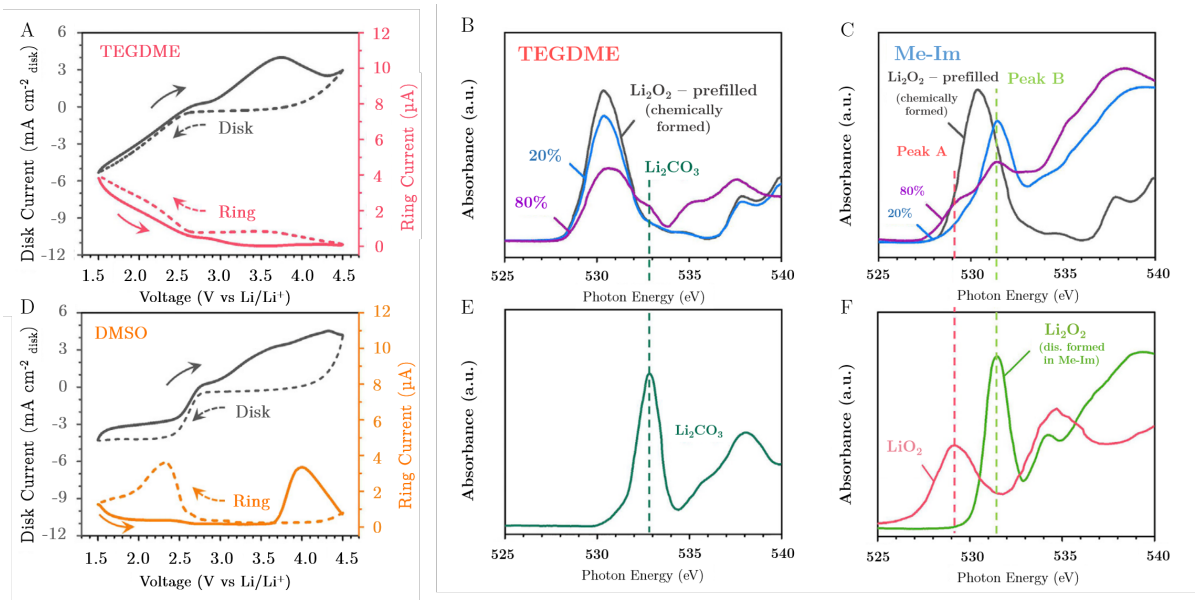


Figure 1.6: RRDE (a,d) and XANES spectra (b,c,e,f) providing evidence for the solution mediated charge mechanism. Using RRDE, LiO_2 is detected at the ring during the positive sweep at the disk in DMSO (d) whereas this peak is absent when using TEGDME (a). Spectroscopic evidence of LiO_2 formation is observed by XANES when using 1-methylimidazole (c,f), the Li_2O_2 peak splits into a LiO_2 peak and a nanocrystalline Li_2O_2 peak during charge. In TEGDME, the Li_2O_2 peak decreases gradually during charge with no evidence for the formation of LiO_2 (b,e). Adapted under terms of the CC-BY license.[31]. Copyright 2018, Wang *et al.*, published by Joule.

apparent until the end of charge where a peak characteristic of Li_2CO_3 appears. This is consistent with the delithiation mechanism proposed by Kang *et al.*[67] and Ganapathy *et al.*[66]. When repeating the experiment in a high DN solvent, 1-methylimidazole, the peak at 530.3 eV splits into two peaks at 529.4 eV and 531.4 eV; as charging proceeds, the peak at 529.4 eV increases in intensity while the peak at 531.4 eV decreases. The peak at 529.4 eV is assigned to LiO_2 while the peak at 531.4 eV is attributed to nanocrystalline Li_2O_2. The XANES spectra during charge in 1-methylimidazole are indicative of the formation of soluble LiO_2 which can disproportionate to form nanocrystalline Li_2O_2 (Reactions 1.18 and 1.19).

Interface of Charge Reaction

There are conflicting viewpoints on the interface at which Li_2O_2 oxidation occurs in Li-O_2 batteries. An early microscopy study by Zhong *et al.* showed that oxidation occurred preferentially at the Li_2O_2/electrode interface in a solid state cell using multi-walled CNTs as the cathode.[70] However, this study required the transfer of electrochemically

formed Li_2O_2 into a TEM cell, so contamination cannot be ruled out. As well as this, potentials over 8 V were required to induce Li_2O_2 decomposition, which, as discussed in section 1.3.1, can affect the charge transport properties of Li_2O_2. In contrast, Zheng *et al.* utilised *in situ* SEM to probe both discharge and charge in a solid state cell.[71] They formed a hollow-sphere Li_2O_2 on discharge where oxidation was initiated at the Li_2O_2/electrolyte surface on charge. Kushima *et al.* utilised *in situ* liquid cell TEM with a DMSO-based electrolyte.[49] They observed a porous layer of nanosized Li_2O_2 particles on discharge which grew from the Li_2O_2/electrolyte surface. On charge, the Li_2O_2 decomposed from the Li_2O_2/electrode surface, demonstrating an asymmetry in the reaction site interfaces on charge and discharge.[49]

Although the microscopy studies cited above are powerful techniques to directly observe Li_2O_2 formation and decomposition *in situ*, they suffer from large overpotentials required to induce cell reactions. The widely differing product morphologies make these studies difficult to compare with each other and do not translate to cell chemistry in a practical Li-O_2 cell. Electrochemical techniques such as EIS,[54] or isotopic labelling combined with mass spectrometry,[19,72] can be used to probe the reaction interface during charge under more realistic operating conditions.

For example, Huang *et al.* used dynamic EIS under galvanostatic and potentiostatic conditions.[54] They identified two impedance semicircles during discharge related to the Li_2O_2 film and the ORR electron transfer, respectively. When switching to oxidative potentials, only one impedance semicircle is observed. This implies that the reaction interface switched from the Li_2O_2/electrolyte interface on discharge to the Li_2O_2/electrode interface on charge.[54] These results support those of Kushima *et al.* as discussed above.[49]

1.3.3 Parasitic Electrochemistry

Parasitic electrochemistry represents *the* major barrier towards reversible operation of Li-O_2 cells. Despite many electrolyte/cathode formulations achieving the desired 2 e^-/O_2 on discharge, the yield of Li_2O_2 is often less than expected from the amount

of O_2 consumed.[73–75] Discharge products such as Li_2CO_3, Li-acetate and Li-formate as well as the desired Li_2O_2 have been detected at the end of discharge.[76] These side products are formed due to electrolyte and carbon degradation during ORR and require higher voltages to decompose, often forming CO_2 upon decomposition, exacerbating the problem on further cycles. Upon charging, the e^-/O_2 ratio is often $\gg 2$, indicating significant side reactions upon charge. These parasitic reactions are caused by reactive oxygen species such as superoxide (O_2^-, LiO_2), peroxides (Li_2O_2, $Li_{(2-x)}O_2$) and singlet oxygen ($^1O_2$), which are formed as intermediates during the ORR and OER. Accordingly, the Li-O_2 battery cycles poorly with rapid polarisation after multiple cycles before the capacity begins to fade. A thorough understanding of the parasitic electrochemistry occurring during ORR and OER is required in order to develop mitigation strategies to improve the reversibility of the Li-O_2 battery.

Reactive Oxygen Species in Li-O_2 Batteries

Reactive oxygen species are formed as intermediates or products of the ORR and OER in Li-O_2 batteries and are described below:

- Superoxide (O_2^-): This is a radical species formed by the one-electron reduction of oxygen. Molecular oxygen has two unpaired electrons, and superoxide results from the addition of an electron which fills one of the two degenerate molecular orbitals, leaving a species with a single unpaired electron and a negative charge of -1. O_2^- is a strong nucleophile and radical species which can undergo reactions with the electrolyte, carbon and impurities such as water.

- Singlet oxygen ($^1O_2$): Singlet oxygen is an excited state of dioxygen where Hund's rule of maximum multiplicity is broken, which states that the lowest energy term is the one with the greatest multiplicity -this rule implies that if two or more orbitals of equal energy are available, electrons will occupy them singly before filling them in pairs. In the lower of the two singlet states, the two valence electrons are spin-paired in one π^* orbital, and the second π^* orbital is empty; this singlet state in 95 kJ mol^{-1} higher in energy than the triplet ground state.

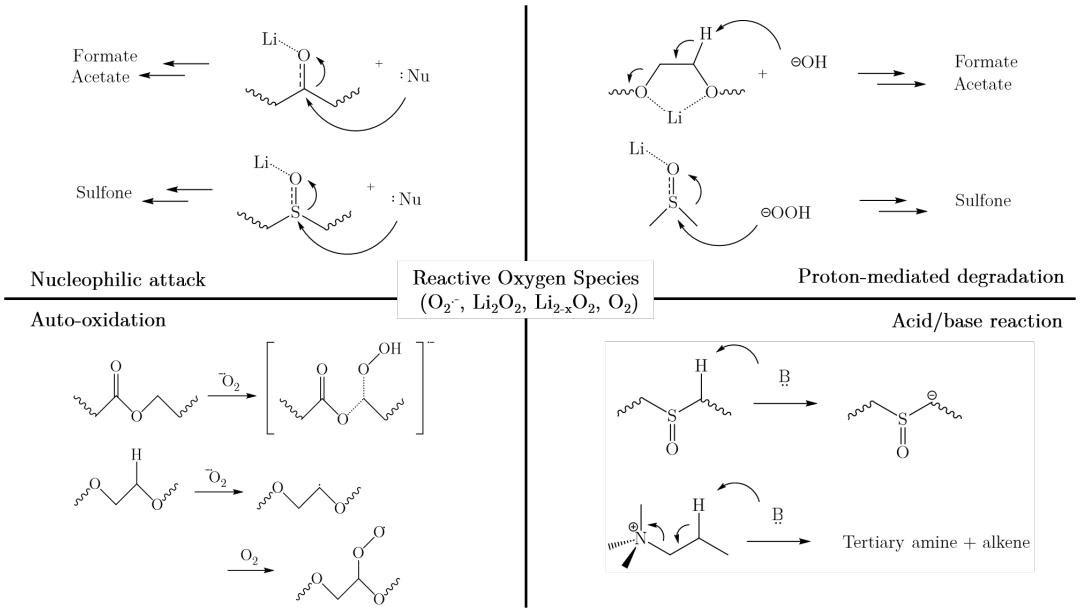


Figure 1.7: Degradation pathways for the electrolyte solvent in contact with reactive oxygen species. Reproduced under terms of the CC-BY license.[78]. Copyright 2016, Yao *et al.*, published by Angewandte Chemie International Edition.

- Lithium peroxide (Li_2O_2 or $Li_{(2-x)}O_2$): Lithium peroxide is the desired product of the ORR. However lithium peroxide itself is very basic and can react with the electrolyte and carbon, as well as impurities such as H_2O and CO_2 forming H_2O_2 and Li_2CO_3 respectively.

Impact of Superoxide on the Electrolyte and Carbon

Superoxide has been identified as an intermediate in the ORR and oxygen evolution reaction (OER). The DN of the solvent influences its stability and solubility. As such, superoxide has been observed as a soluble species in the electrolyte solvent and as a surface-adsorbed species on the carbon electrode. Previous studies in Li-O_2 cells utilising carbonate-based electrolytes revealed the potent nucleophilicity of superoxide, which degraded the electrolyte through nucleophilic attacks at the C=O group, ultimately leading to the formation of Li-alkyl carbonate species and Li_2CO_3, Figure 1.7.[77]

Similarly, DMSO, considered a more stable alternative to carbonate electrolytes,[79] was susceptible to nucleophilic attacks at the S=O moiety.[80,81] Although amides and ethers were predicted to be more stable towards nucleophilic attack, research indicated their instability.[82] Walker *et al.* reported improved stability using

N,N-dimethylacetamide (DMA) and $LiNO_3$, attributing this to the inertness of the amide core.[83] However, Sharon *et al.* later demonstrated that DMA could undergo nucleophilic attacks at the carbonyl group by LiO_2 and Li_2O_2.[84]

Glyme solvents such as DME and TEGDME are considered the most stable for Li-O_2 applications. Still, early research by Freunberger *et al.* indicated their instability, forming Li-alkyl-carbonate species after discharge.[76] The reaction mechanism proposed by Freunberger et al. was based on α-H abstraction.[76] It was supported by a computational study by Bryanstev *et al.* that suggested the process would likely occur in the presence of superoxide.[85] Ethers can undergo auto-oxidation in the presence of oxygen, but the reaction is slow due to its endothermic nature. However, Bryanstev's experiments suggested that the process is more likely to occur in the presence of superoxide.[85]

Superoxide can also attack other cell components such as the electrolyte salt,[86], the carbon cathode,[87] and the polymer binder.[88] In glyme solvents, the electrolyte salt is degraded due to a reaction with reduced oxygen species. Nasybulin *et al.* conducted a systematic investigation of several commonly employed electrolyte salts for Li-O_2 batteries to examine the discharge products formed during cycling.[86] The researchers observed LiF in cells using fluorinated salts such as LiTFSI and $LiPF_6$ after only the first discharge and found that $LiBF_4$ underwent severe decomposition. Nonetheless, the study did not distinguish between the effects of LiO_2/O_2^- or Li_2O_2, making it challenging to determine the primary cause of degradation.[86] Itkis *et al.* revealed that superoxide on the surface of the carbon cathode could react with functional groups and defects on the carbon.[87] The removal of functional groups from the carbon, by high-temperature treatment under Ar/H_2 flow, improved its stability.[89] Black *et al.* showed that superoxide could abstract an H atom from poly(vinylidene fluoride) (PVdF), forming HO_2, which could then form H_2O_2 by disproportionation or react with glyme solvent by H abstraction.[88]

Impact of Singlet Oxygen on the Electrolyte and Carbon

In recent studies on Li-O_2 batteries, the presence of $^1O_2$ during battery operation has been identified. Wandt *et al.* detected $^1O_2$ formation when charging Li_2O_2 above 3.5 V in a glyme-based electrolyte.[90] They employed a selective spin trap which forms a stable radical that was measured *operando* using EPR spectroscopy.[90] Based on their findings, they estimated that at least 0.5 % of the oxygen generated during charging is converted to $^1O_2$, as a lower limit.[90] This discovery was significant as $^1O_2$ may be essential to cathode and electrolyte stability.

Subsequent investigations carried out by Mahne *et al.* provided further evidence supporting the role of $^1O_2$ in Li-O_2 batteries.[91] They conducted a comprehensive study on the production of $^1O_2$ in ether-based electrolytes and its correlation with the formation of commonly observed side products, such as Li_2CO_3, Li-formate, and Li-acetate. To detect $^1O_2$, they employed a stable and selective trap called DMA, which is compatible with the operating potential of a Li-O_2 cell, and performed *operando* fluorescence spectroscopy to measure the formation of DMA-O_2.

Their findings revealed that the formation of $^1O_2$ occurs at the early stages of charging and is exacerbated by the presence of H_2O impurities in the electrolyte. Furthermore, through treatment with acid or Fenton's reagent coupled with Differential Electrochemical Mass Spectrometry (DEMS), they quantified the formation of Li_2CO_3 and alkyl carbonates. They observed that the formation of these side products correlated with the production of $^1O_2$. Notably, they observed that the presence of high concentrations of DMA or the addition of a singlet oxygen quencher, 1,4-diazabicyclo[2.2.2]octane (DABCO), reduced side product formation. This research confirmed $^1O_2$ as a reactive species in ether solvents and proposed a mitigation strategy wherein a trap, such as DMA, or a quencher, such as DABCO, can capture $^1O_2$. A quencher that captures O_2 in the singlet state and releases it in the less reactive triplet state might be more suitable for long-term applications. However, it should be noted that the Lewis basicity of DABCO renders it unstable within the oxidative operating potentials of a Li-O_2 cell. Subsequent work by Petit *et al.* showed that the monoalkylated

form of DABCO exhibited improved oxidative stability as a quencher while maintaining its ability to quench $^1O_2$.[92]

Although $^1O_2$ had been identified during the charging of Li_2O_2, further mechanistic understanding was required to elucidate the cause. Apart from the direct electrochemical oxidation of Li_2O_2 above 3.5 V, Mahne *et al.* proposed that $^1O_2$ could also be formed during disproportionation, which occurs during both discharge and charge processes.[91] Computational investigations by Pierini *et al.* suggested that disproportionation in the presence of Li^+ was not directly involved in the production of $^1O_2$ due to high activation energy barriers, which were insurmountable at room temperature or lower overpotentials. However, their work demonstrated that O_2^- disproportionation in the presence of H^+ had a lower energy barrier and could potentially lead to the release of $^1O_2$ at small overpotentials and room temperature. They suggested that the mitigation of $^1O_2$ could be achieved by controlling H^+ impurities. Experimental findings from Mourad *et al.* contradicted the earlier work by Pierini and colleagues, as they demonstrated that while strong Lewis acids like H^+ and Li^+ promote disproportionation, the production of $^1O_2$ increases in the presence of weak Lewis acids like TBA^+ (tetra-n-butylammonium cation).[93] Notably, TBA^+ itself is unable to promote disproportionation. This contradicts the earlier suggestion by Pierini *et al.* that disproportionation in the presence of Li^+ was not directly involved in the production of $^1O_2$ due to high activation energy barriers.[94] Mourad *et al.*'s findings highlight the complex interplay between different species in the electrolyte, and emphasise the importance of considering the nature and strength of Lewis acids in understanding the mechanisms of $^1O_2$ production in lithium-oxygen batteries. Furthermore, subsequent research by Dong *et al.* provided further evidence supporting the role of disproportionation as the predominant pathway to Li_2O_2 formation during discharge in Li-O_2 batteries.[95] Using isotopic labelling of oxygen combined with time-of-flight secondary ion mass spectrometry analysis of the discharge products, they determined that approximately 4.5 % of O_2 undergoes bond cleavage during disproportionation resulting in the production of 40 % of $^1O_2$ through this pathway. These findings highlight the significance of disproportionation in the

formation of $^1O_2$ and emphasise the need for effective control of this pathway to mitigate $^1O_2$ formation in Li-O_2 batteries.

Sagadevan *et al.* conducted research which revealed that in etheral solvents, $^1O_2$ can participate in reactions with the α-H to form hydroperoxide and lactone products, as depicted in Figure 1.7.[96] The researchers observed that coordination of the ethereal oxygen with Lewis acids, which withdraw electrons, led to a favourable attack at the α-H and increased yield of C-H peroxidation. In addition to this, $^1O_2$ is known to undergo reactions at C=C moieties.[97] Building upon this knowledge, Kwak *et al.* demonstrated that the attack of $^1O_2$ on redox mediators, which are necessary for the solution-based formation and decomposition of Li_2O_2 in low-DN solvents, led to the deactivation of these mediators.[98] In addition, the oxidation of Li_2CO_3, which is partly generated by parasitic reactions involving $^1O_2$, can also produce $^1O_2$, thereby exacerbating the issue.[99]

Impact of Li_2O_2 on the Electrolyte and Carbon

Despite being the desired reaction product on discharge, Li_2O_2 is a strong base and can react with the carbon cathode and many of the salts and solvents commonly used for Li-O_2 batteries. In an ideal battery, the measured number of electrons passed per molecule of oxygen consumed would be $2e^-/O_2$ on ORR/OER, and the amount of Li_2O_2 measured at the end of discharge would be equal to 100 % of the charge passed. However, despite frequently measuring nearly $2e^-/O_2$ on discharge, the yield of Li_2O_2 measured is much lower, often between 70-90 %.[21,93,100–102] As well as this, CO_2 evolution is nearly always observed at higher charging voltages when monitoring the gas evolution during charge, indicative of Li_2CO_3 decomposition.[103–105] This indicates that even though many electrolyte and solvent formulations are stable towards superoxide and singlet oxygen, the lithium peroxide can react once formed and that much of the parasitic chemistry in Li-O_2 batteries is chemical rather than electrochemical. Of course, an important question is how much decomposition comes from the reaction between Li_2O_2 and C and how much from Li_2O_2 in contact with the electrolyte?

When considering the carbon cathode, Li_2O_2 is only metastable on C as it can

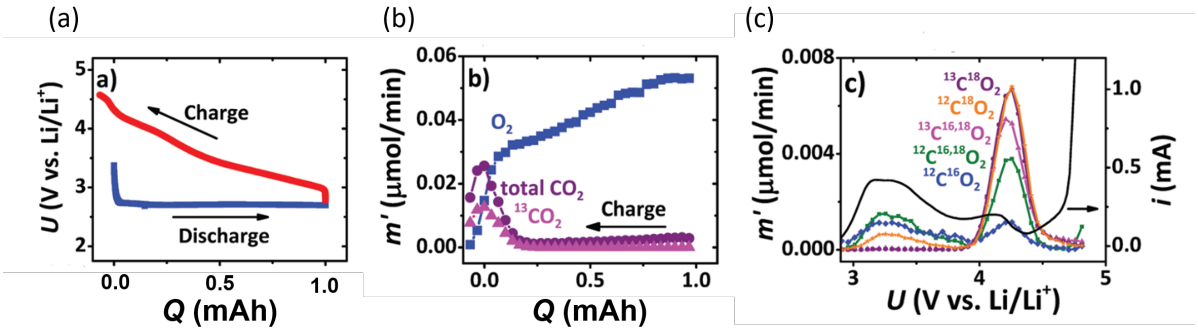


Figure 1.8: DEMS data of isotopically labelled carbon collected by McCloskey *et al.* showing the reaction of Li_2O_2 with the cathode and electrolyte.a, shows the galvanostatic discharge-charge cycle with 1 M LiTFSI in DME on a ^{13}C cathode.**b,** DEMS data during charge showing the evolution of both ^{13}C from the degradation of Li_2O_2 with the cathode and ^{12}C from the electrolyte.**c,** DEMS data of a positive linear sweep voltammetry after discharge in $^{18}O_2$ showing isotopic scrambling of O_2 in the evolved CO_2. Adapted from McCloskey *et al.*.[74] Copyright 2012 American Chemical Society.

chemically react with Li_2O_2 via exothermic reactions as shown below:[74]

$$Li_2O_2 + C + \frac{1}{2}O_2 \rightarrow Li_2CO_3 \quad \Delta G = -542.4 kJmol^{-1} \tag{1.20}$$

$$2Li_2O_2 + C \rightarrow Li_2O + Li_2CO_3 \quad \Delta G = -533.6 kJmol^{-1} \tag{1.21}$$

Because the Li_2O_2 is in contact with the carbon cathode during discharge, the amount of Li_2CO_3 formed at the C/Li_2O_2 interface will equate to a few monolayers before the Li_2CO_3 blocks access between the carbon and Li_2O_2. The most compelling way to determine the amount of decomposition coming from the cathode and electrolyte is by monitoring the gas evolution with DEMS combined with isotopic labelling of the carbon. McCloskey *et al.* carried out a discharge-charge cycle using a cathode formed from 99 % ^{13}C in an electrolyte of 1 M LiTFSI in DME and used DEMS to monitor the gas evolution on charge; the results are shown in Figure 1.8.[74]

Figure 1.8(a) shows the discharge-charge curve typical for an unmediated cell using a DME-based electrolyte. Figure 1.8(b) shows the DEMS results recorded during charge; both $^{13}CO_2$ and $^{12}CO_2$ are evolved in the peak between 4-4.5 V, indicating that decomposition with Li_2O_2 occurs with both the carbon cathode and the electrolyte. Roughly 50 % of the evolved CO_2 is $^{13}CO_2$. Figure 1.8(c) shows the DEMS data

collected after discharge in $^{18}O_2$. Both the $^{13}CO_2$ and $^{12}CO_2$ show isotopic scrambling of O_2, which comes from the oxidation of Li_2CO_3 produced on the cathode during discharge and charge. As well as this, the CO_2 peaks observed in the earlier stages of charge are predominantly $^{12}CO_2$ indicating that electrolyte decomposition occurs between the Li_2O_2 and electrolyte a the onset of charge, which likely causes further Li_2CO_3 formation. A follow-up study by McCloskey combined DEMS experiments with Li_2O_2 titration and acid treatment of the discharge/charge products.[75] In contrast to previous results, they found that decomposition between Li_2O_2 and C only accounts for a small proportion of the $^{13}CO_2$ generated from Li_2CO_3 and other Li-carbonate products as measured by acid treatment. Interestingly, when measuring the Li_2O_2 yield as a function of discharge rate, the authors found that the Li_2O_2 yield decreased with decreasing discharge rate, despite the e^-/O_2 ratio remaining close to 2. They attribute this to the length of time which freshly generated Li_2O_2 is exposed to the electrolyte, allowing for a greater amount of chemical decomposition to occur. Upon charging, the researchers found that the Li_2O_2 oxidation rate was always slightly greater than the O_2 evolution rate, indicating that a small amount of Li_2O_2 is oxidised in other parasitic reactions. At higher oxidation potentials, the O_2 evolution rate deviates further from the Li_2O_2 oxidation rate, indicating that the higher potentials induce more parasitic chemistry.

1.3.4 Redox Mediators

Redox mediators are molecules with electrochemical activity that can be reversibly reduced and oxidised during cell cycling. During cycling, the redox mediator acts as an intermediary electron carrier or reservoir between the electrode and the active species, namely oxygen or Li_2O_2. Due to their ability to preserve electrons or holes from a half-reaction, they can decouple the electrochemical formation of Li_2O_2 into separate electrochemical and chemical steps. Good redox mediators will have high reversibility, fast kinetics and negligible side reactions. Good solubility is required if they are to be used in the electrolyte. Furthermore, OER redox mediators must be selected so that their

oxidative potential is below the direct electrochemical potential of Li_2O_2 decomposition and the reductive potential of ORR mediators is above that of the direct electrochemical potential of O_2 reduction.

Discharge Mediators

Discharge mediators provide a strategy to overcome the anti-correlated properties of good intermediate solubility and solvent stability. By bringing the formation of Li_2O_2 into the solution, these molecules allow for high discharge capacities in weakly solvating and stable electrolyte solutions. As well as this, by forming particulate Li_2O_2 in solution, the interfacial contact between Li_2O_2 and the carbon is reduced, thereby reducing parasitic chemistry between Li_2O_2 and the cathode. Early studies by Lacey *et al.* identified ethyl viologen as a suitable mediator for the Li-O_2 discharge reaction.[27,106] They described a one-electron reduction of EV^{2+} to $EV^{\cdot+}$ which can reduce O_2 to O_2^- away from the electrode surface.[106] The O_2^- combines with a Li^+ cation and disproportionates to form Li_2O_2. Despite the promising results, the direct electrochemical formation of Li_2O_2 persisted due to the low reduction potential of EV^{2+}. The passivation of the electrode still occurred during discharge leading to early cell death.

In contrast, the quinone molecule 2,5-di-*tert*-butyl-1,4-benzoquinone (DBBQ) raises the potential of the discharge reaction above that of the direct O_2 reduction potential.[107] DBBQ acts as an electrocatalyst, changing the formation route of Li_2O_2. It is reduced at the electrode surface during discharge, forming Li-$DBBQ_{(sol)}$, which forms a complex with O_2. The free energy of the complex with DBBQ is lowered with respect to that of LiO_2, and the potential is correspondingly raised.[107] The DBBQ is regenerated from Li-DBBQ by reducing O_2 to Li_2O_2 in an EC_{cat} mechanism. The process is shown schematically in Figure 1.9 and can be summarised by the following steps:

$$DBBQ_{(sol)} + Li^+_{(sol)} + e^- \rightarrow LiDBBQ_{(sol)} \tag{1.22}$$

$$LiDBBQ_{(sol)} + O_{2(sol)} \rightleftharpoons LiDBBQO_{2(sol)} \tag{1.23}$$

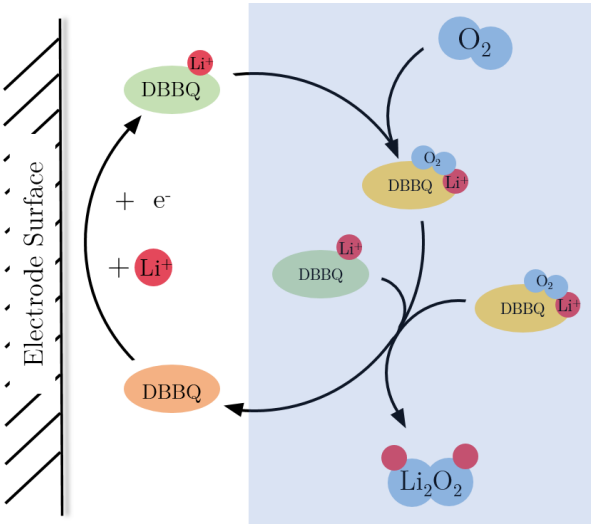


Figure 1.9: Schematic illustration of the DBBQ mechanism. DBBQ is reduced to Li-DBBQ at the electrode surface and combines with oxygen in the solution. Li-DBBQ-O_2 can form Li_2O_2 by a disproportionation reaction with another Li-DBBQ-O_2 or Li-DBBQ, with DBBQ being regenerated as a result. Reproduced with permission from Gao *et al.*.[107] Copyright 2016 Springer Nature.

$$2LiDBBQO_{2(sol)} \rightarrow Li_2O_{2(s)} + O_{2(sol)} + DBBQ_{(sol)} \tag{1.24}$$

$$LiDBBQ_{(sol)} + LiDBBQO_{2(sol)} \rightarrow Li_2O_{2(s)} + 2DBBQ_{(sol)} \tag{1.25}$$

As a result of forming Li_2O_2 in solution, the capacity of a cell utilising a carbon paper cathode is increased 80 to 100-fold when using DBBQ compared to unmediated discharge.[107] In the case of DBBQ, large toroidal particles of Li_2O_2 are formed, and the cathode surface is exposed for charge transfer longer into discharge.

Noticing these results, several other quinone molecules have since been reported to work similarly to DBBQ. For example, coenzyme-Q10 and vitamin K2 have been employed in Li-O_2 cells providing 100-fold increases in discharge capacity.[100,108] Work by Liu *et al.* demonstrated a synergistic effect between H_2O and DBBQ.[109] In this case, the H_2O stabilises the quinone monoanion and dianion, shifting the reduction potentials to more positive values. They observed improved discharge capacities and potentials when both H_2O and DBBQ are used together in a largely dry DME electrolyte, observing Li_2O_2 crystallites up to 30 μm in size.[109] Efforts have been made to improve the reversibility of the quinone-based redox reaction. Liu *et al.* showed that benzo[1,2-b:4,5-b]dithiophene-4,8-dione, a symmetrical and highly conjugated quinone molecule without α-H could offer improved rechargeability at the cost of a reduction

in the full discharge capacity.[110] An interesting study by Han *et al.* looked at adding electron withdrawing or electron donating groups to anthraquinone (AQ) to increase or decrease the reduction potential, respectively.[111] They showed that adding two -NO_2 groups to the AQ moiety both increased the discharge capacity and the voltage plateau of the discharge reaction.[111] These studies demonstrate the diversity of discharge redox mediators and the different strategies that can be employed to improve the capacity and rechargeability of the discharge reaction.

Charging Mediators

The solution formation of Li_2O_2 in Li-O_2 batteries through the use of ORR mediators necessitates the presence of a charging redox mediator. This is because the particulate Li_2O_2 which is formed has low interfacial contact with the cathode, such that oxidation at the cathode-Li_2O_2 interface can cause detachment of the Li_2O_2 particles from the cathode surface, leading to electronic isolation. Charging mediators can oxidise Li_2O_2 in solution after being electrochemically oxidised at the electrode surface, allowing for the decomposition of electronically isolated Li_2O_2. By decoupling the electrochemical and chemical steps of Li_2O_2 decomposition, the potential of the charging reaction is set by the oxidation potential of the redox mediator. The charging overpotential can be lowered with respect to the direct electrochemical oxidation of Li_2O_2, bringing the potential within that of the electrolyte's oxidative potential while improving the cell's energy efficiency. Therefore, the investigation of charging mediators has received significant attention in the research community, as discussed herein.

Charging mediators can be broadly classified into two categories: inorganic and organic. Inorganic redox mediators are comprised of molecules like LiI,[112] LiBr,[113] and CsI,[114] while organic redox mediators can be further subdivided based on their structures. These subdivisions include amines, nitroxy and thiol compounds, such as tris[4-(diethylamino)phenyl]amine, 2,2,6,6-tetramethyl-1-piperidinyloxy (TEMPO), and 10-methylphenothiazine.[115–117] Chen *et al.* conducted a formative study on the prospective use of tetrathiofulvalene (TTF) as a charging mediator in a DMSO-based

electrolyte.[118] They demonstrated TTF's ability to oxidise Li_2O_2 by generating TTF^+ electrochemically, equivalent to 0.03 mAh, and adding it to an excess of Li_2O_2. By measuring O_2 evolution with mass spectrometry, they determined that the quantity of O_2 evolved was equivalent to 2.01 e^-/O_2. The researchers then compared cells cycled with and without TTF at a nanoporous gold electrode. DMSO has a high DN and would have promoted the solution formation of Li_2O_2. They found that TTF greatly reduced the overpotential on charge and improved the coulombic efficiency of the cell. Cells that cycled without TTF polarised rapidly and had low coulombic efficiencies, likely due to particulate Li_2O_2 becoming detached from the cathode surface. In a subsequent study, Bergner *et al.* investigated the suitability of TEMPO as a charging mediator for Li-O_2 batteries. TEMPO is a radical species characterised by its four α-methyl groups, which offer steric protection to the radical. The researchers demonstrated that TEMPO could oxidise Li_2O_2 at lower overpotentials compared to direct electrochemical reduction. *In situ* pressure monitoring revealed a charge of 2.01 e^-/O_2. Importantly, the cycling performance of Li-O_2 batteries was significantly improved with TEMPO compared to other charging mediators such as TTF and LiI. The battery cycled for 50 cycles with TEMPO, while TTF and LiI could only sustain cycling for 27 and 20 cycles, respectively.

These investigations have demonstrated the advantages of using charging redox mediators during cycling. Current research aims to achieve two primary goals: decreasing the charging overpotential through the discovery of molecules with lower formal potentials (E_0) and improving the reaction rate to enable faster charging (high apparent rate constants for Li_2O_2 oxidation, k_{app}). A thorough understanding of the reaction mechanisms and kinetics is necessary to identify new materials. In this context, Chen *et al.* conducted a scanning electrochemical microscopy (SECM) study on the kinetics of Li_2O_2 oxidation by several organic molecules.[119] By measuring the magnitude of a feedback current between the redox mediator and Li_2O_2, where the SECM tip is held at a potential that achieves a steady current for the oxidation of the redox mediator, SECM provides a measure of the kinetics of Li_2O_2 oxidation. The researchers found no correlation between the standard heterogeneous electron transfer rate constant (k_0)

and k_{app} and no simple correlation between E_0 and k_{app}. They concluded that the oxidation of Li_2O_2 by redox mediators is mainly an inner-sphere electron transfer process. They attributed the differences in k_{app} to the steric hindrances of the redox mediators, with smaller molecules such as nitroxyl radicals being more effective at accessing Li_2O_2 surfaces.

1.4 Challenges at the Cathode

In contrast to lithium-ion batteries, the cathode in Li-O_2 batteries is not the active material but rather the framework in which the formation and decomposition of the active materials, O_2/Li_2O_2, can take place. The cathode must have good electronic conductivity, it must be sufficiently porous to effectively transport Li^+ and O_2 and store Li_2O_2, and it must be both chemically and mechanically stable during cell operation. Carbon is the preferred cathode material due to its low cost, low mass and good electrical conductivity. The following section will look at the various carbon materials applied in Li-O_2 batteries and discuss important factors that govern high-performance Li-O_2 cathodes.

1.4.1 Carbon Materials

Carbon materials used for Li-O_2 batteries can be broadly grouped into three categories as shown schematically in Figure 1.10: 0D materials which include carbon blacks such as Super P,[120], Vulcan Carbon,[121] and Ketjen Black,[122] which are point-like spherical nanoparticles. 1D materials which include Carbon Nanotubes (CNT's),[123–125] and Carbon Nanofibres,[126] which are string-like particles. And 2D materials such as graphene,[127] which are sheet-like materials. Each of these materials is diverse in its properties, such as surface area, porosity and electrical conductivity, and each has different considerations when forming cathodes for Li-O_2 batteries.

Carbon black is the most common form of carbon used in Li-O_2 research. This material is produced by decomposing liquid or gaseous hydrocarbons at high

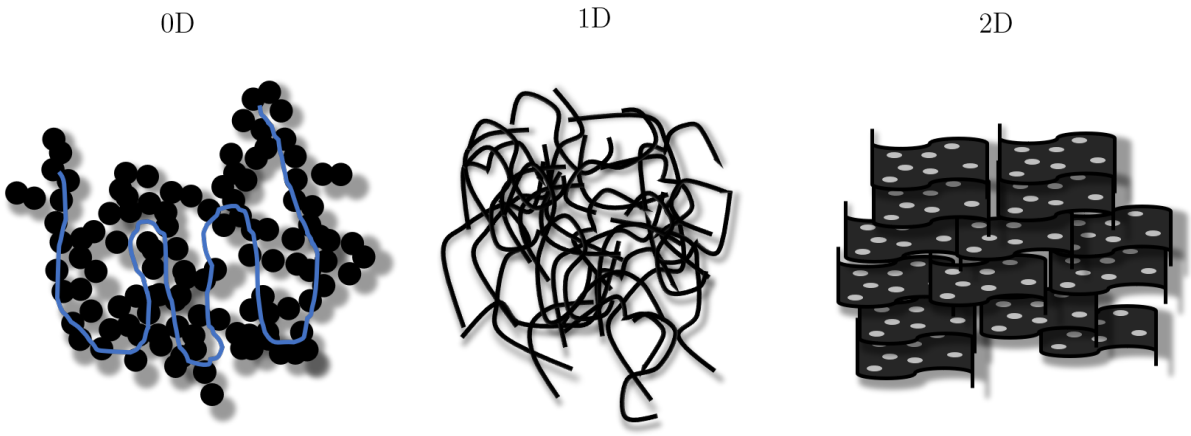


Figure 1.10: Schematic of the various forms of carbon commonly used in Li-O_2 batteries. 0D represents point-like spherical carbons such as carbon black. 1D represents string-like carbons such as carbon nanotubes and carbon nanofibres. 2D represents carbons with a sheet-lie structure such as graphene.

temperatures under an oxygen-free environment. The primary carbon black particle consists of several quasi-graphitic layers which combine to form a spherical particle.[128] The particles combine to form aggregates of fused primary particles. The crystalline graphitic-like layers and interconnectivity of the aggregates afford electrical conductivity to carbon black. Depending on the feedstock and production method, the graphitic layers have functional groups containing elements such as oxygen, hydrogen and sulfur, usually < 1 % by mass altogether. Due to the point-like nature of the carbon black particles, a polymer is often required to form self-standing cathodes. Perfluorinated polymers such as PTFE and PVDF are commonly employed, but several polymers have been utilised as discussed in Section 1.4.3.

CNTs, first discovered in 1991 by Lijima, comprise coaxial sheets of graphitic carbon, with the hexagonal carbons arranged helically around the tube axis.[129] In his original paper, CNTs were formed by an arc discharge of C under reduced pressure in an Ar-filled vessel but have since been produced using other methods, such as laser ablation and chemical vapour deposition.[130,131] CNTs are well-known for having favourable properties for the fabrication of Li-O_2 battery cathodes: they possess high electrical conductivity, mechanical tensile strength, surface area and aspect ratio.[132] The latter of these properties allows for the fabrication of self-standing, binder-free cathodes by a facile vacuum filtration method.[123,124,133] Carbon nanofibres, formed via electrospinning

or by chemical vapour deposition, can similarly form self-standing cathodes by way of their high aspect ratio and have found application in Li-O_2 batteries.[124,126,134]

Graphene is an isolated single layer of carbon hexagons consisting of sp^2-hybridised C-C bonding with π-electron clouds.[135] Graphene can be produced via the cleavage or exfoliation of graphite as well as by chemical vapour deposition and other methods.[136–138] Graphene similarly possesses high electrical conductivity and high surface area as well as a low density, allowing for the formation of cathodes with a low mass-loading. Graphene has been utilised to form free-standing cathodes achieving high discharge capacities.[127,139,140]

1.4.2 Pore Structure and Surface Area

Several studies have explored the effect of surface area on discharge capacity in Li-O_2 batteries.[141,142] The morphology of Li_2O_2 has been shown to depend on the discharge rate, with higher discharge rates leading to film-like morphologies.[57–59] The true surface area discharge current depends on the accessible surface area of the cathode, which calls for a balancing of the electrode surface area and pore volume. In their study, Meini *et al.* employed carbon blacks with various surface areas and showed a strong positive correlation between surface area and first discharge capacity.[141] Noticing from previous studies by Yang *et al.*[143] and Kuboki *et al.*[144], that micropores were inaccessible to O_2 transport and wettability by the electrolyte, Meini *et al.* normalised the discharge capacities to the *external* surface area of the cathodes (external surface area = total BET surface area - micropore surface area). They observed that the specific discharge capacity increased as the surface area of the cathode increased, but the capacity normalised to the *external* surface area stayed approximately constant. By taking the *external* surface area of the cathodes and calculating the number of Li_2O_2 monolayers that would be formed based on a film morphology, Meini *et al.* showed an approximate coverage of two monolayers in each cathode, thus concluding that the discharge capacity was dependent on the accessible surface area for reaction.[141]

As well as cathode surface area, the pore volume and pore size distribution in the

cathode affect the discharge capacity. In studies such as that carried out by Meini *et al.*[141] where a film morphology of Li_2O_2 is observed, the cathode surface area may have a large influence. However, the formation of Li_2O_2 can occur by a solution or surface mechanism (Section 1.3.1), and larger particulate forms of Li_2O_2 may have to be stored within the pore volume. Ma *et al.* investigated the effect of porosity on discharge capacity by comparing two activated carbons with high surface area but low pore volume (1195 and 1908 m^2g^{-1} and 0.85 and 0.55 cm^3g^{-1} respectively) and a carbon aerogel with a moderately high surface area with a large pore volume (688 m^2g^{-1} and 2.53 cm^3g^{-1}).[145] Using N_2 adsorption/desorption analysis Ma *et al.* showed that the carbon aerogel had significant pore volume in the pore size range 20-40 nm, compared to the activated carbons, which had mainly micropores, < 2 nm. They observed a much higher discharge capacity when employing the carbon aerogel, 4155 mAh g^{-1}, compared to the activated carbons, 264 and 124 mAh g^{-1}. They concluded that pore volume was more important than the surface area in determining the discharge capacity and that mesopore volume rather than micropore volume was more beneficial.[145]

Ding *et al.* extended the above studies to include more carbon materials with varying surface areas and pore structures.[146] They explored a range of carbon blacks, multi-walled CNTs, reduced graphene oxide and synthesised ordered mesoporous carbons. In contradiction to previous studies by Meini *et al.*[141] and Ma *et al.*[145] above, they observed no correlation of discharge capacity with surface area or pore volume. Instead, they observed a positive correlation between average pore size and discharge capacity.[146] To further verify their results, they synthesised ordered mesoporous carbons with pore sizes between 20 and 100 nm in 20 nm increments whilst maintaining a constant surface area and total pore volume between each carbon sample. They found an optimal pore size of 80 nm where the highest discharge capacities were achieved. They attributed this to a model of Li_2O_2 formation where smaller pore sizes are blocked or have increasingly restricted oxygen diffusion as discharge progresses due to the formation of insoluble Li_2O_2. As the pore sizes are increased up to 80 nm, the pores are left open to oxygen diffusion for longer into discharge, allowing for improved utilisation of the

cathode volume. Above 80 nm, the surface area available to charge transfer is reduced, which has a slight detrimental effect on the capacity.[146]

Several other studies have explored the importance of pore size on cathode performance. For example, Guo *et al.* synthesised mesoporous/macroporous carbon sphere arrays and formed cathodes by combining with carbon Super P.[147] They showed an increase in discharge capacity when combining mesoporous/macroporous carbon sphere arrays with Super P up to a 50:50 weight ratio and attribute the boost in performance to increased O_2 and Li^+ diffusion as well as better electronic conductivity.[147] A similar study by Nie *et al.* compared a synthesised hierarchically porous carbon consisting of macro and mesopores to a mostly mesoporous carbon material.[148] Using CV, they demonstrated improved oxygen diffusivity in the hierarchically porous carbon compared to the mesoporous carbon material, which translated to higher discharge capacities.[148] Park *et al.* studied the effect of mesopores on the rate capability and charging overpotentials during cycling.[149] They observed larger discharge capacities and lower charging overpotentials in a mesoporous carbon with small pores compared to a mesoporous carbon with larger interconnected pores under mild current densities. However, the mesoporous carbon with larger interconnected pores demonstrated higher performance at higher current densities.[149]

Pore interconnectivity can also affect the discharge performance in Li-O_2 batteries.[150,151] An interesting study by Torayev *et al.* utilised nanocomputed tomography to probe the pore structure of a Super P-based carbon cathode.[150] They were able to develop a pore network model (PNM), which enabled them to calculate transport properties and simulate electrochemical reactions in a reconstructed 3D cathode; this is illustrated in Figure 1.11.

The pore network is extracted by assigning a pore to each void voxel in the tomography data and expanding the pore until a carbon voxel is located, Figure 1.11 (a). Clusters of overlapping pores are then assigned as *pore families*, Figure 1.11 (b). Two parameters are then calculated: the effective pore radius, l_i and l_j, where the volume of the effective pore is the same volume as the pore family, and the length and radius of the

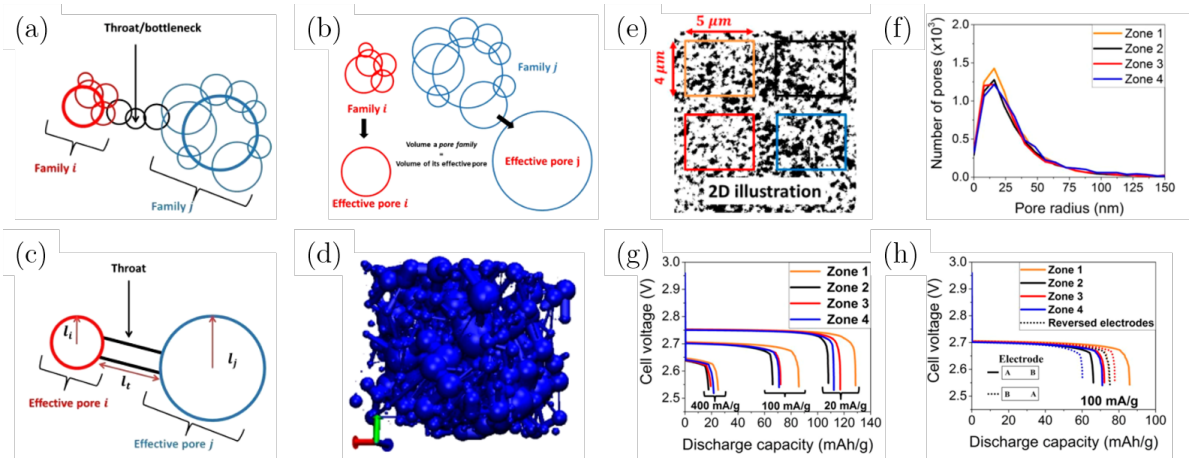


Figure 1.11: Pore network model developed from nanocomputed tomography developed by Torayev *et al.*.(a-d) The pore network model *et al.*. (e-h) The discharge data modelled from the PNM established in the coloured zones in (e). Adapted with permission from Torayev *et al.*.[150] Copyright 2018 American Chemical Society.

throat/bottleneck that connects them, Figure 1.11 (c). A 3D PNM can be established, such as that in Figure 1.11 (d). An interesting result is obtained from modelling the discharge reaction in the PNM. They selected four random zones from a single tomography image as shown in Figure 1.11 (e) and applied their discharge model to these distinct regions. The pore volumes and pore size distributions show negligible differences between each zone, Figure 1.11 (f). However, the discharge capacities obtained from each zone differ by as much as 16-29 % between zones over discharge rates from 20-400 mA g^{-1}, Figure 1.11 (g). To show that this is not due to some small variations in the pore size distributions, the air inlet and separator sides are flipped and the discharge data is modelled again, however there is still a large variation in the capacities achieved, Figure 1.11 (h). The variations in discharge capacity are attributed to the stochasticity of the pore's interconnectivity. The transport of O_2 and Li^+ throughout the cathode are critical to the discharge capacity. The pore structure develops dramatically as the discharge reaction proceeds and solid Li_2O_2 builds up in the pores of the cathode. As pores become clogged the transport of O_2 and Li^+ to neighbouring connected pores is blocked impeding long-range transport of active material.[150]

Taking the above points and summarising, it can be seen that the pore structure and surface area of the cathode can affect the discharge capacity in several ways:

- Higher surface area carbons are generally able to achieve higher discharge capacities

- Larger porosities generally lead to higher discharge capacities
- Micropores are inaccessible to the electrolyte and active materials and do not contribute to the discharge capacity
- Mesopores are more beneficial to the discharge capacity compared to macropores
- Macropores are beneficial to O_2 and Li^+ mass transport
- Pore inter-connectivity is beneficial to long-range transport of O_2 and Li^+

1.4.3 Polymer Binders

Polymer binders play a vital role in Li-O_2 batteries as they are essential for forming free-standing cathodes based on carbon materials. Carbon black is the most commonly employed among the various carbon materials utilised in Li-O_2 batteries. However, as previously mentioned, carbon black consists of spherical particles, rendering them incapable of forming self-supporting cathodes without a polymer binder. The binder envelops the carbon particles with a fibrous coating, resulting in an interconnected network of carbon particles and polymer. Numerous materials have been investigated for this purpose. The structures of the most prevalent polymers used as binders are illustrated in Figure 1.12.

Initially, several early studies employed PVdF as a binder in Li-O_2 batteries.[120,152,153] However, a study conducted by Black *et al.* revealed the instability of PVdF in the presence of O_2^-, an intermediate species generated during discharge.[88] LiO_2 was chemically generated by dissolving KO_2 in a solution of TEGDME/$LiPF_6$, with the addition of a crown ether that complexed K^+ ions. The resulting O_2^- species reacted with Li^+ ions from $LiPF_6$ to form LiO_2. When PVdF was introduced into this solution, the researchers observed gas evolution and a colour change from colourless to dark brown. The authors proposed that the strong base LiO_2/O_2^- could abstract a hydrogen atom from the PVdF polymer backbone, leading to the release of F^- and the formation of a conjugated double bond. The resulting HO_2 species underwent disproportionation, yielding H_2O_2 and O_2 gas. This finding was further supported by Nasybulin *et al.*, who demonstrated the instability of PVdF upon contact with Li_2O_2. Through ball milling

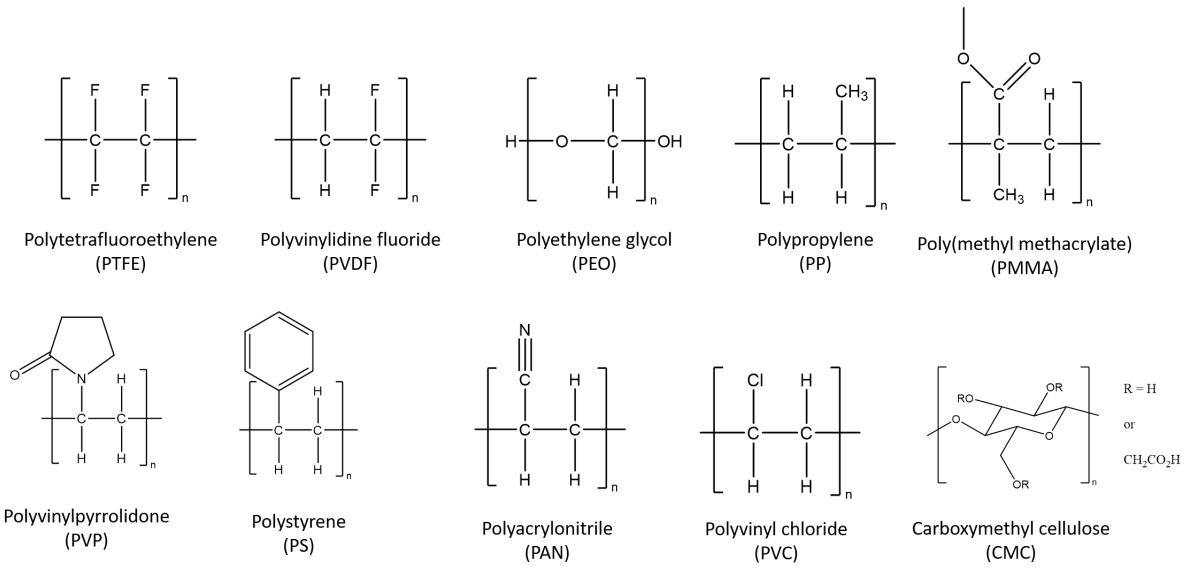


Figure 1.12: Chemical structures of commonly used polymer binders for Li-O_2 batteries. The polymers depicted have found application as both carbon binders and electrolyte components for Li-O_2 cells.

PVdF with Li_2O_2 and analysing X-ray photoelectron spectroscopy (XPS) spectra before and after the milling process, they observed a shift to lower energies, indicating the formation of unsaturated carbons.[154] Another notable study by Papp *et al.* highlighted that PVdF exhibited peaks in the Raman spectra that strongly overlapped with peaks exhibited by LiO_2.[155] Consequently, caution should be exercised when characterising discharge products in the presence of PVdF as a binder.

Noticing this work, Nasybulin *et al.* conducted a comprehensive investigation on the stability of various commonly used polymers in both Li-O_2 and Li-ion applications, as depicted in Figure 1.12.[154] To evaluate the stability, the authors subjected the polymers to reactive oxygen species, namely KO_2 and Li_2O_2, under ball-milling conditions. As an illustration, the authors obtained XRD patterns of the polymers before and after ball-milling with KO_2, revealing that only three polymers, namely polyethylene (PE), polypropylene (PP), and PTFE, remained stable under these conditions. In contrast, polymers such as polystyrene reacted to form K_2CO_3, while polyethylene oxide underwent complete decomposition into multiple products. Similarly, polyacrylonitrile (PAN) and polyvinylchloride experienced decyanation and dechlorination, respectively, resulting in the formation of KCN and KCl. Additionally, the authors employed XPS analysis on PE, PP, and PTFE to ensure that any amorphous products were not missed

due to using XRD. When individually ball-milled with KO_2 and Li_2O_2, PP and PTFE exhibited additional small peaks in the XPS spectra, indicating changes induced by the ball-milling process. Conversely, PE demonstrated the highest stability, with no other peaks observed in the XPS spectra after ball-milling. Interestingly, the authors also explored the impact of binding strength on the discharge capacity and found that, in general, polymers with weaker binding strength exhibited higher discharge capacity. This observation can be attributed to the fact that stronger binders cause shrinkage of the carbon network within the cathode, reducing the available pore volume for Li_2O_2 storage.

Amanchukwu *et al.* expanded on the previous work conducted by Nasybulin to propose reaction mechanisms for several of the polymers above.[156] Employing a wide range of characterisation techniques, including UV-vis, Fourier transform infrared (FTIR) spectroscopy, NMR, and gel permeation chromatography, they monitored the reactions between each polymer and Li_2O_2. For instance, they identified the nitrile group in PAN as the reactive chemical functionality (rather than the carbon backbone or adjacent hydrogen atoms). By observing a colour change in a PAN/dimethyl formamide solution upon interaction with Li_2O_2 and measuring the corresponding decrease in peak intensity for the nitrile group using FTIR, they proposed that Li_2O_2 attacks the nitrile group, leading to the formation of soluble imine-like conjugated species responsible for the observed colour change. Similarly, they suggested a reaction mechanism involving β-CH_2 elimination, subsequent alkene formation, and fluoride elimination in PVdF. In the case of polyvinyl chloride, they proposed an S_N2-type reaction due to the good leaving ability of chloride. Notably, the researchers established a reactivity trend for the polymers within the context of Li-O_2 electrochemistry: (i) the polymers exhibited greater reactivity if they possessed electron-withdrawing groups on the side chain, and (ii) if the carbon backbone was aliphatic, the polymers exhibited greater reactivity with α or β hydrogens adjacent to the side groups.

One approach is to carbonise the polymer to address the stability concerns associated with polymer binders. Cui *et al.* conducted an interesting study in which they utilised

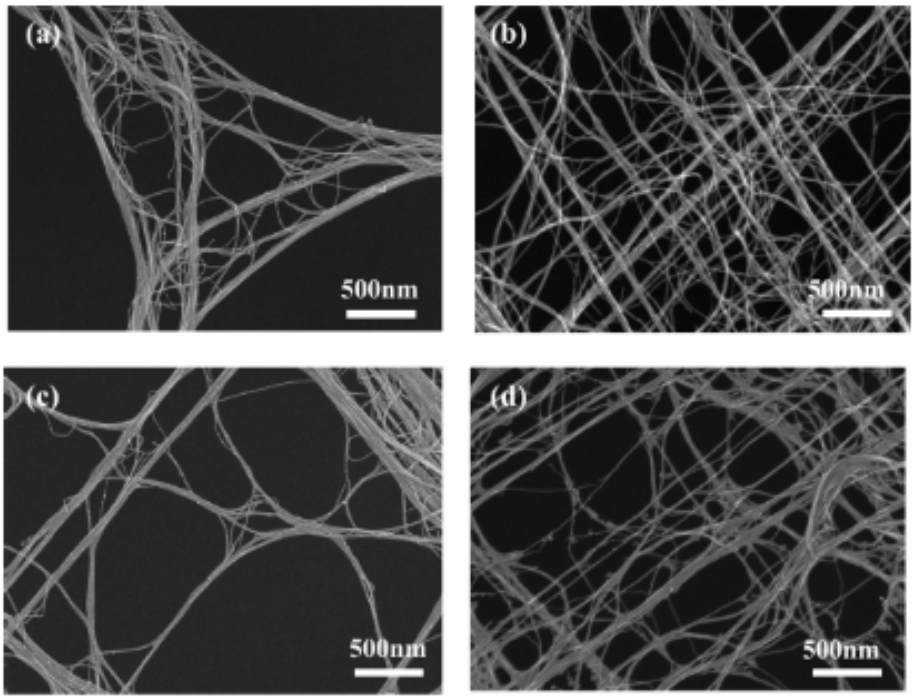


Figure 1.13: PAN Cross-linked CNT network by Cui *et al.* **a-d,** SEM images of the CNT cathodes after dip-coating with PAN, stabilisation at 280 °C and then carbonised at 1000 °C. Concentrations of PAN used were 0.01 (a) 0.05, (b) 0.1, and (d) 0.2 wt. %. Adapted with permission from Cui *et al.*.[157] Copyright 2013 American Chemical Society.

PAN to create cross-links between CNTs to enhance the macroscopic CNT network.[157] They achieved this by dip-coating CNT sheets into a PAN/dimethylformamide solution to coat the CNTs, followed by a stabilisation step at 280 °C and carbonisation at 1000 °C under a nitrogen atmosphere, the resulting cross-linked network is shown in Figure 1.13.

The PAN underwent dehydrogenation and denitrogenation during the carbonisation process, converting its structure into a graphitic form. The carbonised PAN formed cross-links at the CNT joints, reinforcing the network structure. In a subsequent study by the same research group, they introduced polymethyl methacrylate microspheres to introduce porosity into the electrode, further enhancing its properties.[158] In this instance, the polymethyl methacrylate spheres were depolymerised and expelled during the stabilisation step at 280 °C.

1.4.4 Oxygen Mass Transport and Pore Clogging

The efficient transport of oxygen to reaction sites within the porous carbon cathode is crucial for the discharge reaction in Li-O_2 batteries. During operation, oxygen is

introduced at the cathode/gas interface and dissolves into the electrolyte that permeates the cathode. The oxygen then needs to be transported through the porous network of the cathode to reach reaction sites distributed throughout its volume. Achieving effective oxygen mass transport is essential for sustaining the discharge reaction and attaining high discharge capacity at practical discharge rates. Various factors influence oxygen mass transport, including:

- Solubility and diffusion coefficient of oxygen in the electrolyte.
- Concentration gradient of oxygen within the cathode.
- Pore sizes, pore distribution, and tortuosity of the cathode.
- Formation of discharge products.
- Temperature of the battery.

Once oxygen is dissolved in the electrolyte, its transport occurs via diffusion from high-concentration regions at the cathode/gas interface to areas of low concentration at the cathode/separator interface. The oxygen diffusion in the electrolyte can be described using Fick's Laws of Diffusion.[159] The first law describes the flux of a species (oxygen in this case) perpendicular to a plane, indicating that substances will diffuse from areas of high concentration to areas of low concentration until an equilibrium is reached. This is given by the equation:

$$Flux = -D_i \frac{dc_i}{dx} \tag{1.26}$$

Where D_i is the diffusion coefficient of species i, in this case oxygen. The second law of Fick's describes the change in concentration of oxygen over time due to diffusion, taking into account diffusion into and out of the solution element and is given by:

$$\frac{\delta c_i}{\delta t} = D_i \frac{\delta^2 c_i}{\delta x^2} \tag{1.27}$$

The influence of oxygen concentration and diffusion coefficient on the discharge capacity of lithium-oxygen batteries has been extensively investigated. Read *et al.* examined the relationship between oxygen concentration, diffusion coefficient, and discharge

capacity using various salt and solvent formulations in a previous study.[160] Their results were intuitively expected, as they demonstrated that increasing the oxygen concentration, either by reformulating the electrolyte or by increasing the partial pressure of oxygen in the cell, led to enhanced discharge capacities. Furthermore, they observed higher discharge capacities when the viscosity was decreased, resulting in an increased diffusion coefficient. Similarly, Mohazabrad *et al.* reported comparable findings when studying the effect of increasing salt concentration (0.005 - 1 M LiTFSI in TEGDME) on O_2 diffusivity.[161] They observed a decrease in O_2 diffusivity with increasing salt concentration due to the higher viscosity caused by the salt. To explore the effects of the salt anion on oxygen mass transport properties in DMSO, Gunasekara *et al.* conducted a microelectrode study.[162] Surprisingly, they did not observe a clear correlation between the properties of the salt anion and the oxygen diffusion coefficient or concentration. In a combined approach using molecular dynamic simulations and electrochemical measurements, Gittleson *et al.* investigated the effects of solvent and salt selection on the first discharge performance of lithium-oxygen batteries.[163] They found that in high-DN solvents such as DMSO, the oxygen diffusivity was largely independent of salt concentration. However, in TEGDME, the salt concentration had an effect due to reduced electrostatic screening from TEGDME. Additionally, they discovered that the diffusivity of superoxide, a solvated species, was significantly lower than that of oxygen. This decrease in diffusivity was attributed to interactions between superoxide and the solvent or salt anion, resulting in a larger solvation sphere

Perfluorinated carbon (PFC) has emerged as a promising additive in Li-O_2 electrolytes, aiming to enhance oxygen diffusivity and concentration.[164–168] PFC possesses several desirable properties that make it suitable for use as an electrolyte additive. It exhibits excellent thermal, chemical, and electrochemical stability, and can dissolve oxygen in high concentrations while demonstrating superior oxygen diffusivity. Balaish *et al.* created an artificial three-phase reaction zone in a carbon cathode by drop-casting an immiscible PFC.[166] Due to its low polarity, the PFC does not dissolve the electrolyte salt, and thus cannot support the electrochemical reduction of oxygen

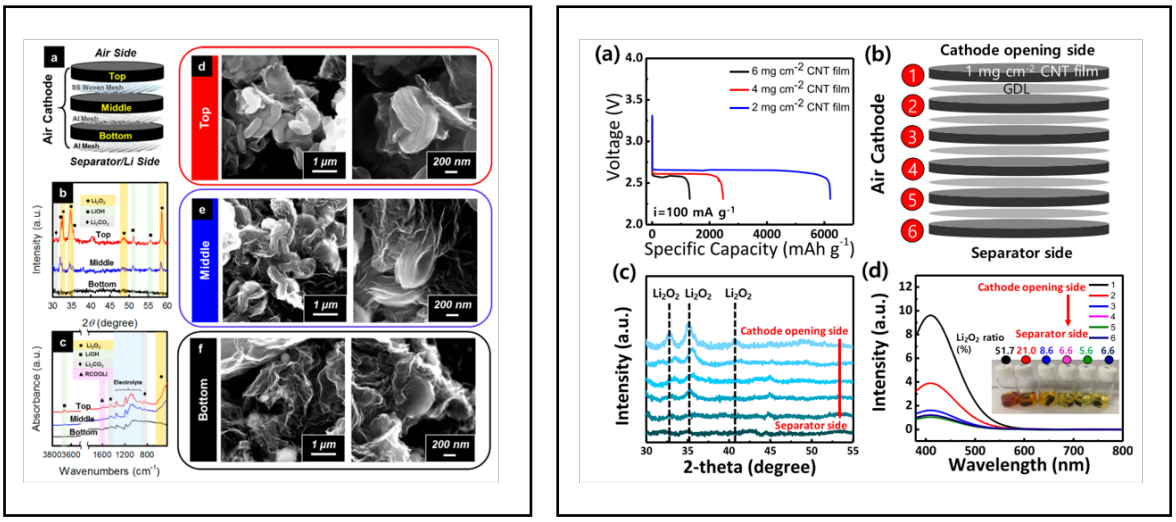
to Li_2O_2. Consequently, the PFC facilitates efficient oxygen mass transport throughout the cathode while the electrolyte solvent (such as TEGDME) dissolves the Li^+ salt. The researchers observed a notable increase in discharge capacity, from 175 mAh g^{-1} to 275 mAh g^{-1}, utilising this method. However, subsequent research by Balaish and colleagues demonstrated that immiscible PFCs exhibit reduced efficacy at higher rates when drop-casting onto an activated carbon cathode. This is attributed to the preferential deposition of PFC near pore openings, leading to localised Li_2O_2 formation that blocks further oxygen mass transport.

During the discharge process of lithium-oxygen batteries, the formation of Li_2O_2 and other insulating side products can block pores, hindering efficient oxygen mass transport. Li_2O_2, in particular, tends to accumulate predominantly at the gas interface of the cathode, as shown in Figure 1.14. This is attributed to the low solubility and sluggish mass transport of oxygen in organic electrolytes. As oxygen dissolves into the electrolyte, it undergoes rapid charge transfer at the electrode, reacting with highly concentrated Li^+ ions (typically 1 M) to form Li_2O_2. This accumulation of Li_2O_2 at the gas interface restricts further oxygen transport to other cathode regions. Several researchers have observed skewed Li_2O_2 distributions, predominantly concentrated near the gas interface, resulting from this phenomenon.

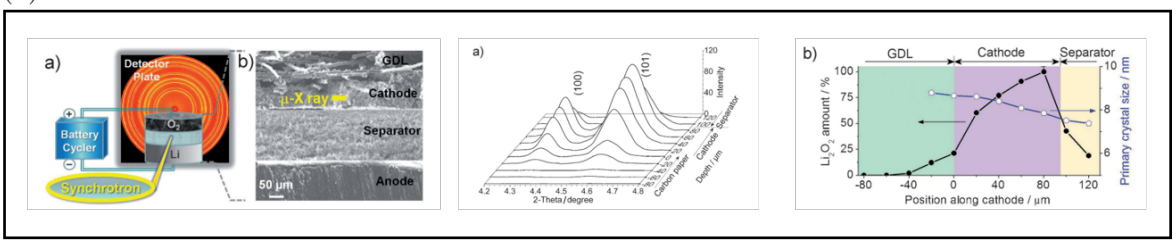
For instance, Lin *et al.* conducted a study to examine the distribution of Li_2O_2 at the end of discharge in a graphene-based cathode, Figure 1.14 (a).[139] They fabricated a cathode comprising three layers of holey-graphene (hG) separated by a stainless steel mesh. By analysing the XRD patterns of each layer individually, they observed more intense Li_2O_2 peaks at the air interface compared to the middle and separator layers. The obtained SEM images were consistent with these findings.

Similarly, Park *et al.* investigated the distribution of Li_2O_2 in a cathode composed of six layers of CNT films separated by a gas diffusion layer (GDL), Figure 1.14 (b).[169] Combining XRD, $TiOSO_4$ titration, and SEM techniques, they demonstrated the effect of oxygen mass transport limitation. The XRD and UV-vis signals decreased when measuring layers from the air interface towards the separator interface, indicating a

(a) (b)



(c)



(d)

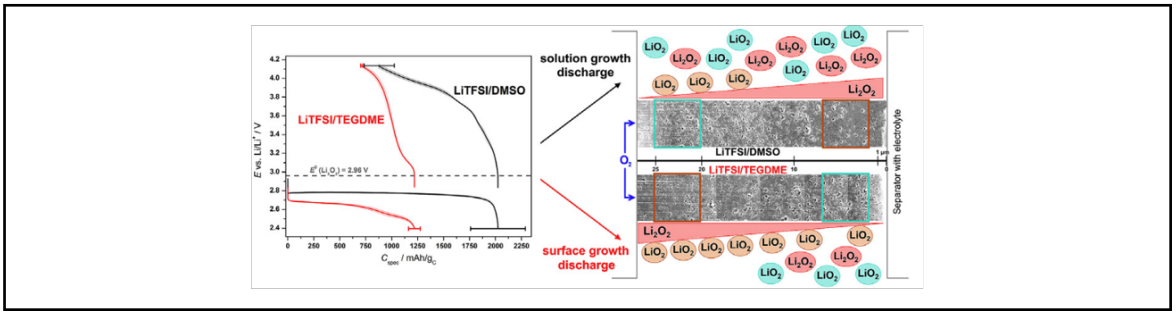


Figure 1.14: Experimental results collected for Li_2O_2 distributions in the cathode of Li-O_2 batteries from the literature. **a,** Li_2O_2 distribution in a cathode consisting of graphene layers with stainless steel meshes recorded with XRD. Adapted with permission from Lin *et al.*.[139] Copyright 2017 American Chemical Society.**b,** Li_2O_2 distribution collected for a cathode with six layers of CNTs separated by GDL layer, The data is collected using $TiOSO_4$/UV-vis titration. Adapted with permission from Park *et al.*.[169] Copyright 2019 American Chemical Society.**c,** Li_2O_2 distribution data collected by microfocused *in situ* synchrotron-XRD. Adapted with permission from Shui *et al.*.[170] Printed by ChemSusChem. **d,** Li_2O_2distribution data collected by SEM, Augustin *et al.*. Adapted from Augustin *et al.*.[171] Copyright 2019 Elsevier.

decline in Li_2O_2 content. Additionally, the SEM images revealed smaller and fewer particles of Li_2O_2 in the cathode as the measurement moved towards the separator interface.

However, conflicting results have been reported by other research groups. In an *operando* XRD study conducted by Shui *et al.*, the Li_2O_2 distribution during discharge in a TEGDME-based electrolyte with a Super P cathode was examined, Figure 1.14 (c).[170] The researchers utilised synchrotron radiation, enabling layer-by-layer XRD pattern analysis through the depth of the cathode. Intriguingly, they found that Li_2O_2 preferentially formed at the separator interface. From this observation, they concluded that the Li_2O_2 distribution is more sensitive to the Li^+ ion concentration, which depletes at the oxygen interface during discharge.

Augustin *et al.* observed different distributions of Li_2O_2 at the end of discharge depending on the electrolyte solvent used, Figure 1.14 (d).[171] In DMSO, Li_2O_2 was skewed towards the separator interface, while in TEGDME, Li_2O_2 exhibited preferential distribution at the oxygen interface. This variation was attributed to the dissolving ability of the solvent for LiO_2. DMSO, with its high DN, solvates LiO_2 as it forms, allowing the solvated LiO_2 to travel through the electrolyte towards the separator interface before reacting to form Li_2O_2. In contrast, TEGDME, with its low DN, retains LiO_2 as an adsorbed species on the electrode surface, limiting its diffusion through the electrolyte and leading to the formation of Li_2O_2 at the oxygen interface.

Torayev *et al.* conducted a study investigating the impact of Li_2O_2 formation on diffusion processes within a porous electrode. To measure the long-range diffusion of solvent molecules, they employed ^1H pulsed-field gradient nuclear magnetic resonance spectroscopy. However, direct probing of oxygen diffusion was not feasible due to the paramagnetic nature of O_2 and the low abundance of ^{17}O. Instead, the researchers measured the bulk diffusion of the electrolyte, excluding diffusion within the electrode, and compared it to the effective diffusion coefficient within the electrode. This allowed them to calculate the tortuosity factor, characterising the deviation of diffusion pathways in the electrode from a straight line.

By comparing the discharge behaviour of a TEGDME-based electrolyte with that of a DME-based electrolyte, Torayev *et al.* observed that the tortuosity factor increased more rapidly in the case of DME. They attributed this observation to the different morphologies of the formed Li_2O_2. In TEGDME, Li_2O_2 predominantly exists as a surface product, while in DME, it takes the form of particulates. Consequently, the effective diffusion coefficients decrease more rapidly during discharge in DME, indicating a greater hindrance to diffusion caused by the presence of particulate Li_2O_2.

1.4.5 High-Capacity Cathodes

To achieve a high energy density in Li-O_2 batteries at the cell level, it is necessary to use a thick cathode capable of storing a significant amount of Li_2O_2. The cathode should occupy a substantial portion of the cell volume to compensate for the reduced energy density caused by non-active components like cell packaging, electrolyte, and separators.[172] However, thick electrodes require efficient oxygen mass transport to effectively utilise the cathode volume for charge transfer and Li_2O_2 storage. Overcoming the challenge of delivering oxygen throughout the cathode volume during discharge at practical rates is crucial for Li-O_2 cathodes. This can be partly overcome by tuning the pore structure and surface area of the cathode as discussed above. Similarly, carefully selecting the electrolyte and additives for their oxygen transport properties can enhance the discharge capacity.

Another key method to boost oxygen transport through thick cathodes is to introduce new architectures which can decouple the oxygen, Li^+ and electron pathways. Considerable research efforts have been devoted to this and some key publications in this area are discussed below. Xu *et al.* devised a textile-inspired cathode design with separate pathways for oxygen gas and the electrolyte, shown in Figure 1.15 (a).[173] They coated an interwoven mesh of cotton fibres with CNTs by repeatedly immersing the textile in a CNT ink. The resulting mesh facilitated the transport of electrolyte through the textile while maintaining electrical conductivity through the CNT coating. Oxygen transport pathways were created by the holes in the textile mesh, enabling distinct

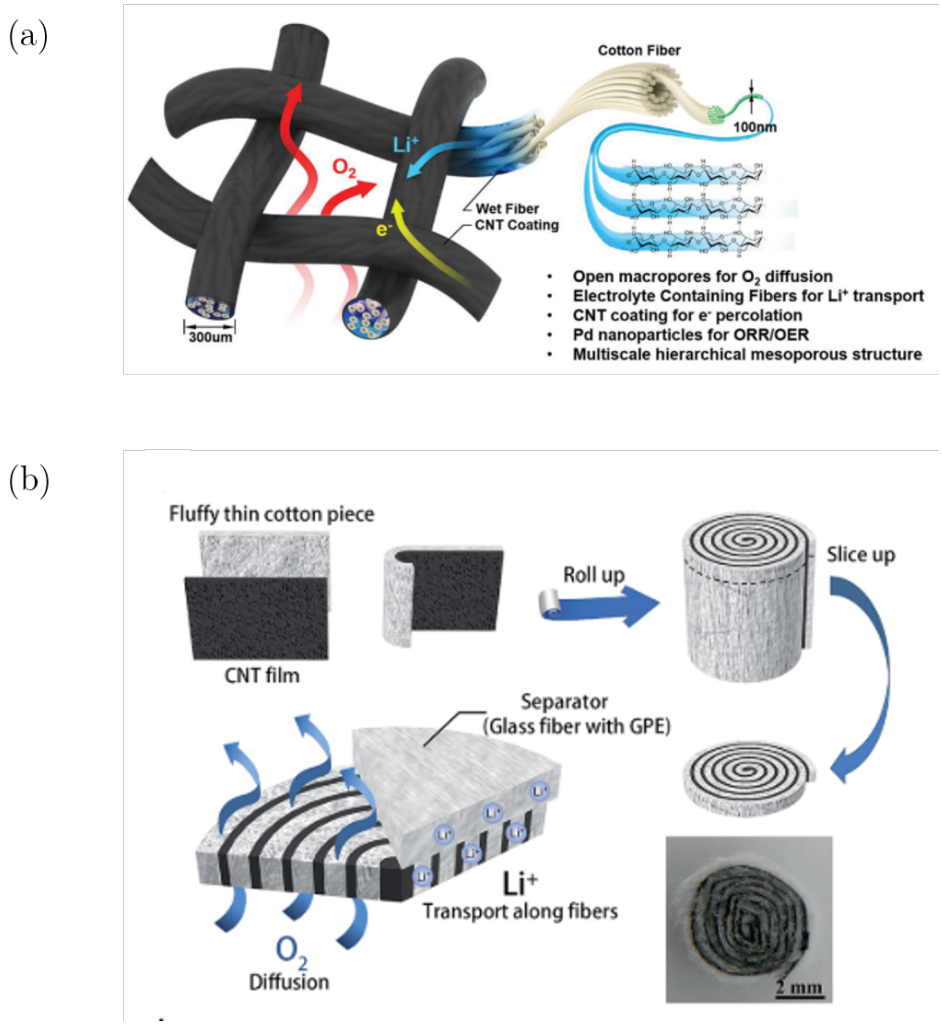


Figure 1.15: High-capacity cathodes with decoupled Li^+, e^- and O_2 pathways. **a,** Textile-inspired cathode architecture by Xu *et al.*. Adapted with permission from Xu *et al.*.[173] Copyright 2017 John Wiley and Sons. **b,** Rolled-layered cathode by Huang *et al.*.Adapted with permission from Huang *et al.*.[174] Copyright 2019 Royal Society of Chemistry

electron, Li^+, and oxygen pathways. With this approach, the researchers achieved a discharge capacity of 8.6 mAh cm^{-2} at a discharge rate of 0.1 mA cm^{-2} using a 1 M LiTFSI/TEGDME electrolyte. Interestingly, they observed that Li_2O_2 formed on the outer surface of the CNT coating rather than within the textile where the electrolyte was present.

A similar method was employed by Huang *et al.* who fabricated a cathode by rolling a layer of glass fibre with a layer of CNT, as shown in Figure 1.15 (b).[174] They then cut a cross-section of the rolled sheets into 400 μm thick disks, the glass fibre was then partially wetted with a gel polymer electrolyte. The vertically aligned CNT sheet provided electronic transport while partially wetting the glass fibre meant

good oxygen transport could be maintained. The gel polymer electrolyte provided Li^+ transport. Li_2O_2 could be formed on both sides of the CNT sheet resulting in efficient carbon utilisation. Using this method, the researchers obtained a discharge capacity of 13564 mAh g^{-1} at 100 mA g^{-1}, based on the mass of carbon in the electrode.

Other studies have looked to nature to inspire, Figure 1.16. Song *et al.* introduced a unique cathode design using natural basswood, which possesses well-aligned elongated microchannels.[175] They carbonised the basswood to activate it and then decorated the microchannels with a Ru catalyst. The activated cathode exhibited favourable wettability, allowing the electrolyte to penetrate and form a thin layer on the microchannel walls, enabling efficient Li^+ transport throughout the cathode. The thin electrolyte layer ensured the microchannel pores remained open for oxygen mass transport. The cathode structure is illustrated in Figure 1.16 (a). By implementing this design, the researchers achieved a remarkable capacity of 8.58 mAh cm^{-2} at a discharge rate of 0.1 mA cm^{-2} using a 1 M LiTFSI/TEGDME electrolyte in a cathode that was 700 μm thick. Furthermore, when the cathode thickness was increased to 3.4 mm, an impressive capacity of 56 mAh cm^{-2} was obtained.

A follow-up study by Chen *et al.* utilised balsa wood, this time introducing mechanical flexibility to the cathode by chemically removing the lignin and hemicellulose, the cathode architecture is shown in Figure 1.16 (b).[176] They then coated the surface of the cathode and the walls of the internal microchannels with CNTs without sacrificing the mechanical flexibility, followed by dispersing Ru catalysts throughout. By drop-casting a moderate volume of electrolyte consisting of 1 M LiTFSI in TEGDME, they could form a thin electrolyte layer on the channel walls without flooding the cathode. Using this cathode design the authors achieved a high discharge capacity of 67 mAh cm^{-2}.

In addition to the significant focus on developing innovative cathode architectures to effectively tackle challenges related to oxygen mass transport, electrical conductivity, and ionic conductivity, researchers have also investigated the potential of new carbon materials with substantial surface areas and favourable processing capabilities. Notably,

(a)

(b)

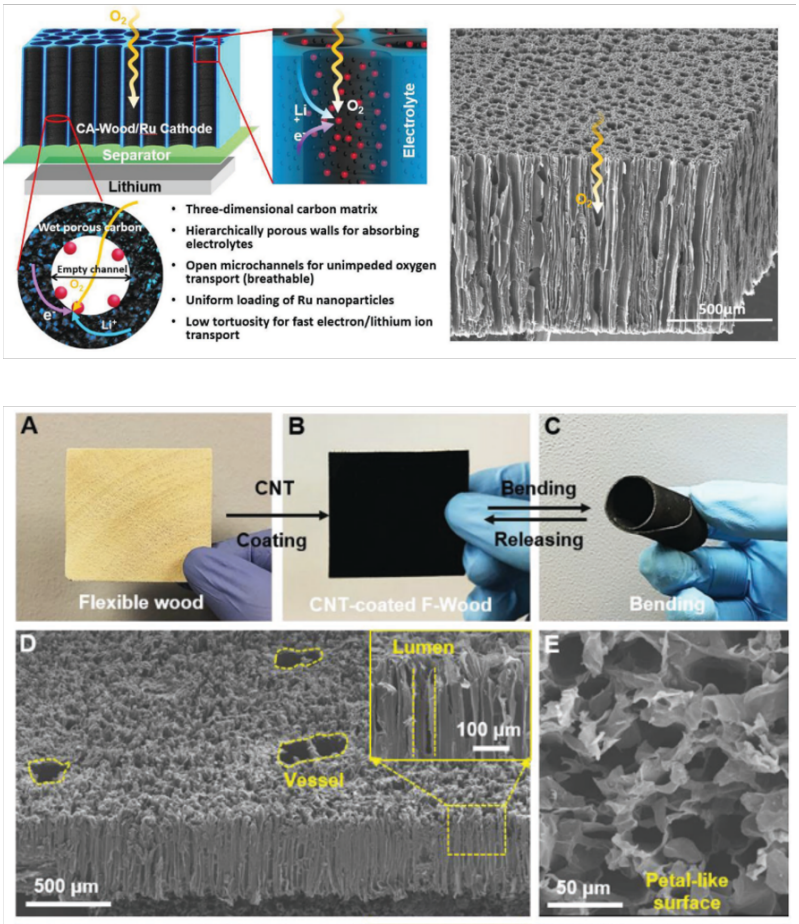


Figure 1.16: Nature-inspired high-capacity cathodes for Li-O_2 batteries. **a,** Natural basswood cathode by Song *et al.*. Adapted with permission from Song *et al.*.[175] Copyright 2017 John Wiley and Sons.**b,** Balsa wood cathode as produced by Chen *et al.*. Adapted with permission from Chen *et al.*.[176] Copyright 2019 John Wiley and Sons.

Lin *et al.* utilised holey graphene (hG) as a material for fabricating thick cathodes with high mass-loading.[139] Through a dry pressing method, they successfully created binder-free, free-standing cathodes. The unique properties of hG proved advantageous in this investigation, enabling air escape during cathode formation while facilitating oxygen mass transport during discharge and charge cycles. Impressively, a discharge capacity of 38 mAh cm^{-2} at 0.1 mA cm^{-2} was achieved using a cathode with a mass of 10 mg cm^{-2} and an electrolyte comprising 1 M LiTFSI in TEGDME. Using a similar method, Lacey *et al.* achieved a discharge capacity of 42 mAh cm^{-2} at 0.2 mA cm^{-2} with the introduction of a nickel-based catalyst within the structure.[140]

A subsequent investigation by Greenburg *et al.* delved into the utilisation of different carbon additives in conjunction with hG for the production of free-standing cathodes. Their study examined the inclusion of 0D carbon black, 1D CNTs with diameters of 150 nm and 8 nm, and 2D graphene sheets (chemically reduced and thermally reduced) in a 1:5 mass ratio of additive to hG for each case.[177] Notably, except for the addition of thermally-reduced graphene (t-G), introducing these carbon additives resulted in a decrease in the overall discharge capacity compared to cathodes comprised solely of hG. Conversely, when t-G was incorporated, the capacity increased from 47 mAh cm^{-2} to 53 mAh cm^{-2} at 0.2 mA cm^{-2}. However, the researchers attributed these high discharge capacities to substantial volume changes within the cathode during discharge. It is important to note that although significant volume changes may contribute to favourable areal capacities, they are not desirable for achieving high volumetric energy densities, which are crucial for lithium-oxygen cells. Additionally, the study revealed that cathodes allowing for significant volume expansion, such as those composed of hG and hG/t-G, exhibited poor cycling performance. In contrast, cathodes resistant to volume expansion, such as those incorporating CNTs, demonstrated superior cycling behaviour.

1.5 Thesis Objectives

The high theoretical specific energy and energy density of Li-O_2 electrochemistry has yet to be realised in cathodes of practical volume and at practical discharge rates. Early studies exploring the discharge-charge capabilities of Li-O_2 batteries employed cathodes with low mass-loading. This, coupled with the reporting of specific discharge capacities in terms of the mass of the cathode resulted in the publication of capacities which appeared extremely high, but translate to poor specific capacities when other inactive cell components, such as the cell packaging and air- and solvent-handling components are considered.

In brief, the following thesis aims to demonstrate that high energy densities can be achieved at practical discharge rates in gas diffusion electrodes (GDE) of high volume. The results are considered in the context of a system-level battery which includes all air- and solvent-handling components. The aim is to show that Li-O_2 batteries can exceed the energy density and specific energy of Li-ion batteries.

Chapter 3 explores using a gas diffusion polymer (GDP) which can transport oxygen throughout the cathode whilst binding the carbon together. The distribution of Li_2O_2 throughout the discharged GDE is measured, which provides insight into the oxygen transport capabilities of the GDP. Chapter 4 explores the fabrication of gas diffusion electrodes with gas diffusion channels. The gas diffusion channels separate the oxygen transport pathways from those of lithium ions and electrons, allowing oxygen to be transported further into the electrode before forming lithium peroxide. Chapter 5 then looks at the cyclability of Li-O_2 batteries at high energy densities and practical discharge rates. Even at curtailed capacities, high energy density gas diffusion electrodes can only cycle for 12 cycles before failure. The avoidance of parasitic chemistry which forms insulating products such as lithium carbonate is the greatest remaining challenge which Li-O_2 batteries face.

1.6 References

[1] IPCC. In *Climate Change 2021: The Physical Science Basis. Contribution of Working*

Group I to the Sixth Assessment Report of the Intergovernmental Panel on Climate Change (2021).

[2] UNFCCC. In *The Paris Agreement (UNFCCC 2015)* (2015).

[3] UNFCCC. In *Glasgow Climate Pact*, 1–8 (2021).

[4] IEA (2021), Tracking Transport 2021, IEA, Paris. Tech. Rep. (2021). URL `https://www.iea.org/reports/tracking-transport-2021`.

[5] IEA (2021), Global EV Outlook 2021, IEA, Paris. Tech. Rep. (2021). URL `https://www.iea.org/reports/global-ev-outlook-2021`.

[6] Mizushima, K., Jones, P. C., Wiseman, P. J. & Goodenough, J. B. Li_xCoO_2 ($0<x\leq1$): A new cathode material for batteries of high energy density. *Materials Research Bulletin* **15**, 783–789 (1980).

[7] Yazami, R. & Touzain, P. A reversible graphite-lithium negative electrode for electrochemical generators. *Journal of Power Sources* **9**, 365–371 (1983).

[8] Yoshino, A., Sanechika, K. & Nakajima, T. United States Patent (1987).

[9] Tarascon, J. M. & Guyomard, D. Li Metal-Free Rechargeable Batteries Based on $Li_{1+x}Mn_2O_4$ Cathodes ($0<x\leq1$) and Carbon Anodes. *Journal of the Electrochemical Society* **138**, 2864 (1991).

[10] Tarascon, J. M., Guyomard, D. & Baker, G. L. An update of the Li metal-free rechargeable battery based on $Li_{1+x}Mn_2O_4$ cathodes and carbon anodes. *Journal of Power Sources* **44**, 689–700 (1993).

[11] Padhi, A. K., Nanjundaswamy, K. S. & Goodenough, J. B. Phospho-olivines as Positive-Electrode Materials for Rechargeable Lithium Batteries. *Journal of the Electrochemical Society* **144**, 1188 (1997).

[12] Thackeray, M. M., Johnson, C. S., Amine, K. & Kim, J. US 6,677,082 B2 (2004).

[13] Au, H., Crespo-Ribadeneyra, M. & Titirici, M.-M. Beyond Li-ion batteries: performance, materials diversification, and sustainability. *One Earth* 207–211 (2022).

[14] Bruce, P. G., Freunberger, S. A., Hardwick, L. J. & Tarascon, J.-M. Li-O_2 and Li-S batteries with high energy storage. *Nature Materials* **11**, 19–29 (2012).

[15] Kwak, W.-J. *et al.* Lithium-Oxygen Batteries and Related Systems: Potential, Status, and Future. *Chemical Reviews* **120**, 6626–6683 (2020).

[16] Abraham, K. M. & Jiang, Z. A Polymer Electrolyte-Based Rechargeable Lithium/Oxygen Battery. *Journal of the Electrochemical Society* **143**, 1–5 (1996).

[17] Laorie, C. O., Mukerjee, S., Abraham, K. M., Plichta, E. J. & Hendrickson, M. A. Elucidating the Mechanism of Oxygen Reduction for Lithium-Air Battery Applications. *Journal of Physical Chemistry C* **113**, 20127–20134 (2009).

[18] Laorie, C. O., Mukerjee, S., Abraham, K. M., Plichta, E. J. & Hendrickson, M. A. Influence of Nonaqueous Solvents on the Electrochemistry of Oxygen in the Rechargeable Lithium-Air Battery. *Journal of Physical Chemistry C* **114**, 9178–9186 (2010).

[19] McCloskey, B. D., Scheffler, R., Speidel, A., Girishkumar, G. & Luntz, A. C. On the mechanism of nonaqueous Li-O_2 electrochemistry on C and its kinetic overpotentials: Some implications for Li-air batteries. *Journal of Physical Chemistry C* **116**, 23897–23905 (2012).

[20] Johnson, L. *et al.* The role of LiO_2 solubility in O_2 reduction in aprotic solvents and its consequences for Li-O_2 batteries. *Nature Chemistry* **6**, 1091–1099 (2014).

[21] Aetukuri, N. B. *et al.* Solvating additives drive solution-mediated electrochemistry and enhance toroid growth in non-aqueous Li-O_2 batteries. *Nature Chemistry* **7**, 50–56 (2015).

[22] Burke, C. M., Pande, V., Khetan, A., Viswanathan, V. & McCloskey, B. D. Enhancing electrochemical intermediate solvation through electrolyte anion selection to increase nonaqueous Li-O_2 battery capacity. *Proceedings of the National Academy of Sciences* **112**, 9293–9298 (2015).

[23] Peng, Z. *et al.* Oxygen reactions in a non-aqueous Li^+ Electrolyte. *Angewandte Chemie International Edition* **50**, 6351–6355 (2011).

[24] Trahan, M. J., Mukerjee, S., Plichta, E. J., Hendrickson, M. A. & Abraham, K. M. Studies of Li-Air Cells Utilizing Dimethyl Sulfoxide-Based Electrolyte. *Journal of the Electrochemical Society* **160**, A259–A267 (2013).

[25] Torres, W., Mozhzhukhina, N., Tesio, A. Y. & Calvo, E. J. A Rotating Ring Disk Electrode Study of the Oxygen Reduction Reaction in Lithium Containing Dimethyl Sulfoxide Electrolyte: Role of Superoxide. *Journal of the Electrochemical Society* **161**, A2204–A2209 (2014).

[26] Yu, Q. & Ye, S. In Situ Study of Oxygen Reduction in Dimethyl Sulfoxide (DMSO) Solution: A Fundamental Study for Development of the Lithium-Oxygen Battery. *Journal of Physical Chemistry C* **119**, 12236–12250 (2015).

[27] Yang, L., Frith, J. T., Garcia-Araez, N. & Owen, J. R. A new method to prevent degradation of lithium-oxygen batteries: Reduction of superoxide by viologen. *Chemical Communications* **51**, 1705–1708 (2015).

[28] Kwabi, D. G. *et al.* Controlling Solution-Mediated Reaction Mechanisms of Oxygen Reduction Using Potential and Solvent for Aprotic Lithium-Oxygen Batteries. *Journal of Physical Chemistry Letters* **7**, 1204–1212 (2016).

[29] Galloway, T. A. & Hardwick, L. J. Utilizing in Situ Electrochemical SHINERS for Oxygen Reduction Reaction Studies in Aprotic Electrolytes. *Journal of Physical Chemistry Letters* **7**, 2119–2124 (2016).

[30] Schwager, P., Dongmo, S., Fenske, D. & Wittstock, G. Reactive oxygen species formed in organic lithium-oxygen batteries. *Physical Chemistry Chemical Physics* **18**, 10774–10780 (2016).

[31] Wang, Y. *et al.* A Solvent Controlled Oxidation Mechanism of Li_2O_2 in Lithium-Oxygen Batteries. *Joule* **2**, 1–17 (2018).

[32] Cao, R. *et al.* The Mechanisms of Oxygen Reduction and Evolution Reactions in Nonaqueous Lithium–Oxygen Batteries. *ChemSusChem* **7**, 2436–2440 (2014).

[33] Luo, L. *et al.* Revealing the Reaction Mechanism of Li-O_2 Batteries using Environmental Transmission Electron Microscopy. *Nature Nanotechnology* **12**, 535–539 (2017).

[34] Mitchell, R. R., Gallant, B. M., Shao-Horn, Y. & Thompson, C. V. Mechanisms of morphological evolution of Li_2O_2 particles during electrochemical growth. *Journal of Physical Chemistry Letters* **4**, 1060–1064 (2013).

[35] Xia, C. *et al.* Evolution of Li_2O_2 Growth and Its Effect on Kinetics of Li-O_2 Batteries. *ACS Applied Materials Interfaces* **6**, 12083–12092 (2014).

[36] Liu, C. *et al.* Towards an Understanding of Li_2O_2 Evolution in Li-O_2 Batteries: An In Operando Synchrotron X-ray Diffraction Study. *ChemSusChem* **10**, 1592–1599 (2017).

[37] Albertus, P. *et al.* Identifying Capacity Limitations in the Li/Oxygen Battery Using Experiments and Modeling. *Journal of The Electrochemical Society* **158**, A343 (2011).

[38] Huang, J. & Peng, Z. Understanding the Reaction Interface in Lithium-Oxygen Batteries. *Batteries & Supercaps* **2**, 37–48 (2019).

[39] Viswanathan, V. *et al.* Electrical conductivity in Li_2O_2 and its role in determining capacity limitations in non-aqueous Li-O_2 batteries. *The Journal of Chemical Physics* **135**, 214704 (2011).

[40] Knudsen, K. B., Luntz, A. C., Jensen, S. H., Vegge, T. & Hjelm, J. Redox Probing Study of the Potential Dependence of Charge Transport Through Li_2O_2. *Journal of Physical Chemistry C* **119**, 28292–28299 (2015).

[41] Simmons, J. G. Generalized Formula for the Electric Tunnel Effect between Similar Electrodes Separated by a Thin Insulating Film. *Journal of Applied Physics* **34**, 1793–1803 (1963).

[42] Franchini, C., Reticcioli, M., Setvin, M. & Diebold, U. Polarons in materials. *Nature Reviews Materials* **6**, 560–586 (2021).

[43] Ong, S. P., Mo, Y. & Ceder, G. Low hole polaron migration barrier in lithium peroxide. *Physical Review B - Condensed Matter and Materials Physics* **85**, 2–5 (2012).

[44] Radin, M. D. & Siegel, D. J. Charge transport in lithium peroxide: Relevance for rechargeable metal-air batteries. *Energy & Environmental Science* **6**, 2370–2379 (2013).

[45] Tian, F., Radin, M. D. & Siegel, D. J. Enhanced Charge Transport in Amorphous Li_2O_2. *Chemistry of Materials* **26**, 2952–2959 (2014).

[46] Luntz, A. C. *et al.* Tunneling and Polaron Charge Transport through Li_2O_2 in Li-O_2 Batteries. *Journal of Physical Chemistry Letters* **4**, 3494–3499 (2013).

[47] Radin, M. D., Monroe, C. W. & Siegel, D. J. Impact of Space-Charge Layers on Sudden Death in Li/O_2 Batteries. *Journal of Physical Chemistry Letters* **6**, 3017–3022 (2015).

[48] Luntz, A. C. & McCloskey, B. D. Nonaqueous li–air batteries: A status report. *Chemical Reviews* **114**, 11721–11750 (2014).

[49] Kushima, A. *et al.* Charging/Discharging Nanomorphology Asymmetry and Rate-Dependent Capacity Degradation in Li-Oxygen Battery. *Nano Letters* **15**, 8260–8265 (2015).

[50] He, K. *et al.* Operando liquid cell electron microscopy of discharge and charge kinetics in lithium-oxygen batteries. *Nano Energy* **49**, 338–345 (2018).

[51] Liu, P. *et al.* Operando characterization of cathodic reactions in a liquid-state lithium-oxygen micro-battery by scanning transmission electron microscopy. *Scientific Reports* **8**, 3134 (2018).

[52] Radin, M. D., Tian, F. & Siegel, D. J. Electronic structure of Li_2O_2 {0001} surfaces. *Journal of Materials Science* **47**, 7564–7570 (2012).

[53] Huang, J. & Tong, B. Probing the reaction interface in Li-O_2 batteries using electrochemical impedance spectroscopy: Dual roles of Li_2O_2. *Chemical Communications* **53**, 11418–11421 (2017).

[54] Huang, J. *et al.* Probing the Reaction Interface in Li-Oxygen Batteries Using Dynamic Electrochemical Impedance Spectroscopy: Discharge-Charge Asymmetry in Reaction Sites and Electronic Conductivity. *Journal of Physical Chemistry Letters* **9**, 3403–3408 (2018).

[55] Wang, J., Zhang, Y., Guo, L., Wang, E. & Peng, Z. Identifying Reactive Sites and Transport Limitations of Oxygen Reactions in Aprotic Lithium-O_2 Batteries at the Stage of Sudden Death. *Angewandte Chemie International Edition* **55**, 5201–5205 (2016).

[56] Prehal, C. *et al.* In situ small-angle X-ray scattering reveals solution phase discharge of Li-O_2 batteries with weakly solvating electrolytes. *Proceedings of the National Academy of Sciences of the United States of America* **118**, 1–11 (2021).

[57] Adams, B. D. *et al.* Current density dependence of peroxide formation in the Li-O_2 battery and its effect on charge. *Energy & Environmental Science* **6**, 1772–1778 (2013).

[58] Griffith, L. D., Sleightholme, A. E. S., Mansfield, J. F., Siegel, D. J. & Monroe, C. W. Correlating Li/O_2 cell capacity and product morphology with discharge current. *ACS Applied Materials Interfaces* **7**, 7670–7678 (2015).

[59] Yin, Y., Torayev, A., Gaya, C., Mammeri, Y. & Franco, A. A. Linking the Performances of Li-O_2 Batteries to Discharge Rate and Electrode and Electrolyte Properties through the Nucleation Mechanism of Li_2O_2. *Journal of Physical Chemistry C* **121**, 19577–19585 (2017).

[60] Smirnov, V. S. & Kislenko, S. A. Effect of Solvents on the Behavior of Lithium and Superoxide Ions in Lithium–Oxygen Battery Electrolytes. *ChemPhysChem* **19**, 75–81 (2018).

[61] Sharon, D. *et al.* Mechanistic Role of Li^+ Dissociation Level in Aprotic Li-O_2 Battery. *ACS Applied Materials Interfaces* **8**, 5300–5307 (2016).

[62] Meini, S., Piana, M., Tsiouvaras, N., Garsuch, A. & Gasteiger, H. A. The Effect of Water on the Discharge Capacity of a Non-Catalyzed Carbon Cathode for Li-O_2 Batteries. *Electrochemical and Solid-State Letters* **15**, A45–A48 (2012).

[63] Gao, X., Jovanov, Z. P., Chen, Y., Johnson, L. R. & Bruce, P. G. Phenol-Catalyzed Discharge in the Aprotic Lithium-Oxygen Battery. *Angewandte Chemie* **129**, 6539–6543 (2017).

[64] Gutmann, V. Solvent effects on the reactivities of organometallic compounds. *Coordination Chemistry Reviews* **18**, 225–255 (1976).

[65] Xie, J. *et al.* Achieving Low Overpotential Li-O_2 Battery Operations by Li_2O_2 Decomposition through One-Electron Processes. *Nano Letters* **15**, 8371–8376 (2015).

[66] Ganapathy, S. *et al.* Nature of Li_2O_2 Oxidation in a Li-O_2 Battery Revealed by Operando X-ray Diffraction. *Journal of the American Chemical Society* **136**, 16335–16344 (2014).

[67] Kang, S., Mo, Y., Ong, S. P. & Ceder, G. A facile mechanism for recharging Li_2O_2 in Li-O_2 batteries. *Chemistry of Materials* **25**, 3328–3336 (2013).

[68] Lu, Y.-C. & Shao-Horn, Y. Probing the Reaction Kinetics of the Charge Reactions of Nonaqueous Li-O_2 Batteries. *Journal of Physical Chemistry Letters* 93–99 (2013).

[69] Gallant, B. M. *et al.* Influence of Li_2O_2 morphology on oxygen reduction and evolution kinetics in Li-O_2 batteries. *Energy & Environmental Science* **6**, 2518–2528 (2013).

[70] Zhong, L. *et al.* In Situ Transmission Electron Microscopy Observations of Electrochemical Oxidation of Li_2O_2. *Nano Letters* **13**, 2209–2214 (2013).

[71] Zheng, H. *et al.* New insight in Understanding Oxygen Reduction and Evolution in Solid-State Lithium-Oxygen Batteries Using an in Situ Environmental Scanning Electron Microscope. *Nano Letters* **14**, 4245–4249 (2014).

[72] Wang, Y. & Lu, Y.-C. Isotopic Labeling Reveals Active Reaction Interfaces for Electrochemical Oxidation of Lithium Peroxide. *Angewandte Chemie* **131**, 7036–7040 (2019).

[73] McCloskey, B. D. *et al.* Limitations in Rechargeability of Li-O_2 Batteries and Possible Origins. *Jouranl of Physical Chemistry Letters* **3**, 3043–3047 (2012).

[74] McCloskey, B. D. *et al.* Twin Problems of Interfacial Carbonate Formation in Non-Aqueous Li-O_2 Batteries. *Journal of Physical Chemistry Letters* **3**, 997–1001 (2012).

[75] McCloskey, B. D. *et al.* Combining accurate O_2 and Li_2O_2 assays to separate discharge and charge stability limitations in nonaqueous Li-O_2 Batteries. *Journal of Physical Chemistry Letters* **4**, 2989–2993 (2013).

[76] Freunberger, S. A. *et al.* The lithium-oxygen battery with ether-based electrolytes. *Angewandte Chemie - International Edition* **50**, 8609–8613 (2011).

[77] Freunberger, S. A. *et al.* Reactions in the Rechargeable Lithium–O_2 Battery with Alkyl Carbonate Electrolytes. *Journal of the American Chemical Society* **133**, 8040–8047 (2011).

[78] Yao, X., Dong, Q., Cheng, Q. & Wang, D. Why Do Lithium–Oxygen Batteries Fail: Parasitic Chemical Reactions and Their Synergistic Effect. *Angewandte Chemie International Edition* **55**, 11344–11353 (2016).

[79] Peng, Z., Freunberger, S. A., Chen, Y. & Bruce, P. G. A reversible and higher-rate Li-O_2 battery. *Science* **337**, 563–566 (2012).

[80] Kwabi, D. G. *et al.* Chemical instability of dimethyl sulfoxide in lithium-air batteries. *Journal of Physical Chemistry Letters* **5**, 2850–2856 (2014).

[81] Sharon, D. *et al.* Oxidation of Dimethyl Sulfoxide Solutions by Electrochemical Reduction of Oxygen. *Journal of Physical Chemistry Letters* **4**, 3115–3119 (2013).

[82] Bryantsev, Vyacheslav S. Giordani, V. *et al.* Predicting Solvent Stability in Aprotic Electrolyte Li – Air Batteries : Nucleophilic Substitution by the Superoxide Anion Radical (O_2^-). *Journal of Physical Chemistry A* **115**, 12399–12409 (2011).

[83] Walker, W. *et al.* A rechargeable Li-O_2 battery using a lithium nitrate/N,N-dimethylacetamide electrolyte. *Journal of the American Chemical Society* **135**, 2076–2079 (2013).

[84] Sharon, D. *et al.* Reactivity of amide based solutions in lithium-oxygen cells. *Journal of Physical Chemistry C* **118**, 15207–15213 (2014).

[85] Bryantsev, V. S. & Faglioni, F. Predicting autoxidation stability of ether- and amide-based electrolyte solvents for Li-air batteries. *Journal of Physical Chemistry A* **116**, 7128–7138 (2012).

[86] Nasybulin, E. *et al.* Effects of electrolyte salts on the performance of Li-O_2 batteries. *Journal of Physical Chemistry C* **117**, 2635–2645 (2013).

[87] Itkis, D. M. *et al.* Reactivity of Carbon in Lithium-Oxygen Battery Positive Electrodes. *Nano Letters* **13**, 4697–4701 (2013).

[88] Black, R. *et al.* Screening for superoxide reactivity in Li-O_2 batteries: Effect on Li_2O_2/LiOH crystallization. *Journal of the American Chemical Society* **134**, 2902–2905 (2012).

[89] Thotiyl, M. M. O., Freunberger, S. A., Peng, Z. & Bruce, P. G. The Carbon Electrode in Nonaqueous Li-O_2 Cells. *Journal of the Americn Chemical Society* **135**, 494–500 (2013).

[90] Wandt, J., Jakes, P., Granwehr, J., Gasteiger, H. A. & Eichel, R.-A. Singlet Oxygen Formation during the Charging Process of an Aprotic Lithium-Oxygen Battery. *Angewandte Chemie* **128**, 7006–7009 (2016).

[91] Mahne, N. *et al.* Singlet oxygen generation as a major cause for parasitic reactions during cycling of aprotic lithium-oxygen batteries. *Nature Energy* **2**, 1–9 (2017).

[92] Petit, Y. K. *et al.* DABCOnium: An Efficient and High-Voltage Stable Singlet Oxygen Quencher for Metal–O_2 Cells. *Angewandte Chemie International Edition* **58**, 6535–6539 (2019).

[93] Mourad, E. *et al.* Singlet oxygen from cation driven superoxide disproportionation and consequences for aprotic metal–O_2 batteries. *Energy Environmental Science* **2**, 2559–2568 (2019).

[94] Pierini, A., Brutti, S. & Bodo, E. Superoxide anions disproportionation induced by Li^+ and H^+: pathways to $^1O_2$ release in Li-O_2 batteries. *ChemPhysChem* (2017).

[95] Dong, S. *et al.* Singlet oxygen and dioxygen bond cleavage in the aprotic lithium-oxygen battery Singlet oxygen and dioxygen bond cleavage in the aprotic lithium-oxygen battery. *Joule* 1–8 (2021).

[96] Sagadevan, A., Hwang, K.-C. & Su, M.-D. Singlet oxygen-mediated selective C-H bond hydroperoxidation of ethereal hydrocarbons. *Nature Commununications* **8**, 1–8 (2017).

[97] Singleton, D. A. *et al.* Mechanism of ene reactions of singlet oxygen. A two-step no-intermediate mechanism. *Journal of the American Chemical Society* **125**, 1319–1328 (2003).

[98] Kwak, W.-j. *et al.* Deactivation of redox mediators in lithium-oxygen batteries by singlet oxygen. *Nat. Commun.* **10**, 1–8 (2019).

[99] Mahne, N., Renfrew, S. E., McCloskey, B. D. & Freunberger, S. A. Electrochemical Oxidation of Lithium Carbonate Generates Singlet Oxygen. *Angewandte Chemie International Edition* **57**, 5529–5533 (2018).

[100] Ko, Y. *et al.* Biological Redox Mediation in Electron Transport Chain of Bacteria for Oxygen Reduction Reaction Catalysts in Lithium–Oxygen Batteries. *Advanced Functional Materials* **29**, 1805623 (2019).

[101] Gao, X., Chen, Y., Johnson, L. R., Jovanov, Z. P. & Bruce, P. G. A rechargeable lithium–oxygen battery with dual mediators stabilizing the carbon cathode. *Nature Energy* **2**, 17118 (2017).

[102] Cao, D. *et al.* Conductive Polymer Coated Cathodes in Li-O2 Batteries. *ACS Applied Energy Materials* (2019).

[103] Kwak, W.-J. *et al.* Oxidation Stability of Organic Redox Mediators as Mobile Catalysts in LithiumOxygen Batteries. *ACS Energy Letters* **5**, 2122–2129 (2020).

[104] Matsuda, S. & Asahina, H. Highly Efficient Oxygen Evolution Reaction in Rechargeable Lithium Oxygen Batteries with Triethylphosphate-Based Electrolytes. *Journal of Physical Chemistry C* **124**, 25784–25789 (2020).

[105] Ue, M., Asahina, H., Matsuda, S. & Uosaki, K. Material balance in the O_2 electrode of Li-O_2 cells with a porous carbon electrode and TEGDME-based electrolytes. *RSC Advances* **10**, 42971–42982 (2020).

[106] Lacey, M. J., Frith, J. T. & Owen, J. R. A redox shuttle to facilitate oxygen reduction in the lithium air battery. *Electrochemistry Communications* **26**, 74–76 (2013).

[107] Gao, X., Chen, Y., Johnson, L. & Bruce, P. G. Promoting solution phase discharge in Li-O_2 batteries containing weakly solvating electrolyte solutions. *Nature Materials* **15**, 882–888 (2016).

[108] Zhang, Y. *et al.* High-Capacity and High-Rate Discharging of a Coenzyme Q10-Catalyzed Li-O_2 Battery. *Advanced Materials* **30**, 1705571 (2018).

[109] Liu, T. *et al.* The Effect of Water on Quinone Redox Mediators in Nonaqueous Li-O_2 Batteries. *Journal of the American Chemical Society* **140**, 1428–1437 (2018).

[110] Liu, X. *et al.* Inhibition of Discharge Side Reactions by Promoting Solution-Mediated Oxygen Reduction Reaction with Stable Quinone in Li-O_2 Batteries. *ACS Applied Materials Interfaces* **12**, 10607–10615 (2020).

[111] Han, X. B. & Ye, S. Structural Design of Oxygen Reduction Redox Mediators (ORRMs) Based on Anthraquinone (AQ) for the Li-O_2 Battery. *ACS Catalysis* **10**, 9790–9803 (2020).

[112] Kwak, W.-J. *et al.* Understanding the behavior of Li-oxygen cells containing LiI. *Journal of Materials Chemistry A* **3**, 8855–8864 (2015).

[113] Liang, Z. & Lu, Y.-C. Critical Role of Redox Mediator in Suppressing Charging Instabilities of Lithium-Oxygen Batteries. *Journal of the American Chemical Society* **138**, 7574–7583 (2016).

[114] Lee, C. K. & Park, Y. J. CsI as Multifunctional Redox Mediator for Enhanced Li-Air Batteries. *ACS Applied Materials Interfaces* **8**, 8561–8567 (2016).

[115] Kundu, D., Black, R., Adams, B. & Nazar, L. F. A highly active low voltage redox mediator for enhanced rechargeability of lithium-oxygen batteries. *ACS Central Science* **1**, 510–515 (2015).

[116] Bergner, B. J., Schürmann, A., Peppler, K., Garsuch, A. & Janek, J. TEMPO: A Mobile Catalyst for Rechargeable Li-O_2 Batteries. *Journal of the American Chemical Society* **136**, 15054–15064 (2014).

[117] Feng, N., Mu, X., Zhang, X., He, P. & Zhou, H. Intensive study on the catalytical behavior of N-methylphenothiazine as a soluble mediator to oxidize the Li_2O_2 cathode of the Li-O_2 battery. *ACS Applied Materials Interfaces* **9**, 3733–3739 (2017).

[118] Chen, Y., Freunberger, S. A., Peng, Z., Fontaine, O. & Bruce, P. G. Charging a Li-O_2 battery using a redox mediator. *Nature Chemistry* **5**, 489–494 (2013).

[119] Chen, Y., Gao, X., Johnson, L. R. & Bruce, P. G. Kinetics of lithium peroxide oxidation by redox mediators and consequences for the lithium-oxygen cell. *Nature Communications* **9**, 1–6 (2018).

[120] Read, J. Characterization of the Lithium/Oxygen Organic Electrolyte Battery. *Journal of the Electrochemical Society* **149**, A1190–A1195 (2002).

[121] Lu, Y.-C. *et al.* The discharge rate capability of rechargeable Li-O_2 batteries. *Energy & Environmental Science* **4**, 2999–3007 (2011).

[122] Matsuda, S. & Yasukawa, E. Carbon-black-based self-standing porous electrode for 500 Wh/kg rechargeable lithium-oxygen batteries. *Cell Reports Physical Science* **2**, 100506 (2021).

[123] Nomura, A. *et al.* Highly-porous Super-Growth carbon nanotube sheet cathode develops high-power Lithium-Air Batteries. *Electrochimica Acta* **400**, 139415 (2021).

[124] Ushijima, K., Iwamura, S. & Mukai, S. R. Simple and Cost-Effective Method to Increase the Capacity of Carbon Nanotube Sheet Cathodes for Lithium-Air Batteries. *ACS Applied Energy Materials* **3**, 6915–6921 (2020).

[125] Liu, B., Yang, J., Duan, H., Liu, X. & Shui, J. Cathode Local Curvature Affect Lithium Peroxide Growth in Li-O_2 Battery. *ACS Applied Materials Interfaces* (2019).

[126] Mitchell, R. R., Gallant, B. M., Thompson, C. V. & Shao-Horn, Y. All-carbon-nanofiber electrodes for high-energy rechargeable Li-O_2 batteries. *Energy & Environmental Science* **4**, 2952–2958 (2011).

[127] Jung, I.-S. *et al.* Rapid oxygen diffusive lithium-oxygen batteries using a restacking-inhibited, free-standing graphene cathode film. *Journal of Materials Chemistry A* **7**, 10397–10404 (2019).

[128] Wissler, M. Graphite and carbon powders for electrochemical applications. *Journal of Power Sources* **156**, 142–150 (2006).

[129] Lijima, S. Helical microtubules of graphitic carbon. *Nature* **354**, 56–58 (1991).

[130] Lee, R. S., Kim, H. J., Fischer, J. E., Thess, A. & Smalley, R. E. Conductivity enhancement in single-walled carbon nanotube bundles doped with K and Br. *Nature* **388**, 255–257 (1997).

[131] Endo, M. *et al.* The production and structure of pyrolytic carbon nanotubes (PCNTs). *Journal of Physics and Chemistry of Solids* **54**, 1841–1848 (1993).

[132] Maruyama, T. Chapter 6 - carbon nanotubes. In Thomas, S., Sarathchandran, C., Ilangovan, S. & Moreno-Piraján, J. C. (eds.) *Handbook of Carbon-Based Nanomaterials*, Micro and Nano Technologies, 299–319 (Elsevier, 2021).

[133] Liu, S. *et al.* Free-standing, hierarchically porous carbon nanotube film as a binder-free electrode for high-energy Li-O2 batteries. *Journal of Materials Chemistry A* **1**, 12033–12037 (2013).

[134] Kim, M. C. *et al.* Nature inspired cathodes using high-density carbon papers with an eddy current effect for high-rate performance lithium-air batteries. *Journal of Materials Chemistry A* **6**, 9550–9560 (2018).

[135] Inagaki, M., Kang, F., Toyoda, M. & Konno, H. Chapter 3 - graphene: Synthesis and preparation. In Inagaki, M., Kang, F., Toyoda, M. & Konno, H. (eds.) *Advanced Materials Science and Engineering of Carbon*, 41–65 (Butterworth-Heinemann, Boston, 2014).

[136] K. S. Novoselov et al. Electric Field Effect in Atomically Thin Carbon Films. *Science* **306**, 666–669 (2016).

[137] Schniepp, H. C. *et al.* Functionalized single graphene sheets derived from splitting graphite oxide. *Journal of Physical Chemistry B* **110**, 8535–8539 (2006).

[138] Land, T. A., Michely, T., Behm, R. J., Hemminger, J. C. & Comsa, G. STM investigation of single layer graphite structures produced on Pt(111) by hydrocarbon decomposition. *Surface Science* **264**, 261–270 (1992).

[139] Lin, Y. *et al.* Ultrahigh-Capacity Lithium-Oxygen Batteries Enabled by Dry-Pressed Holey Graphene Air Cathodes. *Nano Letters* **17**, 3252–3260 (2017).

[140] Lacey, S. D. *et al.* Highly compressible, binderless and ultrathick holey graphene-based electrode architectures. *Nano Energy* **31**, 386–392 (2017).

[141] Meini, S., Piana, M., Beyer, H., Schwämmlein, J. & Gasteiger, H. A. Effect of Carbon Surface Area on First Discharge Capacity of Li-O_2 Cathodes and Cycle-Life Behavior in Ether-Based Electrolytes. *Journal of the Electrochemical Society* **159**, A2135–A2142 (2012).

[142] Wang, F., Kahol, P. K., Gupta, R. & Li, X. Experimental Studies of Carbon Electrodes With Various Surface Area for Li-O_2 Batteries. *Journal of Electrochemical Energy Conversion and Storage* **16**, 1–7 (2019).

[143] Yang, X.-H., He, P. & Xia, Y.-Y. Preparation of mesocellular carbon foam and its application for lithium/oxygen battery. *Electrochemistry Communications* **11**, 1127–1130 (2009).

[144] Kuboki, T., Okuyama, T., Ohsaki, T. & Takami, N. Lithium-air batteries using hydrophobic room temperature ionic liquid electrolyte. *Journal of Power Sources* **146**, 766–769 (2005).

[145] Ma, S. B., Lee, D. J., Roev, V., Im, D. & Doo, S.-G. Effect of porosity on electrochemical properties of carbon materials as cathode for lithium-oxygen battery. *Journal of Power Sources* **244**, 494–498 (2013).

[146] Ding, N. *et al.* Influence of carbon pore size on the discharge capacity of Li-O_2 batteries. *Journal of Materials Chemistry A* **2**, 12433–12441 (2014).

[147] Guo, Z. *et al.* Ordered Hierarchical Mesoporous/Macroporous Carbon: A High-Performance Catalyst for Rechargeable Li-O_2 Batteries. *Advanced Materials* **25**, 5668–5672 (2013).

[148] Nie, H. *et al.* Synthesis of a meso-macro hierarchical porous carbon material for improvement of O_2 diffusivity in Li-O_2 batteries. *RSC Advances* **4**, 17141–17145 (2014).

[149] Park, J., Jeong, J., Lee, S., Jo, C. & Lee, J. Effect of mesoporous structured cathode materials on charging potentials and rate capability of lithium-oxygen batteries. *ChemSusChem* **8**, 3146–3152 (2015).

[150] Torayev, A. *et al.* Stochasticity of Pores Interconnectivity in Li-O_2 Batteries and its Impact on the Variations in Electrochemical Performance. *Journal of Physical Chemistry Letters* **9**, 791–797 (2018).

[151] Su, Z. *et al.* X-ray Nanocomputed Tomography in Zernike Phase Contrast for Studying 3D Morphology of Li-O_2 Battery Electrode. *ACS Applied Energy Materials* (2020).

[152] Ogasawara, T., Debart, A., Holzapfel, M., Nova, P. & Bruce, P. G. Rechargeable Li_2O_2 Electrode for Lithium Batteries. *Journal of the American Chemical Society* **128**, 1390–1393 (2006).

[153] Beattie, S. D., Manolescu, D. M. & Blair, S. L. High-Capacity Lithium–Air Cathodes. *Journal of the Electrochemical Society* **156**, A44–A47 (2009).

[154] Nasybulin, E. *et al.* Stability of polymer binders in Li-O_2 batteries. *Journal of Power Sources* **243**, 899–907 (2013).

[155] Papp, J. K. *et al.* Poly(vinylidene fluoride) (PVDF) Binder Degradation in Li-O_2 Batteries: A Consideration for the Characterization of Lithium Superoxide. *Journal of Physical Chemistry Letters* **8**, 1169–1174 (2017).

[156] Amanchukwu, C. V., Harding, J. R., Shao-Horn, Y. & Hammond, P. T. Understanding the chemical stability of polymers for lithium-air batteries. *Chemistry of Materials* **27**, 550–561 (2015).

[157] Cui, Y. & Zhang, M. Cross-links in carbon nanotube assembly introduced by using polyacrylonitrile as precursor. *ACS Applied Materials and Interfaces* **5**, 8173–8178 (2013).

[158] Cui, Y. & Zhang, M. Fabrication of cross-linked carbon nanotube foam using polymethylmethacrylate microspheres as templates. *Journal of Materials Chemistry A* **1**, 13984–13988 (2013).

[159] Fick, D. A. V. on liquid diffusion. *The London, Edinburgh, and Dublin Philosophical Magazine and Journal of Science* **10**, 30–39 (1855).

[160] Read, J. *et al.* Oxygen Transport Properties of Organic Electrolytes and Performance of Lithium/Oxygen Battery. *Journal of the Electrochemical Society* **150**, A1351–A1356 (2003).

[161] Mohazabrad, F., Wang, F. & Li, X. Experimental Studies of Salt Concentration in Electrolyte on the Performance of Li-O_2 Batteries at Various Current Densities . *Journal of The Electrochemical Society* **163**, A2623–A2627 (2016).

[162] Gunasekara, I., Mukerjee, S., Plichta, E. J., Hendrickson, M. A. & Abraham, K. M. Microelectrode Diagnostics of Lithium-Air Batteries. *Journal of The Electrochemical Society* **161**, A381–A392 (2014).

[163] Gittleson, F. S., Jones, R. E., Ward, D. K. & Foster, M. E. Oxygen solubility and transport in Li-air battery electrolytes: Establishing criteria and strategies for electrolyte design. *Energy and Environmental Science* **10**, 1167–1179 (2017).

[164] Balaish, M., Kraytsberg, A. & Ein-Eli, Y. Realization of an artificial three-phase reaction zone in a Li-Air battery. *ChemElectroChem* **1**, 90–94 (2014).

[165] Kuritz, N., Murat, M., Balaish, M., Ein-Eli, Y. & Natan, A. PFC and Triglyme for Li-Air Batteries: A Molecular Dynamics Study. *Journal of Physical Chemistry B* **120**, 3370–3377 (2016).

[166] Balaish, M. & Ein-Eli, Y. The Role of Air-Electrode Structure on the Incorporation of Immiscible PFCs in Nonaqueous Li-O2 Battery. *ACS Applied Materials and Interfaces* **9**, 9726–9737 (2017).

[167] Balaish, M. & Ein-Eli, Y. Enhancing oxygen adsorption capabilities in Li-O2 battery cathodes through solid perfluorocarbons. *Journal of Materials Chemistry A* **5**, 14152–14164 (2017).

[168] Balaish, M., Gao, X., Bruce, P. G. & Ein-Eli, Y. Enhanced Li-O_2 Battery Performance in a Binary "Liquid Teflon" and Dual Redox Mediators. *Advanced Materials Technologies* **4**, 1–6 (2019).

[169] Park, S. H. *et al.* Maximal Utilization of a High-Loading Cathode in Li-O_2 Batteries: A Double Oxygen Supply System. *ACS Applied Materials Interfaces* **11**, 30872–30879 (2019).

[170] Shui, J.-L., Okasinski, J. S., Chen, C., Almer, J. D. & Liu, D.-J. In operando spatiotemporal study of Li_2O_2 grain growth and its distribution inside operating Li-O_2 batteries. *ChemSusChem* **7**, 543–548 (2014).

[171] Augustin, M., Vullum, P. E., Vullum-Bruer, F. & Svensson, A. M. Inside the electrode: Looking at cycling products in Li/O_2 batteries. *Journal of Power Sources* **414**, 130–140 (2019).

[172] Gallagher, K. G. *et al.* Quantifying the promise of lithium-air batteries for electric vehicles. *Energy Environmental Science* **7**, 1555–1563 (2014).

[173] Xu, S. *et al.* Textile Inspired Lithium–Oxygen Battery Cathode with Decoupled Oxygen and Electrolyte Pathways. *Advanced Materials* **30**, 1704907 (2018).

[174] Huang, Z. *et al.* A Li-O_2 battery cathode with vertical mass/charge transfer pathways. *Journal of Materials Chemistry A* **7**, 3000–3005.

[175] Song, H. *et al.* Hierarchically Porous, Ultrathick,"Breathable" Wood-Derived Cathode for Lithium-Oxygen Batteries. *Advanced Energy Materials* **8**, 1701203 (2018).

[176] Chen, C. *et al.* Nature-Inspired Tri-Pathway Design Enabling High-Performance Flexible Li-O_2 Batteries. *Advanced Energy Materials* **9**, 1802964 (2019).

[177] Greenburg, L. C., Plaza-Rivera, C. O., Kim, J., Connell, J. W. & Lin, Y. Architecture Transformations of Ultrahigh Areal Capacity Air Cathodes for Lithium-Oxygen Batteries. *Batteries & Supercaps* **4**, 120–130 (2021).

2

Experimental

Contents

2.1 Materials Preparation 68
2.1.1 Electrode Fabrication 68
2.1.2 Water control measures 69
2.1.3 3D-Printing 71
2.2 Electrochemical Techniques 74
2.2.1 Cell Assembly 74
2.2.2 Galvanostatic Cycling with Potential Limitation (GCPL) . . 74
2.2.3 Linear Sweep Voltammetry (LSV) and Cyclic Voltammetry (CV) 76
2.2.4 Chronoamperometry (CA) 77
2.3 Characterisation 78
2.3.1 Scanning Electron Microscopy (SEM) 78
2.3.2 Energy Dispersive X-Ray Spectroscopy (EDX) 80
2.3.3 Fourier Transform Infrared Spectroscopy (FTIR) 81
2.3.4 Raman Spectroscopy 84
2.3.5 Powder X-Ray Diffraction (PXRD) 86
2.3.6 UV-vis Spectroscopy and Li_2O_2 Titration Technique 87
2.3.7 BET Surface Area Analysis 89
2.3.8 Mercury Intrusion Porosimetry (MIP) 93
2.3.9 Thermogravimetric Analysis (TGA) 94
2.3.10 Differential Electrochemical Mass Spectrometry (DEMS) . . 95
2.3.11 Pressure Monitoring 97
2.4 References 98

2.1 Materials Preparation

2.1.1 Electrode Fabrication

Gas Diffusion Electrode Fabrication

Commercially available carbon black was used to form GDEs in this study. Carbon black is produced by heating any carbon-containing material at a temperature exceeding 1000 °C in an oxygen-free and inert environment.[1,2] The resulting carbon black particles are nearly spherical with diameters ranging between 5-100 nm, depending on the processing conditions. These primary particles tend to group together in aggregates or agglomerates, which are approximately 250 nm in diameter. The size and distribution of particles are influenced by the source material and processing conditions, which in turn affect the surface area and electrical conductivity of the final product.

Before using carbon black in Li-O_2 cells, the carbon material was ground in a pestle and mortar to disperse the carbon aggregates. The resulting carbon aggregates were then subjected to heating at 900 °C (ramp rate of 5 °C min^{-1}) using a Lenton split tube furnace. This was carried out under the flow of Ar/H_2, to remove any hydrophilic side groups, such as C-O, COOH, and C-OH. These side groups can react with nucleophilic intermediates such as O_2^-/LiO_2, thereby affecting the performance of the cathode material.[3]

To ensure the carbon material remains intact during cell operation, a polymer binder was added. Long polymer chains are formed which wrap around the carbon particles, holding them in place. Common practice involves dissolving or dispersing the polymer in a solvent and mixing it with the carbon to form a slurry. The resulting mixture can then be dried and pressed into free-standing pellets or cast directly onto the current collector. Alternatively, the dried agglomeration can be calendered to form a free-standing sheet, which can be cut to the desired size. Exact details for the preparation of the electrodes are provided in the Experimental sections of each chapter.

Anode Fabrication

Partially delithiated lithium iron phosphate ($LiFePO_4$) anodes are employed in Li-O_2 cells where the focus of the study is on the cathode or electrolyte.[4–6] The $LiFePO_4$ anodes act as counter/reference electrodes by maintaining a stable voltage of 3.45 V vs Li^+/Li (described below). The $LiFePO_4$ is also the source of Li^+ ions during discharge and charge. This is to avoid any limitations caused by the reactivity of Li metal with the electrolyte and oxygen, which need to be decoupled from the cathode electrochemistry. Because $LiFePO_4$ has poor electrical conductivity, it is mixed with conductive carbon, typically carbon Super P, to facilitate charge transport. Similarly, the cathode utilises a polymer binder, namely polytetrafluoroethylene (PTFE), to bind the $LiFePO_4$ and carbon together. The $LiFePO_4$, carbon and polymer binder are mixed together in an aqueous suspension, consisting of Milli Q water and isopropylalcohol, in an 8: 1: 1 weight ratio of $LiFePO_4$: Super P: PTFE. The suspension is heated during stirring to drive off excess water and the resulting putty is calendared to the desired thickness and cut into discs. The $LiFePO_4$ electrodes are partially delithiated by stirring in Milli Q water with glacial acetic acid (1.5 mL, 99 %) and peroxide (3.6 mL, 30 wt. % in water). The following reaction occurs:

$$\frac{1}{2}H_2O_{2(aq.)} + CH_3COOH_{(aq.)} + LiFePO_{4(s)} \rightarrow H_2O + xCH_3COOLi_{(aq.)} + Li_{(1-x)}FePO_{4(s)} \tag{2.1}$$

By partially delithiating the $LiFePO_4$ electrode, the $LiFePO_4$ maintains a stable voltage plateau at 3.45 V vs Li^+/Li during discharge-charge experiments in Li-O_2 cells, Figure 2.1.

2.1.2 Water control measures

Water contamination can adversely affect the performance of Li-O_2 cells by reacting with reactive oxygen species and Li_2O_2 to form LiOH.[7–9] As such, it is necessary to minimise the amount of water in Li-O_2 cells during operation. All cell components, including the

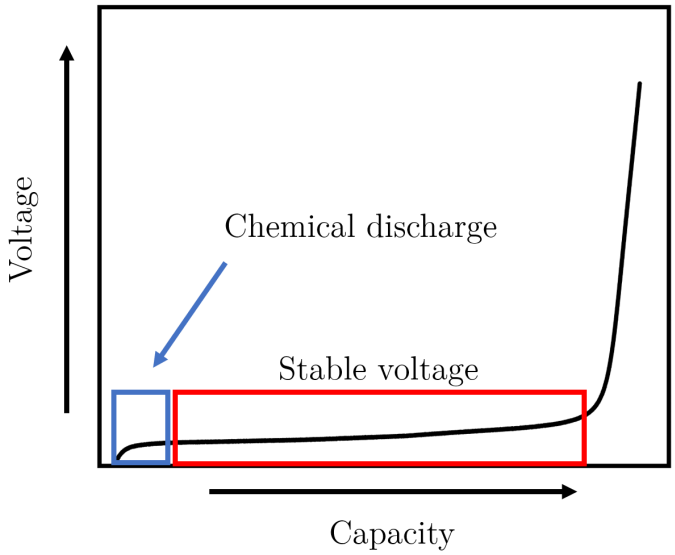


Figure 2.1: Schematic of the $Li_{(1-x)}FePO_4$ voltage profile during the discharge of a Li-O_2 cell. The $LiFePO_4$ is partially delithiated to bring the voltage profile into the stable plateau region highlighted by the red box.

GDEs, $LiFePO_4$ anode, salt, and separators, are dried under vacuum in an antechamber or Buchi tube before use. In this study, lithium bis(trifluoromethanesulfonyl)imide salt is dried for 72 hours at 120 °C, and the polypropylene or glass fibre separators are dried for 48 hours at 50 °C. The GDEs and $LiFePO_4$ electrodes are dried at 70 °C for 72 hours.

In this study, the main source of water contamination in the Li-O_2 cells, after the cell components have been thoroughly dried, is the electrolyte solvent. To minimise the water content in solvents, molecular sieves are employed. Molecular sieves are molecules, typically zeolites, with uniform pore sizes, which selectively allow water to enter or be adsorbed while excluding larger molecules such as the organic solvent, for example, 1,2-dimethoxyethane (DME). For this study, 3 Å molecular sieves are used to dry the solvents. Solvents containing redox mediators are dried over molecular sieves for several days before the addition of dried lithium salt. To avoid any ionic exchange between the lithium salt and the molecular sieves, the sieves are removed before adding the salt. Karl Fischer titration is used to measure the water content of the solvents.[10,11] This method involves the oxidation of sulfur dioxide by iodine in the presence of water in a buffered solution.

$$2H_2O + SO_2 + I_2 \rightarrow H_2SO_4 + 2HI \tag{2.2}$$

The reaction consumes a stoichiometric amount of water versus iodine and can be monitored by potentiometry. Karl Fischer titration is a fast, accurate, and precise method to measure the water content of a solvent in low concentrations. In this study, ether-based solvents are dried over molecular sieves until a water concentration of less than 10 ppm is achieved.

2.1.3 3D-Printing

3D printing by two-photon polymerisation (2PP) is one of the most versatile additive manufacturing techniques for fabricating arbitrary 3D prototypes using computer-aided design (CAD), with resolution down to 100 nm.[12] 3D-printing with 2PP is utilised in this thesis to fabricate sacrificial templates which are used during GDE fabrication to introduce new architectures such as gas diffusion channels. The high resolution of 2PP allows for intricate control over the channel dimensions.

2PP

2PP is based on the two-photon absorption (TPA) theory, which was first described by Göbert-Mayer in 1931.[13] In TPA, a molecule is excited to a higher state through the simultaneous absorption of two photons of equal or different frequencies, which is a nonlinear optical process, as shown in Figure 2.2. This differs from one-photon absorption (OPA), which is a linear mechanism in which the energy absorbed is a linear function of the intensity, I. In TPA, the absorption is proportional to I^2, which results in a significant increase in the resolution of absorption by the photoactive polymer.

While employing a focused laser featuring a Gaussian beam profile, the energy absorption pattern follows an exponential decay in both TPA and OPA processes. However, an intriguing distinction arises in the rate of energy attenuation. In TPA, owing to its nonlinear characteristics, the energy absorption experiences a doubly exponential decline in comparison to OPA. This phenomenon contributes to a significantly enhanced

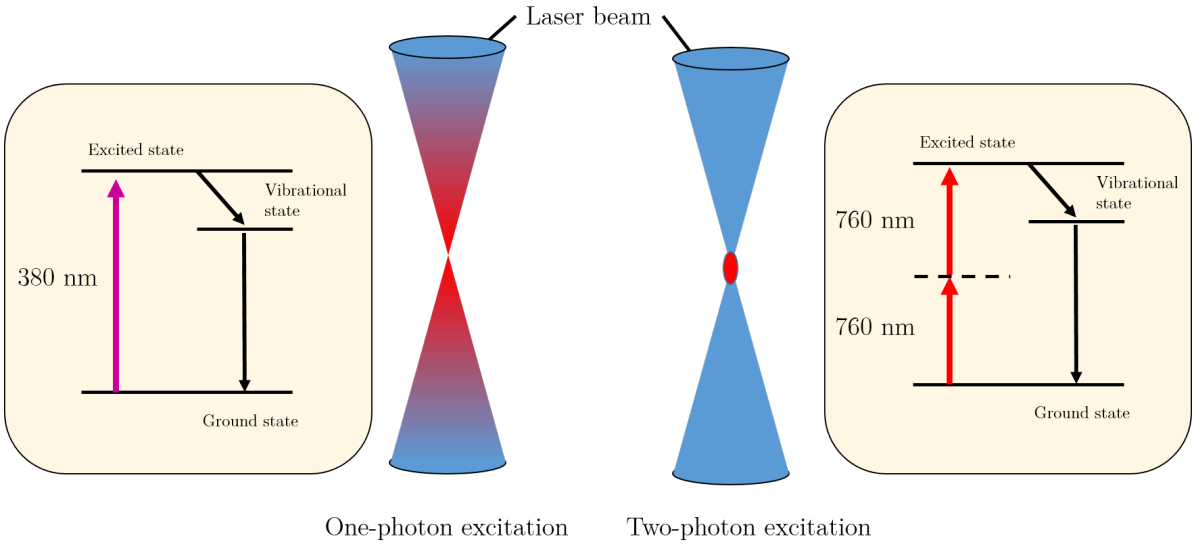


Figure 2.2: Schematic of the two-photon polymerisation process compared to one-photon polymerisation. The cones represent the laser beams with the red indicating the volume in which polymerisation takes place. The insets show the photon absorption and relaxation to the ground state. Reproduced under terms of the CC-BY license.[12]. Copyright 2021, Zahra Faraji Rad *et al.*, published by Springer Nature.

resolution and heightened precision in the creation of 3D structures through TPA.

Within the framework of resist exposure, the underlying mechanism involves the transition of molecules from a photon-excited state to a vibrational state. This transition prompts specific outcomes contingent on the type of resist employed. In the case of a positive-tone photoresist, it leads to the cleavage of polymer bonds, while for a negative-tone resist, it results in the formation of polymer crosslinking bonds. This orchestrated interplay between molecular states forms the basis for achieving intricate fabrication outcomes

Polymerisation Process

The 2PP optical process leverages its nonlinear property to tightly focus a laser on a specific spot, forming the smallest building block called a volume pixel (voxel) for creating 3D structures. In contrast to OPA, which involves excitation along the beam trace, 2PP confines excitation to the voxel surrounding the focal point. The voxel takes on an ellipsoidal shape, influenced by factors such as the objective numerical aperture, laser mode, and refractive index. These parameters also impact the distribution of laser focus intensity.

In the context of 2PP, photoresist materials are comprised of a photoinitiator coalesced with diverse monomers and oligomers. The onset of the polymerisation process is initiated by the presence of the photoinitiator, which generates an active radical species within a tightly confined spatial region around the focal point of the focused laser beam. This radical formation subsequently induces the solidification of a voxel, the fundamental unit akin to a miniature 3D pixel.

The dimensions of this voxel and the duration required for its fabrication exhibit an inverse correlation. The optimal choice of the objective lens, characterized by its numerical aperture, serves to enhance the efficiency of the fabrication process. The rate of polymerization of the photosensitive material is directly proportional to the square of the laser intensity within the system. Thus, employing a high-numerical-aperture objective lens in conjunction with a femtosecond or picosecond laser pulse yields intricately detailed structures, yielding resolutions below the threshold of 100 nm.

Design of Structures

To fabricate 3D structures using 2PP, a design is first created in CAD software, and then converted into an STL (Standard Tessellation Language) file. This file is sliced into layers and used to generate interpreted general writing language (GWL) code for printing. The code is then sent to a system equipped with a femtosecond laser source that uses tightly focused laser beams to expose photosensitive resins layer-by-layer, based on the GWL code.

Commercial 2PP systems typically use three scanning modes for photosensitive material polymerisation: galvo, piezo, and stage scan modes. In the galvo scanner, the laser pulses move in the XY directions while the photoresist remains stationary, and the z-drive movement is adjusted by either a stage motor or a piezo drive. The piezo and stage scan modes move the stage in the XYZ direction while the laser beam remains fixed. The piezo scan mode is useful for fabricating high-resolution 3D structures due to its large travel range in the XYZ directions, while the galvo scan mode is better for larger structures because of its faster writing speed. The stage scan mode can pattern

significantly larger areas but with lower resolution than the other scanning modes.

To monitor the polymerisation process in real-time, complementary metal oxide semiconductor or charge-coupled device cameras can be integrated into the system. Finally, unexposed regions of negative-tone resist and laser-exposed regions of positive-tone resist are removed in a developer bath. Additional flood exposure by ultraviolet (UV) light may be performed after development to trigger additional chemical crosslinking of the photoresists.

2.2 Electrochemical Techniques

2.2.1 Cell Assembly

The cells used in this study were constructed using Swagelok components, as depicted in Figure 2.3. The cells were composed of a stainless steel current collector for the anode, onto which the $LiFePO_4$, two separators, the GDE, and a stainless steel mesh current collector for the GDE were stacked within an electronically insulating PTFE casing. The GDE current collector was a hollow stainless steel tube that acted as an O_2 reservoir. Compression ferrules were used at all connections to ensure the cell was hermetically sealed. Prior to use, all cell casings were dried under vacuum at 70 °C for at least 24 hours.

To maintain dryness throughout the assembly, the cells were constructed within a dry, Ar-filled glovebox. Two valves were attached to the top of the O_2 reservoir to allow for purging with O_2. O_2 was purged through a moisture trap to minimise water contamination in the feed gas. After assembly, the cells were allowed to equilibrate for 3 hours to ensure saturation of the electrolyte with O_2 and complete wetting of the $LiFePO_4$ electrode, GDE, and separators with the electrolyte.

2.2.2 Galvanostatic Cycling with Potential Limitation (GCPL)

Galvanostatic Cycling with Potential Limitation (GCPL) is a widely used technique to assess the performance of a Li-O_2 cell. Its importance lies in its ability to provide

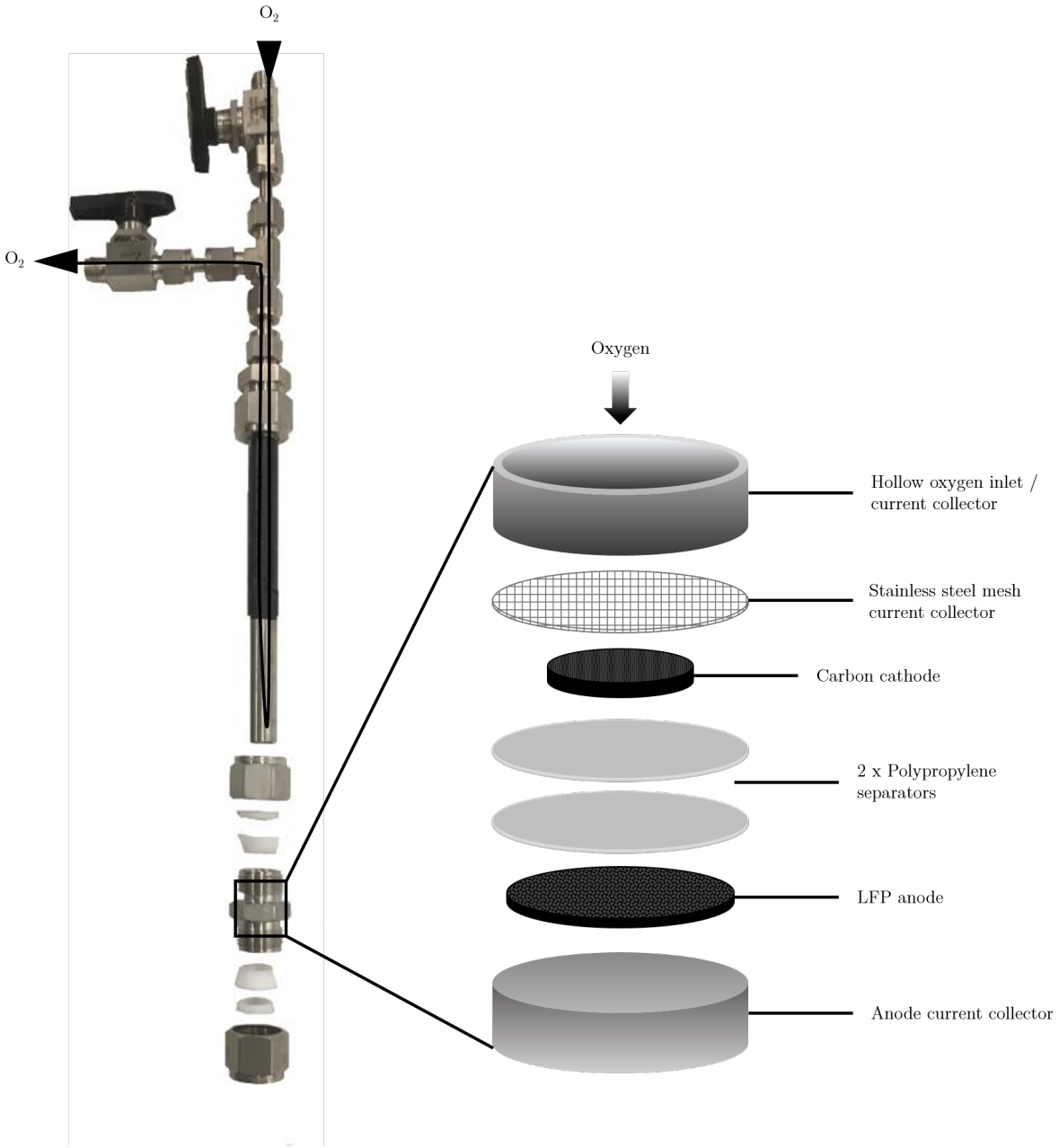


Figure 2.3: Swagelok cell design used for discharge experiments. The cell is hermetically sealed and can be purged with O_2 which is held in the reservoir above the GDE. The O_2 reservoir also acts as the GDE current collector which has electrical contact with a stainless steel mesh which itself is in contact with the GDE.

valuable information on the reaction overpotentials and achievable capacities, which are crucial for understanding the cell's electrochemical behaviour and capabilities. The technique involves keeping the current constant and measuring the voltage response as a function of the charge passed. The GDE's mass or areal surface area determines the constant current, which is expressed as mA g^{-1} or mA cm^{-2}, respectively. The capacity is expressed as the charge passed normalised to the mass or area of the cathode, given by mAh g^{-1} or mAh cm^{-2}.

It is essential to note that capacities normalised to the GDE's mass or carbon content may give superficially high values, as discussed in Chapter 1. In this thesis, the capacities are expressed as areal capacities and energy densities (Wh L^{-1}) to allow proper comparison against established technologies such as Li-ion.

A typical discharge and charge curve for a Li-O_2 battery is shown in Figure 1.2. During discharge, an overpotential of approximately 0.3-0.4 V is observed, and the discharge voltage plateaus before rapidly dropping towards the cut-off voltage (typically 2.4 V vs Li^+/Li). This region at the end of discharge is often referred to as the *sudden death* region. On charge, the cell voltage increases rapidly towards 4 V vs Li^+/Li (without a redox mediator), where it plateaus before increasing again to the positive cut-off voltage.

2.2.3 Linear Sweep Voltammetry (LSV) and Cyclic Voltammetry (CV)

GCPL is the most common technique used to measure the performance of Li-O_2 cells. However, potential sweep methods such as linear sweep voltammetry (LSV) and cyclic voltammetry (CV) are particularly useful for preliminary mechanistic investigations of a system. These techniques allow for a quick establishment of an 'electrochemical spectrum' that indicates the potentials at which processes occur. Additionally, sweep rate dependence can provide insight into coupled homogeneous reactions as well as other processes such as adsorption.

In CV experiments, the potential is swept between two potentials, E_1 and E_2, at a

known sweep rate, v, before being reversed. For Li-O_2 studies, an electrochemical cell is typically used, which allows for purging with oxygen. Three-electrode experiments are the most common, employing a working electrode, a counter electrode, and a reference electrode. The working electrode is typically a planar disk of known dimensions that is thoroughly polished to ensure that the surface area of the electrode is measurable. The current density is measured by the geometric area of the working electrode. The working electrode is commonly made from metals such as Au or Ag or from glassy carbon, and it is the electrode of interest during experiments. The counter electrode serves to supply the current required by the working electrode without limiting or contributing to the measured response of the cell. It usually has a higher surface area than the working electrode, and it is typically made from a metal such as a Pt wire mesh. The reference electrode provides a fixed potential that does not vary during the experiment. In Li-O_2 experiments, this electrode is typically an $LiFePO_4$ electrode filled with a Li^+ containing electrolyte. This is separated from the supporting electrolyte in the cell by an ion-conductive glass frit.

2.2.4 Chronoamperometry (CA)

In chronoamperometry (CA) experiments, the potential is changed instantaneously and the current-time response is recorded. The initial voltage is set at a potential where no electrochemical reaction occurs and is changed to one at which, for example, the reduction of O occurs at a diffusion-controlled rate. A CA curve will have a current that falls as $t^{-1/2}$ in line with the Cottrell equation, which describes the current response with respect to time in a potential step experiment:

$$I = \frac{nFAD^{1/2}c_o^{\infty}}{\pi^{1/2}t^{1/2}} \tag{2.3}$$

where n is the number of electrons transferred per molecule, F is Faraday's constant in C mol^{-1}, A is the area of a planar electrode in cm^2, c_O^{∞} is the concentration of the reducible analyte in mol cm_{-3}, D is the diffusion coefficient in cm s^{-1} of the analyte and t is time in s.

2.3 Characterisation

2.3.1 Scanning Electron Microscopy (SEM)

Scanning electron microscopy (SEM) offers a robust imaging technique, revealing high-magnification and high-resolution views of features beyond human ocular and optical microscopic capabilities. Unlike optical microscopes, SEM employs high-energy electrons, not visible light, for imaging. The reduced electron wavelength enables SEM to resolve finer material details. Modern SEM instruments can discern features as small as 1 nm.[14] A schematic diagram of the electron column is presented in Figure 2.4.

The electron column comprises several integral components: the electron gun, one or more electron lenses, scanning coils, as well as condenser and objective apertures. Within the electron gun, labelled as the 'electron source' in Figure 2.4, electrons originate and their magnitudes and accelerations can be modulated during their traversal through the column. The electron gun's luminance significantly impacts image quality, denoting the count of electrons focused on a specific specimen point within a second. Four primary electron gun variants exist, varying in luminance: tungsten filament, LaB_6 emitter, Schottky field emission, and cold field emission guns. In this investigation, we employed a Zeiss Merlin apparatus equipped with a Schottky field emission gun.

Field emission guns apply a negative potential to the cathode tip, which emits electrons. The electrons are accelerated towards the sample through a hole in the anode grounded at zero potential. The small size of the cathode tip concentrates the electric field in a small region, allowing electrons to escape the tip surface *via* the tunnelling effect.

Electrons emitted from a tungsten filament gun have a diameter of approximately 50 μm and must be demagnified and focused to be useful for imaging. This is accomplished through a series of electromagnetic lenses, including condenser and objective lenses, scanning coils, stigmators, and apertures. Electromagnetic lenses are constructed from a copper coil housed in an iron casing with cylindrical pole pieces. When a direct current passes through the coil, it generates a strong magnetic field

confined within the iron shroud, except for a gap between the lens pole pieces, allowing the magnetic field to exert a force on the electrons passing through. The interaction between the electrons emanating from the gun and the magnetic field deflects the electrons toward the axis (through the centre of the electron column). Electrons farther from the axis are deflected more strongly towards the axis, producing a focusing effect.

The objective lens, which is the final lens in the electron column, plays a crucial role in demagnifying and focusing the electron beam onto the surface of the sample. It incorporates a beam-limiting aperture and a stigmator, which are used to correct for lens aberrations, as well as scan coils. Spherical aberration is one such aberration that occurs because electrons towards the edge of the lens are bent more strongly than those near the optical axis, causing the electrons to focus at different points depending on which part of the lens they pass through. As a result, a disc rather than a point is formed at the image plane, leading to image blurring. The beam-limiting aperture blocks off-axis electrons, which reduces the angle of convergence and hence the spherical aberration.

Another aberration that can occur is astigmatism, which is caused by imperfections in lens construction or contaminated apertures, resulting in an inconsistent electromagnetic field. This results in two line foci perpendicular to each other being formed at two different focal lengths, causing the image to stretch in one direction, resulting in an elliptical probe rather than a spherical one. To rectify this, the stigmator applies an electromagnetic field at 90° relative to the field distortion, thereby cancelling it out.

Finally, the scan coils deflect the electron beam, enabling the beam to be scanned from left to right across the sample, generating the raster on the specimen. The combination of these components allows for precise control of the electron beam and the production of high-resolution images.

To generate an image, a beam of high-energy electrons is scanned across the surface of the sample. The electrons penetrate a few microns into the sample and interact with its atoms, generating various signals, including backscattered electrons, secondary electrons, and characteristic X-rays. The most common imaging mode is secondary electrons. In this mode, secondary electrons are generated when the beam electrons inelastically

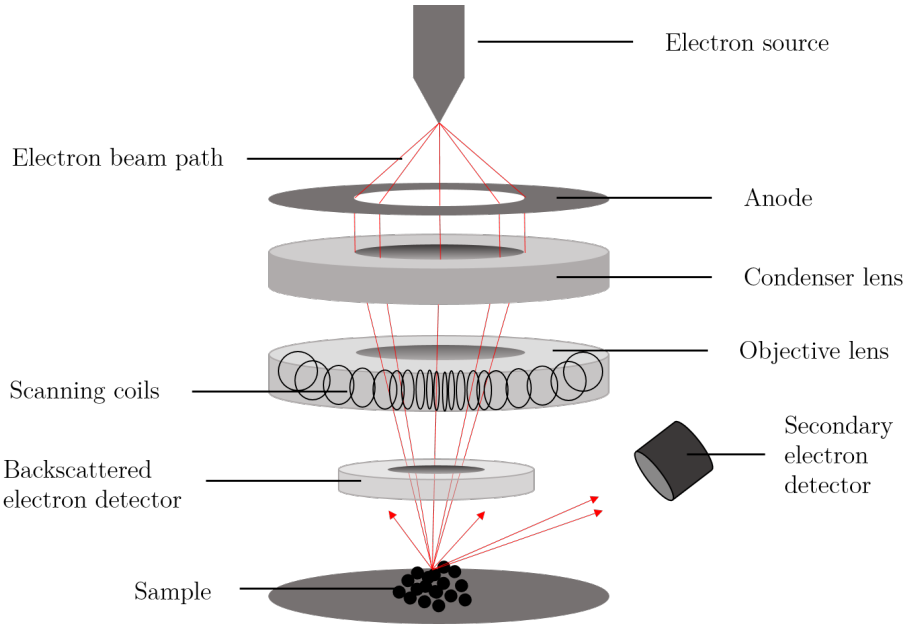


Figure 2.4: Schematic of a scanning electron microscope. The high-energy electron beam is focused through a series of lenses onto the sample's surface. The electron detectors capture the electrons emitted from the sample to form an image.

scatter, ejecting weakly bound valence electrons from the parent atom. The key feature of secondary electrons is their very low kinetic energy and monotonic dependence on the local surface inclination, producing topographic contrast, and revealing the shape of an object.[15]

Throughout this thesis, SEM is utilised to qualitatively investigate the discharge and charge reactions taking place at the GDE. SEM allows for easy analysis of the pristine GDE morphology and the morphology of the discharge products, namely Li_2O_2, at both the air interface and the separator interface. This technique enables the detection of potential pore-blocking phenomena that may occur at the end of discharge and facilitates facile measurement of the particle size of the Li_2O_2 formed during discharge. Due to the instability of Li_2O_2 towards atmospheric constituents, such as H_2O and CO_2, the samples are loaded into the SEM under vacuum *via* an antechamber.

2.3.2 Energy Dispersive X-Ray Spectroscopy (EDX)

EDX is an analytical technique that allows the determination of the chemical composition of a sample. When a beam of high-energy electrons is focused onto a sample, an electron may be ejected from the inner shell of an atom in the sample, creating an

electron hole. This causes an electron from a higher energy outer shell to relax into the electron-hole. The difference in energy between the two electron shells is emitted as an X-ray, the energy of which is unique to the difference in energy between the two shells and the atomic number of the element. EDX can be used in conjunction with SEM, which also utilises a focused beam of high-energy electrons to image a sample. EDX can record an elemental map of a sample, giving information on the chemical composition, spatial arrangement of elements and their concentration. For example, EDX is used in this work to determine the distribution of the perfluorinated polymer binder (indicated by the fluorine EDX) throughout electrodes formed with carbon black.

2.3.3 Fourier Transform Infrared Spectroscopy (FTIR)

Infrared spectroscopy is a powerful tool for investigating the vibrational frequency of chemical bonds. In infrared spectroscopy, the absorption of infrared light is measured as a function of frequency.[16] For diatomics, the vibrational frequency ν_m is a function of the mass of the atoms and the strength of the chemical bond that connects them. In the classical treatment, a diatomic can be modelled as a harmonic oscillator that obeys Hooke's Law. The vibrational frequency can be related to the force constant, K, and the reduced mass, μ, as expressed by the following equation:

$$\nu_m = \frac{1}{2\pi}\sqrt{\frac{K}{\mu}} \tag{2.4}$$

where the reduced mass is given by the equation:

$$\mu = \frac{m_1 m_2}{m_1 + m_2} \tag{2.5}$$

This simple expression shows that the frequency of vibration for a diatomic depends on the force constant, K, which increases with single, double, and triple bonds. Higher force constants lead to higher vibrational frequencies. The vibrational frequency also depends on the mass of the two atoms involved in the vibration, with larger masses leading to lower vibrational frequencies.

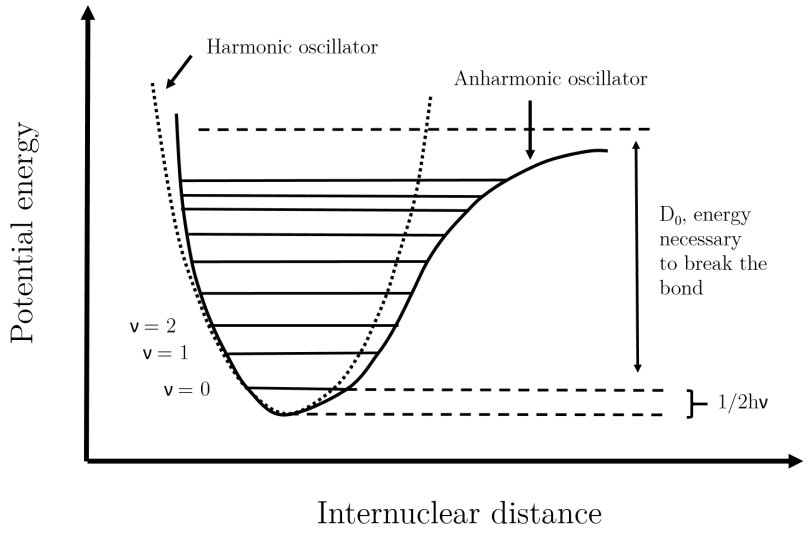


Figure 2.5: Schematic of the potential energy with internuclear distance of a harmonic and anharmonic oscillator. The lines marked $\nu = 0$, 1, 2, etc. are the quantised vibrational energy states of the diatomic. Anharmonicity is introduced as a more realistic way to model the vibrational frequency of a diatomic. Adapted with permission from Larkin *et al.*.[16] Copyright 2018 Elsevier.

For the classic harmonic oscillation of a diatomic, the potential energy can be represented by the following equation:

$$PE = \frac{1}{2}KX^2 \tag{2.6}$$

X is the distance between the two atoms in m, X_e is the equilibrium internuclear distance in m, and K is the force constant in N m^{-1}. A plot of potential energy as a function of distance X is a symmetric parabola around X_e, as shown in Figure 2.5. X_e is the energy minimum, and the force constant measures the curvature of the potential well near X_e.

Quantum mechanics shows that molecules can exist only in quantised energy states, labelled $\nu = 0, \nu = 1$, etc. Infrared spectroscopy probes transitions between these energy states, $\Delta\nu = \pm 1$. A more realistic approach to the potential energy of a diatomic is to introduce anharmonicity, as shown in Figure 2.5, which results if the change in the dipole moment is not linearly proportional. Anharmonicity introduces additional features, such as additional transitions, $\Delta\nu = \pm 2$, and smaller gaps between higher energy states until the dissociation limit is reached where the chemical bond breaks.

The molecule absorbs $\Delta E = hv$ at each vibrational transition, and the intensity of the absorbed light is governed by the Beer-Lambert Law:

$$I = I_0 e^{-\varepsilon c d} \tag{2.7}$$

where I is the intensity of the transmitted beam, I_0 is the intensity of the incident beam, ε is the molecular absorption coefficient in mol dm^{-3}, and c and d are the concentration of the sample in mol dm^{-3} and the cell length in cm, respectively.

Two crucial factors for infrared absorption are the radiation frequency and the molecular dipole moment. The interaction of the radiation with the molecule is described by a resonance condition, where the specific oscillating radiation frequency matches the natural vibrational frequency of a normal mode of vibration. The molecular vibration must also cause a change in the dipole moment of the molecule for the energy of the infrared photon to be transferred to the molecule *via* absorption. The dipole moment of a molecule is a function of the magnitude of the atomic charges (e_i) and their positions (r_i), as expressed by the following equation:

$$\mu = \Sigma e_i r_i \tag{2.8}$$

As an approximation, the dipole moment can be estimated from the electronegativity of the atoms. Homonuclear diatomics such as H_2 and N_2 do not have a dipole moment and are inactive in infrared spectroscopy but are active in Raman spectroscopy, while HCl and CO are active in FTIR spectroscopy.

FTIR is used throughout this work to determine the discharge and charge products in *ex-situ* experiments. Due to the characteristic peaks of Li_2O_2 lying in the Far-IR region (400-10 cm^{-1}), a CsI beamsplitter must be used, and samples must be prepared using CsI as a supporting transmitting material. This is because KBr, typically used in FTIR instruments, absorbs radiation in the Far-IR region. The FTIR is also housed in a dry N_2-filled glovebox to avoid contamination due to atmospheric constituents.

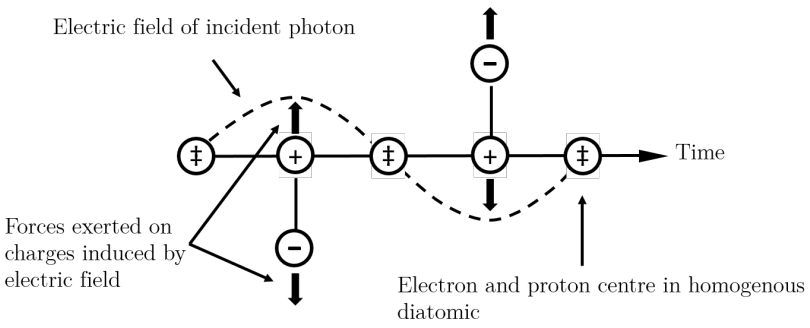


Figure 2.6: Schematic of the induced dipole moment on a homonuclear diatomic by the electric field of radiation. The polarisability of the electron cloud around the molecule by the external electric field leads to the induced dipole moment. The field relative to the proton centre displaces the electron cloud. Adapted with permission from Larkin *et al.*.[16] Copyright 2018 Elsevier.

2.3.4 Raman Spectroscopy

Raman spectroscopy is a method for measuring the vibrational frequency of chemical bonds, similar to FTIR. However, instead of measuring the absorption of the incident radiation, Raman spectroscopy measures the change in energy of light which is inelastically scattered, thus the vibrational frequency is measured as a shift from the incident beam energy. The classical electromagnetic radiation produced by oscillating dipoles induced in the molecule by the electromagnetic fields of the incident radiation explains the light scattering phenomena. The polarisability, α, of the electron cloud around the molecule by the external electric field leads to the induced dipole moment, as illustrated in Figure 2.6, where the field relative to the proton centre displaces the electron cloud. This can be likened to the charged plates of a capacitor inducing a dipole in a polarisable cloud of electrons, where the positively charged plate attracts the electrons, and the negatively charged plate attracts the protons.

Figure 2.7 depicts a schematic illustration of light scattering in Raman spectroscopy. Monochromatic radiation sources in the UV, visible or near-IR spectral region are used to irradiate the sample in Raman experiments. Most scattered light is scattered elastically, referred to as 'Rayleigh scattering,' where the scattered light has the same energy as the incident radiation and its intensity is approximately 10^{-3} that of the incident radiation. A much smaller portion is scattered with increased or decreased energy, referred to as 'anti-Stokes or Stokes Raman scattering,' respectively, with an intensity approximately

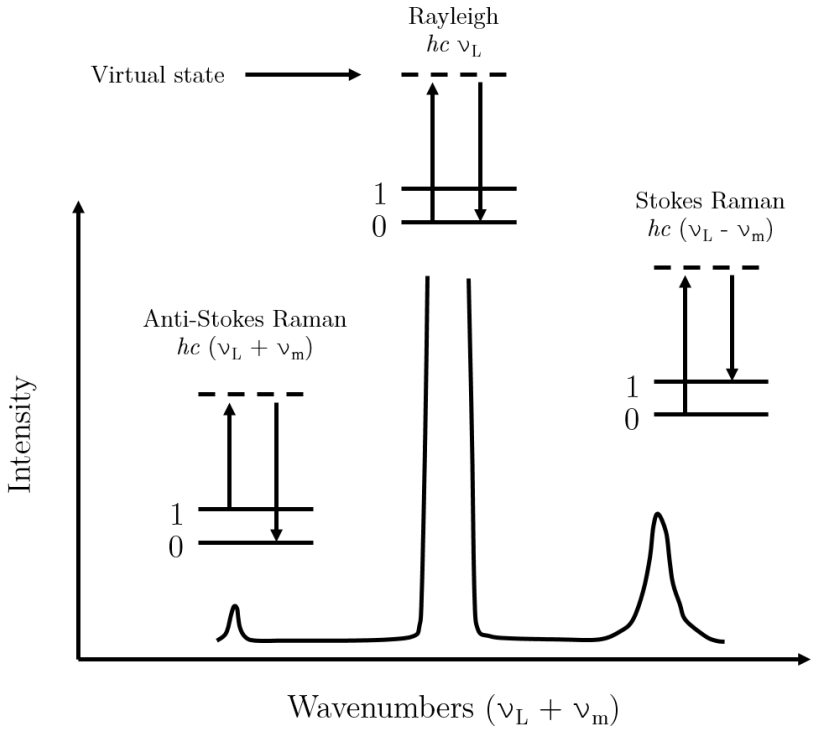


Figure 2.7: Schematic of the photon released after relaxation from a virtual excited state. The incident photon is momentarily absorbed by a transition from a ground state into a virtual excited state. A new photon is then created and scattered by relaxation from the virtual state. Stokes Raman scattering is more intense than anti-Stokes Raman scattering as most molecules are found in their ground state at ambient temperature. Adapted with permission from Larkin *et al.*.[16] Copyright 2018 Elsevier.

10^{-6} that of the incident radiation. Both Rayleigh and Raman scattering are two-photon processes whereby an incident photon is momentarily absorbed by a transition from the ground state into a 'virtual state', and a new photon is created and scattered by a transition from this virtual state.

Under ambient conditions, Stokes-Raman scattering is more intense than anti-Stokes scattering because, at ambient temperature, most molecules are found in the ground state. The Raman signal's intensity is given by the equation:

$$I_R \propto \nu^4 I_0 N \left(\frac{\delta\alpha}{\delta Q}\right) \tag{2.9}$$

where I_0 is the incident laser intensity, N is the number of scattering molecules in a given state, ν is the frequency of the exciting laser, α is the polarisability of the molecules, and Q is the vibrational amplitude. This expression shows that the Raman signal is concentration-dependent, that shorter-wavelength excitation or increasing laser

flux power density can increase the signal, and that only molecular vibrations that cause a change in polarisability are Raman active.

Raman spectroscopy is employed to determine the discharge and charge products in the GDE.

2.3.5 Powder X-Ray Diffraction (PXRD)

X-ray diffraction is an essential technique in materials characterisation to obtain information on the atomic scale in a crystalline structure. As well as the identification of crystal structures, X-ray diffraction can be applied to determine fine structure such as crystallite size, chemical composition and state of ordering, etc.[17]

Diffraction occurs whenever the wavefront of a beam of radiation is obstructed in some way; in the case of X-rays, this happens when they are scattered by electrons in an atom as represented schematically in Figure 2.8. Analogous to the diffraction of visible light through slits in a grating arranged in a regular array, in the diffraction of X-rays by crystals (planes of atoms arranged in a regular array), the intensities of diffraction maxima show a variation in different directions and vary significantly with the angle of scattering. The scattering can be considered to reflect off of the planes of atoms in the crystal at an angle identical to the angle of incidence of the radiation. The planes of atoms can be described by three values known as the Miller indices h, k and l, which are the reciprocal values of the intercepts of each plane with the a, b and c axes of the unit cell respectively. When the path length of X-rays scattered from adjacent parallel planes is equal to an integer wavelength value, constructive interference occurs, and a peak in intensity is observed in the detected radiation.[18] This is known as Bragg's Law:

$$n\lambda = 2d_{\mathrm{hkl}}sin(\theta) \tag{2.10}$$

Where λ is the wavelength of radiation used, n is an integer value, d is the perpendicular spacing between the lattice planes and θ is the complement (90°- θ) of the angle of incidence of the X-ray beam. Therefore, the number and position of peaks in the diffraction pattern depend on the crystal's space group and unit cell.

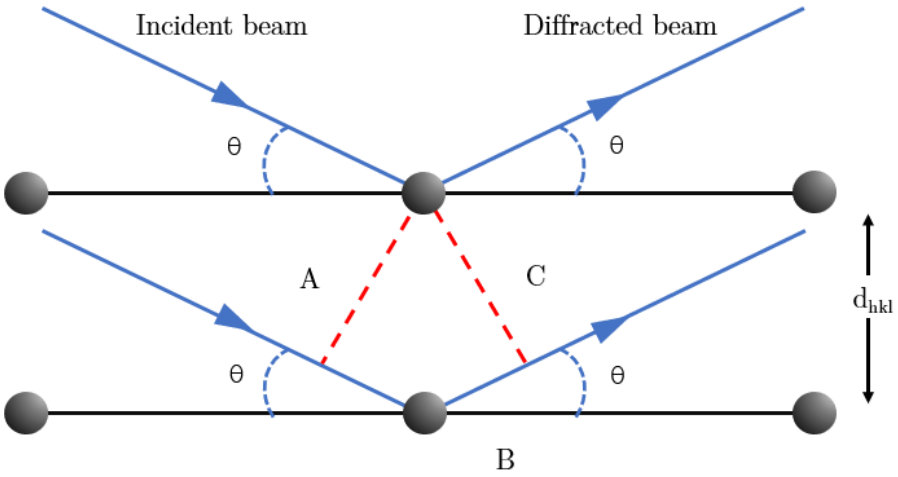


Figure 2.8: Schematic of X-rays diffracting off of planes of atoms in a crystal. X-rays can be considered to reflect off of the planes of atoms in the crystal at an angle identical to the radiation's incidence angle. When the path length of X-rays scattered from adjacent parallel planes is equal to an integer value of the wavelength, constructive interference occurs, and a peak in intensity is observed in the detected radiation

PXRD is used throughout this thesis to characterise the discharge product at the end of discharge. Typically the discharged GDE is removed from the cell and washed and dried using DME. The GDE is then broken down into a powder and placed on a Si sample holder for measurement. The PXRD is placed inside a N_2-filled glovebox to avoid contamination with atmospheric constituents. The PXRD patterns are compared with the inorganic crystal structure database standards to confirm the discharge products.

2.3.6 UV-vis Spectroscopy and Li_2O_2 Titration Technique

The energies associated with the transitions between different valence electron arrangements fall within the UV and visible regions of the electromagnetic spectrum. For example, many transition metal complexes are coloured, and their colour can change quite dramatically upon altering the oxidation state of the metal (iron(II) complexes are green-coloured, and their analogous iron(III) complexes are red/brown). Therefore, UV-vis spectroscopy is the measurement of the transitions involved in the rearrangement of valence electrons.

In a similar principle to infrared spectroscopy, UV-vis spectroscopy measures the absorption of electronic transitions, and the absorbance of the molecule is related to the concentration and molar extinction coefficient by the Beer-Lambert Law (equation

2.3.3). UV-vis spectroscopy also has selection rules which determine which transitions are formally allowed. There are three for electronic spectroscopy: the first of these is $\Delta l = \pm 1$ (where $l = 0$ corresponds to an *s*-orbital, $l = 1$ corresponds to a *p*-orbital and so on). The second relates to spin-multiplicity, with transitions between states with the same multiplicity being allowed but not those between different multiplicity states. The third is the *parity* selection rule, which applies to molecules with a centre of symmetry, i. The parity rule forbids transitions between energy levels with the same symmetry with respect to the centre of inversion.[19]

In Li-O_2 studies, UV-vis is commonly used as a titration technique to quantify the amount of Li_2O_2 in a sample, such as a discharged GDE. In these experiments, the sample containing Li_2O_2 is submerged in purified (Milli Q) water, forming a stoichiometric amount of H_2O_2 *via* the reaction:

$$Li_2O_2 + 2H_2O \rightarrow 2LiOH + H_2O_2 \tag{2.11}$$

The peroxide forms a complex with $TiOSO_4$, which leads to a ligand-to-metal charge transfer band at 410 nm.[20] This charge transfer band can only occur with complexation with a peroxide. As well as this, the colour formation is not due to a redox process meaning the $TiOSO_4$ does not react with oxidising reagents that may be present in the solution. The selectivity, intense colour and lack of reversibility make the Ti(IV)-peroxide complex ideal for colourimetric detection of peroxides. The concentration of Li_2O_2 in a sample is determined by comparing the absorbance value of the titrated sample with a calibration curve formed from known quantities of Li_2O_2.

This technique was combined with microtomy for experiments where the distribution of Li_2O_2 in a discharged GDE is measured (Figure 2.9). For these experiments, the electrode was washed with DME before drying. The electrode was then infiltrated with melted paraffin wax under a vacuum and affixed to a cassette. A high vacuum was applied to ensure that the wax entered the electrode's pores. The wax-infiltrated electrode was cooled to -10 °C before assembling onto a manual microtome. Cooling the wax ensures that well-defined and reproducible slices can be taken. Each slice was

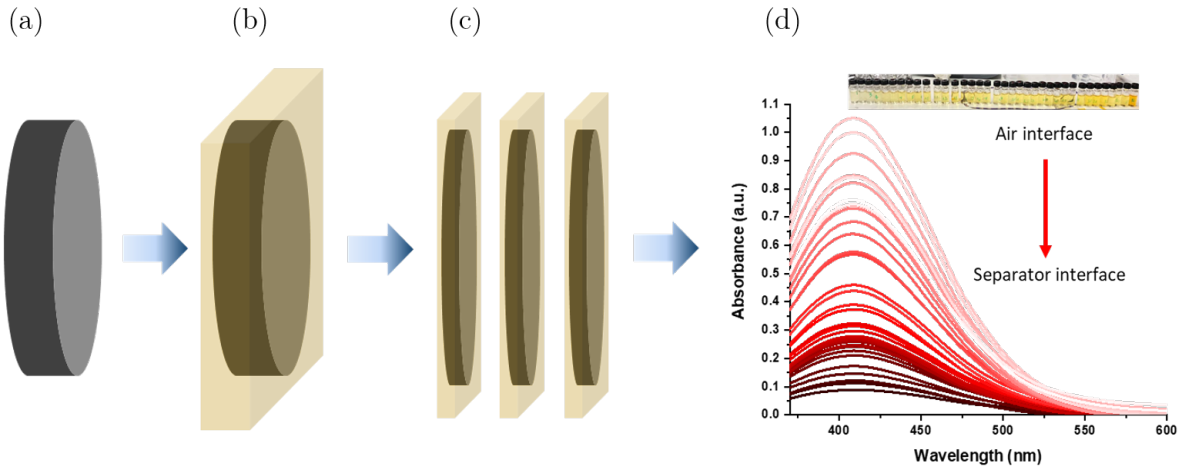


Figure 2.9: Schematic of the process used to determine the distribution of Li_2O_2 in discharged GDEs. The discharged cathode (a) is infiltrated with molten paraffin wax (b), and cross sections are taken using a microtome (c) before submerging in an acidic $TiOSO_4$ solution to determine the peroxide concentration by UV-vis spectroscopy (d)

instantly submerged in aqueous acidic $TiOSO_4$ solution to minimise any reaction between Li_2O_2 and atmospheric constituents, such as CO_2, forming Li_2CO_3 and other products. Before measurement, the analyte was filtered to remove any paraffin wax or carbon.

2.3.7 BET Surface Area Analysis

Gas adsorption/desorption analysis is the most widespread method used to characterise a material's surface area and microporous structure. This involves measuring the molar volume of a gas adsorbed or desorbed on the surface of a clean solid at a fixed temperature as a function of the gas pressure. The resulting adsorption/desorption isotherm is typically obtained at a cryogenic temperature, such as the boiling point of liquid nitrogen at atmospheric pressure (77.35 K). It is expressed in terms of the relative pressure of the gas.[21]

Adsorption isotherms are generally classified into six types, five of which were originally defined by Brunauer.[22] Type I indicates materials with extremely small pores, while Type II corresponds to nonporous solids or those with relatively large pores. Types III and V indicate conditions where the adsorbate has a greater affinity for itself than for the solid surface, and no identifiable monolayer is observed. In Type III, the adsorbate clusters at the most favourable sites on the adsorbent; in Type V, clustering is then

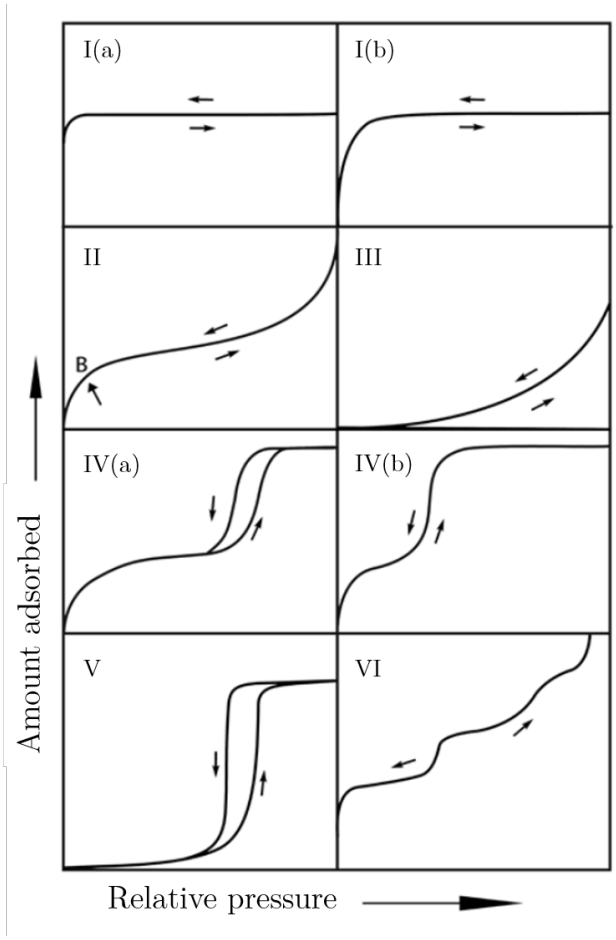


Figure 2.10: Illustration of the different types of isotherm typically observed in BET experiments. Type I is indicative of materials with extremely small pores, while Type II corresponds to nonporous solids or those with relatively large pores. Types III and V indicate conditions where the adsorbate has a greater affinity for itself than for the solid surface, and no identifiable monolayer is observed. Mesoporous samples give type IV isotherms. Type VI is a rare case of a nonporous solid with a completely uniform surface. Reproduced from Thommes *et al.*.[23] Copyright 2015 IUPAC De Gruyter

followed by pore filling. Mesoporous samples give type IV isotherms. Type VI is a rare case of a nonporous solid with a completely uniform surface; the step-wise increase represents a layer-by-layer adsorption. The step height now represents the capacity for each adsorbed layer, while the sharpness of the step is dependent on the system and the temperature.[23]

In a typical Type II isotherm, such as those observed for the GDEs in this study, the adsorption rapidly rises at low pressures due to the adsorbate molecules' interactions with the solid surface's most energetic regions. As the surface becomes increasingly covered with adsorbate, the adsorption rate slows until a plateau is reached. At the plateau's midpoint, the adsorbate forms multiple layers on the surface, leading to a

linear rise in the isotherm. Finally, at higher pressures, the adsorbate undergoes bulk condensation, resulting in a sharp increase in the adsorption. The surface area of the material can be determined from the initial slope of the isotherm.

Hysteresis loops located in the multilayer range of the physisorption isotherm are typically associated with capillary condensation, which can result from adsorption metastability and network effects. The delayed condensation observed in an open-ended pore of cylindrical geometry is due to the metastability of the adsorbed multilayer. In a collection of such pores, the adsorption branch of the hysteresis loop is not in thermodynamic equilibrium. On the other hand, the desorption stage is equivalent to a reversible liquid-vapour transition since it does not involve nucleation. Consequently, if the pores are filled with liquid-like condensate, thermodynamic equilibration is established on the desorption branch. However, the desorption path can depend on various forms of pore blocking in more complex structures, such as GDEs made from carbon black and a polymer binder. This phenomenon can occur where wide pores only have access to the external surface through a narrow pore, leading to the wide pores filling as usual but remaining filled during desorption until the narrow necks empty at lower vapour pressures.[23]

Different types of hysteresis loops have been observed, related to specific pore structures and underlying adsorption mechanisms. Figure 2.11 overviews some of these loops. Type H1 loops are typically observed in materials with a narrow range of uniform mesopores. In contrast, Type H2 loops are associated with more complex pore structures, where network effects play a crucial role. In particular, H2(a) loops are characterised by a very steep desorption branch that can be attributed to pore-blocking/percolation in a narrow range of pore necks or to cavitation-induced evaporation.

Type H3 loops are characterised by an adsorption branch that resembles a Type II isotherm, and the lower limit of the desorption branch is usually located at the cavitation-induced P/P_0. H4 loops, on the other hand, have a composite adsorption branch consisting of Types I and II, with the more pronounced uptake at low P/P_0 associated with the filling of micropores. These types of hysteresis loops are commonly

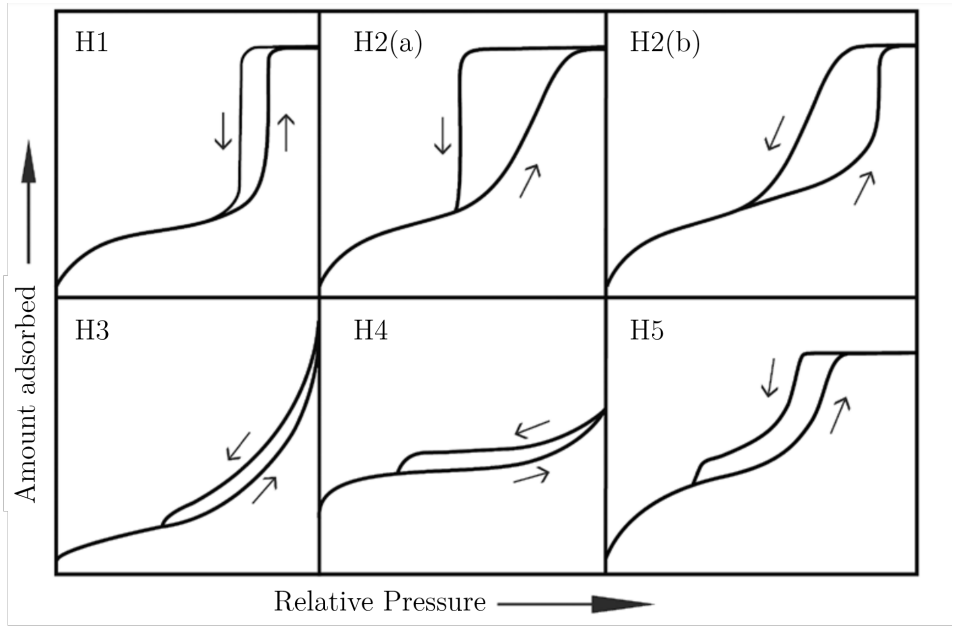


Figure 2.11: Illustration of the different types of hysteresis typically observed in nitrogen adsorption/desorption experiments. Type H1 loops are typically observed in materials with a narrow range of uniform mesopores. Type H2 loops are associated with more complex pore structures, where network effects are crucial. Type H3 loops are characterised by an adsorption branch that resembles a Type II isotherm, and the lower limit of the desorption branch is usually located at the cavitation-induced P/P_0. H4 loops have a composite adsorption branch consisting of Types I and II, with the more pronounced uptake at low P/P_0 associated with the filling of micropores, commonly found in micro-mesoporous carbons. Type H5 loops are less common but have a distinct form associated with pore structures containing both open and partially blocked mesopores. Reproduced from Thommes *et al.*.[23] Copyright 2015 IUPAC De Gruyter

found in micro-mesoporous carbons. Finally, Type H5 loops are less common, but they have a distinct form associated with pore structures containing both open and partially blocked mesopores.

BET theory is named after its originators Brunaeuer, Emmett and Teller. The theory assumes that the forces active in gas condensation are also responsible for the binding energy in multi-layer adsorption. By equating the rate of condensation of gases onto an already adsorbed layer and summing over an infinite number of layers, the following expression is obtained:

$$V_{\mathrm{a}} = \frac{V_{\mathrm{m}} C P}{(P_0 - P)\left[1 + (C-1)\frac{P}{P_0}\right]} \tag{2.12}$$

Where C, is a constant given by

$$C \propto exp \frac{q_1 - q_{\mathrm{L}}}{RT} \tag{2.13}$$

Where q_1 is the heat of adsorption of the first layer, q_{L} is the heat of liquefaction of the adsorptive and R and T are the gas constant and absolute temperature, respectively. This can be written in linear form as follows:

$$\frac{P}{V_{\mathrm{a}}(P_0 - P)} = \frac{1}{V_{\mathrm{m}} C} + \frac{C-1}{V_{\mathrm{m}} C}\left(\frac{P}{P_0}\right) \tag{2.14}$$

If a plot of $P/[V_{\mathrm{a}}(P - P_0]$ vs. P/P_0 this will yield a straight line with intercept $1/V_{\mathrm{m}}C$ and a gradient of $(C-1)/V_{\mathrm{m}}$. The volume of the monolayer has been determined, so the surface area can be estimated from the area occupied by a single molecule of the adsorbate assuming a cubic close-packed structure. An area of 16.2 Å^2 for one molecule of N_2 is used in this work.

2.3.8 Mercury Intrusion Porosimetry (MIP)

Mercury intrusion porosimetry allows for measuring the bulk properties of a material by the intrusion of mercury under a range of pressures. A single experiment can gather information on the pore size distribution, pore volume, wall area, and bulk and absolute

densities of the material. As well as this, the pore sizes that MIP can probe span five orders of magnitude, making MIP an extremely informative technique.

The pressure required to force mercury into a capillary pore was first described by E. W. Washburn in 1921.[24] He described the pressure required to force mercury into a capillary of radius, r, by the relation:

$$p = \frac{-2\gamma cos\Theta}{r} \tag{2.15}$$

p is the pressure, γ is the surface tension and Θ is the contact angle. Equation 2.15 shows that the pressure required to force mercury into a pore is inversely proportional to the pore size. Mercury is used as it is a non-wetting liquid and will not penetrate pores by capillary action. Instead, it has to be forced to do so, Figure 2.12.

In a typical experiment, a thoroughly dried and degassed material is weighed out and sealed in a penetrometer. The sample is then exposed to a high vacuum to remove any adsorbed gases. Once a suitably low pressure is achieved, pure mercury is introduced to fill the penetrometer and stem, and a series of pressure and volume measurements are taken. In modern instruments, the volume of mercury forced into the sample is determined by measuring the capacitance of the stem of the penetrometer; the reduction in capacitance is proportional to the volume of mercury that travels through the stem. Any change in volume after a small pressure increase, Δp, is evidently due to filling of pores with radii between r and $r - \Delta r$.

To achieve accurate results, a blank experiment must be run without any sample. The compressibility of the mercury, penetrometer and other components under pressure can be corrected for. Similarly, the variation of γ and Θ with p must be known for the range of pressures used and the operating temperature.

2.3.9 Thermogravimetric Analysis (TGA)

Thermogravimetric analysis is a thermal technique in which the mass of a sample is recorded over time during a temperature change. This allows for analysing physical phenomena, such as phase changes and adsorption or desorption events, or chemical

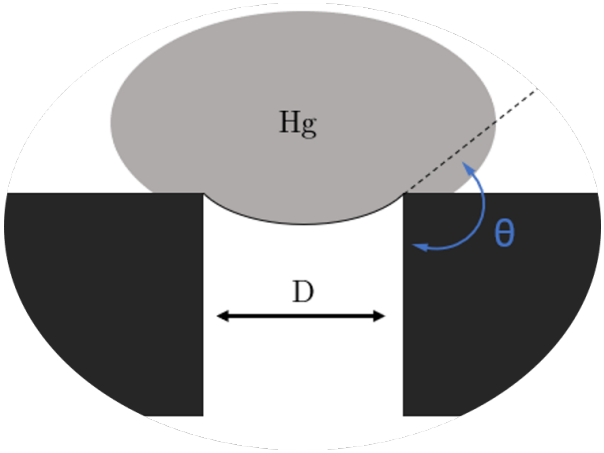


Figure 2.12: Schematic illustration of mercury intrusion into a capillary pore. Due to the non-wettability of Hg, intrusion only occurs due to increased pressure. The pressure is related to the pore size by the Washburn equation and the capacitance of the penetrometer stem measures the amount of intrusion. Figure adapted from [21]

phenomena, such as thermal decomposition. A thermogravimetric analyser consists of a precision balance contained inside a furnace with a programmable temperature and atmospheric control. Commonly, the temperature is increased linearly while the mass is continuously measured over time. Measurements can be carried out under inert conditions with a feed gas such as argon or nitrogen or in ambient conditions or a vacuum. TGA was used in this work to measure the degradation temperatures of polymers used as binders (PTFE or Teflon AF2400), and the polymerised photoresist (Nanoscribe IP-S) was used as a sacrificial template to fabricate electrodes.

2.3.10 Differential Electrochemical Mass Spectrometry (DEMS)

Differential Electrochemical Mass Spectrometry (DEMS) is an analytical technique which combines electrochemical half-cell experimentation with the *in situ* detection of gaseous and volatile reaction products and intermediates *via* mass spectrometry. The development of the technique is primarily credited to Bruckenstein and Gadde, who used a porous electrode with one side contacting the high-vacuum system of a mass spectrometer. In contrast, the other side contacted a perchloric acid solution to be electrolysed.[26] They were able to measure oxygen generation by monitoring the mass-32 peak on the mass spectrometer whilst passing charge in the cell.[26]

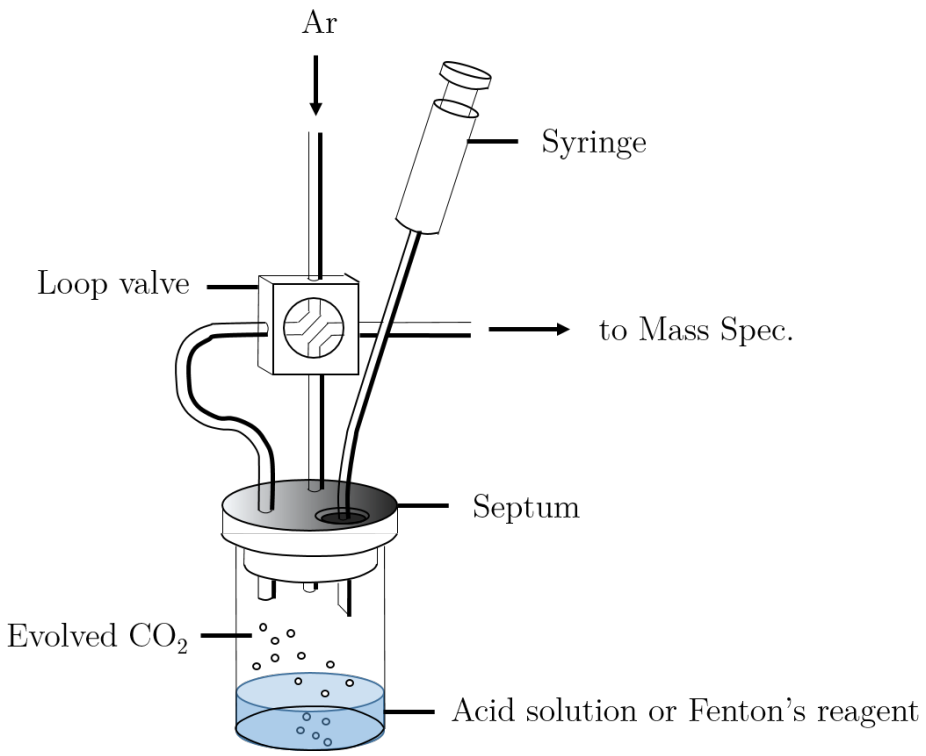


Figure 2.13: Schematic illustration of a typical *ex situ* DEMS experimental setup. Acid or Fenton's reagent is injected onto a sample, and the amount of evolved CO_2 is measured using DEMS. Adapted with permission from Schafzahl *et al.*.[25] Copyright 2018 American Chemical Society.

DEMS experiments can be carried out *ex-situ* to quantify the amounts of each side product formed after discharge or charge. A cell design which allows the constant flow of carrier gas is used, Figure 2.13. The discharged/charged GDE is sealed inside the cell and purged with carrier gas. Acid or Fenton's reagent is then injected through a septum which will react with inorganic or organic carbonates respectively to form a stoichiometric amount of CO_2. The CO_2 is monitored using a mass spectrometer and the amount of each side product can be calculated from the amount of CO_2 detected. Phosphoric acid is used to detect inorganic carbonates, namely Li_2CO_3, by the reaction:

$$Li_2CO_3 + 2H_3PO_4 \rightarrow 2LiH_2PO4 + CO_2 + H_2O \tag{2.16}$$

while Fenton's reagent forms the reactive hydroxyl radical *via* the reaction:

$$Fe^{2+} + H_2O_2 \rightarrow Fe^{3+} + OH^- + {}^{\bullet}OH \tag{2.17}$$

the ${}^{\bullet}OH$ then decomposes organic carbonates, such as lithium formate and lithium

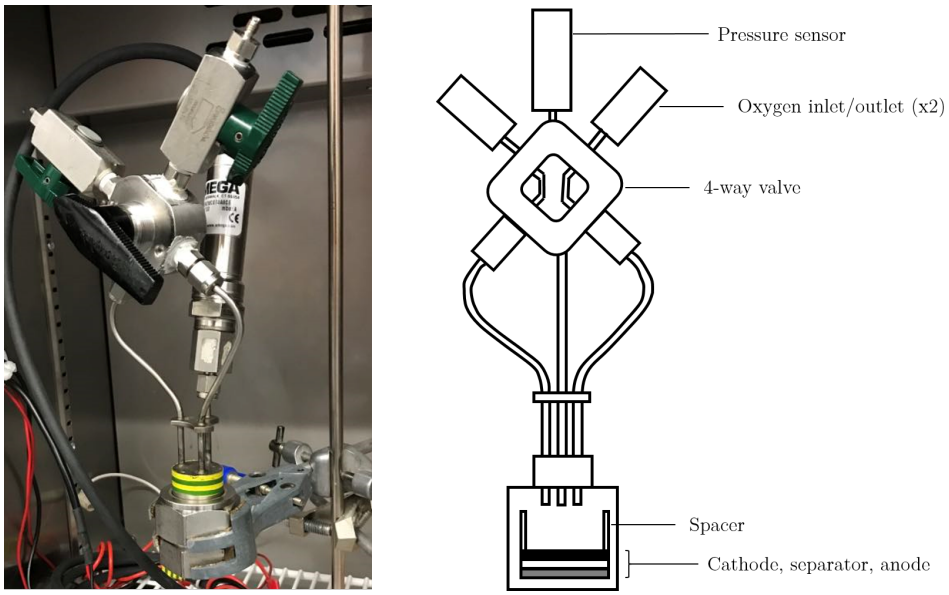


Figure 2.14: Cell setup for pressure monitoring experiments. (left) Image of the pressure cell as assembled in the incubator. (right) Schematic of the pressure cell

acetate, into stoichiometric amounts of CO_2.[25]

2.3.11 Pressure Monitoring

Monitoring the pressure changes in the headspace above a Li-O_2 cell during operation can provide important information on the Faradaic efficiency of the ORR and OER.[27] The number of electrons transferred per molecule of O_2 consumed or released can be calculated by using the ideal gas law:

$$PV = nRT \tag{2.18}$$

where P is the pressure, V is the volume of the head space, n is the amount of substance (moles), R is the ideal gas constant and T is the temperature. The amount of substance, n, can be calculated from Faraday's Law of Electrolysis:

$$Q = mnF \tag{2.19}$$

where Q is the charge passed ($= current \times time$), m is the amount of substance in moles, n is the number of electrons transferred per mole of substance formed and F is Faraday's constant (96485 C mol^{-1}). Of course, without monitoring which gases are

released during charge, it is impossible to say whether it is Li_2O_2 that is being oxidised or other products, such as Li_2CO_3. However, this can be achieved with techniques such as DEMS.

In a typical pressure monitoring experiment a Swagelok-type cell is assembled with a pressure transducer as shown in Figure 2.14. The cell is assembled with an oxygen inlet and outlet that can be closed with a quarter-turn valve. A spacer is used in the cell to ensure the headspace is large enough that changes in pressure due to the formation and decomposition of Li_2O_2 do not cause pressure changes that exceed the measurable range of the transducer. The pressure transducer undergoes a change in potential with a change in pressure and can be monitored with a potentiostat. The cell reaction can also be controlled with a potentiostat. To achieve accurate and reliable results several experimental procedures must be followed. For example, the temperature of the cell must be carefully controlled and monitored. From Equation 2.18 it can be seen that an increase in T will cause a proportional increase in P and give artificially high results for the amount of substance, n. The cell itself must be hermetically sealed so that any pressure lost due to leakage is negligible over the experimental timeframe. The volume of the headspace must be accurately known. To achieve this, a thoroughly dried cell was assembled and filled with oxygen. The cell was then assembled on a mass spectrometer which measured the flux of oxygen which could be converted into a molar quantity and hence volume.

2.4 References

[1] Dicks, A. L. The role of carbon in fuel cells. *Journal of Power Sources* **156**, 128–141 (2006).

[2] Wissler, M. Graphite and carbon powders for electrochemical applications. *Journal of Power Sources* **156**, 142–150 (2006).

[3] Thotiyl, M. M. O., Freunberger, S. A., Peng, Z. & Bruce, P. G. The Carbon Electrode in Nonaqueous Li-O_2 Cells. *Journal of the Americn Chemical Society* **135**, 494–500 (2013).

[4] Gao, X., Chen, Y., Johnson, L. & Bruce, P. G. Promoting solution phase discharge in Li-O_2 batteries containing weakly solvating electrolyte solutions. *Nature Materials* **15**, 882–888 (2016).

[5] Gao, X., Chen, Y., Johnson, L. R., Jovanov, Z. P. & Bruce, P. G. A rechargeable lithium–oxygen battery with dual mediators stabilizing the carbon cathode. *Nature Energy* **2**, 17118 (2017).

[6] Ko, Y. *et al.* Biological Redox Mediation in Electron Transport Chain of Bacteria for Oxygen Reduction Reaction Catalysts in Lithium–Oxygen Batteries. *Advanced Functional Materials* **29**, 1805623 (2019).

[7] Mahne, N. *et al.* Singlet oxygen generation as a major cause for parasitic reactions during cycling of aprotic lithium-oxygen batteries. *Nature Energy* **2**, 1–9 (2017).

[8] Schwenke, K. U., Metzger, M., Restle, T., Piana, M. & Gasteiger, H. A. The Influence of Water and Protons on Li_2O_2 Crystal Growth in Aprotic Li-O_2 Cells. *Journal of the Electrochemical Society* **162**, A573–A584 (2015).

[9] Meini, S., Piana, M., Tsiouvaras, N., Garsuch, A. & Gasteiger, H. A. The Effect of Water on the Discharge Capacity of a Non-Catalyzed Carbon Cathode for Li-O_2 Batteries. *Electrochemical and Solid-State Letters* **15**, A45–A48 (2012).

[10] Fischer, K. Neues Verfahren zur mdanalytischen Bestimmung des Wassergehaltes von Fllissigkeiten und festen Kgrpern. *Angewandte Chemie* **28**, 394–396 (1935).

[11] Schöffski, K. & Strohm, D. *Karl Fischer Moisture Determination* (John Wiley Sons, Ltd, 2006).

[12] Faraji Rad, Z., Prewett, P. D. & Davies, G. J. High-resolution two-photon polymerization: the most versatile technique for the fabrication of microneedle arrays. *Microsystems and Nanoengineering* **7** (2021).

[13] Göppert-Mayer, M. Über elementarakte mit zwei quantensprüngen. *Annalen der Physik* **401**, 273–294 (1931).

[14] Ul-Hamid, A. *A Beginner's Guide to Scanning Electron Microscopy* (Springer Cham, 2018).

[15] Golstein, J. I. *et al. Scanning Electron Microscopy and X-Ray Microanalysis* (Springer New York, New York, 2017).

[16] Larkin, P. *Infrared and Raman Spectroscopy: Principles and Spectral Interpretation* (Elsevier, Saint Louis, 2011).

[17] Glusker, J. P. & Trueblood, K. N. *Crystal Structure Analysis: A Primer* (Oxford University Press, Oxford, 2010).

[18] Hammond, C. *The basics of Crystallography and Diffraction* (Oxford University Press, Oxford, 2015).

[19] Hollas, J. M. *Modern Spectroscopy* (John Wiley & Sons, Chichester, 1995).

[20] Hossain, R., Dickinson, J. J., Apblett, A. & Materer, N. F. Detection of Hydrogen Peroxide in Liquid and Vapors Using Titanium(IV)-Based Test Strips and Low-Cost Hardware. *Sensors* **22** (2022).

[21] Webb, P. A. & Orr, C. *Analytical Methods in Fine Particle Technology* (Micromeritics Instrument Corp, 1997).

[22] Brunauer, S., Deming, L. S., Deming, W. E. & Teller, E. On a Theory of the van der Waals Adsorption of Gases. *Journal of the American Chemical Society* **62**, 1723–1732 (1940).

[23] Thommes, M. *et al.* Physisorption of gases, with special reference to the evaluation of surface area and pore size distribution (IUPAC Technical Report). *Pure and Applied Chemistry* **87**, 1051–1069 (2015).

[24] Washburn, E. W. Note on a Method of Determining the Distribution of Pore Sizes in a Porous Material. *Proceedings of the National Academy of Sciences* **7**, 115–116 (1921).

[25] Schafzahl, B. *et al.* Quantifying Total Superoxide, Peroxide, and Carbonaceous Compounds in Metal-O_2 Batteries and the Solid Electrolyte Interphase. *ACS Energy Letters* **3**, 170–176 (2018).

[26] Bruckenstein, S. & Gadde, R. R. Use of a Porous Electrode for in situ Mass Spectrometric Determination of Volatile Electrode Reaction Products. *Journal of the American Chemical Society* **93**, 793–794 (1971).

[27] Lepoivre, F., Grimaud, A., Larcher, D. & Tarascon, J.-M. Long-Time and Reliable Gas Monitoring in Li-O_2 Batteries via a Swagelok Derived Electrochemical Cell. *Journal of the Electrochemical Society* **163**, A923–A929 (2016).

3

Gas Diffusion Polymer as a Dual Purpose Binder

Contents

3.1 Introduction 101
3.2 Experimental 102
3.3 Results and Discussion 105
3.3.1 Structural Characterisation of the Pristine GDE 105
3.3.2 Optimisation of the GDE Composition and Thickness 110
3.3.3 Rate Analysis and Li_2O_2 Distribution 112
3.3.4 Visualisation of the Discharged GDE 116
3.3.5 Chemical Characterisation of the Discharge Product 118
3.4 Conclusion 122
3.5 References 123

3.1 Introduction

Efficient utilisation of high-capacity gas diffusion electrodes (GDEs) for Li-O_2 batteries face a significant obstacle in the form of O_2 mass transport.[1–3] A GDE for Li-O_2 batteries must transport oxygen sufficiently rapidly throughout a porous structure several hundred microns thick to achieve high discharge capacities at practical discharge rates. However, previous studies have shown that the Li_2O_2 discharge product is predominantly formed

at the GDE/gas interface and is not distributed throughout the electrode, indicating poor O_2 mass transport.[4–6] This leads to poor utilisation of the electrode volume for Li_2O_2 storage and poor cell performance.

The GDE commonly comprises a conductive carbon bound together with a polymer.[7–9] Carbon is typically preferred as the material of choice due to its conductivity, affordability, low mass, and its capacity to create porous structures that can be saturated with electrolyte, serving as effective storage for Li_2O_2. High surface area carbons, such as Ketjen Black, achieve the highest discharge capacities.[10] Likewise, configurations possessing significant pore volume within the mesopore/macropore range attain enhanced discharge capacities, as they can accommodate larger amounts of Li_2O_2 while simultaneously avoiding hindrances to ongoing O_2 mass transport.[7,11,12] Perfluorinated polymers, such as polytetrafluoroethylene (PTFE), are commonly used as binders due to their chemical and electrochemical stability.[13]

Here, a GDE for the Li-O_2 cell that can store 30 mAh cm^{-2} at a rate of 1 mA cm^{-2} in a 300 μm thick electrode is reported. This corresponds to an electrode with a specific energy of 1465 Wh kg^{-1} based on the mass of the electrode + electrolyte within the electrode volume + mass of Li_2O_2 formed and an energy density of 2650 Wh L^{-1} calculated from the volume of the electrode at the end of discharge and the integrated area underneath the discharge curve. These numbers can be compared with a typical Li-ion cathode (in this case Li-rich NMC), 1100 Wh kg^{-1}(cathode + electrolyte) and 1550 Wh L^{-1}(cathode). The GDE reported here employs a perfluorinated polymer which possesses enhanced O_2 transport properties. The polymer serves the dual purpose of binding the carbon together while delivering O_2 through the volume of the GDE.

3.2 Experimental

200 mg of Ketjen Black/Teflon AF2400 GDE material was prepared by dissolving Teflon AF2400 (Sigma) in Perfluoro(methylcyclohexane) (Sigma, technical grade, 90%). The carbon material, Ketjen Black, was added to the resulting solution and stirred at 70 °C until dry. The resulting agglomeration of Ketjen Black/Teflon AF2400 was weighed out

and pressed into 5 mm disks at 250 MPa using a die set and hydraulic press (Specac).

200 mg of Ketjen Black/PTFE GDE material was prepared by mixing carbon with the desired amount of 10 wt. % dispersion of PTFE (Sigma) and making up to 15 mL with 4:1 MilliQ water to isopropyl alcohol solution. The resulting mixture was stirred at 70 °C until dry. The Ketjen Black/PTFE agglomeration was weighed and pressed into 5 mm disks at 250 MPa using a die set and hydraulic press (Specac).

Electrochemical measurements were carried out using a Swagelok-type cell as detailed in 2.3 using 1 M Lithium bis(trifluoromethanesulfonyl)imide (LiTFSI) (Sigma, 99.95 %) in 1,2-dimethoxyethane (DME) (Sigma, 99.9 %) with 50 mM 2,5-Di-tert-butyl-1,4-benzoquinone (DBBQ) (Sigma, 99 %) electrolyte. The DME solvent was dried over molecular sieves to <10 ppm water before use as measured by Karl-Fischer titration. The cells were assembled with a partially discharged $Li_{(1-x)}FePO_4$ anode. The $LiFePO_4$ anode acts as counter/reference electrodes by maintaining a stable voltage of 3.45 V vs Li^+/Li and is also the source of Li^+ ions during discharge. Two polypropylene separators (Celgard® 2500) are utilised along with a stainless steel mesh used as a current collector. Electrochemical measurements were carried out using a Biologic VMP3 Multichannel Potentiostat. Before discharge, the cells were purged with oxygen (BOC, zero grade) through a Big Moisture Trap (Agilent) and allowed to equilibrate for 3 hours.

Pressure cell measurements were carried out using 40 wt. % Teflon AF2400/Ketjen Black as the GDE and partially discharged $Li_{(1-x)}FePO_4$ as the anode. The electrolyte was 50 mM DBBQ and 1 M LiTFSI in DME. A pressure sensor (Omega Engineering) was connected to the headspace of a cell to monitor the change in pressure during linear sweep voltammetry (LSV). The cell was assembled in an Ar-filled glovebox and purged with O_2 through a Big Moisture Trap. The cell was allowed to equilibrate for 6 hrs in an incubator maintained at 25 °C (Labcold) to avoid any pressure change due to temperature fluctuation.[14] LSV was run at 5.5 mV s^{-1} between open circuit potential to -1 V vs Li^+/Li. Raman spectra of the discharged GDEs were collected with a Renishaw InVia spectrometer equipped with a diode laser (λ = 785 nm). The

discharged GDEs were retrieved from the discharged cell, washed with DME, and dried to remove any residue electrolyte. The discharged GDEs were sealed between two glass plates under an Ar atmosphere before measurement. Powder X-ray diffraction (PXRD) data was collected with a Rigaku MiniFlex diffractometer with Cu $K_{\alpha 1}$ inside an Ar-filled glovebox. Discharged GDEs were washed and dried using DME and were loaded onto a low-background silicon holder for measurement. FT-IR spectra were collected on a Nicolet 6700 spectrometer (Thermo Fischer Scientific) in a N_2-filled glovebox and using a CsI beamsplitter. Discharged GDEs were ground in a pestle and mortar with CsI and formed into a pellet using a die set and hydraulic press. Spectra were collected in transmission mode between 250-4000 cm^{-1}.

Lithium peroxide depth-profiling data was collected using a microtome and UV-vis technique. The discharged GDE was washed and dried using DME. The discharged GDE was placed in a ParaFree Metal Base Mould 15 x 15 x 4 mm (TAAB) and infiltrated with molten paraffin wax (Paraplast X-TRA, Merck)) under vacuum and affixed to a cassette (TAAB). The affixed sample was then cooled to (-10 °C) to ensure clean and reproducible slices could be taken using an RM2125 RTS manual microtome (Leica Biosystems). Each slice was submerged in a known volume of 7.5% $TiOSO_4/H_2SO_4$ solution. UV-vis data was collected with an Evolution 220 spectrophotometer (Thermo Scientific^{TM}). The amount of Li_2O_2 in each slice was calculated by comparing it with a calibration curve of known Li_2O_2 concentrations.

BET surface area analysis was carried out using a Micromeritics 3Flex Adsorption Analyser. Samples were dried under vacuum in a heated antechamber at 70 °C overnight before analysis and further dried with *in-situ* degassing once assembled on the analyser. Mercury intrusion porosimetry (MIP) was carried out on an Autopore IV 9500 (Micromeritics). The samples were dried under vacuum at 70 °C overnight before transferring to a 3 cc penetrometer (Micromeritics). Porosimetry was carried out between 14.7 psia and 33,000 psia, corresponding to pores between 100 µm and 6 nm. Scanning electron microscopy (SEM) images and energy dispersive X-ray (EDX) spectra were collected on a Zeiss Merlin Field Emission Scanning Electron Microscope. Samples

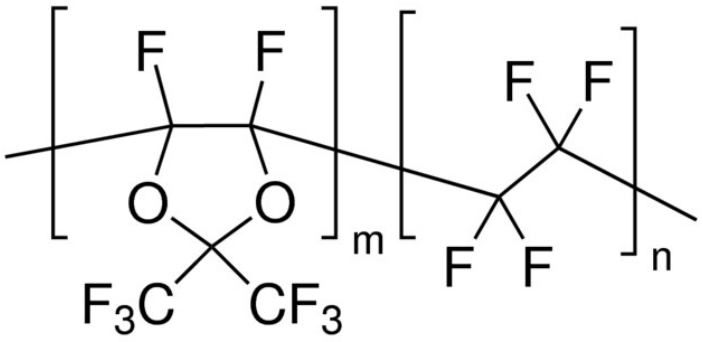


Figure 3.1: Structure of the gas diffusion polymer, Teflon AF2400. The gas diffusion polymer is a co-polymer of 4,5-difluoro-2,2-bis(trifluoromethyl)-1,3-dioxole (m, 87 % mol.) with tetrafluoroethylene (n, 13 % mol.).

were transferred into the SEM chamber via an air-sensitive holder to avoid exposure to the atmosphere.

3.3 Results and Discussion

3.3.1 Structural Characterisation of the Pristine GDE

The GDE is a porous composite of carbon (Ketjen Black) and a fluorocarbon polymer subsequently referred to as the gas diffusion polymer (GDP) with the structural formula poly[4,5-difluoro-2,2-bis(trifluoromethyl)-1,3-dioxole-co-tetrafluoroethylene], Figure 3.1.

The polymer shares a structural similarity with the established binder, polytetrafluoroethylene (PTFE), which is extensively and effectively employed in conjunction with carbon to fashion porous electrodes for Li-O_2 cells. The GDP belongs to a group of glassy amorphous polymers with a high fractional free volume, defined as the volume of the total mass not occupied by polymer chains, i.e., the gaps or pores occupied between polymer chains. The free volume elements occur at the molecular scale into which small diffusing molecules (i.e. oxygen) can enter. According to free volume theory, diffusion in the polymer membrane occurs due to the random redistribution of the free volume elements.[15] Polymers possessing a high free volume can rapidly transport gases, of which the GDP has the highest oxygen permeability out of any perfluorinated polymer.[16–19] The GDP was chosen for this work as it is a perfluorinated polymer with

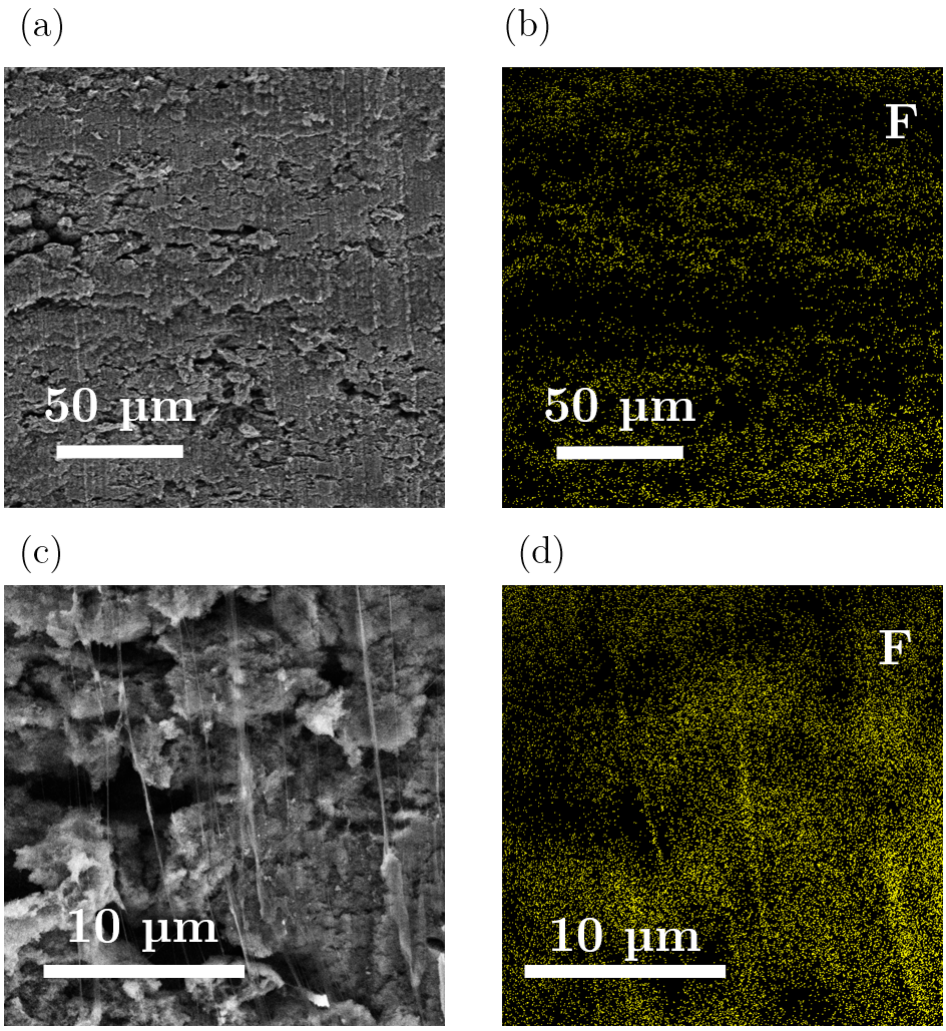


Figure 3.2: SEM and EDX mapping of cross-sections of the pristine gas diffusion electrode. (a) and (c) SEM images of the cross-sectioned gas diffusion electrode. (b) and (d) Fluorine EDX maps of the corresponding SEM images

a similar structure to PTFE, which is the most stable in Li-O_2 applications.[13,20]

The GDEs were formed by a solution process whereby the GDP was dissolved into a perfluorinated solvent (perfluoro(methylcyclohexane)), into which an appropriate mass of Ketjen Black was added, followed by heating and stirring until a dried agglomeration of material remained. The carbon/polymer mixture was then pressed into disks with a hydraulic press and die set, forming the GDEs. To assess the distribution of the polymer, scanning electron microscopy (SEM) combined with energy dispersive X-ray (EDX) spectroscopy was carried out; the results are shown in Figure 3.2.

In the pristine electrode (before any electrolyte has been added), the GDP is the only additive which contains fluorine; as such, the fluorine EDX analysis provides insight into

how the polymer is distributed. Figure 3.2(a) shows an SEM image of the cross-sectioned GDE showing a range of pore sizes and is typical of a GDE formed from a carbon black and polymer binder.[21] The corresponding fluorine EDX map in Figure 3.2(b) shows that the GDP is evenly distributed throughout the GDE. Figure 3.2 (c) provides a closer look at the GDE and clearly illustrates the formation of polymer fibres within the electrode. It should be noted that the fibres run from top to bottom in a straight line due to obtaining the cross-sections using a scalpel to cut the GDE, but the polymer fibres are expected to be formed in the GDE in random order. The corresponding EDX map in Figure 3.2(d) confirms that the fibres observed are the GDP, indicated by the strong fluorine EDX signal that overlaps with the corresponding fibre structures.

The surface area, porosity and pore size distribution of the GDE are all crucial factors which affect the discharge capacity in Li-O_2 batteries.[10,11,22,23] The Li_2O_2 discharge product is poorly soluble in most organic electrolytes and immediately precipitates as it is formed. As such, the Li_2O_2 must be stored in the porous network of the GDE. Similarly, Li_2O_2 is electronically insulating, and as it precipitates on the electrode surface, it prevents further charge transfer.[24] Therefore, high surface area and high porosity should lead to higher discharge capacities. The surface area of the GDEs was determined by N_2 adsorption/desorption spectroscopy, Figure 3.3, and analysed by Brunauer–Emmett–Teller (BET) theory, Section 2.3.7. The results are summarised in Table 3.1.

The adsorption/desorption isotherms for GDEs formed from 40 wt. % GDP and 10 wt. % PTFE are shown in Figure 3.3 (a) and the BET plots are shown in Figure 3.3 (b). Comparisons are made to GDEs fabricated from 90:10 mass ratios of Ketjen Black to PTFE as this is the commonly used composition in Li-O_2 studies.[25,26] The plots are typical for electrodes formed using KB, displaying Type H4 isotherms with a hysteresis, as seen elsewhere.[27] This type of N_2 adsorption/desorption isotherm is typical of carbons containing a large proportion of micro/mesopore volume.[28,29] There is little difference in the isotherms between each of the GDEs formed using the GDP or PTFE, showing that the carbon dominates the pore structure and surface area. The

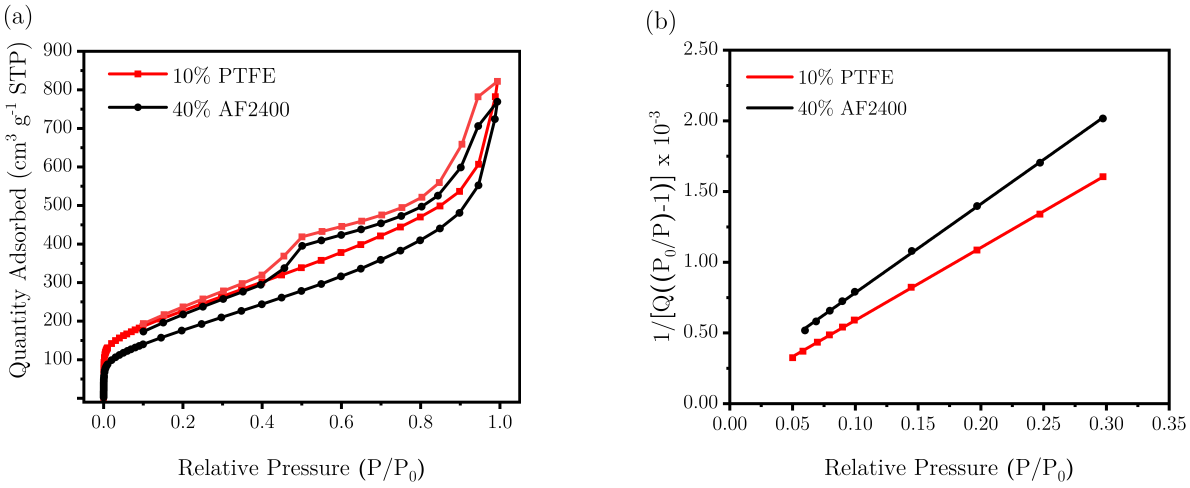


Figure 3.3: N_2 adsorption/desorption analysis for gas diffusion electrodes with 40 wt. % GDP or 10 wt. % PTFE. (a) N_2 adsorption/desorption isotherms for gas diffusion electrodes with 40 wt. % GDP (red) or 10 wt. % PTFE (black). (b) BET plots based on the isotherms in *(a)*.

surface areas are measured at 676.6 ± 4.1 m^2 g^{-1} and 834.4 ± 3.2 m^2 g^{-1} for 40 wt. % GDP and 10 wt. % PTFE GDEs respectively. The surface area of the GDEs is dominated by the Ketjen Black, which has a surface area of 1010.7 ± 3.8 m^2 g^{-1} as measured by BET. The addition of the polymer binders, which have a low surface area, and the formation of the GDEs by pressing into a pellet is expected to decrease the exposed surface area. Similarly, a lower surface area is expected for the GDEs formed from 40 wt. % GDP due to the higher ratio of binder to carbon. The BET data provides evidence that the increase in capacity observed with the GDP is not due to differences in the surface area between the GDEs, particularly as the BET surface area of the GDEs formed with 40 wt. % GDP is lower than that for 10 wt. % PTFE.

Mercury intrusion porosimetry (MIP) provides information on a sample's pore volume and size distribution. Measurements were carried out on GDEs formed from 40 wt. % GDP or 10 wt. % PTFE with KB, the results are shown in Figure 3.4.

There is little difference in the porosity and pore size distribution between the GDEs formed using 40 wt. % GDP or 10 wt. % PTFE, the results are summarised in Table 3.1. The porosity values between the two GDE formulations are almost identical at 61.7 % and 62.1 % for the GDP and PTFE GDEs, respectively. As the Li_2O_2 must be stored within the porous volume of the GDE, the maximum achievable capacity in both GDEs

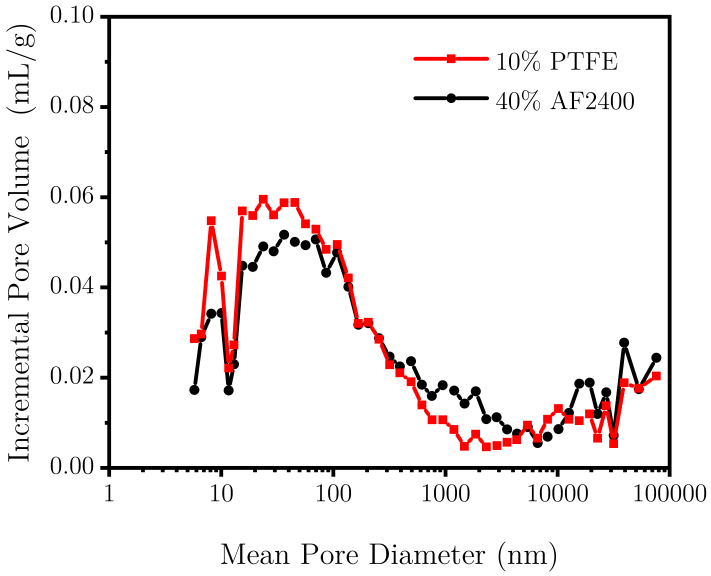


Figure 3.4: Pore size distribution analysis by mercury intrusion porosimetry. Mercury intrusion porosimetry comparison between 40 wt. % GDP (black line) and 10 wt. % PTFE (red line) gas diffusion electrodes

is similar if based on the porosity of the GDEs. There are subtle differences in the pore size distributions; for example, the median pore diameter by volume is 151.1 nm for the GDP electrodes, whereas it is 75.9 nm for the PTFE electrodes.

Similarly, the average pore diameter (the bulk of the porosity) is 40.5 nm for the GDP electrodes compared to 31.1 nm for the PTFE electrodes. The results from MIP support the BET data in Figure 3.3 and the SEM image in Figure 3.2, which all show significant mesopore volume. Although the values for the average pore diameter measured by MIP both lie within the range of mesopores, the larger pore diameter may afford the GDEs fabricated with the GDP some increased capacity. For example, Ding *et al.* observed an approximately 50 % increase in capacity in ordered mesoporous carbons with pore sizes 20 nm to 40 nm and a smaller increase in capacity of < 20 % between 40 nm and 60 nm, a smaller increase in capacity would be expected between 30 nm to 40 nm.[7] It should be noted, however, that their study utilised an extremely low mass loading and hence low thickness (< 1 mg cm^{-2}) and employed very low discharge currents of 0.05 mA or 50 mA g^{-1}.[7] O_2 mass transport would not be expected to be limiting in this case, particularly compared to the GDE thickness and discharge currents employed in the current work. The results from MIP indicate that the difference in discharge capacities

obtained in GDEs utilising the GDP or PTFE are not due to any significant differences in the porosity and pore size distributions.

	40 % GDP	**10 % PTFE**
BET Surface Area (m^2 g^{-1})	676.6 ± 4.1	843.4 ± 3.2
Porosity (%)	61.7	62.1
Median Pore Diameter - Volume (nm)	151.1	75.9
Median Pore Diameter - Area (nm)	12.4	11.4
Average Pore Diameter (nm)	40.5	31.1
Bulk Density (g mL^{-1})	0.46	0.47
Apparent Skeletal Density (g mL^{-1})	1.20	1.25

Table 3.1: Summary of the surface areas and pore structures for gas diffusion electrodes formed from 40 wt. % GDP or 10 wt. % PTFE with KB. Results are obtained from MIP and BET experiments

3.3.2 Optimisation of the GDE Composition and Thickness

The effect of varying the composition and thickness of the porous GDE is shown in Figure 3.5. All cells shown in Figure 3.5 are discharged in an electrolyte of 1 M LiTFSI in DME with 50 mM DBBQ at the rate of 2 mA cm^{-2}. The GDE expanded from a pristine thickness of 200 μm to 290 ± 16 μm after the addition of electrolyte, as measured by digital callipers. No further expansion occurred during the discharge process, regardless of the discharge capacity, as determined by the measured thickness at the end of discharge. A partially discharged $Li_{(1-x)}FePO_4$ is used as the anode instead of lithium metal to avoid possible degradation effects from the latter, a strategy employed previously to focus on the cathode.[30] The partially discharged $Li_{(1-x)}FePO_4$ has a stable voltage at 3.45 V vs Li^+/Li allowing for the voltage to be given versus Li^+/Li as the reference.

The effect of varying the composition is shown in Figures 3.5 (a) and (b). Here, the GDP increases in place of KB, between 10-40 wt. % GDP, while the GDE thickness is kept constant. The energy density is calculated from the GDE thickness at the end of the discharge and the integrated area underneath the discharge curve. The capacity and energy density of the GDE increases to a maximum of 40 wt. % GDP, where an

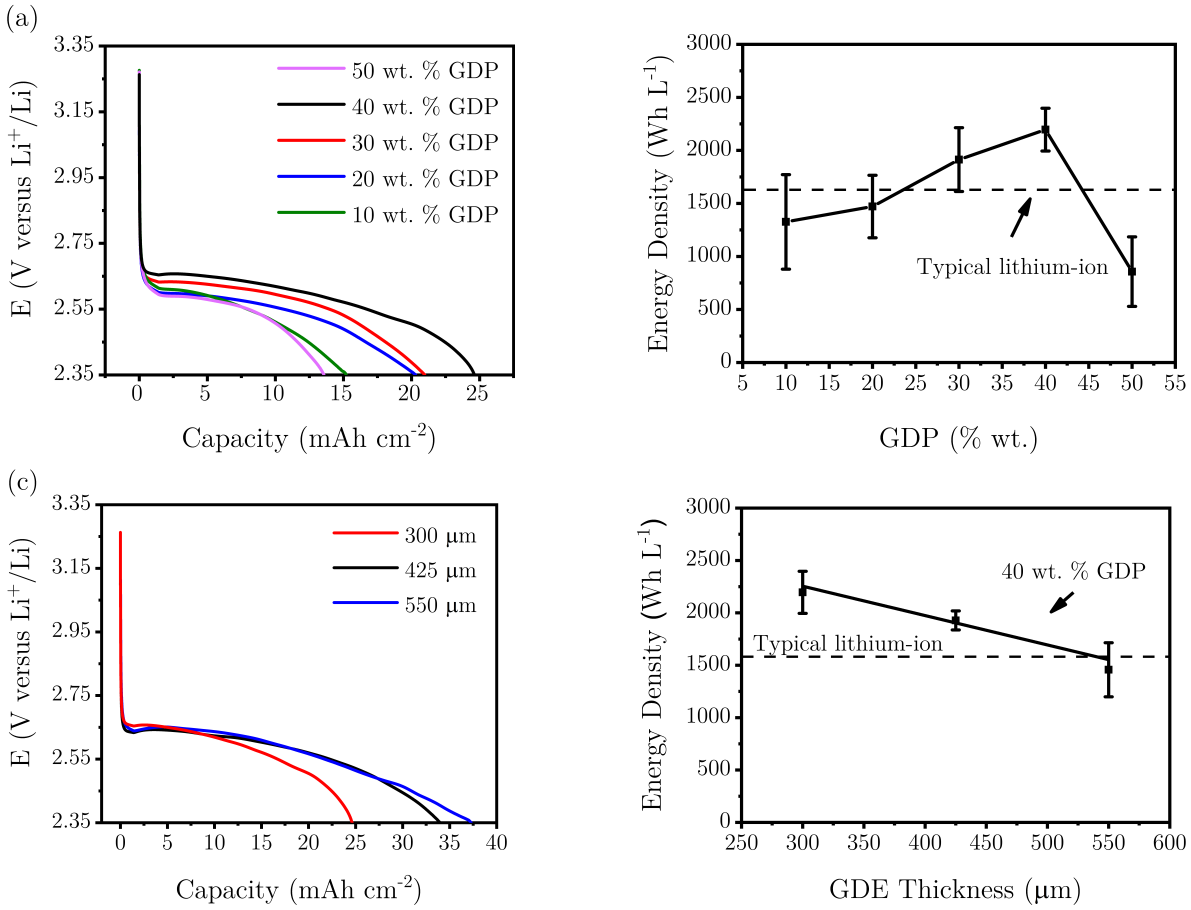


Figure 3.5: Discharge data and energy density plots showing that 40% wt. GDP with 60% wt. Ketjen Black at 300 μm is the optimal GDE formulation and thickness. (a) Representative discharge profiles of GDEs with various amounts of GDP (% wt.) (b) The corresponding energy densities with the discharge data collected in *(a)*. (c) Representative discharge profiles for GDEs fabricated with 40 % wt. GDP at varied thicknesses. (d) Energy densities of the GDEs discharged in *(c)*. The cells are discharged with 1 M LiTFSI in DME with 50 mM DBBQ. The error bars indicate one standard deviation.

energy density of 2200 Wh L^{-1} is achieved, calculated from the volume of the electrode after discharge and the integrated area underneath the discharge curve. This may be compared with a typical Li-ion cathode such as $LiNi_{0.8}Mn_{0.1}Co_{0.1}O_2$, which attains 1550 Wh L^{-1}(electrode), calculated from a cathode with a typical thickness of 125 μm, which delivers a capacity of 5 mAh cm^{-2} at 3.6 V. This is represented by the dashed line in Figure 3.5. The 60:40 mass ratio of KB to GDP is optimal in this case. This may represent a balance between sufficient carbon to ensure good electronic transport and sufficient GDP to ensure good O_2 transport. After increasing the GDP content to 50 wt. %, the capacity and energy density rapidly drop; this may be due to the passivation of the electrode by the GDP, which is not electronically conductive.

The effect of varying the thickness of the GDE between 300 - 550 μm is considered in Figures 3.5 (c) and (d). The composition of the GDE is kept constant at the 60:40 mass ratio of KB to GDP. Although the areal capacity increases from 25 to 37.5 mAh cm^{-2} with increasing thickness, this is more than offset by the increasing volume of the GDE at the end of discharge. This is reflected in the values for the energy density as a function of electrode thickness in Figure 3.5 (d), where the energy density decreases from 2200 to 1450 Wh L^{-1} when increasing the thickness from 300 to 550 μm. As the thickness of the GDE increases, oxygen mass transport limitations likely mean that the availability of oxygen in the depths of the cathode is insufficient to sustain the discharge reaction. Consequently, the porous volume available to form and store Li_2O_2 is poorly utilised, leading to the low energy densities measured. In this instance, the optimal GDE composition and thickness to achieve a high areal capacity and energy density was a 60:40 mass ratio of KB: GDP at a thickness of 300 μm at the end of discharge.

3.3.3 Rate Analysis and Li_2O_2 Distribution

The discharge profiles of the optimised GDEs at three different current densities are shown in Figure 3.6 (a) along with the corresponding energy density plot in Figure 3.6 (b). At 1 mA cm^{-2}, the optimised GDE achieves an energy density of 2650 Wh L^{-1}, which decreases to 2200 and 1500 Wh L^{-1} upon increasing the discharge rate to

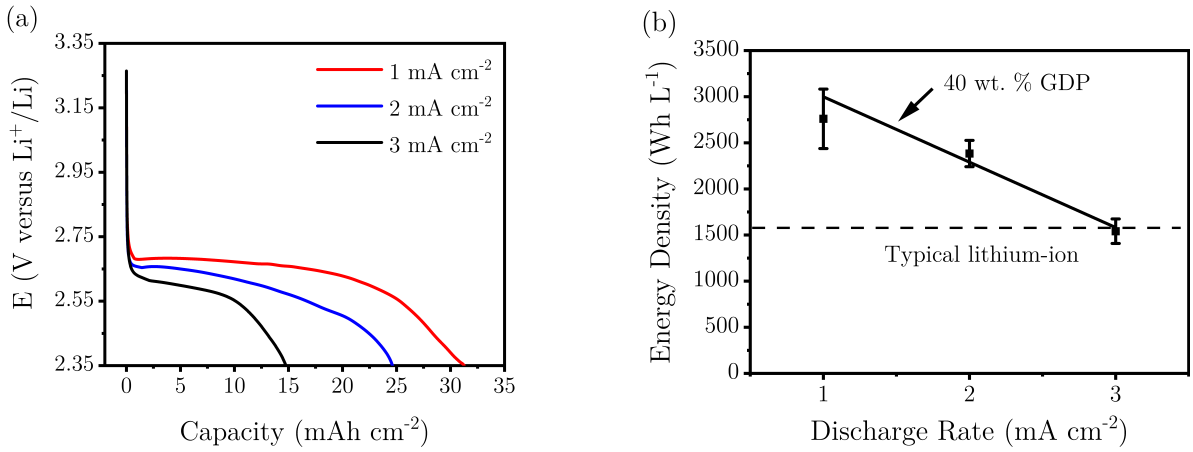


Figure 3.6: Discharge profiles and gas diffusion electrode energy densities at several discharge rates. (a) Representative discharge profiles at various rates for gas diffusion electrodes comprised 40 wt. % GDP / 60 wt. % KB, discharged with 1 M LiTFSI with 50 mM DBBQ in DME. (b) The corresponding energy densities associated with the discharge data collected in *a*

2 mA cm^{-2} and 3 mA cm^{-2} respectively. The discharge profiles in Figure 3.6 (a) show a decreasing capacity and increasing overpotential as the discharge rate increases. This is characteristic of Li-O_2 cells where increased rate leads to more nucleation and a more surface-like Li_2O_2 morphology, leading to more rapid polarisation and passivation of the electrode.[31–33] Similarly, at higher rates, O_2 is depleted more rapidly within the GDE, which can lead to higher overpotentials and uneven Li_2O_2 distribution.

The distribution of Li_2O_2 across the GDE from the gas/electrode interface towards the separator was determined for each of the three current densities. 20 μm cross sections of the GDEs were taken using a microtome, and the amount of Li_2O_2 was determined by titration with $TiOSO_4$. The results are shown in Figure 3.7, where depth into the cathode refers to the distance from the gas/electrode interface (at 0 μm) towards the separator. The y-axis is the amount of Li_2O_2 titrated in each cross-section normalised to the cross-section with the largest amount of Li_2O_2 titrated (as measured by UV-vis) for all three sets of data.

At 1 mA cm^{-2}, Li_2O_2 is well distributed, with significant Li_2O_2 forming at the GDE/separator interface, Figure 3.7 (a) and (b). As the current density increases, the amount of Li_2O_2 formed in the GDE decreases overall in line with the lower discharge capacities measured. As well as this, the quantity of Li_2O_2 formed in the region of the GDE/separator interface drops significantly as the discharge rate increases. These

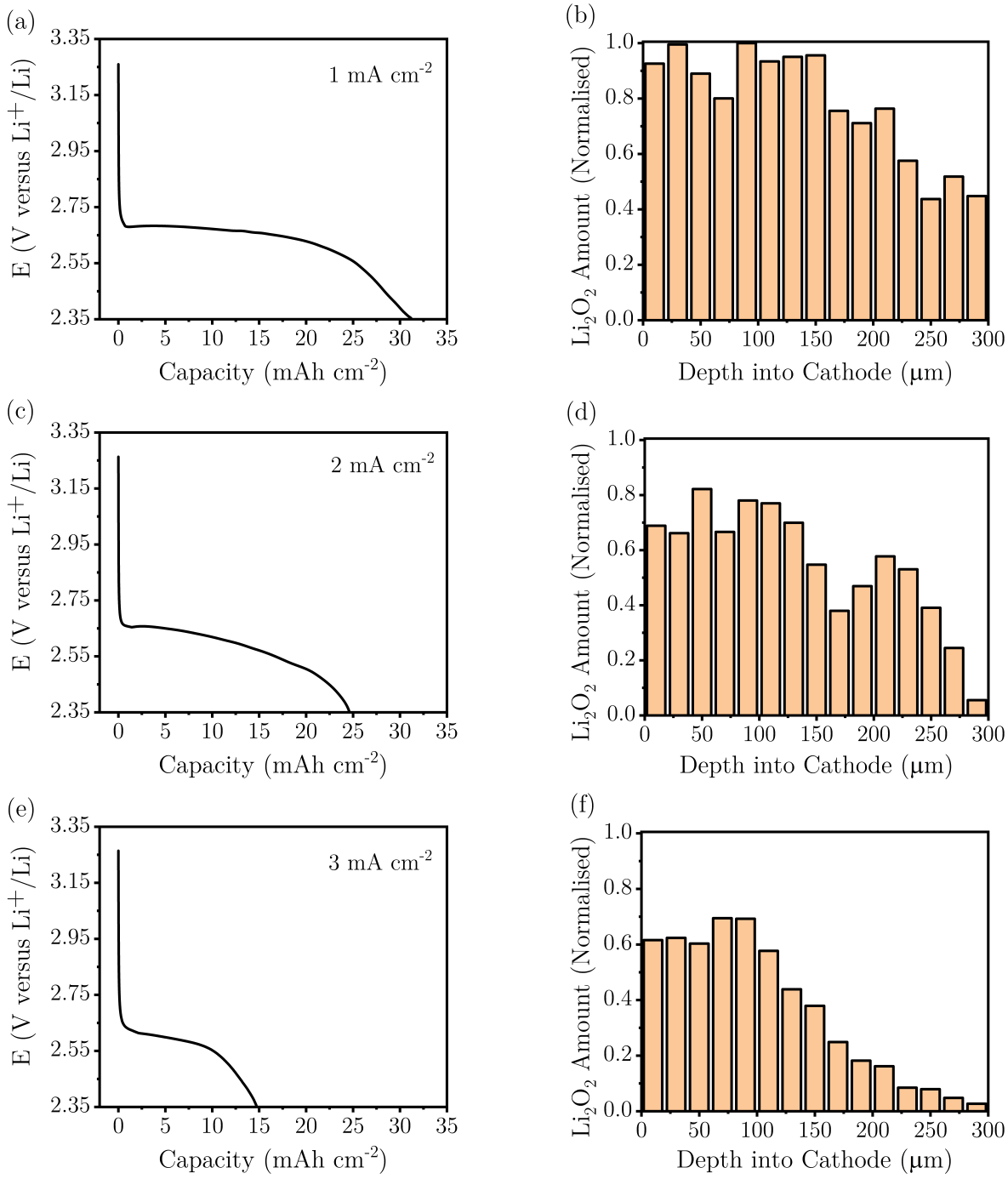


Figure 3.7: Discharge voltage profiles and the corresponding distribution of Li_2O_2 across the gas diffusion electrodes after discharge. (left) Load curves for Ketjen Black gas diffusion electrodes with 40 wt. % GDP discharged in 1 M LiTFSI in DME with 50 mM DBBQ, discharged between 1-3 mA cm^{-2}. (right) Distribution of Li_2O_2 across the gas diffusion electrodes. Each slice corresponds to 20 μm thickness

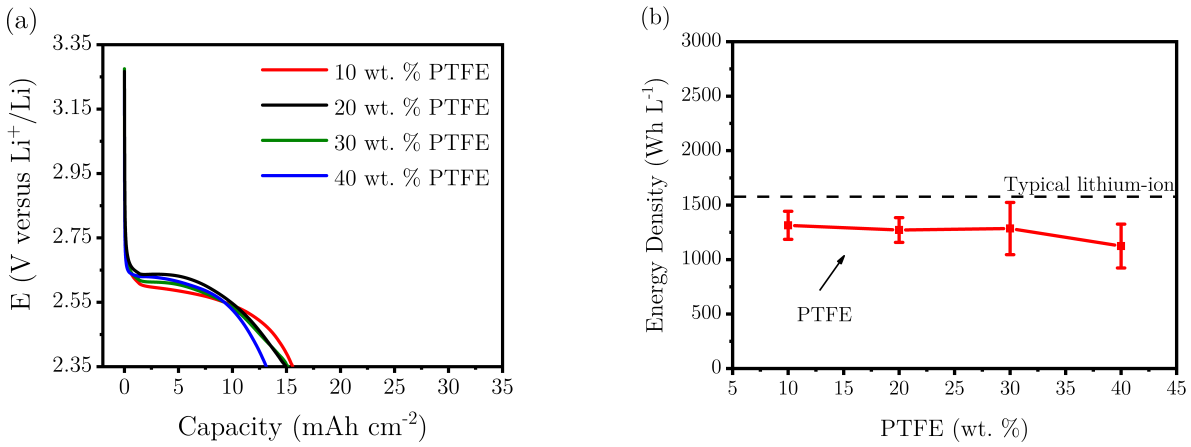


Figure 3.8: Discharge profiles and energy density plots for GDEs formed with varied amounts of PTFE. (a) Representative discharge profiles of GDEs comprised of PTFE employing 10-40 wt. % PTFE with KB, discharged at 2 mA cm^{-2} with 1 M LiTFSI with 50 mM DBBQ in DME. (b) The corresponding energy densities associated with the discharge data collected in *(a)*

results, especially the distribution of Li_2O_2 as a function of current density, are in accord with the rate of discharge being controlled primarily by O_2 mass transport through the electrode.[4,9,34–36].

The GDP was used because of its enhanced O_2 transport properties. The optimised GDE utilising the GDP was compared with similar porous electrodes based on the same carbon but using the widely employed polymer binder in Li-O_2 cells, polytetrafluoroethylene (PTFE), itself, of course, a fluorinated hydrocarbon. The GDP has similar mechanical properties and potential stability window but a much higher oxygen permeability (99000 cB) than PTFE (420 cB).[18,37] The commonly used composition is a 90:10 mass ratio of carbon: PTFE.[25,26] An exploration into the impact of altering these ratios revealed that different compositions do not yield a higher capacity, as depicted in Figure 3.8.

The observation that a higher proportion of polymer is advantageous when the polymer can transport O_2 is in accord with these observations. To demonstrate the superior performance and O_2 transport properties of the electrode formed with the GDP, cells with the 60:40 mass ratio of carbon: GDP was compared with those for 90:10 mass ratio of carbon: PTFE, Figure 3.9.

When discharged at 2 mA cm^{-2} under constant static pressure with no O_2 gas flow, the capacity of the 40 wt. % GDP electrode is much higher than that of the 10 wt.

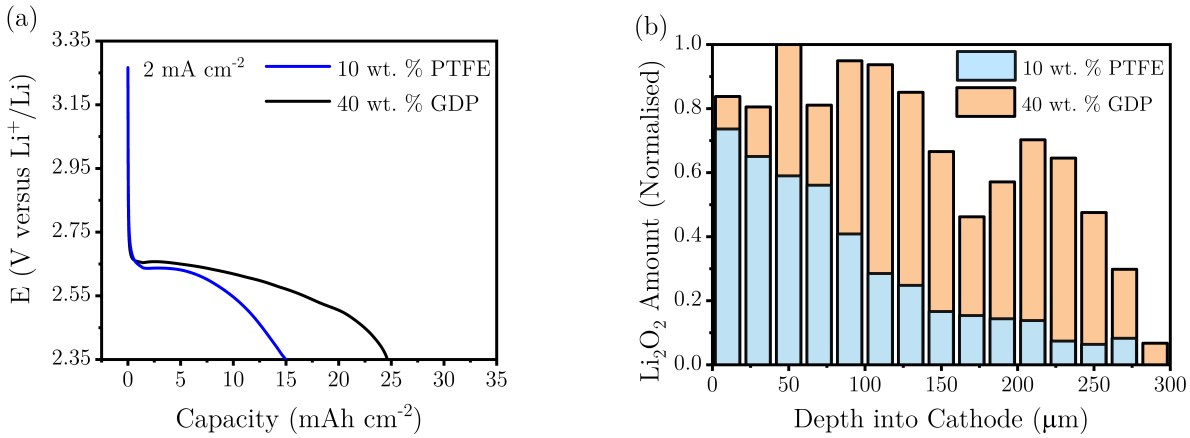


Figure 3.9: Discharge profiles and the corresponding distribution of Li_2O_2 in the gas diffusion electrodes after discharge, comparing the GDP with PTFE. (a) Load curves for gas diffusion electrodes with 40 wt. % GDP (black line) or 10 wt. % PTFE (red line) discharged in 1 M LiTFSI in DME with 50 mM DBBQ at 2 mA cm^{-2}. (b) Distribution of Li_2O_2 in 10 wt. % PTFE (red line) or 40 wt. % GDP (black line) gas diffusion electrodes, as measured by $TiOSO_4$ titration combined with microtomy, normalised to the highest absorbance value measured.

% PTFE electrode, Figure 3.9 (a). The distribution of Li_2O_2 across the two GDEs is compared in Fig. 3.9 (b). The amount of Li_2O_2 stored in the electrode drops rapidly, moving away from the GDE/gas interface in the case of PTFE, in accord with inferior O_2 transport compared with the GDP. This is compared to a more even distribution of Li_2O_2 with the GDP, which possesses much enhanced O_2 transport properties.

3.3.4 Visualisation of the Discharged GDE

SEM imaging was carried out on discharged GDEs with the optimised formulation of 40 wt. % GDP/KB at various rates of discharge. Figure 3.10 (a) shows the pristine electrode. The pristine GDE has a typical morphology for a GDE formed by mixing a carbon black with a polymer binder. A range of pore sizes can be observed with significant pore volume in the mesopore/macropore range, corroborating with MIP and BET data in Section 3.3.1. Figures 3.10 (b) and (c) show the oxygen and separator interfaces, respectively, of the GDE after discharging at 1 mA cm^{-2} until the cut-off potential. Spherical particles of $Li_2O_2 \sim 500$ nm in diameter can be observed at the oxygen interface, while a more film-like deposition can be seen at the separator interface. This aligns with the depth-profiling results, which indicate that Li_2O_2 is deposited evenly throughout the whole GDE. The Li_2O_2 deposited at the oxygen interface completely

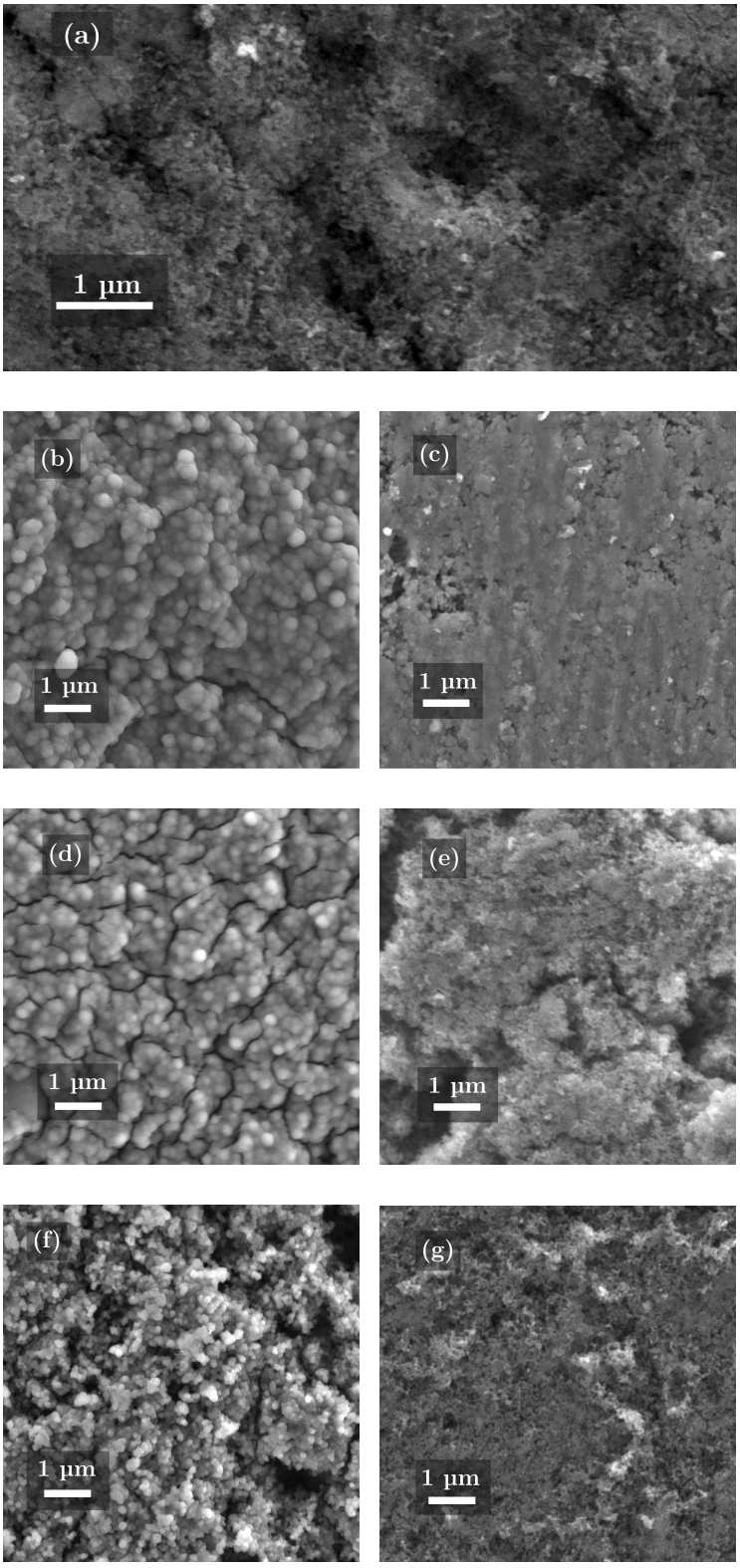


Figure 3.10: SEM images showing the Li_2O_2 morphology and distribution in gas diffusion electrodes with 40 wt. % GDP. The gas diffusion electrodes are discharged in 1 M LiTFSI in DME with 50 mM DBBQ. (a) Pristine gas diffusion electrode. (b, d, f) Oxygen interface of the discharge gas diffusion electrodes. (c, e, g) Separator interface of the discharged gas diffusion electrodes. (b, c) Discharged at 1 mA cm^{-2}.(d, e) Discharged at 2 mA cm^{-2}.(f, g) Discharged at 3 mA cm^{-2}.

coats the surface of the GDE and indicates that pore blocking leads to cell death at 1 mA cm^{-2}.

Figures 3.10 (d) and (e) show the oxygen and separator interfaces, respectively, of a fully discharged GDE at 2 mA cm^{-2}. At the oxygen interface, spherical particles $\sim$ 200 nm can be observed, which completely coat the surface of the GDE. The smaller Li_2O_2 particles formed at higher rates are in line with previous observations by Adams *et al.*[34] and Griffith *et al.*[31]. At higher rates, more frequent nucleation events occur on discharge leading to more numerous but smaller Li_2O_2 particles. The separator interface of the GDE has a similar appearance to the pristine GDE in Figure 3.10 (a), indicating that there is little Li_2O_2 deposition at the separator interface; these results also support those collected in the depth profiling experiments in Figure 3.7 (d).

Figures 3.10 (f) and (g) show the oxygen and separator interfaces of the GDE after full discharge at 3 mA cm^{-2}. Spherical Li_2O_2 particles of $\sim$ 100 nm can be observed at the oxygen interface. Much of the porosity of the GDE is still visible at the end of discharge, indicating that the failure mechanism at high rates may differ from that at lower rates. The GDE is likely starved of oxygen at high discharge rates due to the rapid consumption of oxygen in the electrolyte. The oxygen supply in the GDE cannot keep up with the discharge rate, causing the cell to polarise.

Similarly, as Li_2O_2 is formed on the GDE, the GDE is passivated towards charge transfer which also causes cell polarisation and low discharge capacity. The separator interface has an almost identical appearance to the pristine GDE in Figure 3.10 (a), indicating that no detectable Li_2O_2 formation has occurred. This aligns with the depth-profiling experiments showing no Li_2O_2 at the separator interface.

3.3.5 Chemical Characterisation of the Discharge Product

Pressure Cell

The discharge reaction in a cell utilising the optimised GDE was measured *operando* by monitoring the pressure change in the head-space above the cell during Linear Sweep Voltammetry (LSV). Pressure measurements during potential sweeps allow for

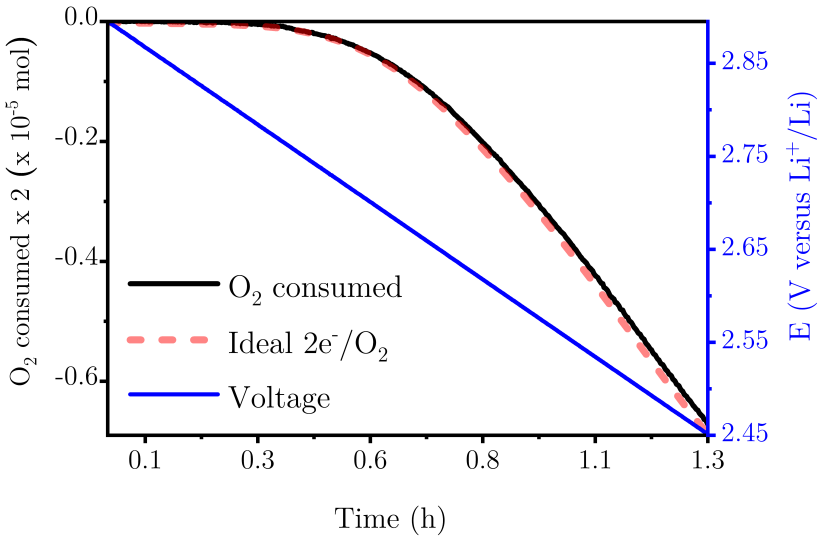


Figure 3.11: *Operando* pressure cell measurement showing 2.02 e⁻ per O_2 consumed. Voltage profile and corresponding *operando* pressure response in the headspace above a Li-O_2 cell with a gas diffusion electrode fabricated with 40 wt. % GDP. Recorded with 1 M LiTFSI in DME with 50 mM DBBQ under 1 atm O_2 at 20 ° C. The LSV is recorded at 5 mV s^{-1}.

the calculation of the number of electrons transferred per O_2 consumed. Figure 3.11 shows the amount of O_2 consumed during LSV (black line) compared to the amount of O_2 that would be consumed in an ideal $2e^-/O_2$ reaction (red dashed line), the blue line shows the cell voltage. In an ideal case, the lines representing the ideal $2e^-/O_2$ and O_2 consumed would exactly overlap. As can be seen in Figure 3.11, the amount of O_2 consumed and the the ideal $2e^-/O_2$ correspond well, with a slight deviation at higher overpotentials. The pressure drop due to oxygen consumption on the negative sweep during LSV corresponds to 2.02 e^-/O_2. This agrees well with the 2 e^-/O_2 expected for Li_2O_2 formation.[38–40] This result indicates that the polymer is stable in the presence of reactive intermediates such as O_2^-/LiO_2 or $^1O_2$, where any reaction would cause the number of electrons transferred per oxygen consumed to increase.

PXRD, FT-IR and Raman Characterisation

To confirm the presence of Li_2O_2 after discharge PXRD measurements of the discharged electrodes were taken. Figure 3.12 (a) shows the PXRD pattern collected with a fully discharged GDE of 40 wt. % GDP at 2 mA cm^{-2} with reference peak positions and intensities of Li_2O_2, LiOH and Li_2CO_3 taken from the ICSD database. The PXRD pattern exhibits peaks associated with Li_2O_2 and is absent of peaks associated with

LiOH and Li_2CO_3. This indicates that Li_2O_2 is the dominant crystalline solid product at the end of discharge.

Further characterisation was carried out by FT-IR and Raman spectroscopy, shown in Figures 3.12 (b) and (c) respectively. The FT-IR spectra indicate peaks associated with Li_2O_2 and again are absent of peaks associated with common side products such as Li_2CO_3, LiOH and Li-acetate. The Raman spectrum shows a low intensity and broad peak with a centre at 790 cm^{-1} related to Li_2O_2. The peak at 289 cm^{-1} may be associated with Li_2O_2 however this is a tenuous link as a peak would be expected at approximately 260 cm^{-1} as shown by the example Li_2O_2 Raman spectrum. The peak at lower wavenumbers is typically of lower intensity than the peak at 790 cm^{-1}, and in this instance may be below the noise level of the instrument. The peaks at 228 and 289 cm^{-1} and peak broadening at 790 cm^{-1} may be attributed to the formation of species such as $LiOH{\cdot}H_2O$ and the intermediate $LiOOH{\cdot}H_2O$, which can form via the following reactions:[41]

$$Li_2O_2 + 3H_2O \rightarrow LiOOH \cdot H_2O + LiOH \cdot H_2O \tag{3.1}$$

$$2LiOOH \cdot H_2O \rightarrow 2LiOH \cdot H_2O + O_2 \tag{3.2}$$

The above reactions are not expected to have occurred in the cell during operation due to the water control measures taken (typically the solvent is below 10 ppm). Water likely reacted with the Li_2O_2 during Raman acquisition due to imperfect sealing of the air-tight container.

Yield Measurement

The PXRD, FT-IR and Raman results in Figure 3.12 show that the predominant discharge product is Li_2O_2 and the pressure monitoring experiment shows good agreement with Li_2O_2 formation during discharge (Figure 3.11). To support these results and to show that there is little or no shuttling of DBBQ during operation, yield

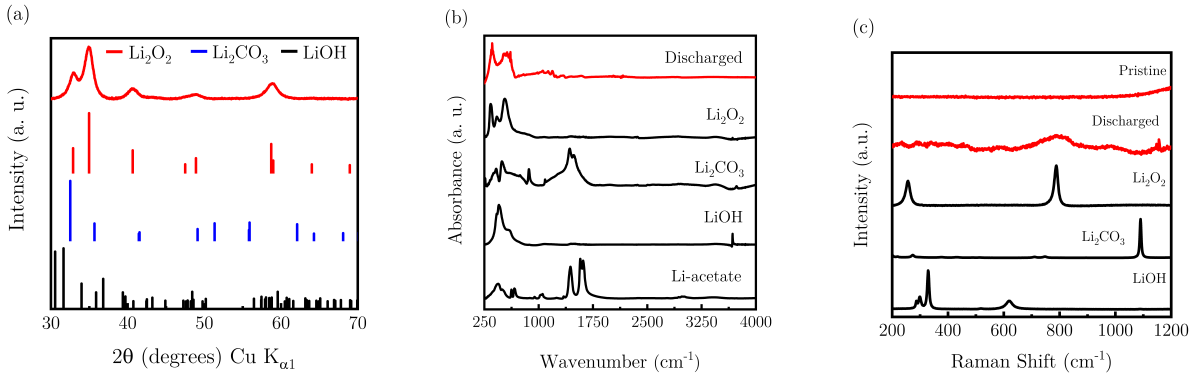


Figure 3.12: Characterisation of the discharged gas diffusion electrodes confirming that Li_2O_2 is dominant. a, PXRD, **b,** FTIR and **c,** Raman spectra of the discharged cathodes

Peak	Position	FWHM
1	228	40
2	289	25
3	370	116
4	458	27
5	587	30
6	790	147
7	970	84

Table 3.2: Peak positions and full-width half maximum values for Raman spectroscopy of the discharged cathode (Figure 3.12 (c)). The peaks are fitted using the peak analyser function in OriginPro 2018.

measurements were carried out to quantify the amount of Li_2O_2 at the end of discharge. The yield percentage of Li_2O_2 was between 80-85% of the discharge capacity for cells utilising 40 wt. % GDP electrodes. These values are in line with those previously reported by Gao *et al.* using an electrolyte of 1 M LiTFSI in DME with DBBQ.[30] A Li_2O_2 yield of 80-85 % is lower than what would be expected based on a 2.02 e^-/O_2 reaction as measured by LSV. This is indicative of a chemical reaction occurring between Li_2O_2 (which is formed in a $2e^-$ reaction) and the electrolyte, carbon or contaminants such as water. For example, Li_2CO_3 is formed spontaneously in contact with carbon by the reaction:

$$Li_2O_2 + C + \frac{1}{2}O_2 \rightarrow Li_2CO_3 \quad \Delta G = -542.4 kJmol^{-1} \tag{3.3}$$

$$2Li_2O_2 + C \rightarrow Li_2O + Li_2CO_3 \quad \Delta G = -533.6kJmol^{-1} \tag{3.4}$$

Li_2O_2 can also form LiOH in the presence of H_2O. These chemical reactions, which occur after the initial formation of Li_2O_2, result in lower than expected yields based on the discharge capacity and 2.02 e^-/O_2 measured via pressure monitoring.

3.4 Conclusion

This work has explored the use of a gas diffusion polymer, Teflon AF2400, for application in gas diffusion electrodes in Li-O_2 batteries. We have shown that a gas diffusion electrode which utilises 40 wt. % GDP with 60 wt. % Ketjen Black is the optimal formulation. This formulation provides a balance between oxygen mass transport and electrical conductivity. A GDE which is 300 μm thick after discharge provides a good balance between high areal capacity and high energy density, indicating efficient utilisation of the electrode volume. At larger thicknesses, the increase in capacity is offset by the increase in volume which is reflected in the decrease in energy density.

The effect of oxygen mass transport limitation was demonstrated by taking well-defined cross-sections of the discharged cathodes and quantifying the amount of lithium peroxide in each section. At lower rates where oxygen diffusion is not limiting, the Li_2O_2 is well distributed throughout the electrode. As the discharge rate is increased, the Li_2O_2 is distributed preferentially at the electrode/gas interface with poor utilisation of the electrode at the separator interface. These results are corroborated by SEM imaging of the gas/electrode and electrode/separator interfaces of fully discharged GDEs at various rates. A comparison of the Li_2O_2 distribution in GDEs employing the GDP and PTFE at the same discharge rate demonstrated the benefit of the GDP on oxygen mass transport.

Structural characterisation by BET and MIP show little difference between GDEs formed from the GDP or PTFE. This provides evidence to the assertion that the increased capacity observed when utilising the GDP is due to increased oxygen provision

in the GDE and not due to the effects of surface area or porosity.

Finally, the discharge reaction and discharge products are characterised by *in operando* pressure monitoring and PXRD, FTIR and Raman spectroscopy. The *in operando* pressure monitoring during LSV shows approximately 2 electrons per oxygen consumed on discharge, which is conducive to Li_2O_2 formation. The PXRD data shows that Li_2O_2 is the dominant crystalline phase and the FTIR and Raman show predominantly Li_2O_2 at the end of discharge. These results indicate that there are no major side reactions occurring with the GDP.

3.5 References

[1] Kwak, W.-J. *et al.* Lithium-Oxygen Batteries and Related Systems: Potential, Status, and Future. *Chemical Reviews* **120**, 6626–6683 (2020).

[2] Liu, T. *et al.* Current Challenges and Routes Forward for Nonaqueous Lithium-Air Batteries. *Chemical Reviews* **120**, 6558–6625 (2020).

[3] Wang, F., Li, X., Hao, X. & Tan, J. Review and Recent Advances in Mass Transfer in Positive Electrodes of Aprotic Li-O_2 Batteries. *ACS Applied Energy Materials* **3**, 2258–2270 (2020).

[4] Park, S. H. *et al.* Maximal Utilization of a High-Loading Cathode in Li-O_2 Batteries: A Double Oxygen Supply System. *ACS Applied Materials Interfaces* **11**, 30872–30879 (2019).

[5] Augustin, M., Vullum, P. E., Vullum-Bruer, F. & Svensson, A. M. Inside the electrode: Looking at cycling products in Li/O_2 batteries. *Journal of Power Sources* **414**, 130–140 (2019).

[6] Su, Z. *et al.* X-ray Nanocomputed Tomography in Zernike Phase Contrast for Studying 3D Morphology of Li-O_2 Battery Electrode. *ACS Applied Energy Materials* (2020).

[7] Ding, N. *et al.* Influence of carbon pore size on the discharge capacity of Li-O_2 batteries. *Journal of Materials Chemistry A* **2**, 12433–12441 (2014).

[8] Zhang, Y. *et al.* The use of mixed carbon materials with improved oxygen transport in a lithium-air battery. *Journal of Power Sources* **240**, 390–396 (2013).

[9] Beattie, S. D., Manolescu, D. M. & Blair, S. L. High-Capacity Lithium–Air Cathodes. *Journal of the Electrochemical Society* **156**, A44–A47 (2009).

[10] Meini, S., Piana, M., Beyer, H., Schwämmlein, J. & Gasteiger, H. A. Effect of Carbon Surface Area on First Discharge Capacity of Li-O_2 Cathodes and Cycle-Life Behavior in Ether-Based Electrolytes. *Journal of the Electrochemical Society* **159**, A2135–A2142 (2012).

[11] Ma, S. B., Lee, D. J., Roev, V., Im, D. & Doo, S.-G. Effect of porosity on electrochemical properties of carbon materials as cathode for lithium-oxygen battery. *Journal of Power Sources* **244**, 494–498 (2013).

[12] Nie, H. *et al.* Synthesis of a meso-macro hierarchical porous carbon material for improvement of O_2 diffusivity in Li-O_2 batteries. *RSC Advances* **4**, 17141–17145 (2014).

[13] Amanchukwu, C. V., Harding, J. R., Shao-Horn, Y. & Hammond, P. T. Understanding the chemical stability of polymers for lithium-air batteries. *Chemistry of Materials* **27**, 550–561 (2015).

[14] Lepoivre, F., Grimaud, A., Larcher, D. & Tarascon, J.-M. Long-Time and Reliable Gas Monitoring in Li-O_2 Batteries via a Swagelok Derived Electrochemical Cell. *Journal of the Electrochemical Society* **163**, A923–A929 (2016).

[15] Jacobson, S. H. Molecular modeling studies of polymeric gas separation and barrier materials: structure and transport mechanisms. *Polymers for Advanced Technologies* **5**, 724–732 (1994).

[16] Pinnau, I. & Toy, L. G. Gas and vapour transport properties of amorphous perfluorinated copolymer membranes based on 2,2-bistrifluoromethyl-4,5-difluoro-1,3-dioxole / tetrafluoroethylene. *Science* **109**, 125–133 (1996).

[17] Dlubek, G., Pionteck, J., Rätzke, K., Kruse, J. & Faupel, F. Temperature dependence of the free volume in amorphous teflon AF1600 and AF2400: A pressure-volume-temperature and positron lifetime study. *Macromolecules* **41**, 6125–6133 (2008).

[18] Bonder, V. I., Freeman, B. D. & Yampolskii, Y. P. Sorption of gases and vapors in an amorphous glassy perfluorodioxole copolymer. *Macromolecules* **32**, 6163–6171 (1999).

[19] Alentiev, A. Y., Yampolskii, Y. P., Shantarovich, V. P., Nemser, S. M. & Plate, N. A. High transport parameters and free volume of perfluorodioxole copolymer. *Journal of Membrane Science* **126**, 123–132 (1997).

[20] Nasybulin, E. *et al.* Stability of polymer binders in Li-O_2 batteries. *Journal of Power Sources* **243**, 899–907 (2013).

[21] Matsuda, S. & Yasukawa, E. Carbon-black-based self-standing porous electrode for 500 Wh/kg rechargeable lithium-oxygen batteries. *Cell Reports Physical Science* **2**, 100506 (2021).

[22] Wang, F., Kahol, P. K., Gupta, R. & Li, X. Experimental Studies of Carbon Electrodes With Various Surface Area for Li-O_2 Batteries. *Journal of Electrochemical Energy Conversion and Storage* **16**, 1–7 (2019).

[23] Guo, Z. *et al.* Ordered Hierarchical Mesoporous/Macroporous Carbon: A High-Performance Catalyst for Rechargeable Li-O_2 Batteries. *Advanced Materials* **25**, 5668–5672 (2013).

[24] Radin, M. D. & Siegel, D. J. Charge transport in lithium peroxide: Relevance for rechargeable metal-air batteries. *Energy & Environmental Science* **6**, 2370–2379 (2013).

[25] Read, J. Characterization of the Lithium/Oxygen Organic Electrolyte Battery. *Journal of the Electrochemical Society* **149**, A1190–A1195 (2002).

[26] Ulissi, U. *et al.* New Electrode and Electrolyte Configurations for Lithium-Oxygen Battery. *Chemistry - A European Journal* **24**, 3178–3185 (2018).

[27] Xia, C., Waletzko, M., Peppler, K. & Janek, J. Silica Nanoparticles as Structural Promoters for Oxygen Cathodes of Lithium-Oxygen Batteries. *Journal of Physical Chemistry C* **117**, 19897–19904 (2013).

[28] Thommes, M. *et al.* Physisorption of gases, with special reference to the evaluation of surface area and pore size distribution (IUPAC Technical Report). *Pure and Applied Chemistry* **87**, 1051–1069 (2015).

[29] Brunauer, S., Deming, L. S., Deming, W. E. & Teller, E. On a Theory of the van der Waals Adsorption of Gases. *Journal of the American Chemical Society* **62**, 1723–1732 (1940).

[30] Gao, X., Chen, Y., Johnson, L. & Bruce, P. G. Promoting solution phase discharge in Li-O_2 batteries containing weakly solvating electrolyte solutions. *Nature Materials* **15**, 882–888 (2016).

[31] Griffith, L. D., Sleightholme, A. E. S., Mansfield, J. F., Siegel, D. J. & Monroe, C. W. Correlating Li/O_2 cell capacity and product morphology with discharge current. *ACS Applied Materials Interfaces* **7**, 7670–7678 (2015).

[32] Yin, Y., Torayev, A., Gaya, C., Mammeri, Y. & Franco, A. A. Linking the Performances of Li-O_2 Batteries to Discharge Rate and Electrode and Electrolyte Properties through the Nucleation Mechanism of Li_2O_2. *Journal of Physical Chemistry C* **121**, 19577–19585 (2017).

[33] Liu, J., Khaleghi Rahimian, S. & Monroe, C. W. Capacity-limiting mechanisms in Li/O_2 batteries. *Physical Chemistry Chemical Physics* **18**, 22840–22851 (2016).

[34] Adams, B. D. *et al.* Current density dependence of peroxide formation in the Li-O_2 battery and its effect on charge. *Energy & Environmental Science* **6**, 1772–1778 (2013).

[35] Horstmann, B. *et al.* Rate-Dependent Morphology of Li_2O_2 Growth in Li-O_2 Batteries. *Journal of Physical Chemistry Letters* **4**, 4217–4222 (2013).

[36] Read, J. *et al.* Oxygen Transport Properties of Organic Electrolytes and Performance of Lithium/Oxygen Battery. *Journal of the Electrochemical Society* **150**, A1351–A1356 (2003).

[37] Sunshine, S. Method for extracting gases dissolved in a liquid. *International Patent WO* **98**, 35739 (1998).

[38] Liu, T. *et al.* The Effect of Water on Quinone Redox Mediators in Nonaqueous Li-O_2 Batteries. *Journal of the American Chemical Society* **140**, 1428–1437 (2018).

[39] Dutta, A. *et al.* Nanostructuring one-dimensional and amorphous lithium peroxide for high round-trip efficiency in lithium-oxygen batteries. *Nature Communications* **9**, 1–10 (2018).

[40] Ue, M., Asahina, H., Matsuda, S. & Uosaki, K. Material balance in the O_2 electrode of Li-O_2 cells with a porous carbon electrode and TEGDME-based electrolytes. *RSC Advances* **10**, 42971–42982 (2020).

[41] Tułodziecki, M. *et al.* The role of iodide in the formation of lithium hydroxide in lithium-oxygen batteries. *Energy and Environmental Science* **10**, 1828–1842 (2017).

4

A Gas Diffusion Electrode with O_2 Diffusion Channels

Contents

4.1 Introduction 126
4.2 Experimental 127
4.3 Results and Discussion 130
4.3.1 Gas Diffusion Electrode Design 130
4.3.2 O_2 Diffusion Channel Fabrication 137
4.3.3 Discharge Behaviour and Li_2O_2 Distribution in Channel GDEs 142
4.3.4 Characterisation of the Discharge Product 144
4.4 Conclusion 146
4.5 References 147

4.1 Introduction

To achieve a high energy density Li-O_2 battery at the cell and pack level, the amount of active material in the battery must be maximised compared to inactive components such as the cell packaging and air- and solvent-handling components.[1,2] This drives research towards achieving high energy densities in thick gas diffusion electrodes (GDEs) where O_2 mass transport becomes a limiting factor.[3–5] Several studies have shown that

separation of O_2 transport pathways from Li^+ and electron pathways can be beneficial in terms of achieving high discharge capacities in thicker GDEs.[6–11] Separate O_2 transport pathways allow for O_2 to be transported further into the GDE before reacting to form solid Li_2O_2. However, despite these works, energy densities and specific energies that compete with the best Li-ion cells have not been realised at practical discharge rates (> 1 mA cm^{-2}).

In this chapter, O_2 diffusion channels are introduced into the GDE, thus separating O_2 transport and Li^+ and electron transport pathways. The GDE achieves an energy density of 2670 Wh L^{-1} (calculated from the volume of the electrode at the end of discharge and the integrated area underneath the discharge curve) at 1 mA cm^{-2} in a GDE that is 500 μm thick, representing a 66 % increase in thickness of the GDE over that reported in the previous chapter. Measurement of the distribution of Li_2O_2 at the end of discharge using flat-disk GDEs is leveraged to inform placement of the O_2 diffusion channels. 3D-printing with two-photon polymerisation is utilised to form the O_2 diffusion channels, which allows for precision over the size and placement of the channels.

4.2 Experimental

Ketjen Black EC600-JD (MSE Supplies) was ground into a fine powder before treating under flow of Ar/H_2 at 900 °C (heat rate of 5 °C min^{-1}) for 12 hours. The carbon was placed in a split tube and heated in a tube furnace (Lenton). Heat treatment of the carbon under Ar/H_2 flow removes any reactive hydrophilic side groups on the carbon surfaces.[12] GDEs were prepared by mixing Ketjen Black with the appropriate mass of 10 wt. % PTFE (Merck) until an agglomerate was formed. A solution containing a known amount of Teflon AF2400 (Merck) in perfluoro(methylcyclohexane) (Merck) was then drop-cast onto the formed agglomerate. A sheet of carbon material was created by calendaring the agglomerate to the desired thickness before cutting it into 5 mm diameter GDE disks. The GDE disks were dried under vacuum in an antechamber held at 70 °C for 24 hours and stored in an Ar-filled glovebox before use.

Electrochemical measurements were carried out using a Swagelok-type cell, as shown in Figure 2.3. 1,2-dimethoxyethane (DME) (Merck, 99 %) was dried over molecular sieves to <10 ppm H_2O prior to use. The electrolyte was prepared by dissolving 50 mM 2,5-di-tert-butyl-1,4-benzoquinone (DBBQ) (TCI) into DME and drying over molecular sieves before adding 1 M Lithium bis(trifluoromethanesulfonyl)imide (LiTFSI) (Merck, 99.99 %). The cells were assembled with a GDE as the cathode, partially delithiated $LiFePO_4$ (MSE supplies) as the anode. The $LiFePO_4$ anodes act as counter/reference electrodes by maintaining a stable voltage of 3.45 V vs Li^+/Li. The $LiFePO_4$ is also the source of Li^+ ions during discharge. Two polypropylene separators (Celgard® 2500) are utilised along with a stainless-steel mesh as the current collector. Before discharge, the cells were purged with O_2 (BOC, zero grade) through a Big Moisture Trap (Agilent) and allowed to equilibrate for 3 hours. The electrochemical measurements were carried out using a Biologic VMP3 Multichannel Potentiostat.

BET surface area analysis was carried out using a Micromeritics 3Flex Adsorption Analyser. The GDEs were dried under vacuum in a heated antechamber at 70 °C overnight before analysis and dried with *in-situ* degassing at 70 °C once assembled on the analyser. Mercury intrusion porosimetry (MIP) was carried out on an Autopore IV 9500 (Micromeritics). The GDEs were dried under vacuum at 70 °C overnight before transferring to a 3 cc penetrometer (Micromeritics). Porosimetry was carried out between 14.7 psia to 33,000 psia corresponding to pores between 100 μm to 6 nm. Scanning electron microscopy (SEM) and energy dispersive X-ray (EDX) was carried out on a Zeiss Merlin Field Emission Scanning Electron Microscope. GDEs were transferred into the SEM chamber via an air-sensitive holder to avoid exposure to the atmosphere. Non-conductive samples, such as the 3D-printed templates, were sputter-coated with a conductive carbon layer using a PECS Gatan II system. Optical microscope images were recorded using a GXML 3030 optical microscope fitted with a GXCAM HiChrome-S mounted camera.

For post-cycling characterisation, the cells were disassembled in a glovebox. After discharge, the GDEs were rinsed with a small amount of DME before drying under

a high vacuum at 70 °C. Powder X-ray diffraction (PXRD) data was collected with a Rigaku MiniFlex diffractometer with Cu $K_{\alpha 1}$ inside an Ar-filled glovebox. The GDEs were washed and dried using DME and were loaded onto a low-background silicon holder for measurement. Fourier transform infrared (FT-IR) spectra was collected on a Nicolet 6700 spectrometer (Thermo Fischer Scientific) in a N_2-filled glovebox and using a CsI beamsplitter. The discharged GDEs were ground in a pestle and mortar with CsI and formed into a pellet using a die set and hydraulic press. Spectra were collected in transmission mode between 250-4000 cm^{-1}. Lithium peroxide depth-profiling data was collected using a microtome and UV-vis technique. The cathode was placed in a ParaFree Metal Base Mould 15 x 15 x 4 mm (TAAB) and infiltrated with molten paraffin wax (Paraplast X-TRA, Merck) under vacuum and affixed to a cassette (TAAB). The affixed sample was cooled to (-10 °C) to ensure clean and reproducible slices could be collected using an RM2125 RTS manual microtome (Leica Biosystems). Each slice was submerged in a known volume of 7.5 % $TiOSO_4/_2SO_4$ solution. UV-vis data was collected with an Evolution 220 spectrophotometer (Thermo Scientific^{TM})

TGA measurements were conducted on a Netzsch Jupiter STA 449 F3 thermogravimetric analysis instrument and a Netzsch Aeolos QMS 403 D mass spectrometer. A heating rate of 5 °C min^{-1} was applied under flow of Ar. GDEs with O_2 diffusion channels were fabricated by pressing a sacrificial 3D-printed template into a Ketjen Black/PTFE/GDP agglomerate before pyrolysing the templates. 3D printing was done on a commercially available femtosecond laser lithography system (Photonic Professional GT, Nanoscribe GmbH) using a commercially available photoresist (IP-S, Nanoscribe GmbH). The structures were designed using Computer-Aided Design (CAD) software (Netfabb Premium 2019, Autodesk) before converting to "Standard Tessellation Language" (.stl) files. The .stl files were imported into the print job development software (DeScribe, Nanoscribe GmbH), where the parameters for the print job were set. Pyrolysis of the 3D-printed templates pressed into the carbon/binder agglomerates was carried out in a tube furnace (Lenton) under Ar flow. The GDEs with the templates were placed in a split tube and heated at 5 °C min^{-1} to 410 °C and held for 15 mins and

then allowed to cool to room temperature.

4.3 Results and Discussion

4.3.1 Gas Diffusion Electrode Design

Structural Characterisation

In Chapter 3, the gas diffusion polymer (GDP), Teflon AF2400, was effectively utilised as a binder and O_2 transport conduit for Li-O_2 batteries. However, noticing the significant volume expansion on the addition of the electrolyte (200 μm to 290 $\pm$ 16 μm), the GDEs are fabricated herein with PTFE (5 wt. %), GDP (35 wt. %) and Ketjen Black (60 wt. %). In this case, the PTFE effectively binds the carbon and provides structural stability, while the GDP provides additional mechanical support whilst acting as an O_2 transport pathway. The detailed fabrication procedure is provided in the Experimental section. In short, an agglomeration of PTFE/GDP/KB is formed and calendered to the desired thickness. This approach produced GDEs with well-defined thicknesses.

Figure 4.1 shows the N_2 adsorption/desorption isotherm (a) and BET surface area analysis (b) of the GDEs. The adsorption/desorption isotherm exhibits Type II behaviour with a hysteresis, typical of microporous materials.[13] It is typical of the isotherms observed for Ketjen Black powder.[14] The surface area and porosity are primarily determined by the carbon, which in this case has a high surface area of 1010 $\pm$ 3.84 m^2 g^{-1} as also measured by BET. The BET surface area analysis of the formed GDEs yields a surface area of 779.9 $\pm$ 4.3 m^2 g^{-1}. Notably, this value is greater than that obtained in Chapter 3 by utilising a hydraulic press during fabrication (676.6 $\pm$ 4.1 m^2 g^{-1}), which is anticipated when considerable pressures are used to form the GDEs.

Figure 4.2 depicts the results of mercury porosimetry. The GDEs developed in this study exhibit a higher porosity of 77.8 %, surpassing the approximately 62 % achieved for the GDEs in Chapter 3. Furthermore, larger pore sizes are observed with the pore

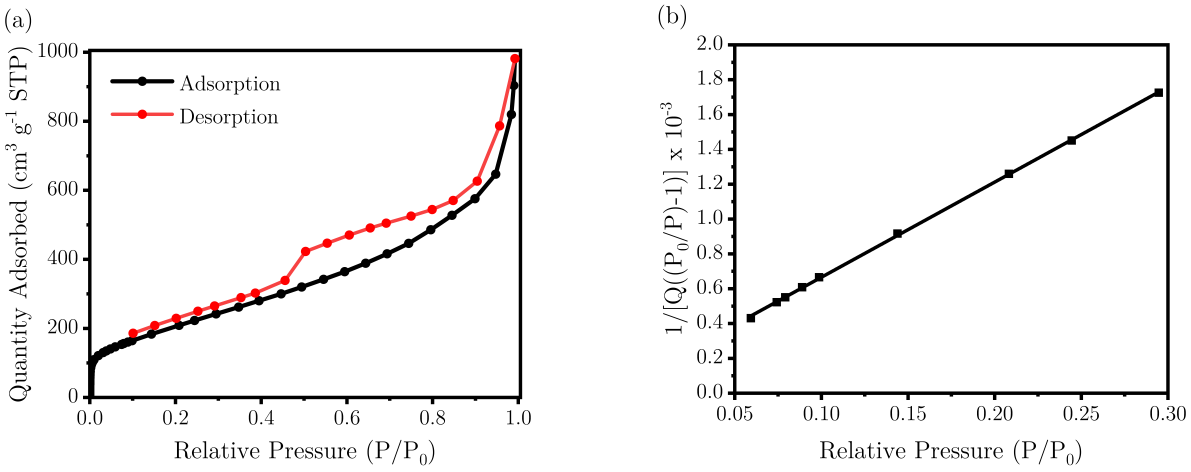


Figure 4.1: N_2 adsorption/desorption analysis for gas diffusion electrodes formed from 5 wt. % PTFE, 35 wt. % GDP and 60 wt. % KB. (a) N_2 adsorption/desorption isotherms. (b) BET plots based on the isotherms in *(a)*.

size distribution skewed towards larger sizes, resulting in an average pore diameter of 123.9 nm, in contrast to 30-40 nm previously reported in Chapter 3. Larger pore sizes have been demonstrated to promote O_2 mass transport and enable higher discharge capacities due to the pores remaining open for O_2 transport for longer into discharge.[15,16]

Figure 4.3 presents a cross-sectional view of the GDE, showing the GDE's structure and pore size distribution and is typical of a GDE formed using a carbon black and polymer binder.[17] The SEM image shows a range of pore sizes and high porosity, consistent with the findings from BET and MIP analyses. The range of pore sizes observed in the GDE favours its performance, with macropores being well-suited for promoting effective O_2 mass transport and a significant quantity of mesopores promoting the formation and storage of a large amount of Li_2O_2. The mercury porosimetry and BET analysis findings are summarised in Table 4.1.

Discharge Data and Li_2O_2 Distribution in Non-Channelled GDEs

Figure 4.4 displays the voltage versus capacity profiles for GDEs with varying thicknesses, discharged at 1 mA cm^{-2} in an electrolyte of 1 M LiTFSI and 50 mM DBBQ in DME. A partially delithiated $Li_{(1-x)}FePO_4$ anode is utilised to avoid instabilities introduced through the use of Li metal. The use of a $Li_{(1-x)}FePO_4$ anode for this purpose

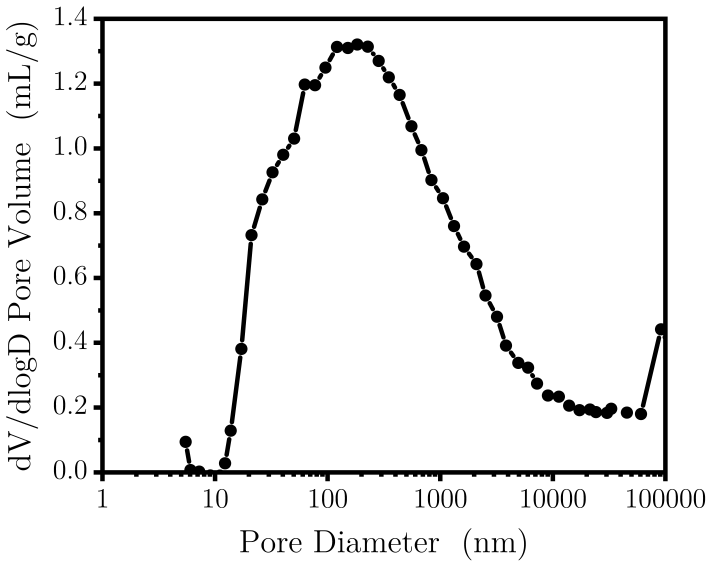


Figure 4.2: Pore size distribution analysis by mercury intrusion porosimetry. Mercury intrusion porosimetry of gas diffusion electrodes formed with 5 wt. % PTFE, 35 wt. % GDP and 60 wt. % KB

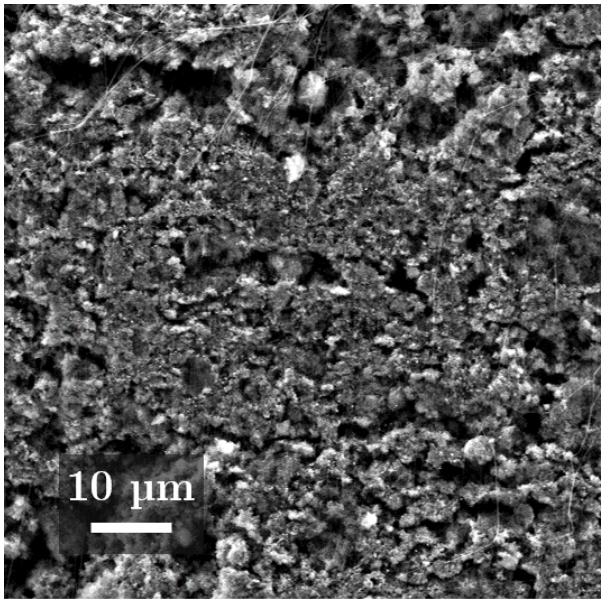


Figure 4.3: SEM image of the cross-section of a pristine gas diffusion electrode showing a range of pore sizes. The gas diffusion electrode is formed with 5 % PTFE, 35 % GDP and 60 % KB

	GDE
BET Surface Area (m^2 g^{-1})	779.7 ± 4.3
Porosity (%)	77.8
Median Pore Diameter - Volume (nm)	364.2
Median Pore Diameter - Area (nm)	41.7
Average Pore Diameter (nm)	123.9
Bulk Density (g mL^{-1})	0.27
Apparent Skeletal Density (g mL^{-1})	1.21

Table 4.1: Summary of MIP and BET results collected in Figure 4.1 and Figure 4.2

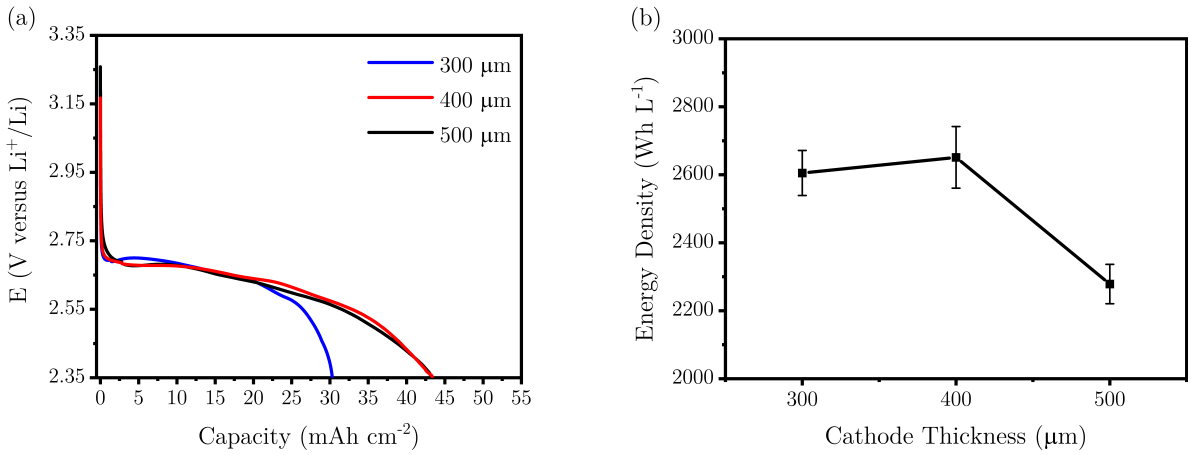


Figure 4.4: Discharge data and corresponding energy density plots for gas diffusion electrodes with varied thickness. (a) Discharge data measured at 1 mA cm^{-2} using 50 mM DBBQ with 1 M LiTFSI in DME. (b) Energy density is calculated from the integrated area under the discharge curve and the thickness of the gas diffusion electrode at the end of discharge in *(a)*.

has been reported previously, allowing for a focus on the cathode.[18–20]

Figure 4.4 (a) shows the discharge profiles. The discharge profiles exhibit typical discharge behaviour for Li-O_2 cells, with a gently sloping plateau region followed by rapid polarisation until cell death.[21–23] Figure 4.4 (b) presents the energy densities of the GDEs, which are determined by the thickness of the GDE at the end of discharge and the integrated areas under the discharge curves.

The discharge capacity achieved for a 300 μm thick GDE is 30 mAh cm^{-2}, corresponding to an energy density of ~2600 Wh L^{-1}. The energy density is calculated using the volume of the electrode at the end of discharge and the integrated area underneath the discharge curve (i.e. average voltage x discharge capacity). An increase in discharge capacity is observed when the GDE thickness is increased to 400 μm,

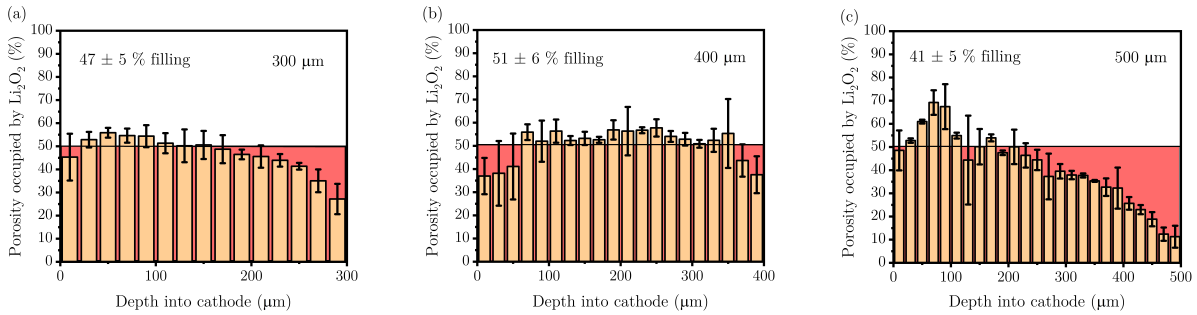


Figure 4.5: Li_2O_2 distributions corresponding to the data in Figure 4.4. (a, b, c) Li_2O_2 distributions for gas diffusion electrodes with thicknesses of 300, 400 and 500 μm, respectively. The distribution data was collected by microtoming the gas diffusion electrode into 20 μm slices and carrying out $TiOSO_4$/UV-vis titration. The Li_2O_2 filling values are calculated using the measured porosity, the discharge capacity and the crystalline density of Li_2O_2 (2.31 g cm^{-3}).

achieving a discharge capacity of ∼45 mAh cm^{-2}, which corresponds to a similar energy density at ∼2650 Wh L^{-1}. However, when the GDE thickness is further increased to 500 μm, the discharge capacity remains the same at ∼45 mAh cm^{-2}, but the energy density decreases to ∼2300 Wh L^{-1} due to the larger volume of the GDE, indicating poorer utilisation of the electrode porosity for the formation and storage of Li_2O_2.

Figure 4.5 shows the distribution of Li_2O_2 in the GDEs with varied thickness as discharged in Figure 4.4. The distribution of Li_2O_2 was measured by taking 20 μm slices of the discharged GDE using a microtome and submerging the slices in $TiOSO_4$. UV-vis spectra of the resulting solutions were then recorded; details are in the Experimental Section.

The x-axis shows the depth into the GDE, with 0 μm corresponding to the gas/electrode interface of the GDE. The y-axis represents the percentage of the porosity occupied by Li_2O_2 within that slice of the GDE. The amount of porosity occupied by Li_2O_2 is calculated by assuming 100 % of the capacity goes into forming Li_2O_2. The amount of Li_2O_2 in each slice is calculated based on the distribution measured by UV-vis titration. The porosity of each slice is taken as the porosity of the GDE as measured by MIP (78 %). The volume of Li_2O_2 is calculated based on the crystalline density (2.31 g cm^{-3}). Li_2CO_3 is known to form as the primary side product during discharge but has a similar density of 2.11 g cm^{-3}. The error bars represent one standard deviation from 3 repeat experiments.

The Li_2O_2 is distributed evenly in the 300 and 400 μm thick electrodes at the end

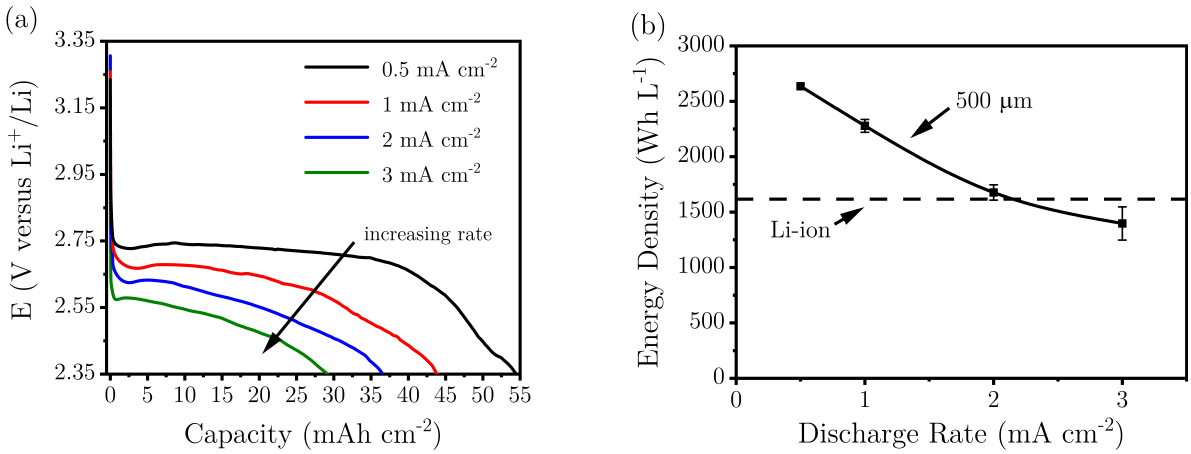


Figure 4.6: Discharge data and corresponding energy density plots for 500 μm thick gas diffusion electrodes discharged at various rates. (a) Discharge data was measured at various rates in an electrolyte of 1 M LiTFSI with 50 mM DBBQ in DME. (b) Energy density is calculated from the integrated area under the discharge curve and the thickness of the gas diffusion electrode at the end of discharge in *(a)*.

of discharge, Figure 4.5 (a) and (b), with approximately 50 % of the total porosity occupied by Li_2O_2 in each case. However, when the GDE thickness is increased to 500 μm, poor distribution of Li_2O_2 is observed towards the GDE/separator interface, suggesting poor O_2 mass transport in that region. The volume of porosity occupied by Li_2O_2 in the 500 μm thick electrode is 41 %, resulting in the lower energy density observed in Figure 4.4 (b). These findings suggest that the maximum achievable porosity filling by discharge product is approximately 50 %, which provides energy densities in the range of 2600-2700 Wh L^{-1}. Pore clogging and electrode passivation likely occur beyond this point, leading to polarisation and cell death. The red shading in Figure 4.5 provides a visual guide to indicate 50 % pore filling. Based on the above results, a 500 μm thick electrode was chosen as the electrode thickness for optimisation with O_2 diffusion channels.

Figure 4.6 (a) shows a 500 μm thick GDE discharged at four different rates between 0.5 - 3 mA cm^{-2}, the corresponding energy densities are shown in Figure 4.6 (b). The dashed line in Figure 4.6 (b) represents the energy density of a typical Li-ion cathode. This is based on a cathode such as $LiNi_{0.8}Mn_{0.1}Co_{0.1}O_2$, which attains 1550 Wh L^{-1}(electrode), calculated from an electrode thickness of 125 μm, which delivers a capacity of 5 mAh cm^{-2} at 3.6 V.

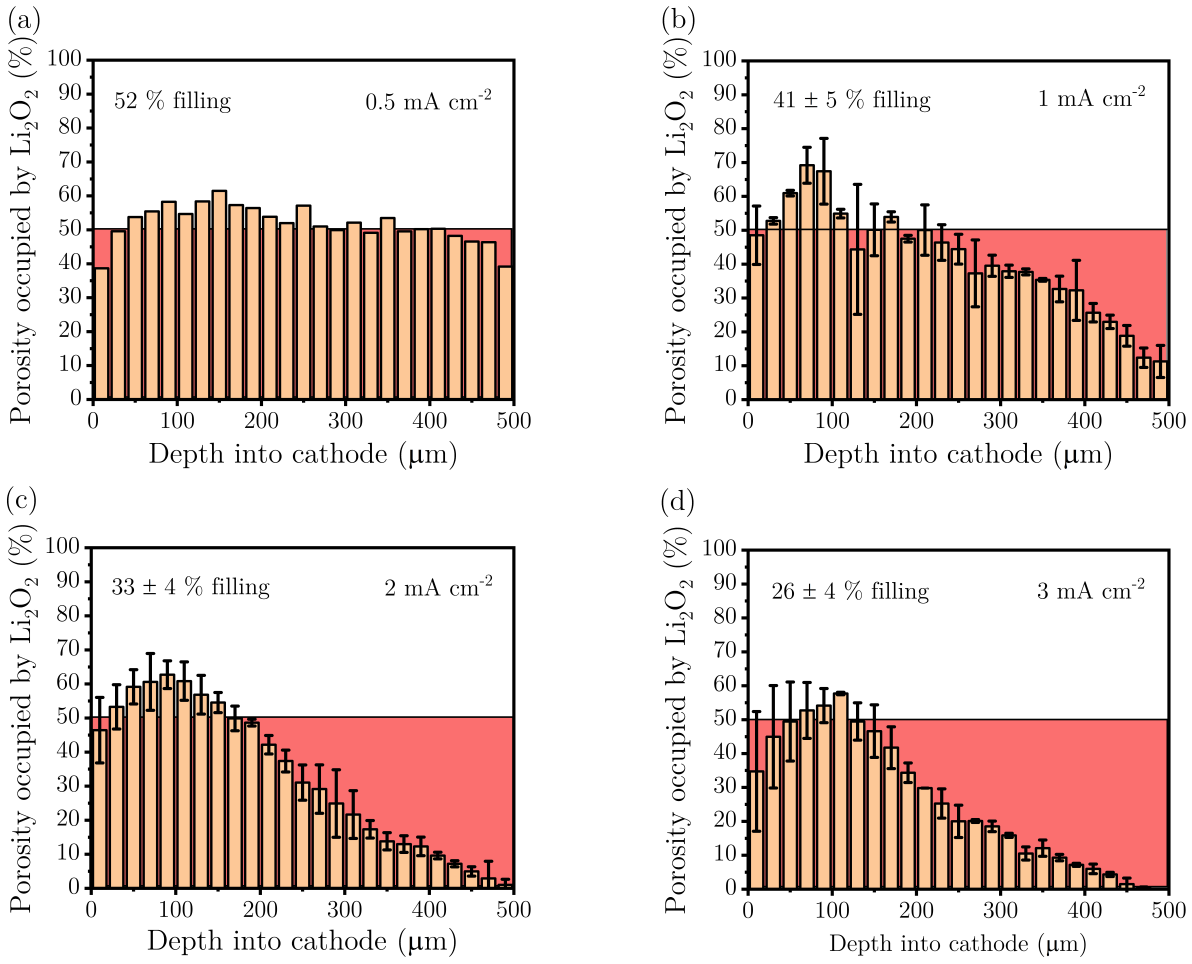


Figure 4.7: Li_2O_2 distributions corresponding to the data in Figure 4.6. (a, b, c, d) Li_2O_2 distributions for gas diffusion electrodes discharged at 0.5, 1, 2 and 3 mA cm^{-2} respectively. The distribution data was collected by microtoming the gas diffusion electrode into 20 μm slices and carrying out $TiOSO_4$/UV-vis titration. The Li_2O_2 filling values are calculated using the measured porosity, the discharge capacity and the crystalline density of Li_2O_2 (2.31 g cm^{-3}). The error bars represent one standard deviation from 3 separate repeat experiments. No error bars are included in (a) as the experiment was not repeated.

The slowest rate, 0.5 mA cm^{-2}, exhibited a relatively flat plateau region followed by a rapid polarisation, which is typical of Li-O_2 discharge at low rates. As the rate increased, the flat plateau region became a slope with a gradual polarisation over the entire discharge curve, and the overpotential on discharge increased. The discharge capacity decreased from 55 mAh cm^{-2} at 0.5 mA cm^{-2} to 30 mAh cm^{-2} at 3 mA cm^{-2}, resulting in energy densities between 2700-1450 Wh L^{-1}.

The distribution of Li_2O_2 at the end of discharge was measured for each rate, and the results are shown in Figure 4.7. At the slowest discharge rate of 0.5 mA cm^{-2}, Li_2O_2 was distributed evenly throughout the cathode, filling ~50 % of the porosity. As the

rate increased, the Li_2O_2 occupied less of the porosity, dropping to 41 % at 1 mA cm^{-2}, 33 % at 2 mA cm^{-2}, and only 25 % at 3 mA cm^{-2}. Furthermore, as the rate increased, the distribution of Li_2O_2 was skewed more toward the gas/electrode interface, where the O_2 concentration is highest. The distribution of Li_2O_2 as a function of current density strongly suggests that the discharge rate is limited primarily by O_2 mass transport through the electrode.

Based on the Li_2O_2 depth profiling experiments, it is possible to approximately infer the optimal placement of O_2 diffusion channels. In GDEs discharged at 2 mA cm^{-2}, the pore filling by Li_2O_2 drops below the 50 % after a depth of 200 μm, which suggests that O_2 mass transport is not limiting up to this point. Therefore, it can be inferred that O_2 diffusion channels should be placed within 400 μm of each other, allowing each channel to supply O_2 into the cathode laterally up to a distance of 200 μm, thereby maximising pore filling and even distribution of Li_2O_2, leading to an increase in energy density. Similarly, at 3 mA cm^{-2}, where pore filling drops below 50 % after 150 μm into the cathode, the channels should be placed within 300 μm of each other. In the following section, GDEs are fabricated with O_2 diffusion channels set according to the estimated placements detailed above.

4.3.2 O_2 Diffusion Channel Fabrication

The GDEs were fabricated in a three-step process whereby a sacrificial template of pillar structures was formed by 3D printing. The template was pressed into the carbon-binder mixture using a hydraulic press, and the template was then removed by pyrolysis to reveal channels of the inverse pattern of the 3D-printed pillar structures.

3D-Printing

The pillar templates were fabricated by direct laser writing using a femtosecond laser lithography system (Nanoscribe Photonic Professional GT). A Dip-in Laser Lithography (DiLL) configuration was used to manufacture the structures. The templates were exposed by two-photon absorption in a UV-sensitive photoresist (IP-S, Nanoscribe) at

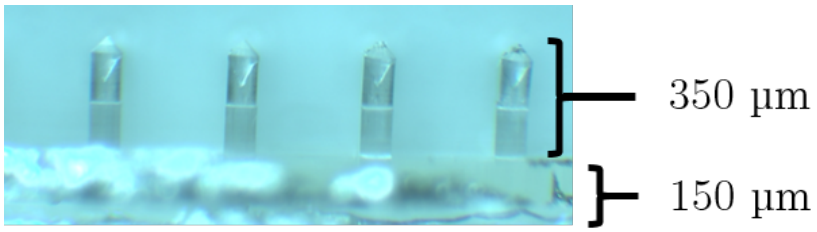


Figure 4.8: Cross-sectional optical image of the pillar template. Cone-topped pillars were formed, which allowed for more successful fabrication of the channelled gas diffusion electrodes.

a wavelength of 780 nm. Two-photon polymerisation allows for the fabrication of 3D structures with a resolution below 200 nm. Consequently, this allows for precision in the dimensions and spatial arrangement of the channels in the GDEs. The structures were written layer-by-layer with a distance of 500 nm between individual layers in axial and lateral directions. It was found that a spacing of 500 nm was the optimal trade-off between printing time ($\sim$ 12 hours per template) and structural stability of the final template. Once printed, the unexposed photoresist was removed in a developer bath of propylene glycol monomethyl ether acetate. The templates were then flooded with UV light to cross-link any unpolymerised photoresist between exposed layers.

Figure 4.8 shows a cross-sectional optical image of the 3D-printed, cone-topped pillar structures. The pillars have a total length of 350 μm, and the height of the cone occupies 50 μm of that height. The base of the template is 150 μm thick, which was optimal for the fabrication speed and stability of the final template. Cone-topped structures were found to be less prone to breaking during the fabrication process compared to cylindrical pillars. The lines that are visible through the centre of the pillars are an artefact of splitting the 3D-printing into 300 μm x 300 μm x 300 μm blocks, which is a requirement when printing larger structures on the 3D-printer. The splitting of the print job can introduce imperfections in the final structure. To mitigate this, the blocks were printed with 10 μm overlap to ensure that the blocks were well-adhered.

Figure 4.9 (a)-(c) shows SEM images of the 3D-printed, cone-topped pillar structures used to create O_2 diffusion channels. The structures were sputter coated with a conductive carbon layer to improve the image quality on SEM. The insets of Figure 4.9 show measurements of the diameters and spacing of the pillars as measured by the

SEM software (Zeiss SmartSEM). The 3D-printed pillars are fabricated with good reproducibility with diameters of 91 ± 1 μm. After printing, the pillar templates were pressed into the agglomerated GDE material using a hydraulic press and die set.

Template Removal

Figure 4.10 shows the mass change for each of the GDE components during heating at a constant rate of 5 °C min^{-1} under Ar flow, as measured by thermogravimetric analysis. The blue curve in Figure 4.10 shows the mass change for the 3D-printed template, which exhibits three mass changes between 100-200 °C, 300-350 °C, and 400-450 °C. The GDP (red curve) shows no mass change until ∼450 °C, where it shows rapid decomposition. The PTFE (black curve) exhibits no mass change until ∼525 °C when it also undergoes rapid decomposition. These results indicate that the GDP or PTFE do not experience any thermal degradation below 450 °C. A temperature of 410 °C was used to remove the templates, this represents a temperature at which the 3D-printed template is decomposed, but the GDP and PTFE are stable.

Figure 4.11 shows SEM images of the GDEs with O_2 diffusion channels after template removal. The templates were removed by heating in a tube furnace under the flow of Ar at 410 °C. The images show near complete removal of any 3D-printed template and highlight the precision of the channels formed by this method. EDX analysis was carried out to assess the efficacy of template removal by pyrolysis. Table 4.2 shows the relative amounts of C, F and O for the GDEs in the pristine state (before heat treatment), the pristine GDE after heat treatment (i.e. a GDE heated without the 3D-printed template) and the templated GDE after heat treatment. The pristine GDE and the pristine GDE after heat treatment both display comparable proportions of C, F, and O, indicating that no GDP or PTFE is lost due to the heat treatment itself. It should be noted that EDX detected no other elements across all three samples. The templated GDE displays a higher concentration of C and O and a lower F concentration in the EDX than the pristine GDE before and after heating. This indicates that some C and O residue remains as an artefact of the 3D-template decomposition.

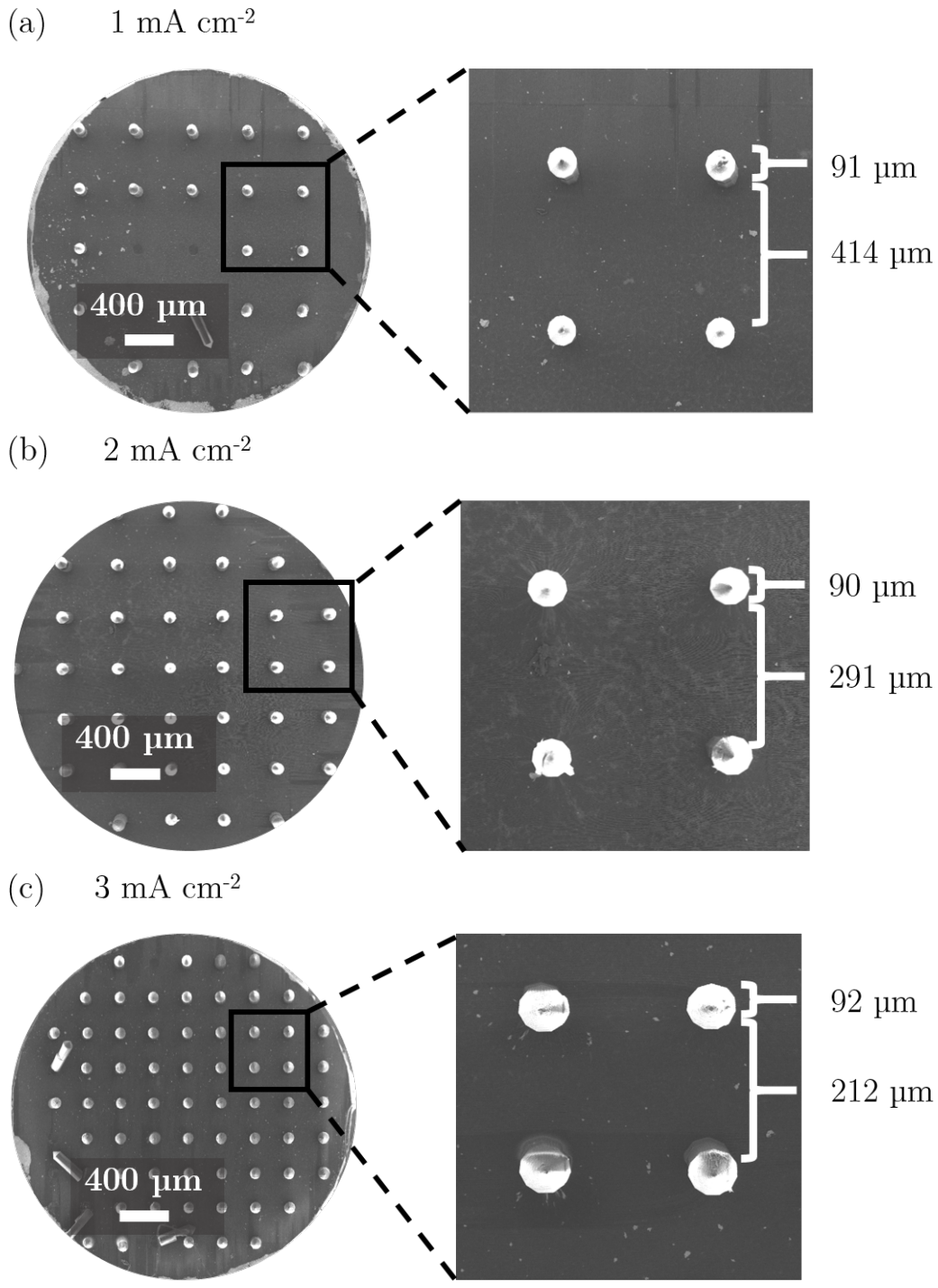


Figure 4.9: SEM images of the 3D-printed pillar templates. (a) Pillar structures for 1 mA cm^{-2} channel gas diffusion electrodes (b) pillar structures for 2 mA cm^{-2} channel gas diffusion electrodes (c) pillar structures for 3 mA cm^{-2} channel gas diffusion electrodes. The insets show measurements of the diameter and spacing of the pillars using the SEM software.

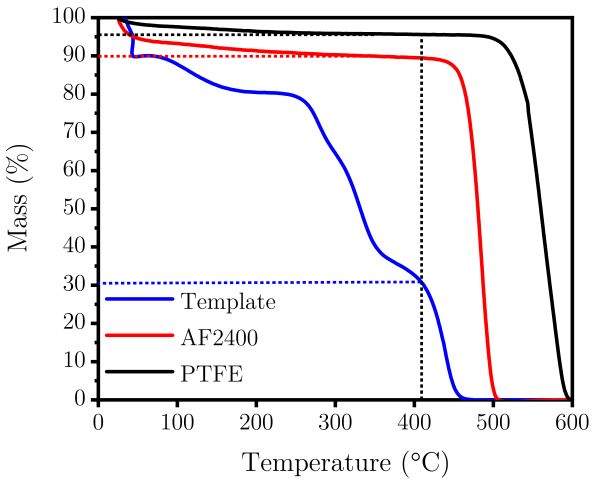


Figure 4.10: Thermogravimetric analysis of the 3D-printed template, GDP and PTFE. The data is recorded with a heating rate of 5 °C min^{-1} under flow of Ar.

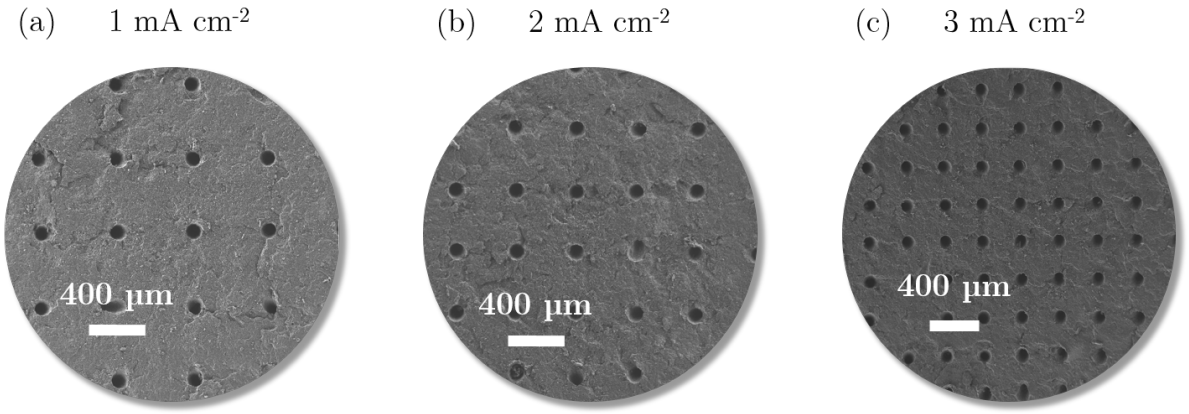


Figure 4.11: SEM images of the channeled gas diffusion electrodes. Channel structures for (a) 1 mA cm^{-2} (b) 2 mA cm^{-2} and (c) 3 mA cm^{-2}.

	C (%)	F (%)	O (%)
Pristine GDE	89	9.4	1.6
Heated GDE (no template)	87.4	11.4	1.2
Heated GDE (with template)	95.5	1.7	2.8

Table 4.2: Summary of EDX results collected for gas diffusion electrodes during channel fabrication

4.3.3 Discharge Behaviour and Li_2O_2 Distribution in Channel GDEs

Discharge data was collected using the channelled GDEs at three different rates between 1 - 3 mA cm^{-2} and compared to the non-channelled GDEs, the results are shown in Figure 4.12 (a, c, e). The black discharge curves represent the non-channelled GDEs, while the blue curves are the channelled GDEs. At each discharge rate, an increase in discharge capacity of approximately 10-15 % is observed when the channelled GDEs are used compared to the non-channelled GDEs. As well as this, the overpotential on discharge is reduced, leading to increased energy densities (Figure 4.13). The reduction in overpotential may indicate superior O_2 transport in the channelled GDEs compared to the non-channelled GDEs.

The distribution of Li_2O_2 is compared between channelled and non-channelled GDEs at each rate and is shown in Figure 4.12 (b, d, f). The blue bars represent the channelled GDEs, and the tan bars represent the non-channelled GDEs. As described previously, the Li_2O_2 distribution data is collected by cutting the GDEs into 20 μm thick slices using a microtome, followed by $TiOSO_4$/UV-vis titration of each slice. On the x-axis, 0 μm represents the GDE/gas interface. The Li_2O_2 is distributed more evenly throughout the GDE at each discharge rate when channelled GDEs are used. Particularly noticeable is the increased Li_2O_2 concentration towards the electrode/separator interface at each rate which would be expected when the provision of O_2 is improved throughout the electrode volume. Despite the addition of O_2 diffusion channels, the distribution of Li_2O_2 towards the GDE/separator interface decreases at 2 and 3 mA cm^{-2}. This would be expected where O_2 mass transport is still limiting. This is likely due to flooding of the O_2 diffusion channels by the electrolyte during cell assembly. O_2 diffusion through the electrolyte is

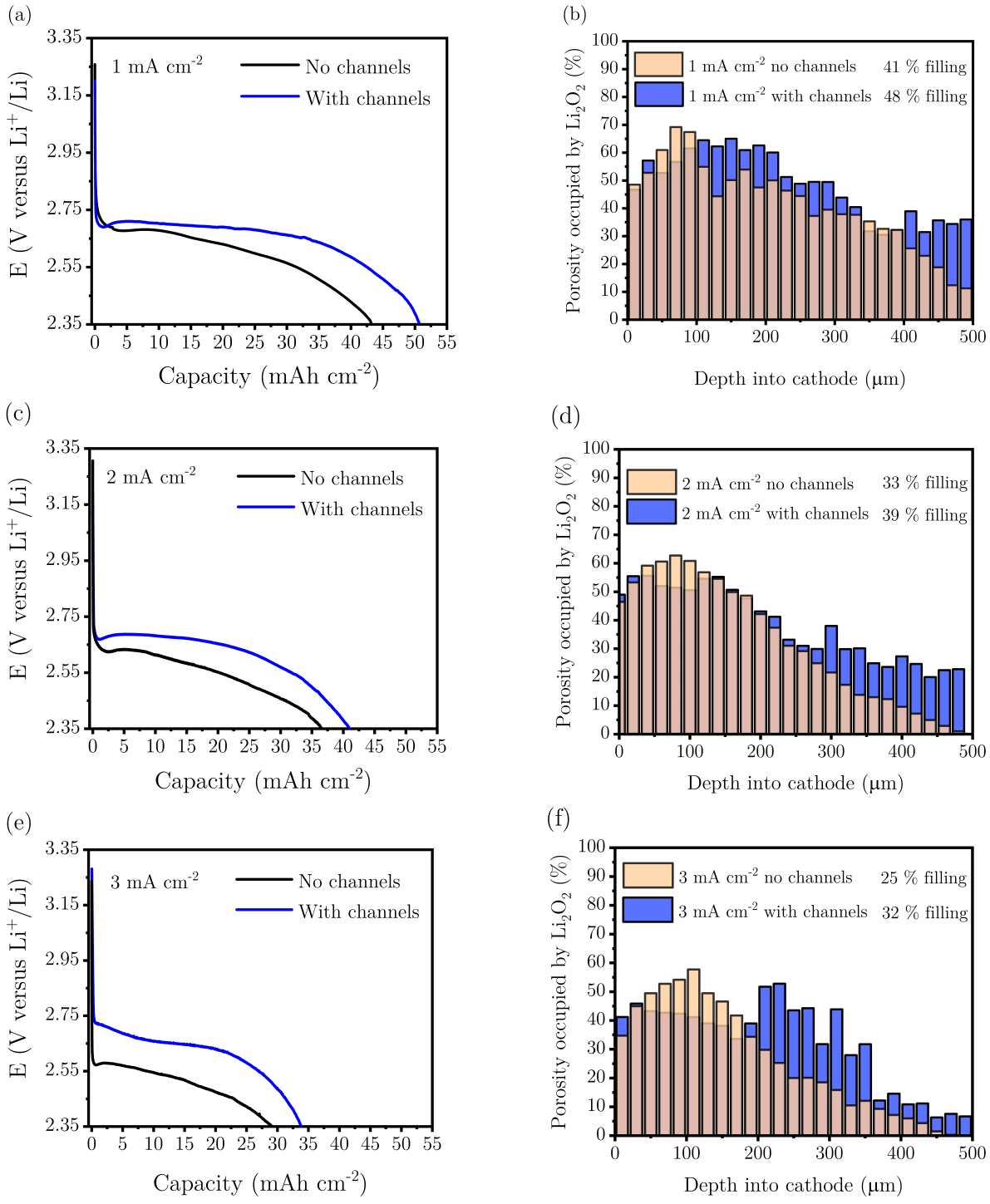


Figure 4.12: Discharge data and Li_2O_2 distribution comparison between channelled and non-channelled gas diffusion electrodes at various discharge rates. (a, c, e) Discharge data collected in an electrolyte of 1 M LiTFSI in DME with 50 mM DBBQ at (a) 1 mA cm^{-2} (b) 2 mA cm^{-2} and (c) 3 mA cm^{-2}. (b, d, f) corresponding distributions of Li_2O_2

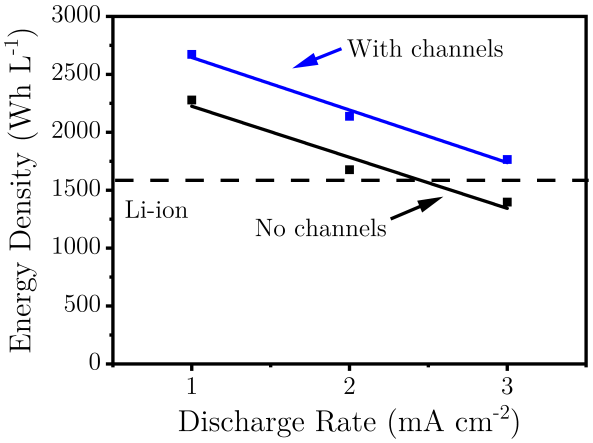


Figure 4.13: Energy density comparison between channeled and non-channeled gas diffusion electrodes. The energy densities are calculated from the integrated area under the discharge curve and the thickness of the gas diffusion electrode at the end of discharge.

sluggish. It cannot keep up with the rate of O_2 depletion due to the discharge reaction, leading to the uneven distribution of Li_2O_2. To improve the capacity at these higher rates, it is likely that the electrolyte will need to be excluded from the channels to allow for O_2 diffusion in the gas phase, which is much faster and more concentrated.

4.3.4 Characterisation of the Discharge Product

PXRD and FTIR

PXRD measurements of the discharged electrodes were taken to confirm the presence of Li_2O_2 after discharge. Figure 4.14 (a) shows the PXRD pattern collected with a fully discharged channelled GDE at 2 mA cm^{-2} with reference peak positions and intensities of Li_2O_2, LiOH and Li_2CO_3 taken from the ICSD database. The PXRD pattern exhibits peaks associated with Li_2O_2 and is absent of the peaks related to LiOH and Li_2CO_3. This indicates that Li_2O_2 is the dominant crystalline solid product at the end of discharge. Further characterisation was carried out by FT-IR spectroscopy shown in Figure 4.14 (b). The FT-IR spectra indicate peaks associated with Li_2O_2 and again are absent of the peaks related to common side products such as Li_2CO_3, LiOH and Li-acetate.

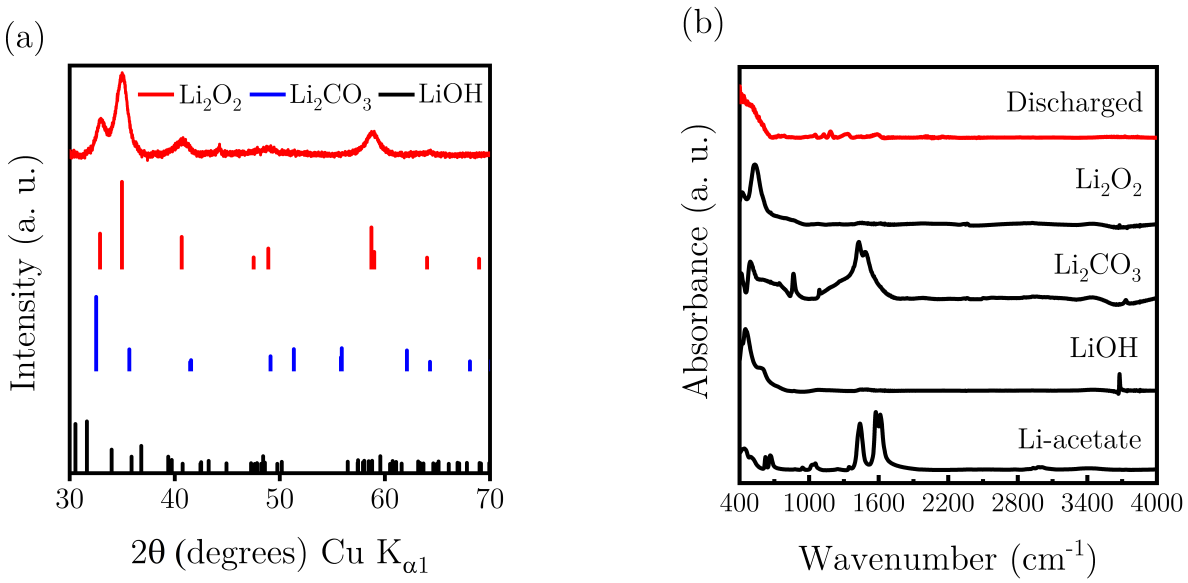


Figure 4.14: Characterisation of the discharged gas diffusion electrodes confirming that Li_2O_2 is dominant. (a) PXRD pattern and (b) FTIR spectra of the discharged gas diffusion electrodes.

Yield Measurement

The PXRD and FT-IR results in Figure 4.14 show that the predominant discharge product is Li_2O_2. To support these results and to show that there is little or no shuttling of DBBQ during operation, yield measurements were carried out to quantify the amount of Li_2O_2. The yield percentage of Li_2O_2 was 87 ± 2 % of the discharge capacity for cells utilising channelled GDEs. These values are in line with those previously reported by Gao *et al.* when carrying out discharge in an electrolyte of 1 M LiTFSI with DBBQ in DME.[18]

SEM

Figure 4.15 shows SEM images collected for the channelled GDEs at various rates at the GDE/gas interface at the end of discharge. Figure 4.15 (a) shows the product morphology at the end of discharge at 1 mA cm^{-2}. Large toroidal-shaped Li_2O_2 particles are formed, which are between 500-1000 nm in diameter. This morphology is typical for cells discharged with a DBBQ redox mediator at lower discharge rates.[18] The carbon surface is completely covered with Li_2O_2 indicating that pore blocking may cause cell death at 1 mA cm^{-2} in channeled GDEs. Figure 4.15 (b) shows the O_2 interface at

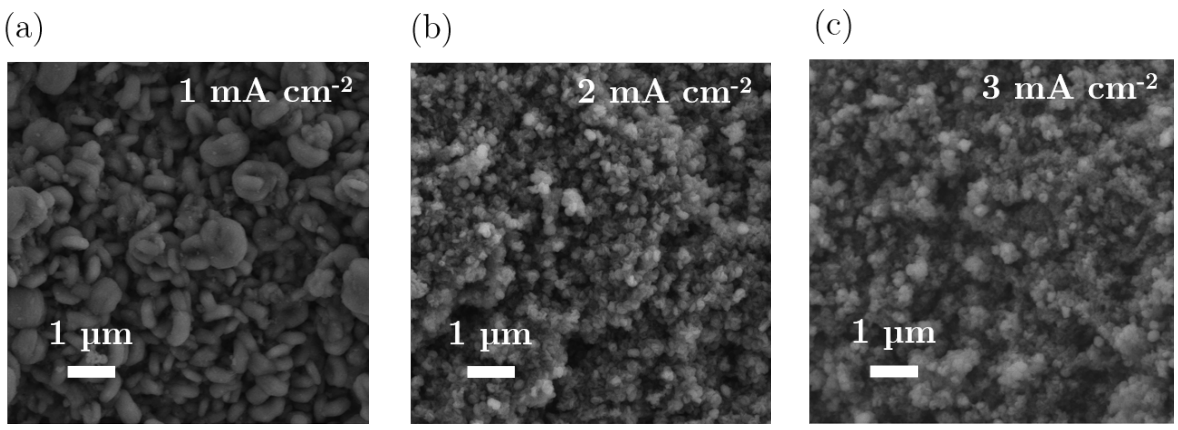


Figure 4.15: SEM images of the gas diffusion electrode/gas interface of the discharged channelled gas diffusion electrodes at rates between 1-3 mA cm^{-2} showing the variation in morphology of the Li_2O_2 discharge product. (a) 1 mA cm^{-2} (b) 2 mA cm^{-2} and (c) 3 mA cm^{-2}. The cells are discharged in an electrolyte of 1 M LiTFSI in DME with 50 mM DBBQ.

the end of discharge at 2 mA cm^{-2}. More Li_2O_2 particles are formed with smaller average diameters, between 250-350 nm. Again, this is typical in Li-O_2 cells at higher discharge rates where Li_2O_2 nucleates more frequently and has a lower particle size. At 3 mA cm^{-2}, Figure 4.15 (c), smaller and more numerous Li_2O_2 particles are formed compared to those at 2 mA cm^{-2}. Some porosity and possibly some of the carbon surface are still visible at the end of discharge at this rate, indicating that the failure mechanism may differ from that at lower discharge rates.

4.4 Conclusion

This work has explored introducing O_2 diffusion channels into a gas diffusion electrode for Li-O_2 batteries. It was shown that in gas diffusion electrodes which utilise a gas diffusion polymer, O_2 mass transport becomes a limiting factor when the thickness of the electrode is 500 μm at a discharge rate of 1 mA cm^{-2} in an electrolyte of 1 M LiTFSI in DME with 50 mM DBBQ. This is evidenced by decreased energy density and poor distribution of Li_2O_2 towards the separator interface. By exploring the distribution of Li_2O_2 at various discharge rates in a 500 μm thick electrode, it is possible to approximately inform the placement of the O_2 diffusion channels.

It was shown that O_2 diffusion channels can be introduced into the gas diffusion electrode via a 3D-printing method. A sacrificial template is fabricated, which can

be pressed into the gas diffusion electrode and removed facilely by heating under an argon atmosphere, leaving behind the inverse structure in the O_2 diffusion channels. The template can be decomposed without destroying the polymer binders by carefully controlling the temperature for pyrolysis, as evidenced by thermogravimetric analysis and EDX. 3D printing via two-photon polymerisation allows for precision over the dimension and spatial arrangement of the channels.

We have shown that the introduction of O_2 diffusion channels improves the discharge capacity and hence the energy density of the gas diffusion electrode at each discharge rate. The distribution of Li_2O_2 in the discharged electrodes is improved in each case. Despite the improvement, at higher discharge rates, the Li_2O_2 is distributed unevenly throughout the electrode at the end of discharge, indicating that O_2 transport is still limiting at higher discharge rates. To overcome this issue, it may be necessary to exclude the electrolyte solvent from the O_2 diffusion channels to allow for O_2 mass transport in the gas phase, which is faster and more concentrated than that in the electrolyte solvent. Li_2O_2 was confirmed as the primary discharge product through the use of PXRD and FTIR analysis, as well as by measurement of the Li_2O_2 yield.

4.5 References

[1] Gallagher, K. G. *et al.* Quantifying the promise of lithium-air batteries for electric vehicles. *Energy Environmental Science* **7**, 1555–1563 (2014).

[2] Jordan, J. W. *et al.* A Lithium-Air Battery and Gas Handling System Demonstrator. *Faraday Discussions* (2023).

[3] Augustin, M., Vullum, P. E., Vullum-Bruer, F. & Svensson, A. M. Inside the electrode: Looking at cycling products in Li/O_2 batteries. *Journal of Power Sources* **414**, 130–140 (2019).

[4] Park, S. H. *et al.* Maximal Utilization of a High-Loading Cathode in Li-O_2 Batteries: A Double Oxygen Supply System. *ACS Applied Materials Interfaces* **11**, 30872–30879 (2019).

[5] Lin, Y. *et al.* Ultrahigh-Capacity Lithium-Oxygen Batteries Enabled by Dry-Pressed Holey Graphene Air Cathodes. *Nano Letters* **17**, 3252–3260 (2017).

[6] Kuang, Y., Chen, C., Kirsch, D. & Hu, L. Thick Electrode Batteries: Principles, Opportunities, and Challenges. *Advanced Energy Materials* **9**, 1–19 (2019).

[7] Huang, Z. *et al.* A Li-O_2 battery cathode with vertical mass/charge transfer pathways. *Journal of Materials Chemistry A* **7**, 3000–3005.

[8] Chen, C. *et al.* Nature-Inspired Tri-Pathway Design Enabling High-Performance Flexible Li-O_2 Batteries. *Advanced Energy Materials* **9**, 1802964 (2019).

[9] Xu, S. *et al.* Textile Inspired Lithium–Oxygen Battery Cathode with Decoupled Oxygen and Electrolyte Pathways. *Advanced Materials* **30**, 1704907 (2018).

[10] Song, H. *et al.* Hierarchically Porous, Ultrathick,"Breathable" Wood-Derived Cathode for Lithium-Oxygen Batteries. *Advanced Energy Materials* **8**, 1701203 (2018).

[11] Kim, M. C. *et al.* Nature inspired cathodes using high-density carbon papers with an eddy current effect for high-rate performance lithium-air batteries. *Journal of Materials Chemistry A* **6**, 9550–9560 (2018).

[12] Thotiyl, M. M. O., Freunberger, S. A., Peng, Z. & Bruce, P. G. The Carbon Electrode in Nonaqueous Li-O_2 Cells. *Journal of the Americn Chemical Society* **135**, 494–500 (2013).

[13] Thommes, M. *et al.* Physisorption of gases, with special reference to the evaluation of surface area and pore size distribution (IUPAC Technical Report). *Pure and Applied Chemistry* **87**, 1051–1069 (2015).

[14] Yang, X. *et al.* Enhanced high rate and low-temperature performances of mesoporous $LiFePO_4$/Ketjen Black nanocomposite cathode material. *Electrochimica Acta* **114**, 259–264 (2013).

[15] Ding, N. *et al.* Influence of carbon pore size on the discharge capacity of Li-O_2 batteries. *Journal of Materials Chemistry A* **2**, 12433–12441 (2014).

[16] Nie, H. *et al.* Synthesis of a meso-macro hierarchical porous carbon material for improvement of O_2 diffusivity in Li-O_2 batteries. *RSC Advances* **4**, 17141–17145 (2014).

[17] Matsuda, S. & Yasukawa, E. Carbon-black-based self-standing porous electrode for 500 Wh/kg rechargeable lithium-oxygen batteries. *Cell Reports Physical Science* **2**, 100506 (2021).

[18] Gao, X., Chen, Y., Johnson, L. & Bruce, P. G. Promoting solution phase discharge in Li-O_2 batteries containing weakly solvating electrolyte solutions. *Nature Materials* **15**, 882–888 (2016).

[19] Gao, X., Chen, Y., Johnson, L. R., Jovanov, Z. P. & Bruce, P. G. A rechargeable lithium–oxygen battery with dual mediators stabilizing the carbon cathode. *Nature Energy* **2**, 17118 (2017).

[20] Askins, E. J. *et al.* Triarylmethyl cation redox mediators enhance Li-O_2 battery discharge capacities. *Nature Chemistry* (2023).

[21] Griffith, L. D., Sleightholme, A. E. S., Mansfield, J. F., Siegel, D. J. & Monroe, C. W. Correlating Li/O_2 cell capacity and product morphology with discharge current. *ACS Applied Materials Interfaces* **7**, 7670–7678 (2015).

[22] Horstmann, B. *et al.* Rate-Dependent Morphology of Li_2O_2 Growth in Li-O_2 Batteries. *Journal of Physical Chemistry Letters* **4**, 4217–4222 (2013).

[23] Lu, Y.-C. *et al.* The discharge rate capability of rechargeable Li-O_2 batteries. *Energy & Environmental Science* **4**, 2999–3007 (2011).

5

The Accumulation of Li_2CO_3 in a Li-O_2 Battery During Cycling

Contents

5.1 Introduction 149
5.2 Experimental 150
5.3 Cycling Results and Discussion 152
5.3.1 Cycling a Gas Diffusion Electrode with Dual Mediators . . . 152
5.3.2 Characterisation of the Cycling Products 154
5.3.3 Li_2CO_3 Removal and Further Cycling 159
5.3.4 Current Status of Li-O_2 Batteries 163
5.4 Conclusion 166
5.5 References 166

5.1 Introduction

Significant barriers remain despite the progress made in the field of Li-O_2 batteries. One such barrier is electrolyte degradation.[1] The role of solvent degradation in shortening the cycle life of Li-O_2 cells has received significant research interest for over a decade.[2–9] Glymes have emerged as one of the most stable electrolyte solvents but still undergo decomposition with Li_2O_2 to form products such as lithium acetate/formate and

Li_2CO_3.[4,10,11] Among them, it is Li_2CO_3 that has been highlighted as the major source of cell failure as it is highly insulating and only removed at potentials >4 V, and therefore tends to accumulate and lead to increasing polarisation during cycling.[12] It has been reported that Li_2CO_3 can also form due to the reaction between Li_2O_2 and the carbon of the gas diffusion electrode (GDE) itself,[13,14] which can be partially alleviated via the dual mediator approach by reducing interfacial contact between the Li_2O_2 grown from solution and the carbon surface.[15] This work examines the accumulation of Li_2O_2 and Li_2CO_3 within the GDE during cycling. It is demonstrated that removing Li_2CO_3 via a redox mediator can partially recover the cell performance. While other sources of degradation are likely to present (e.g. redox mediator decomposition), overcoming the accumulation of Li_2CO_3 with new electrolyte formulations could unlock the next step change in performance improvement for Li-O_2 batteries.

5.2 Experimental

Ketjen Black EC600-JD (MSE Supplies) was ground into a fine powder before treating with Ar/H_2 at 900 °C (heat rate of 5 °C min^{-1}) to remove any reactive hydrophilic side groups on the carbon surfaces.[13] Gas diffusion electrodes (GDEs) were prepared by mixing Ketjen Black with the appropriate mass of 10 wt. % PTFE (Merck) until an agglomeration was formed. A solution containing a known amount of Teflon AF2400 (Merck) in perfluoro(methylcyclohexane) (Merck) was then drop-cast onto the formed agglomerate and dried. A sheet of carbon material was created by calendaring to the desired thickness before cutting into 5 mm diameter GDE disks. The GDE disks were dried under a vacuum and stored in an Ar-filled glovebox before use.

Electrochemical measurements were carried out using a Swagelok-type cell, as detailed in the Experimental Chapter and previous studies.[15,16] 1,2-Dimethoxyethane (DME) (Merck, 99.9%) was dried over molecular sieves to <10 ppm H_2O prior to use. The electrolyte was prepared by dissolving 50 mM 2,5-di-tert-butyl-1,4-benzoquinone (DBBQ) (TCI) or 50 mM 2,5-di-tert-butyl-1,4-dimethoxybenzene (DBDMB) (Fluorochem 95 %) and 50 mM 2,2,6,6-Tetramethyl-1-piperidinyloxy (TEMPO)

(Merck, 99 %) into DME and drying over molecular sieves before adding 1 M LiTFSI (Merck, 99.99 %). The cells were assembled with a GDE as the cathode, partially delithiated $Li_{(1-x)}FePO_4$ (MSE Supplies) as the anode. The $LiFePO_4$ anodes act as counter/reference electrodes by maintaining a stable voltage of 3.45 V vs Li^+/Li. The $LiFePO_4$ is also the source and sink of Li^+ ions during discharge and charge. Two polypropylene separators (Celgard® 2500) are utilised, along with a stainless-steel mesh as the current collector. Before cycling, the cells were purged with oxygen (BOC, zero grade) through a Big Moisture Trap (Agilent) and allowed to equilibrate for 3 hours. The electrochemical measurements were carried out using a Biologic VMP3 Multichannel Potentiostat.

Pressure cell measurements were carried out using the GDE as the cathode and partially delithiated $Li_{(1-x)}FePO_4$ as the anode. The electrolyte was 1 M LiTFSI in DME with 50 mM DBDMB and 50 mM TEMPO. A pressure sensor (Omega Engineering) was connected to the headspace of the cell to monitor the change in pressure during cell cycling/ linear sweep voltammetry/ chronoamperometry. The cell was assembled in an Ar-filled glovebox and purged with O_2 through a Big Moisture Trap. The cell was allowed to equilibrate in an incubator maintained at 25 °C (Labcold) to avoid any pressure change due to temperature fluctuation.[17] Linear sweep voltammetry was performed from 3.5 V to 4.4 V vs Li^+/Li at a scan rate of 0.4 mV s^{-1} .

Conductivity measurements were carried out by removing the cycled GDE from the cell and washing thoroughly with DME before drying under a high vacuum at 70 °C. The GDE was then sandwiched between two stainless steel current collectors, and a voltage of 0.1 V was applied across the GDE, and the current response was measured. The conductivity could be calculated based on the area and thickness of the GDE.

For post-cycling characterisation, the cells were disassembled in a glovebox, and the GDEs, after discharge or charge, were rinsed with a small amount of DME before drying under high vacuum at 70 °C. Mercury intrusion porosimetry (MIP) was carried out on an Autopore IV 9500 (Micromeritics). The samples were dried under vacuum at 70 °C overnight before transferring to a 3 cc penetrometer (Micromeritics). Porosimetry was

carried out between 14.7 psia to 33,000 psia corresponding to pores between 100 μm to 6 nm. Scanning electron microscopy (SEM), images were collected on a Zeiss Merlin Field Emission Scanning Electron Microscope. Samples were transferred via an air-sensitive holder to avoid exposure to the atmosphere. Fourier transform infrared (FT-IR) spectra was collected on a Nicolet 6700 spectrometer (Thermo Fischer Scientific) in a N_2-filled glovebox and using a CsI beamsplitter. Samples were ground in a pestle and mortar with CsI and formed into a pellet using a die set and hydraulic press. Spectra were collected in transmission mode between 250-4000 cm^{-1}. Lithium peroxide depth-profiling data was collected using a microtome and UV-vis technique. The discharged GDE was placed in a ParaFree Metal Base Mould 15 x 15 x 4 mm (TAAB) and infiltrated with molten paraffin wax (Paraplast X-TRA, Merck) under vacuum and affixed to a cassette (TAAB). The sample was cooled to (-10 °C) before taking slices using an RM2125 RTS manual microtome (Leica Biosystems). Each slice was submerged in a known volume of 7.5 % $TiOSO_4/H_2SO_4$ solution. UV-vis data was collected with an Evolution 220 spectrophotometer (Thermo Scientific^{TM}). The Li_2CO_3 depth profiling was carried out by microtoming the cycled GDE into slices and carrying out acid treatment as described in previous studies.[18] Acid treatment was carried out by injecting a known volume of phosphoric acid onto the samples, and a Thermofischer mass spectrometer measured the evolution of CO_2. The flow rate of the Ar carrier gas was 1 mL min^{-1}, and the CO_2 signal was recorded as a % of the total volume of gas flowed through the mass spectrometer. Tap densities of commercial Li_2O_2 (Merck, 90 %) and Li_2CO_3 (Merck, >99 %) were measured using a GeoPyc 1360 Envelope and T.A.P Density Analyser (Micromeritics).

5.3 Cycling Results and Discussion

5.3.1 Cycling a Gas Diffusion Electrode with Dual Mediators

Figure 5.1 illustrates the voltage versus capacity profiles observed during cycling. The experimental setup and electrochemical measurements of the Li-O_2 cell are detailed in the Experimental section. To prevent undesirable reactions, a partially delithiated

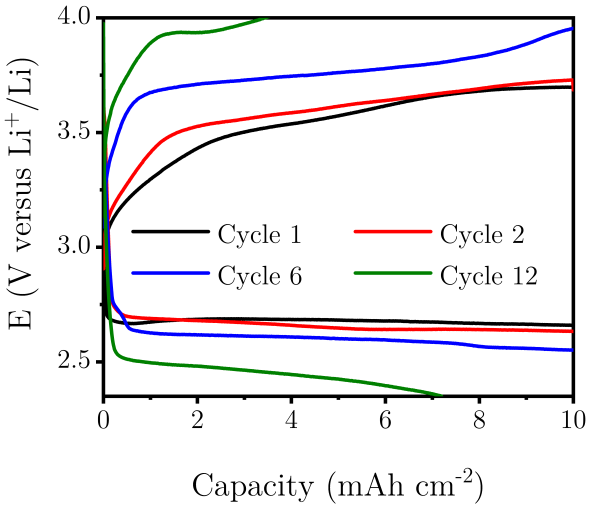


Figure 5.1: Discharge-charge profiles for a gas diffusion electrode with dual mediators. The cell is cycled at 1 mA cm^{-2} to a capacity of 10 mAh cm^{-2} between 2.4-4 V, whichever limit is reached first. The electrolyte is 1 M LiTFSI in DME with 50 mM DBBQ and 50 mM TEMPO acting as redox mediators for discharge and charge, respectively. The cell exhibits 12 cycles before capacity fading and polarisation render the cell inoperable

$Li_{(1-x)}FePO_4$ was used as the anode instead of lithium metal. $Li_{1-x}FePO_4$ maintains a stable voltage of 3.45 V vs Li^+/Li during discharge and charge. Throughout this study, voltages are referenced to Li^+/Li. The electrolyte consisted of 1 M LiTFSI in 1,2-dimethoxyethane (DME) with 50 mM 2,5-di-tert-butyl-1,4-benzoquinone (DBBQ) and 2,2,6,6-tetramethyl-1-piperidinyloxy (TEMPO) serving as redox mediators during discharge and charge, respectively. The gas diffusion electrode (GDE) used in this study comprised 60 wt. % Ketjen Black, 5 wt. % PTFE, and 35 wt. % GDP. The pristine GDE had a thickness of 275 μm.

The cell underwent discharge and charge cycles at a current density of 1 mA cm^{-2}. The cell was cycled with a fixed capacity of 10 mAh cm^{-2} and a voltage range of 2.4-4 V, whichever limit was reached first. The first and second cycles displayed a stable discharge plateau at 2.7 V and a sloping charge plateau between 3.5-3.7 V. The cell experienced increasing polarisation as cycling progressed, as evident from the comparison between cycle 6 (blue) and cycles 1 and 2. The cell failed on the 12^{th} cycle (green). The discharge capacity did not reach the targeted 10 mAh cm^{-2} before reaching the voltage cut-off of 2.4 V, resulting in significantly reduced energy density and premature cell failure.

Figure 5.2 (b) demonstrates that during the first discharge, the cell achieved a

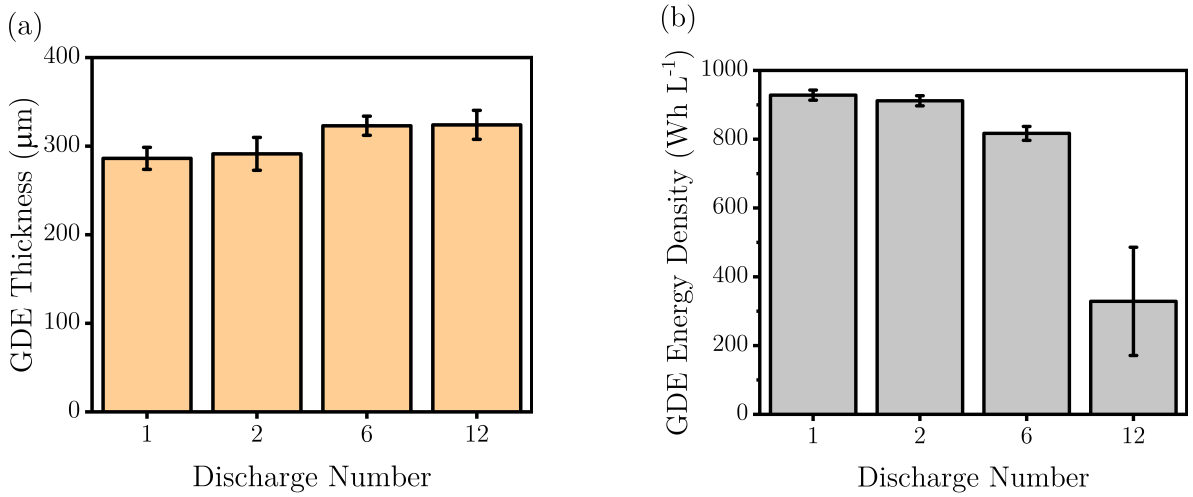


Figure 5.2: Thickness measurements of the gas diffusion electrode after discharge and energy density plot of the gas diffusion electrode during cycling. (a) gas diffusion electrode thicknesses after discharge measured using digital callipers. (b) Energy densities of the gas diffusion electrode during cycling are calculated based on the thickness of the gas diffusion electrode after discharge and the integrated area under the discharge curve. The error bars represent one standard deviation

cathode energy density of 930 Wh L^{-1}. This calculation involved integrating the area under the discharge curve and considering the thickness of the GDE at the end of the first discharge, Figure 5.2 (a). However, over multiple cycles, the GDE thickness increased, which, combined with the escalating polarisation, led to a decrease in energy density despite meeting the 10 mAh cm^{-2} target (Figure 5.2 (b)). The energy density declined rapidly as the cell approached the voltage cut-off, and the capacity diminished.

5.3.2 Characterisation of the Cycling Products

Figure 5.3 shows Fourier-transform infrared (FTIR) spectra of the GDEs after charging over several cycles (black) compared with FTIR spectra of the common side products Li_2CO_3 and Li-formate (red). The reference spectra for Li_2CO_3 and Li-formate are measured from commercially available powders. After the 1st charge, Li_2CO_3 remained in the GDE. Li_2CO_3 accumulated over cycling, as indicated by the growth of the peaks at 1500 cm^{-1}. Li-formate accumulation was also evident from the peak growth at 1700 cm^{-1}.

The distribution of Li_2O_2 at the end of discharge over several cycles was measured (Figure 5.4). The x-axis represents the depth into the GDE from the gas interface to the separator interface, where 0 μm represents the gas interface. The y-axis is the

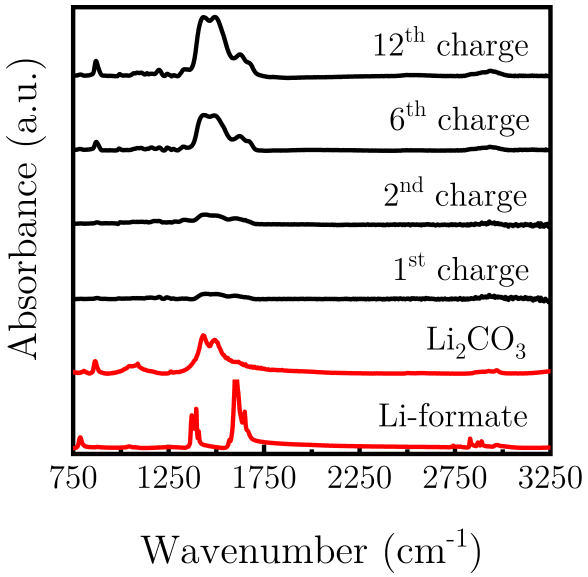


Figure 5.3: FTIR spectra of the charged gas diffusion electrodes during cycling showing accumulation of Li_2CO_3 and Li-formate. Reference spectra for Li_2CO_3 and Li-formate are recorded using commercially available powders and are shown in red

amount of Li_2O_2 normalised to the highest absorbance recorded. Slices of the electrode, 20 μm thick, were cut and titrated against $TiOSO_4$; the procedure is described in the Experimental section. Each bar, therefore, represents one 20 μm slice of GDE, and the blue line is a linear fit of the data and acts as a guide to the eye.

The quantity of Li_2O_2 measured within the first slice (nearest to the gas interface) may be underestimated due to the challenge of ensuring the microtome was perfectly aligned with the surface of the cathode. On the first two discharge cycles, Li_2O_2 was deposited closer to the gas interface on average, with a significant decrease in the amount of Li_2O_2 towards the separator interface, in accord with the established consensus that sluggish oxygen mass transport is a limiting factor in aprotic Li-O_2 batteries.[19–21] On the 6th cycle the Li_2O_2 is distributed more evenly throughout the GDE. It may be possible that the variation in the distribution of Li_2O_2 and the accumulation of Li_2CO_3 are interrelated: if Li_2CO_3 forms by reaction of the carbon electrode or electrolyte solvent with Li_2O_2, then Li_2CO_3 will be deposited towards the gas interface after the first charge, as this is where Li_2O_2 is predominantly formed. The Li_2CO_3 will passivate areas of the electrode where it is formed, preventing charge transfer and Li_2O_2 formation, therefore O_2 will diffuse further into the electrode before forming Li_2O_2, resulting in variations in the Li_2O_2 distribution over multiple cycles. This is also evident on the 12th

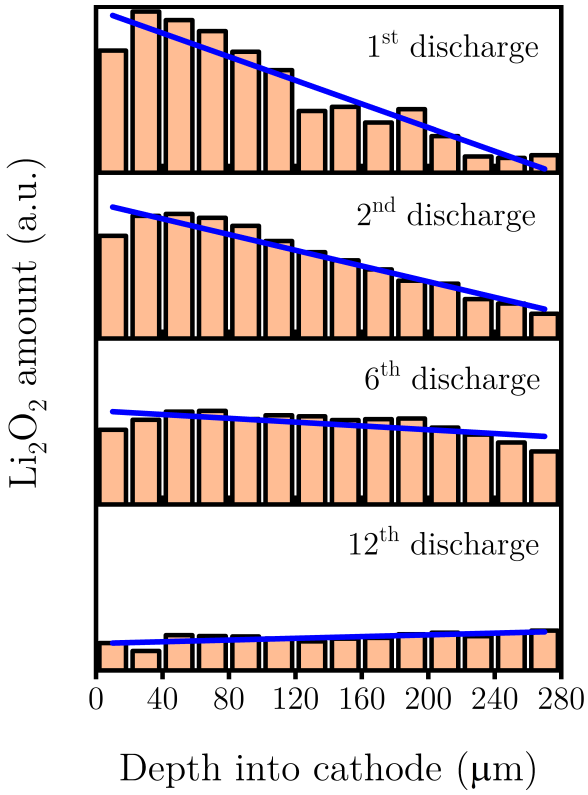


Figure 5.4: Distribution of Li_2O_2 after discharge over several cycles showing variations in how Li_2O_2 is distributed. The discharged gas diffusion electrodes are microtomed into 20 μm slices and titrated using $TiOSO_4$ and UV-vis. On the y-axis, the values are normalised to the highest absorbance recorded. The x-axis represents the depth into the gas diffusion electrode with 0 μm representing the gas interface. The blue lines are linear fits of the data and act as a guide to the eye.

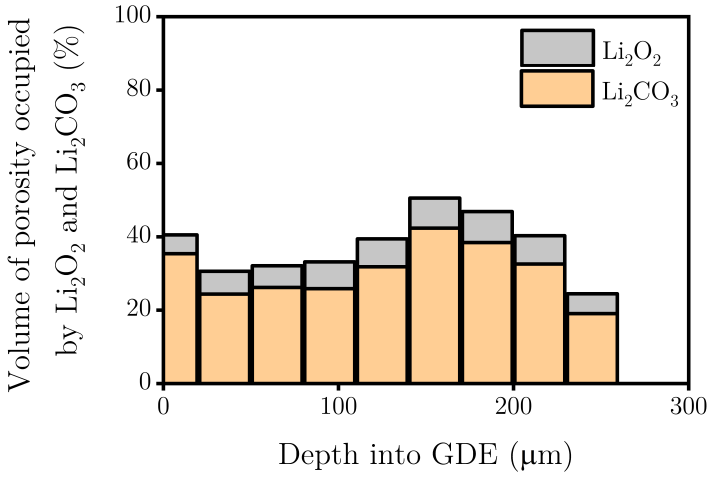


Figure 5.5: Distribution of Li_2CO_3 and Li_2O_2 after the 12th charging cycle. Slices of the cycled gas diffusion electrode are obtained using a microtome. To measure the Li_2CO_3 amount, the slices are treated with acid to release CO_2 from Li_2CO_3 and the CO_2 flux is measured using calibrated mass spectrometry. The Li_2O_2 amount is measured by titration with $TiOSO_4$.

cycle where the distribution of Li_2O_2 is reversed with more Li_2O_2 formed towards the separator, albeit the amount of Li_2O_2 titrated is greatly reduced in line with the reduced capacity observed on cycling (Figure 5.1). The yield of Li_2O_2 after the first discharge was measured to be 86 %, which agrees with previous studies in glyme-based electrolytes with redox mediators.[15,16,22]

The distribution of Li_2CO_3 and Li_2O_2 after the cell failure (after the 12th charge) was determined (Figure 5.5). To measure the distribution of Li_2CO_3, slices of the GDE obtained by microtoming were treated with acid to release CO_2 from Li_2CO_3, which was quantified using calibrated mass spectrometry (MS) as detailed in the Experimental section.[13] In Figure 5.5, we consider the volume of the porosity occupied by Li_2CO_3 and Li_2O_2, calculated using the measured tap densities of commercial Li_2O_2 and Li_2CO_3 powders (0.97 and 1.63 g cm^{-3}, respectively) as an approximation for the packing density of the electrochemically formed products within the pores. The porosity of the pristine GDE was 78 %, measured via mercury intrusion porosimetry (MIP). The total volume occupied by Li_2CO_3 and Li_2O_2 at the end of the 12th charge varied between 30 and 50 % of the pore volume throughout the GDE, with Li_2CO_3 being the dominant product, demonstrating the accumulation of Li_2CO_3 after cell failure.

This is further shown in the scanning electron microscopy (SEM) images at the gas

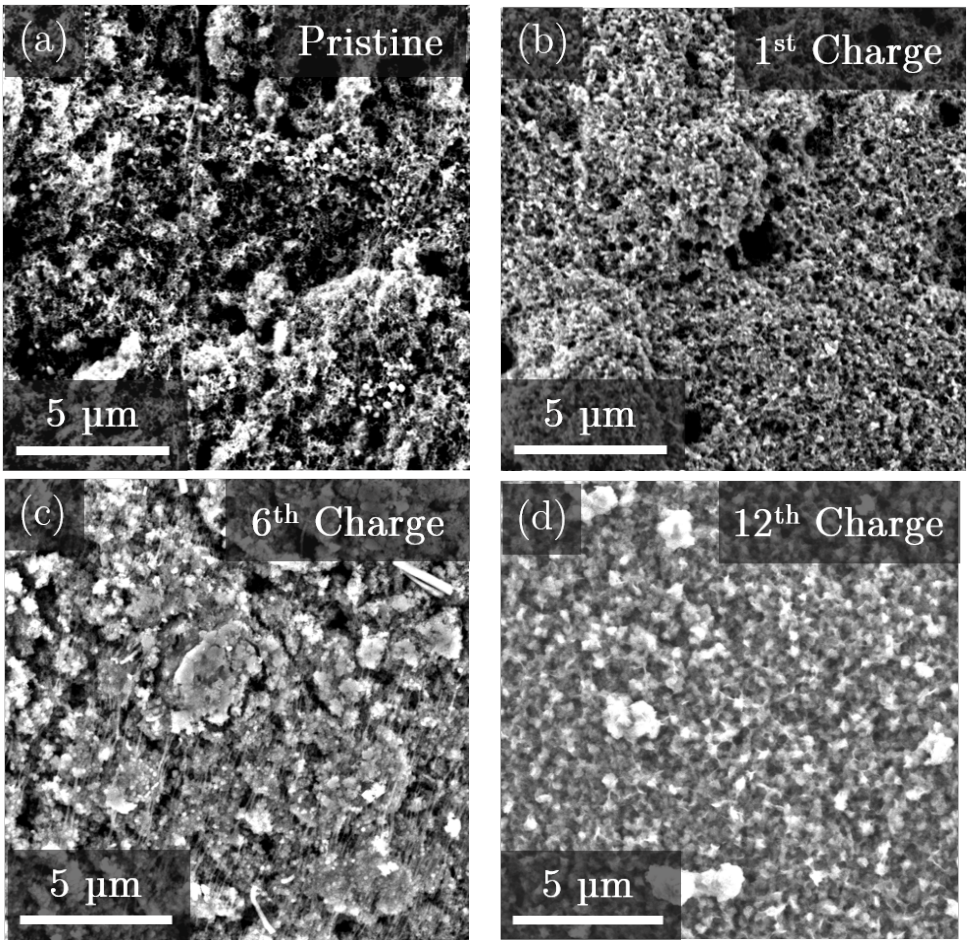


Figure 5.6: SEM images of the gas interface of the gas diffusion electrode over several cycles showing the accumulation of cycling products. SEM images of the gas interface in the (a) pristine state (b) after the 1st charge, (c) after the 6th charge, and (d) after the 12th charge

interface of the GDE at the end of charge on different cycle numbers (Figure 5.6). The pristine GDE, Figure 5.6 (a), is typical of a GDE formed using a carbon black with a polymer binder. After the first charge, Figure 5.6, much of the porosity of the GDE is retained with some evidence of cycling product (either Li_2O_2 or other side products) formed on the surface of the carbon GDE. The 6th charge shows strong evidence of cycling product accumulation with much porosity at the gas interface occupied. Despite this, porosity is still evident at the gas interface, which can allow for O_2 mass transport to sustain discharge to 10 mAh cm^{-2}. After the 12th charge, there is a significant accumulation of cycling product at the gas interface with little porosity still visible. By this point, the amount of cycling product at the gas interface and throughout the GDE is likely enough to restrict O_2 mass transport, whereby the achievable capacity is significantly reduced.

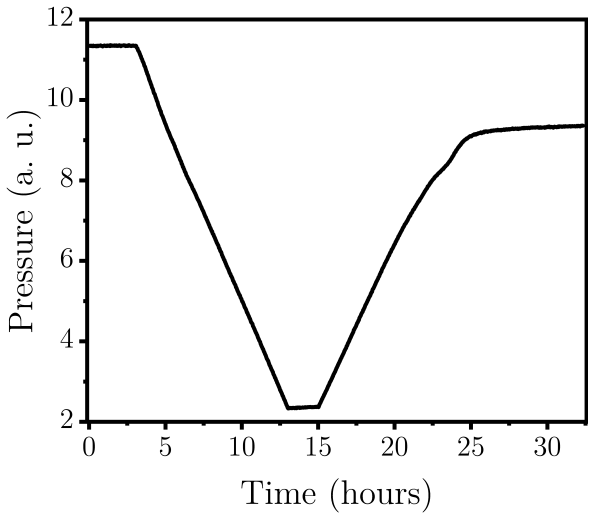


Figure 5.7: *In situ* pressure monitoring of a cell during cycling showing pressure decrease and partial recovery on discharge and charge respectively. The cell was cycled at 1 mA cm^{-2} to 10 mAh cm^{-2} in an electrolyte of 1 M LiTFSI in DME with 50 mM DBDMB and 50 mM TEMPO. The pressure recovery on charge is equal to 78 % of the initial pressure in the cell

5.3.3 Li_2CO_3 Removal and Further Cycling

To demonstrate the role of Li_2CO_3 accumulation in the cell failure, the recovery of cell performance on removing Li_2CO_3 from the GDE after the 12^{th} charge was investigated. A redox mediator, 2,5-di-tert-butyl-1,4-dimethoxybenzene (DBDMB), was employed to oxidise Li_2CO_3.[23,24] DBDMB has a similar structure to DBBQ, as shown in the inset of Figure 5.9, and is also proposed to operate as a redox mediator on discharge via the same mechanism as DBBQ.[24] An electrolyte solution consisting of 1 M LiTFSI in DME with 50 mM DBDMB and 50 mM TEMPO was used. As DBDMB has been shown to oxidise Li_2CO_3 at potentials > 4 V, TEMPO (with a lower working potential) was included as an additive to avoid long exposure of the electrolyte solution to high potentials where it is at risk of electrochemical oxidation. The cell was first discharged and charged with this new additive formulation while monitoring the *in-situ* pressure change.

Figure 5.7 shows that the pressure decreased during discharge as gaseous oxygen was consumed. The pressure was partially recovered on charge. The pressure recovery on charge is 78 % - in line with the Li_2O_2 yield of 80 % after discharge with DBDMB as measured by $TiOSO_4$ titration. No Li_2CO_3 decomposition by DBDMB is expected due to TEMPO maintaining the oxidation potential below that of DBDMB. This result,

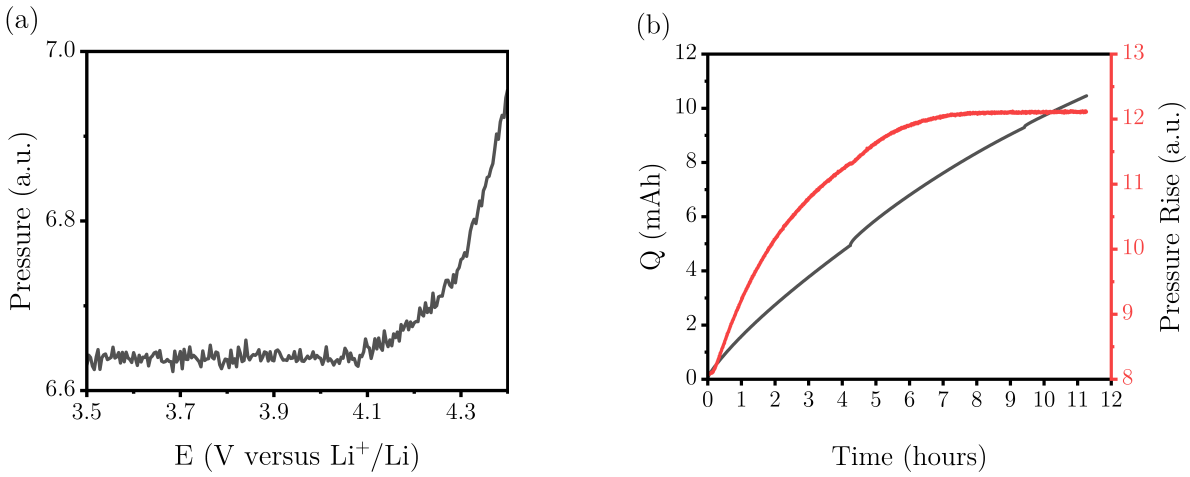


Figure 5.8: *In situ* pressure monitoring during LSV and CA of a cycled electrode after charge showing a pressure increase beginning at 4.1 V (a) LSV recorded at 0.4 mV s^{-1} from 3.5 to 4.4 V (b) CA recorded at 4.3 V. The electrolyte is 1 M LiTFSI in DME with 50 mM DBDMB and 50 mM TEMPO.

together with the yield, is in accord with previous studies suggesting no further side reactions are caused by the introduction of DBDMB.[24]

After cell failure on the 12th charge, linear sweep voltammetry (LSV) was carried out from 3.5 to 4.4 V at 0.4 mV s^{-1} in the presence of DBDMB while monitoring the pressure change (Figure 5.8 (a)). The pressure began to increase at a potential of 4.1 V, consistent with the oxidation of Li_2CO_3 and in accord with previous studies.[24] No pressure increase was observed at potentials between 3.5-4.1 V which would be indicative of Li_2O_2 oxidation, despite Li_2O_2 being present after the 12th charging cycle as measured in Figure 5.5. It is postulated that the Li_2O_2 measured at the end of the 12th charge is both electronically isolated from the GDE and is inaccessible to $DBDMB^+$. This can be possible where Li_2O_2 reacts with the electrolyte or carbon in the GDE, forming Li_2CO_3. In areas where Li_2CO_3 forms around Li_2O_2, the Li_2O_2 can become chemically and electrochemically isolated. Li_2CO_3 oxidation is also demonstrated in the cell with a chronoamperometry (CA) measurement, where after the cell failed, the cell was held at a potential of 4.3 V where DBDMB is oxidised to $DBDMB^+$ which then oxidises Li_2CO_3 (Figure 5.8 (b)). The red plot in Figure 5.8 (b) shows the pressure increase, and the grey plot shows the charge passed. The pressure was shown to increase and then plateau (Figure 5.8 (b)).

To further confirm the oxidation of Li_2CO_3, the GDE after Li_2CO_3 oxidation by

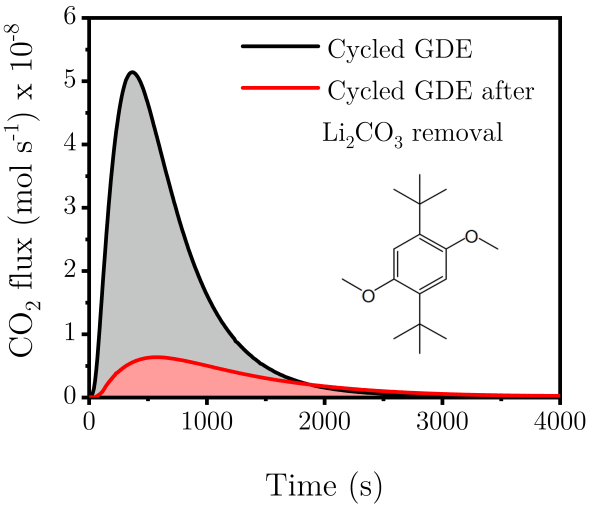


Figure 5.9: Acid treatment comparing a cycled gas diffusion electrode and a cycled gas diffusion electrode after DBDMB$^+$ treatment showing a reduction in CO_2 flux. The gas diffusion electrodes were treated with phosphoric acid to release CO_2 from Li_2CO_3, the flux of CO_2 was measured using calibrated mass spectrometry. The inset of the figure shows the structure of DBDMB

DBDMB$^+$ was treated with acid to release CO_2, indicating the amount of the remaining Li_2CO_3. This was compared with an identically cycled GDE after cell failure but without performing Li_2CO_3 removal by DBDMB$^+$ (Figure 5.9).

A much smaller flux of CO_2 evolution was observed in the GDE after the DBDMB$^+$ treatment which shows that the DBDMB$^+$ treatment effectively removes the majority of the Li_2CO_3. This is in accord with the SEM images in Figure 5.10 (a) and (b), which show the air interface of the GDE after the 12th charge cycle and after the 12th charge cycle after treatment with DBDMB$^+$, respectively. There is clear evidence of product accumulation in Figure 5.10 (a), which is effectively removed in Figure 5.10 (b), revealing the porosity of the GDE with a return to a near pristine GDE (see Figure 5.6).

To evaluate the effect of Li_2CO_3 removal on the cell performance, a cell which had reached the failure condition after the 12th charge was then treated with DBDMB$^+$ (by performing a potential hold at 4.3 V) to remove Li_2CO_3 and then returned to cycling under the same protocol, Figure 5.11.

A partial recovery of the cycling performance was achieved, as shown in Figure 5.11 (a), where the 13th cycle, corresponding to the 1st cycle after the DBDMB$^+$ treatment, achieved the discharge capacity of 10 mAh cm^{-2} before reaching the cut-off voltage. The overpotential on both discharge and charge was smaller than in the 12th

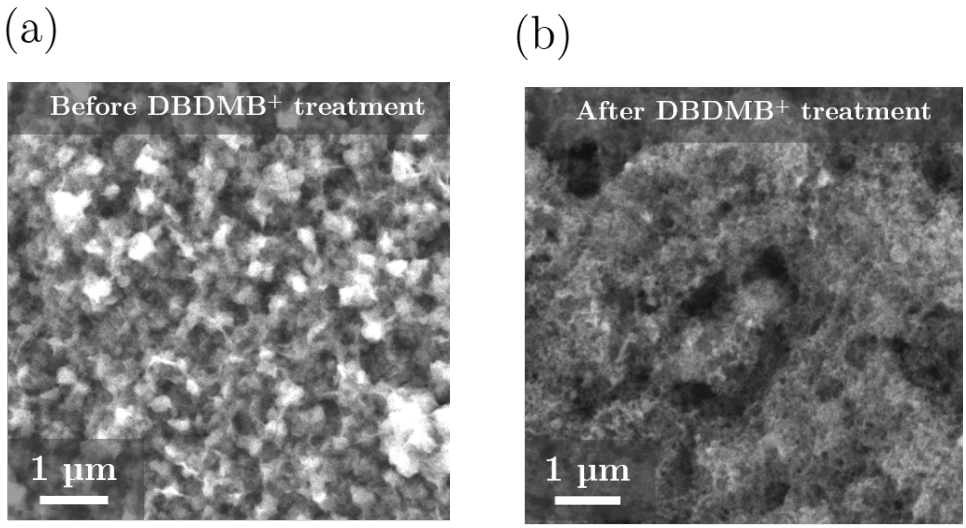


Figure 5.10: SEM images of the gas interface of the gas diffusion electrode before and after treatment with $DBDMB^+$ showing removal of cycling products. (a) SEM image of the gas interface of a gas diffusion electrode after cycling until cell failure showing accumulation of cycling products. (b) SEM image of the gas interface of a gas diffusion electrode which has been cycled until failure and treated with $DBDMB^+$ to remove Li_2CO_3

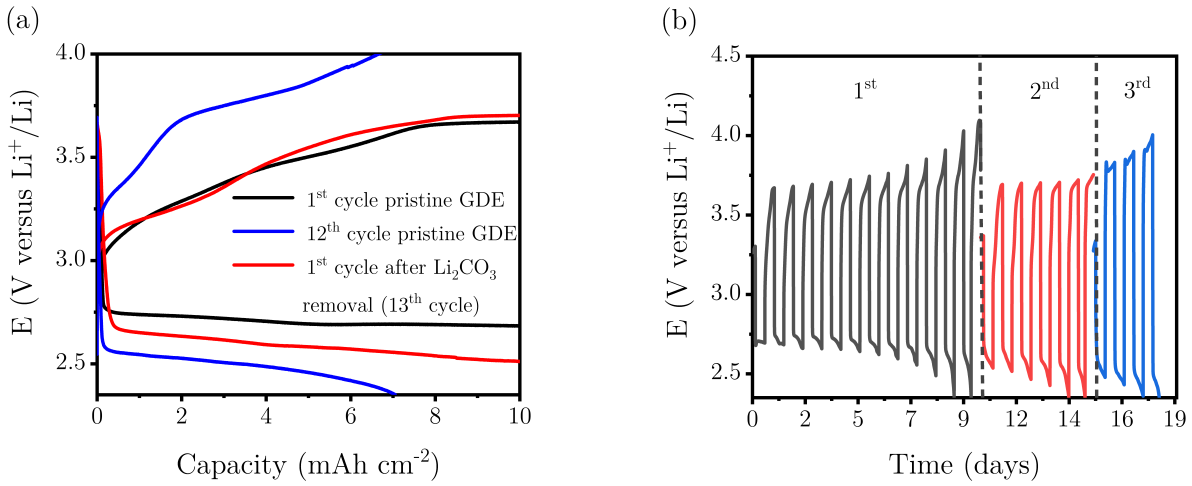


Figure 5.11: Discharge-charge profiles of cells cycled until failure and treated with $DBDMB^+$, showing partial recovery of the cycling performance. (a) Voltage versus capacity plots. (b) Voltage versus time plot. The cells were cycled at 1 mA cm^{-2} to 10 mAh cm^{-2} between 2.4-4 V, whichever limit was reached first. The electrolyte was 1 M LiTFSI in DME with 50 mM DBDMB and 50 M TEMPO.

cycle, and the cycle life of the GDE was increased by 10 cycles using this method, Figure 5.11 (b). This is not being suggested to prolong the lifespan of existing Li-O_2 cells. Developing a more effective method to overcome the accumulation of Li_2CO_3, for example, with novel electrolyte formulations, may be necessary for achieving a long cycle life Li-O_2 battery. It should also be noted that despite removing much of the Li_2CO_3 from the GDE after cell failure, only 6 cycles are achieved after the first treatment, compared to the 12 cycles performed when cycling from the pristine GDE. Other effects may limit the cyclability of the GDE. For instance, the thickness of the GDE increases from 275 μm in the pristine state to 325 μm at the end of 12 cycles. Morphological changes within the GDE may be causing contact loss between the conductive carbon or causing restriction of O_2 transport pathways. However, further work would be required to investigate these effects more thoroughly.

5.3.4 Current Status of Li-O_2 Batteries

Li-O_2 batteries promise an energy density in the region of 3500 Wh kg^{-1} based on the mass of Li_2O_2 delivered at a potential of 2.96 V vs Li^+/Li. This is compared to approximately 600-700 Wh kg^{-1} for Li-ion.[25] However, the theoretical specific energy of 3500 Wh kg^{-1} does not take into account the mass of other cell components, including the electrolyte, anode and cell casings, which are similarly important in Li-ion batteries and significantly reduce the achievable energy density in a practical device. The key difference between Li-ion and Li-O_2 batteries is the requirement for the cathode to be exposed to oxygen gas which leads to the evaporation of the electrolyte solvent. Similarly, suppose the O_2 is taken from the atmosphere. In that case, the feed gas must be scrubbed of other constituents such as CO_2 and H_2O, which can lead to parasitic chemistry within the battery. These requirements add mass and volume to the Li-O_2 battery at the system level where gas and solvent handling components are considered. An early study by Gallagher *et al.* carried out a material-to-system analysis of Li-O_2 batteries in comparison to competing technologies such as Li-metal or Si anodes coupled with Li-rich NMC.[26] They found that when considering the Li-O_2 battery at the system

level, the specific energy can surpass that of Li-rich NMC, however, Li-rich NMC has a greater energy density. The caveat is that Li-O_2 batteries are at a much earlier stage of development and the risks in pursuing such a technology may not outweigh the benefits.[26] However, this study was carried out in 2014 and since then there have been advances in the technology in terms of cell design,[27,28], capacity and cyclic ability,[15,16] as well as a demonstrated tolerance to H_2O, thus reducing the mass of components needed for scrubbing.[29] New assessments of the achievable specific energy are in the region of 610 Wh kg^{-1}_{system}, compared to approximately 500 Wh kg^{-1}_{system} predicted by Gallagher and 300 Wh kg^{-1}_{system} for Li-metal/Li-rich NMC.[26,30]

Taking the above into account, Li-O_2 discharge data need to be reported more rigorously so that easier comparisons can be made with Li-ion batteries and for more facile predictions on whether the values reported translate to a practical system-level Li-O_2 battery when carrying out a material-to-system analysis. Many early reports provided discharge capacities in terms of the mass of carbon in the electrode and did not take into account the mass of Li_2O_2 formed. These reports would use a low mass-loading of carbon (often 1 mg cm^{-2} or less) and the reported discharge capacities and discharge rates appear artificially high despite only forming a low mass of discharge product. Important metrics to provide are the thickness (and hence volume) of the electrode at the end of discharge, the discharge capacity and the rate, the mass of the electrode (carbon + binder), porosity and mass of the electrolyte. This has been done throughout this thesis and allows for predictions to be made for a system-level battery. Figure 5.1 shows a calculation of the system level specific energy and energy density based on a cathode which delivers 31 mAh cm^{-2} at 1 mA cm^{-2} (see chapter 3). The balance of the plant including air and solvent handling accounts for 50 kg or 50 L. Based on these values, the system level specific energy and energy density are predicted as 595.7 Wh kg^{-1} and 651.3 Wh L^{-1} respectively. Which are competitive with a Li-metal/Li-rich NMC couple.

Performance	
Specific capacity (mAh g^{-1})	508.5
Specific energy (Wh kg^{-1})	1357.6
Pack Specific energy (Wh kg^{-1})	848.5
System specific energy (Wh kg^{-1})	**595.7**
Volumetric capacity – (mAh cm^{-3})	832.0
Volumetric energy density (Wh L^{-1})	2221.6
Pack volumetric energy (Wh L^{-1})	965.9
System volumetric energy density (Wh L^{-1})	**651.3**

Electrochemical variables	
Voltage (vs Li^+/Li)	2.66

Pack and power	
Pack energy (kWh)	100
Pack specific energy (Wh kg^{-1})	897.0
Pack volumetric energy (Wh L^{-1})	965.9
Pack mass scaling factor	1.6
Pack volume scaling factor	2
Pack mass (kg)	111.5
Pack volume (L)	103.5
Bilayer thickness (cm)	4.1×10^{-2}
Cell dimension (cm)	30
Current density (mA)	10
Additional volume (%) for volume change	15
Energy per cell (Wh)	82.0
Total cells	1220.0
Length of pack (cm)	50.0
Current per cell (mA)	9000
Power per cell (W)	24.0
Total power (kW)	29.3

Balance of Plant	
BOP volume (L)	50
BOP mass (kg)	50
System volume (L)	153.5
System mass (kg)	161.5
Volumetric energy density (Wh L^{-1} system)	651.3
Specific energy (Wh kg^{-1} system)	619.3

Positive Electrode	
Volume fractions	
Carbon (%)	20.4
Electrolyte (%)	27.5
Binder (%)	13.6
Li_2O_2 (%)	38.5
Total areal weight - (g cm^{-2})	4.4×10^{-2}
Total areal volume (cm^3 per cm^2)	2.0×10^{-2}
Positive electrode thickness - (μm)	200
Areal capacity Li_2O_2 (mAh cm^{-2})	31
Specific capacity (mAh g^{-1})	781.0

Ceramic protected lithium Anode	
Li thickness (μm)	174.6
Lithium excess (%)	10
Ceramic thickness (μm)	10
Current collector thickness (μm)	20
Saving factor due to bipolar	2
Density - (g cm^{-3})	5.1
Areal mass - (g cm^{-2})	1.8×10^{-3}
Areal volume (cm^3 per cm^2)	1.0×10^{-3}

Current collector/flow field	
CC density (g cm^{-3})	2.7
Thickness um	20
Areal weight (g cm^{-2})	4.2×10^{-3}
Areal volume - (cm^3 per cm^2)	1.5×10^{-3}
Saving factor due to bipolar	1.3

Polypropylene Separator	
CC density (g cm^{-3})	0.50
Thickness (μm)	25
Areal weight (g cm^{-2})	$0.0009.5 \times 10^{-3}$
Areal volume - (cm^3 per cm^2)	$0.001.9 \times 10^{-3}$

Additional Electrolyte in Separator	
Solvent density (g cm^{-3})	1
Porosity of separator (%)	55
Thickness (μm)	25
Areal weight (g cm^{-2})	1.4×10^{-3}
Areal volume - (cm^3 per cm^2)	2.5×10^{-3}

Table 5.1: Table for material-to-system analysis of discharge data in chapter 3. The data is based on a cathode that can provide 31 mAh cm^{-2} at 1 mA cm^{-2} and a battery pack that provides 100 kWh. The discharge voltage, size and mass of the pack are accounted for. A cell which utilises a Li-metal anode protected by a ceramic solid electrolyte a polypropylene separator is considered. The values are calculated by using model provided by Gallagher *et al.*[26].

5.4 Conclusion

This work has investigated the effect of Li_2CO_3 accumulation during the cycling of Li-O_2 cells utilising high-capacity gas diffusion electrodes at practical rates. Using dual mediators, 12 cycles are achieved before the polarisation and capacity fading cause the cell to fail. During cycling, the gas diffusion electrode increases in thickness which, with the increasing polarisation, causes the energy density of the electrode to decrease before the capacity fades.

Fourier transform infrared spectroscopy measurements of the charged electrodes demonstrate the accumulation of Li_2CO_3 and Li-formate in the electrode over several cycles. The distribution of Li_2O_2 after discharge over multiple cycles is also measured. The distribution of Li_2O_2 varies over several cycles providing some insight into the effects of Li_2CO_3 accumulation and O_2 mass transport during discharge. After the 12^{th} charge, Li_2CO_3 and Li_2O_2 remain in the electrode, accounting for 30-50 % pore filling throughout based on the measured TAP densities of Li_2CO_3 and Li_2O_2. The accumulation of cycling products is corroborated by scanning electron microscopy images of the air interface of the GDE.

A redox mediator capable of oxidising Li_2CO_3 is employed to remove Li_2CO_3 after cell failure. The Li_2CO_3 oxidation by the mediator is investigated using *in situ* pressure monitoring experiments. Removal of Li_2CO_3 after treatment with the redox mediator is measured by acid treatment combined with mass spectrometry and scanning electron microscopy imaging. Upon removal of Li_2CO_3, the cell can cycle, achieving an additional 6 cycles after the first treatment and 4 cycles after a second treatment.

5.5 References

[1] Yao, X., Dong, Q., Cheng, Q. & Wang, D. Why Do Lithium–Oxygen Batteries Fail: Parasitic Chemical Reactions and Their Synergistic Effect. *Angewandte Chemie International Edition* **55**, 11344–11353 (2016).

[2] Lavi, O. *et al.* Electrolyte Solutions for Rechargeable Li-Ion Batteries Based on Fluorinated Solvents. *ACS Applied Energy Materials* 7485–7499 (2020).

[3] Bryantsev, Vyacheslav S. Giordani, V. *et al.* Predicting Solvent Stability in Aprotic Electrolyte Li – Air Batteries : Nucleophilic Substitution by the Superoxide Anion Radical (O_2^-). *Journal of Physical Chemistry A* **115**, 12399–12409 (2011).

[4] Freunberger, S. A. *et al.* The lithium-oxygen battery with ether-based electrolytes. *Angewandte Chemie - International Edition* **50**, 8609–8613 (2011).

[5] Mccloskey, B. D. *et al.* On the Efficacy of Electrocatalysis in Nonaqueous Li-O_2 Batteries. *Journal of the American Chemical Society* **133**, 18038–18041 (2011).

[6] Bryantsev, V. S. & Faglioni, F. Predicting autoxidation stability of ether- and amide-based electrolyte solvents for Li-air batteries. *Journal of Physical Chemistry A* **116**, 7128–7138 (2012).

[7] Oh, G. *et al.* Seed Layer Formation on Carbon Electrodes to Control Li_2O_2 Discharge Products for Practical Li-O_2 Batteries with High Energy Density and Reversibility. *ACS Applied Materials and Interfaces* **13**, 13200–13211 (2021).

[8] Chalasani, D. & Lucht, B. L. Reactivity of electrolytes for lithium-oxygen batteries with Li_2O_2. *ECS Electrochemistry Letters* **1** (2012).

[9] Xu, W. *et al.* The stability of organic solvents and carbon electrode in nonaqueous Li-O_2 batteries. *Journal of Power Sources* **215**, 240–247 (2012).

[10] Ryan, K. R., Trahey, L., Ingram, B. J. & Burrell, A. K. Limited stability of ether-based solvents in lithium-oxygen batteries. *Journal of Physical Chemistry C* **116**, 19724–19728 (2012).

[11] McCloskey, B. D. *et al.* Combining accurate O_2 and Li_2O_2 assays to separate discharge and charge stability limitations in nonaqueous Li-O_2 Batteries. *Journal of Physical Chemistry Letters* **4**, 2989–2993 (2013).

[12] Zhao, Z., Huang, J. & Peng, Z. Achilles' Heel of Lithium–Air Batteries: Lithium Carbonate. *Angewandte Chemie International Edition* **57**, 3874–3886 (2018).

[13] Thotiyl, M. M. O., Freunberger, S. A., Peng, Z. & Bruce, P. G. The Carbon Electrode in Nonaqueous Li-O_2 Cells. *Journal of the Americn Chemical Society* **135**, 494–500 (2013).

[14] McCloskey, B. D. *et al.* Twin Problems of Interfacial Carbonate Formation in Non-Aqueous Li-O_2 Batteries. *Journal of Physical Chemistry Letters* **3**, 997–1001 (2012).

[15] Gao, X., Chen, Y., Johnson, L. R., Jovanov, Z. P. & Bruce, P. G. A rechargeable lithium–oxygen battery with dual mediators stabilizing the carbon cathode. *Nature Energy* **2**, 17118 (2017).

[16] Gao, X., Chen, Y., Johnson, L. & Bruce, P. G. Promoting solution phase discharge in Li-O_2 batteries containing weakly solvating electrolyte solutions. *Nature Materials* **15**, 882–888 (2016).

[17] Lepoivre, F., Grimaud, A., Larcher, D. & Tarascon, J.-M. Long-Time and Reliable Gas Monitoring in Li-O_2 Batteries via a Swagelok Derived Electrochemical Cell. *Journal of the Electrochemical Society* **163**, A923–A929 (2016).

[18] Ottakam Thotiyl, M. M. *et al.* A stable cathode for the aprotic Li-O_2 battery. *Nature Materials* **12**, 1050–1056 (2013).

[19] Park, S. H. *et al.* Maximal Utilization of a High-Loading Cathode in Li-O_2 Batteries: A Double Oxygen Supply System. *ACS Applied Materials Interfaces* **11**, 30872–30879 (2019).

[20] Augustin, M., Vullum, P. E., Vullum-Bruer, F. & Svensson, A. M. Inside the electrode: Looking at cycling products in Li/O_2 batteries. *Journal of Power Sources* **414**, 130–140 (2019).

[21] Su, Z. *et al.* X-ray Nanocomputed Tomography in Zernike Phase Contrast for Studying 3D Morphology of Li-O_2 Battery Electrode. *ACS Applied Energy Materials* (2020).

[22] Han, X. B. & Ye, S. Structural Design of Oxygen Reduction Redox Mediators (ORRMs) Based on Anthraquinone (AQ) for the Li-O_2 Battery. *ACS Catalysis* **10**, 9790–9803 (2020).

[23] Krueger, B., Rücker, K. K. & Wittstock, G. Redox Mediators for Faster Lithium Peroxide Oxidation in a Lithium-Oxygen Cell: A Scanning Electrochemical Microscopy Study. *ACS Applied Energy Materials* **5**, 3724–3733 (2022).

[24] Xiong, Q., Huang, G. & Zhang, X. B. High-Capacity and Stable Li-O_2 Batteries Enabled by a Trifunctional Soluble Redox Mediator. *Angewandte Chemie International Edition* **59**, 19311–19319 (2020).

[25] Savina, A. A. & Abakumov, A. M. Benchmarking the electrochemical parameters of the $LiNi_{0.8}Mn_{0.1}Co_{0.1}O_2$ positive electrode material for Li-ion batteries. *Heliyon* **9**, 1–11 (2023).

[26] Gallagher, K. G. *et al.* Quantifying the promise of lithium-air batteries for electric vehicles. *Energy Environmental Science* **7**, 1555–1563 (2014).

[27] Matsuda, S. & Yasukawa, E. Carbon-black-based self-standing porous electrode for 500 Wh/kg rechargeable lithium-oxygen batteries. *Cell Reports Physical Science* **2**, 100506 (2021).

[28] Park, J. O. *et al.* A 1000 Wh kg^{-1} Li–Air battery: Cell design and performance. *Journal of Power Sources* **419**, 112–118 (2019).

[29] McNulty, R. *et al.* Oxygen reduction pathways in the Li-O_2 rattery: Understanding solvent-water interactions. *ECS Meeting Abstracts* **MA2020-02**, 492 (2020).

[30] Kwak, W.-J. *et al.* Lithium-Oxygen Batteries and Related Systems: Potential, Status, and Future. *Chemical Reviews* **120**, 6626–6683 (2020).

6

Conclusions and Further Work

Contents

6.1 Conclusions 169
6.2 Further Work 171
6.2.1 Gas Diffusion Polymers 171
6.2.2 O_2 Diffusion Channels 171
6.2.3 Li_2CO_3 Accumulation 172

6.1 Conclusions

The appeal of Li-O_2 batteries lies in their potential to achieve exceptionally high energy densities and gravimetric energies, surpassing those of the best Li-ion batteries and other competing chemistries. High energy densities must be achieved in GDEs with larger volumes to realise this potential, compensating for the mass and volume penalties associated with inactive cell components such as cell packaging and air/solvent handling components. However, oxygen mass transport becomes a significant challenge in GDEs with larger volumes (and thus greater thickness). Previous studies have shown that oxygen mass transport through the electrolyte and GDE is sluggish, resulting in limited discharge rates. In thick GDEs, Li_2O_2 preferentially forms at the gas/electrode interface, leading to premature cell failure and poor utilisation of the GDE volume for Li_2O_2

storage, ultimately resulting in subpar energy densities.

Alongside the challenge of oxygen mass transport in thick electrodes, ensuring the cell's reversibility poses another significant challenge. During cycling, parasitic side products, primarily Li_2CO_3, accumulate within the cell. The formation of Li_2CO_3 arises from chemical interactions involving the Li_2O_2 discharge product, the electrolyte, and carbon components. Additionally, reactive oxygen species, formed as intermediate electrochemical species, contribute to Li_2CO_3 formation. This issue intensifies over subsequent cycles, as the decomposition of Li_2CO_3 often necessitates high voltages, thereby exacerbating its accumulation.

This thesis focused on developing a GDE capable of delivering high energy density at practical discharge rates. For the first time, gas diffusion polymers, characterised by a high fractional free volume and rapid oxygen transport properties, were utilised to fabricate GDEs. When used as binders instead of conventional polymers like PTFE, these polymers have been shown to enhance the discharge capacity in thick GDEs. Additionally, this thesis demonstrated that by incorporating O_2 diffusion channels into the GDE, the energy density can be maintained in even thicker GDEs at higher discharge rates, indicating the possibility of achieving practical devices in terms of energy density. However, it is essential to note that despite achieving high energy density and advancing solvent stability, the battery exhibits limited cycle life, experiencing polarisation and capacity fading after only a few cycles at practical capacities and rates, as shown in the final results chapter.

The most significant challenge that is faced by Li-O_2 batteries is the development of an electrolyte and solvent formulation that remains stable in the presence of reactive oxygen species such as singlet oxygen, superoxide, and Li_2O_2 itself. Incorporating redox mediators capable of promoting Li_2O_2 formation away from the electrode surface has reduced instabilities associated with the carbon in GDEs. Similarly, understanding singlet oxygen formation has facilitated strategies to mitigate its reactivity. Developing an electrolyte and additive formulation that allows for the reversible formation and decomposition of Li_2O_2 could pave the way for the practical development of Li-O_2

batteries.

6.2 Further Work

6.2.1 Gas Diffusion Polymers

Gas diffusion polymers, such as Teflon AF2400, have demonstrated their efficacy in enhancing oxygen diffusivity within GDEs. These polymers, characterised by their high free volume, belong to a material group that exhibits excellent gas diffusion properties. In the present study, Teflon AF2400 was selected due to its perfluorinated nature and structural similarity to polytetrafluoroethylene, a commonly used binder in Li-O_2 batteries known for its chemical stability. Notably, other polymers such as poly(1-trimethylsilyl-1-propyne) and poly(4-methyl-2-pentyne) possess higher oxygen permeabilities than Teflon AF2400, making them potential candidates as binders for augmenting oxygen transport in GDEs. However, it is essential to consider that these polymers incorporate additional side groups and conjugated double bonds, which may introduce degradation concerns during cell operation. Therefore, a comprehensive investigation encompassing a wide range of polymers is warranted. This study should include assessments of capacity and rate capabilities during discharge and charge cycles, as well as an examination of polymer stability. A thorough understanding of the gas transport mechanism through these polymers within the context of Li-O_2 cells could provide valuable insights for the design of novel polymers.

6.2.2 O_2 Diffusion Channels

The incorporation of O_2 diffusion channels within the GDE has demonstrated notable improvements in discharge capacity, particularly at higher discharge rates. In this study, we aimed to leverage the knowledge gained from the distribution of Li_2O_2 at the end of discharge to determine the optimal thickness of the electrode and the appropriate distribution of O_2 diffusion channels. Future work will incorporate these experimental results with computational modelling approaches to investigate oxygen transport and

Li_2O_2 formation dynamics during discharge. The ultimate goal is identifying the ideal electrode architecture to achieve enhanced capacities at high discharge rates. Additionally, we will explore techniques to prevent electrolyte intrusion into the O_2 diffusion channels, enabling oxygen mass transport into the bulk of the GDE in the gas phase, which is much faster and more concentrated than O_2 mass transport in the electrolyte.

6.2.3 Li_2CO_3 Accumulation

The accumulation of Li_2CO_3 within the GDE during Li-O_2 battery operation poses a significant challenge to its cycle life. Identifying an optimal electrolyte and additive mixture that can facilitate the stable formation and decomposition of Li_2O_2 without giving rise to unwanted side reactions is crucial. While the findings in the third chapter demonstrated partial recovery of the cell by removing Li_2CO_3 and other insulating products, this approach may not be a practical long-term solution for addressing the Li_2CO_3 issue. Furthermore, there is a need for further investigation into the mechanistic understanding of the chemical reactions occurring with Li_2O_2 during battery operation, which ultimately lead to the formation of insulating products. By gaining a deeper understanding of these reactions, researchers can develop strategies to mitigate the formation of insulating products and enhance the overall performance and cycle life of Li-O_2 batteries.